

2-P (m x)

NASA CR-130194

Radiation Measurements from Polar and Geosynchronous Satellites

**COLOR ILLUSTRATIONS REPRODUCED
IN BLACK AND WHITE**

ANNUAL REPORT

for

National Aeronautics and Space Administration

GRANT NGR-06-002-102

(Period: 1 October 1971-30 September 1972)

by

Thomas H. Vonder Haar, Principal Investigator

Department of Atmospheric Science

Colorado State University

Details of illustrations in
this document may be better
studied on microfiche

January, 1973

(NASA-CR-130194) RADIATION MEASUREMENTS
FROM POLAR AND GEOSYNCHRONOUS SATELLITES
Annual Report, 1 Oct. 1971 - 30 Sep.
1972 (Colorado State Univ.) 202 p HC
\$12.25

N73-22568

Unclas

310 CSCL 04B G3/20 17203

Technical Monitors:

W. Bandeen and M. Pasternak

Laboratory for Meteorology and Earth Sciences

Goddard Space Flight Center, NASA

TABLE OF CONTENTS

	<u>page</u>
SUMMARY.	1
1.0 INTRODUCTION.	3
2.0 DISCUSSION OF SCIENTIFIC RESULTS.	3
a) Radiation Budget Results from the NIMEUS-3 Satellite.	3
b) Studies of the Solar Energy Absorption in the Atmosphere and the Oceans.	4
c) Studies of the Earth's Oceans and Surface Characteristics	5
d) Natural Variation of the Earth's Radiation Budget and its Relation with Circulation of the Atmosphere	5
e) Other Research under Grant Auspices	6
3.0 PROGRAM FOR THE NEXT REPORTING PERIOD	7

SUMMARY

In contrast with previous years, no new meteorological satellite data were processed during the October 1971-September 1972 reporting period. Rather, vast amounts of satellite measurements were applied to in-depth studies related to:

- a) Long-range weather forecasting and the study of short-term climate variations;
- b) The earth's environment as seen from space, including energy transport in the oceans and the first quantitative survey of the surface albedo of land areas; and
- c) The Global Atmospheric Research Program (GARP) by means of studies of the earth's cloud cover and through testing of a method to parameterize solar energy absorption in the atmosphere and oceans (separately) using satellite measurements. This method is needed to support the 1978 First GARP Global Experiment.

All of the applications are concerned with aspects of the study of the earth's radiation budget, the central area of grant research. Measurement and study of clouds using satellite data is a closely related problem. Methods and sensors to acquire better radiation budget and cloud data from future satellite systems can be guided by the application studies; some work leading in this direction was begun during the reporting period.

Overall the grant research is exceptionally timely. The satellite measurements are being applied to problems of high contemporary interest such as weather forecasting, the earth's global environment, short-term

climate variations and the possible impact of man on regional and global weather and climate. In addition, the satellite data are under study at a time when numerical models of the atmosphere are available to allow test and extrapolation of ideas and hypotheses derived from the satellite measurements.

Continuing research to be proposed under this grant will extend the application of the existing satellite data to the problems noted above, take advantage of new measurements from the polar (i.e., NIMBUS) and geosynchronous (i.e., SMS) satellites, and make even more use of the numerical models in GARP related research based on the global satellite measurements.

1.0 INTRODUCTION

During this second year of research under GRANT NGR 06-002-102, the scientific results noted below have come from detailed study of measurements from meteorological satellites as they can be applied to present-day problems of weather forecasting, short-term climate study and observations of the global atmosphere, ocean and land surface.

Two students (J. Ellis and P. Downey) have completed M.S. theses under grant sponsorship, a post-doctoral visitor (Dr. H. Korff) worked partly on our projects, and two students (J. Ellis and G. Campbell) are Ph.D. candidates being supported by this grant. Cooperative Nimbus-3 radiation budget data processing with E. Raschke, W. Bandeen and M. Pasternak in the first year of grant work lead to final drafts of publications of these basic results during the period of this report. In addition, new cooperative efforts with other LMES scientists are underway in areas of cloud study and determination of surface albedo.

2.0 DISCUSSION OF SCIENTIFIC RESULTS¹

a) Radiation Budget Results from the NIMBUS-3 Satellite

After data processing and production of 15-day average maps of planetary albedo, infrared radiant exitance, net radiation balance, etc., at LMES, the annual maps and averages were computed at Colorado State

¹In view of the economics necessary in research at the present time, detailed discussion of the scientific results will be presented through the attachment of theses, publications and technical reports in Appendix A. A synthesis is still provided and considerable savings accrue by not retyping and reproducing the results.

University. Preliminary results were published by Vonder Haar et al. (1972) - Appendix A1. A synopsis of all satellite radiation budget measurements during the 1960's, including NIMBUS-3 data, is provided by Vonder Haar and Raschke (1972) - Appendix A2. In general, NIMBUS-3 data confirm the earlier satellite results reported by Vonder Haar and Suomi (1971) and have provided the first detailed measurements of geographical variations in the earth's radiation budget. Extensive reports of the NIMBUS-3 results have been written under grant sponsorship and will be published in journals and as a NASA Technical Note in 1973. (There is the possibility that a few more days of radiation budget data from NIMBUS-3 might be processed).

b) Studies of the Solar Energy Absorption in the Atmosphere and the Oceans

Vonder Haar et al. (1972) - Appendix A3 - points out how measurements of planetary albedo from satellites can be used to study the mean value and variance of solar energy reaching the ground. Continued work in this area is important for planning ways to tap solar energy to ease our present energy crisis. Downey (1972) - Appendix A4 - used NIMBUS 3 measurements, the world-wide network of solar energy measurements, cloud-cover inferred (with difficulty) from vidicon data from ESSA 9 and ITOS-1, and some radiosonde humidity data to develop a method to parameterize the separate absorption of solar energy in the ocean and atmosphere. The method requires refinement, but if successful would allow global solar absorption data to be derived using only satellite measurements. This would be an important contribution to FGGE of GARP.

c) Studies of the Earth's Oceans and Surface Characteristics

Satellite radiation budget measurements over the northern hemisphere were combined with radiosonde data to derive a new estimate of the poleward energy transport by oceans (Vonder Haar and Oort, 1973 - Appendix A5). Direct ocean measurements are not possible with our present technology and thus the results derived with heavy dependence on satellite data are the primary data that will aid the development of numerical models of the ocean circulation. Since the role of the oceans was found to be more important, the need for increased air-sea energy exchange in mid-latitudes has been raised by this work.

A new study, in cooperation with NASA scientists, will use NIMBUS-3 data to derive the seasonal variation (and annual mean) surface albedo over land areas. This is a fundamental background measurement needed by both numerical modelers and those concerned with remote sensing from satellites.

d) Natural Variation of the Earth's Radiation Budget and its Relation with Circulation of the Atmosphere

Once NIMBUS-3 and earlier satellite radiation budget data have been processed, mapped and averaged, their application for significant research contribution just begins. Using all available data thus far (17 seasons) Vonder Haar (1972) - Appendix 6 - presented the first detailed phenomenological study of variations in the earth's radiation budget. Such studies can only be done from satellite data; they cannot be based on calculation. Results are currently under study but already show that year-to-year and season-to-season variations will provide much information about regional weather anomalies, biological response and

perhaps even allow long-range weather forecasting and short-term climate monitoring based on satellite data. In this regard, the radiation budget data were combined with northern hemisphere circulation data in a study by Ellis (1972) - Appendix 7. Results of this most interesting work revealed an apparent lag relation that is presently being checked. The next step are diagnostic model studies guided by the satellite results.

e) Other Research under Grant Auspices

Korff and Vonder Haar (1972) - Appendix A8 - reported results of a small measurement program to derive the variation of total directional reflectance of snow. These data were used to check a method required to be used in processing NIMBUS-3 measurements over Greenland and Antarctic.

Downey et al. (1972) - Appendix A9 - completed a study of extreme and persistent cloud cover during 1969-70 (the NIMBUS-3 period). The study was requested by the JOC of GARP and was used by them to plan deployment of buoys in the southern oceans during the upcoming FGGE. In addition, Downey (1972) used the cloud data in his solar energy study.

The principal investigator attended a working meeting of COSPAR WG6 with grant support. He contributed to the radiation budget, cloud measurement, and climate model portion of a document entitled "Application of Space Techniques to some Environmental Problems"; a report to the United Nations Conference.

In addition, with the encouragement of NASA scientists, the principal investigator considered the problem of future measurements of the earth's radiation budget by:

- i) leading a team in proposing for an engineering design study for an "Earth Integral Radiometer to Measure the Long-Term Global Radiation Budget for Climate Study ; and
- ii) participating in a team that proposed a "Long-Term Zonal Earth Energy Budget Experiment"

Although neither effort received funding to begin engineering study, it is hoped that continued cooperation with NASA scientists will provide the needed start on optimum systems to measure radiation budget in the near future. Work in this line, addressed to the general time and space sampling problem is presently underway, but the engineering must begin soon.

3.0 PROGRAM FOR THE NEXT REPORTING PERIOD

A proposal for an extension of grant research was accepted by NASA in September 1972 for the period through September 1973. In view of the many significant problems of a timely nature and the good results obtained thus far another grant extension will be proposed to continue this joint research with LMES.

APPENDIX 1

THE RADIATION BUDGET OF THE EARTH-ATMOSPHERE SYSTEM AS MEASURED FROM THE NIMBUS 3 SATELLITE (1969-1970)

T. H. VONDER HAAR^a, E. RASCHKE^b, M. PASTERNAK^c and W. BANDEEN^c

^a Colorado State University, Fort Collins, Col., USA

^b Ruhr-Universität Bochum, Bochum, FRG

^c Goddard Space Flight Center, Greenbelt, Md, USA

Measurements of the exchange of thermal and solar radiative energy between earth and space give information about the global climate, the prime forcing function that drives the circulation of the oceans and the atmosphere, and the budgets of radiative energy of local regions.

Data from the **Medium Resolution Infrared Radiometer** (MRIR) experiment on Nimbus 3 have provided global radiance measurements during four seasons (April 1969-February 1970). From these data values of the total radiation budget of the earth-atmosphere system were derived on varying time and space scales and compared with previous satellite measurements and theoretical computations.

Results confirm earlier satellite measurements. They show a warmer [254° vs. 250 °K] and darker [albedo: 28-29% vs. 35%] planet than was previously believed: most of the radiative energy input in excess of those older results in tropical regions, significant geographical variation of the local radiation budgets, a very small seasonal variation in global energy exchange with space, and higher poleward energy transport requirements. In addition, the Nimbus 3 data offer the first medium areal resolution views of both the northern and southern hemispheres' radiation budgets during all seasons.

1. Introduction

Measurements from meteorological satellites allow study of the natural variation of energy exchange between earth and space. During the 1960's, a large amount of low area resolution (smoothed) data was acquired [1] to provide results on the planetary scale. Subsequently, global observations from Nimbus 2 in 1966 [2] provided independent information on the planetary scale as well as a first view of the higher resolution radiation patterns during the north in summer only.

This paper contains latest results from the Nimbus 3 satellite measurements in 1969 and 1970. Some preliminary comparisons between Nimbus 2 and 3 data (June 1966-1969) have already shown good agreement [3].

2. The Radiation Measurements

A column of the earth's surface plus atmosphere ranging over any size domain has a radiation budget which is determined by the net radiation flux at the top of the atmosphere. It results from incoming solar radiation flux (derived from knowledge of the solar constant, chosen as $1.95 \text{ cal cm}^{-2} \text{ min}^{-1}$

[4]) and the outgoing fluxes of emitted thermal and reflected and scattered solar radiation. The ratio of the latter to the incoming flux is the planetary albedo. Dimensions are energy per area per time (e.g. $\text{cal cm}^{-2} \text{min}^{-1}$) except albedo, which is given as a percentage. All values were derived as daily averages.

Nimbus 3 satellite was launched on 14 April 1969, into a 1100 km sun-synchronous orbit with ascending node near 1130 LT. These orbit elements were maintained the same throughout the data period for the MRIR experiment (intermittent from launch through early February 1970). A description of the cross-track scanning MRIR experiment, calibration, and data reduction is given in [5]. Detectors were chopped thermistor bolometers in five separately filtered channels (6.5–7.0, 10–11, 14.5–15.5, 20–23, and 0.2–4.0 μm). Procedures for processing the radiance measurements are described in detail for the similar Nimbus 2 experiment in [2] and for the Nimbus 3 in [3].

Total infrared radiant emittance W_L is calculated with the use of all four channels of infrared measurements in a regression method based upon atmosphere model calculations; a limb-darkening correction is used for non-nadir measurements. Planetary albedo values are derived to represent the daily average of this parameter at the location of measurement. This requires integration over the entire daylight period not only to account for the variation in incoming solar energy, but also to account for the non-isotropic bi-directional reflectance characteristics of the scene measured. Three angular reflectance models were applied (ice, clouds, and ocean) to the appropriate measurements of reflected radiance. They were derived from aircraft, satellite, and balloon observations. Error analyses of the basic radiation data and the processing techniques are in progress.

The special temporal sampling characteristics from the sun-synchronous orbit of Nimbus 3 allow measurements over most of the (non-polar) world near 1130 and 2330 LT. In regions where a pronounced diurnal variation of cloud cover or surface conditions may be anticipated, such as in most tropical land areas, the radiation budget results from Nimbus 3 must be interpreted accordingly.

3. Radiation Budget Results

For data recording reasons, only a sample of days in the four seasons of Nimbus 3 coverage are used to represent each specific season. For this paper the days are 15–30 April 1969, 1–15 July 1969, 3–17 October 1969, 20 January–3 February 1970. "Annual" values are formed from averages of these seasonal samples.

3.1. Annual and Seasonal Averages for the Global Case

Table 1 lists a comparison of results from earlier meteorological satellites of the United States, from Nimbus 3, and from medium resolution sensors carried on Meteor satellites (infrared only) during 1969–1970 [6]. The mean values from the early satellites agree with the Nimbus 3 values to within 3–4%, which is almost the measurement accuracy.

Table 1

Global radiation budget — outgoing long-wave radiation fluxes
($\text{cal cm}^{-2} \text{ min}^{-1}$) and albedo (%)

	Satellites 1962–1966	Nimbus 3 1969–1970	Meteor 2 1969–1970
March–May	0.33 (30%)	0.34 (29%)	0.37
June–Aug.	0.34 (26%)	0.36 (28%)	0.37
Sept.–Nov.	0.34 (28%)	0.35 (28%)	0.37
Dec.–Feb.	0.33 (31%)	0.34 (29%)	0.35
Annual	0.34 (30%)	0.35 (29%)	0.36
Annual net radiation	0.00	0.00	—

On the annual scale they both show that the planet is warmer (outgoing flux of long-wave radiation $W_L = 0.34\text{--}0.35$ vs. $0.325 \text{ cal cm}^{-2} \text{ min}^{-1}$) and darker ($A = 28\text{--}30\%$ vs. 35%) than was believed before the satellite measurements [7]. These data point out the lack of a pronounced seasonal variation of the global energy exchange with space. Infrared measurements from Meteor confirm this, even though they are systematically higher than other measurements. Annual net radiation values of 0.00 indicate no net gain or loss of energy to within measurement accuracy (the magnitude depends, of course, on the chosen solar constant).

3.2. Results for Latitude Zones

The annual course of insolation has emphasized study of the earth-atmosphere system in a zonally symmetric mode. Figs. 1, 2, and 3 show the satellite radiation budget data in this context.

In Fig. 1, annual values from the two independent satellite experiments both show that pre-satellite calculations significantly overestimated the albedo

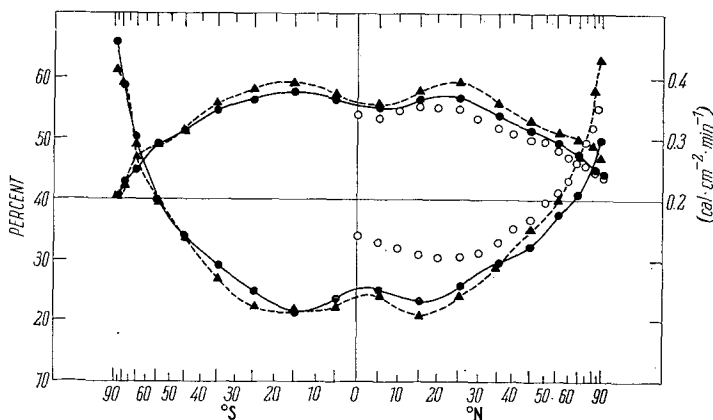


Fig. 1. Comparison of mean annual values of planetary albedo and infrared radiant emittance measured from Nimbus 3 (\blacktriangle --- \blacktriangle), from earlier satellites [1] (\bullet --- \bullet), and calculated in pre-satellite days [7] (\circ).

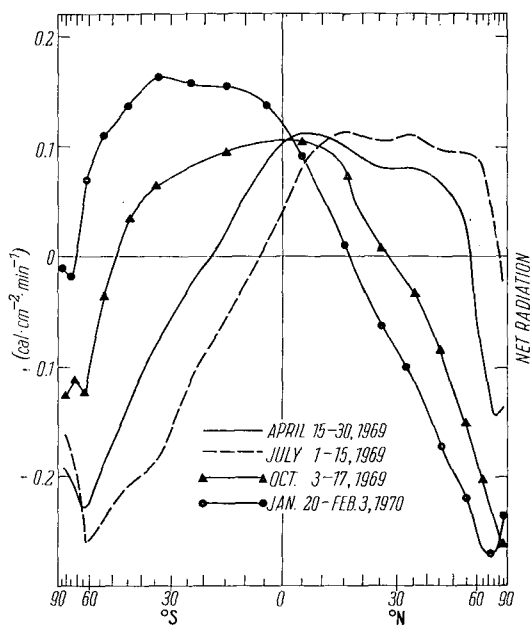


Fig. 2. Values of zonally averaged net radiation as measured from Nimbus 3 during: April (1969 (—)); July 1969 (---); October 1969 (Δ — Δ); January–February 1970 (\bullet — \bullet).

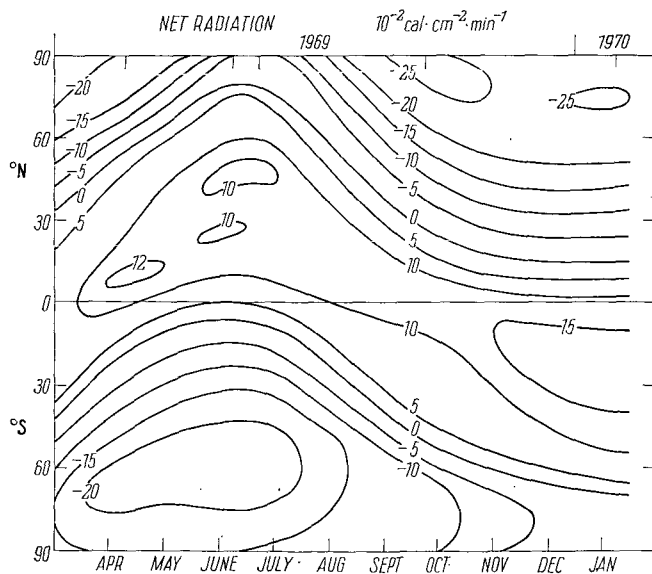


Fig. 3. Time latitude section of radiation balance measured from Nimbus 3.

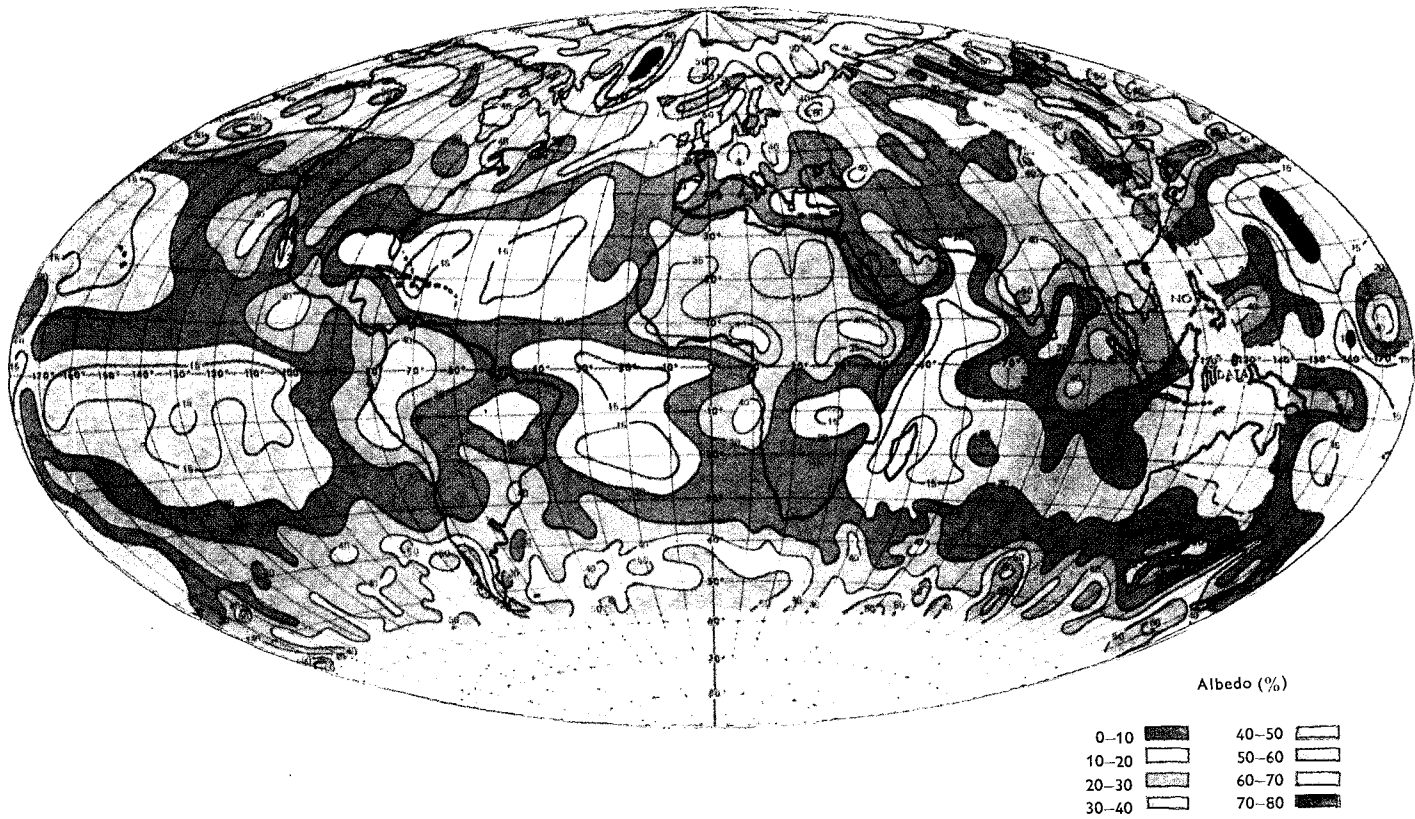


Fig. 4. Example of geographical variation of planetary albedo. Nimbus 3 (0.2-0.4 μm channel). 1-15 July 1969.

in the tropics and uniformly underestimated infrared energy to space at all latitudes. Thus when viewed from space the plant appears "darker" primarily in the tropics, and "warmer" from equator to pole.

Fig. 2 shows seasonal values of net radiation. The gradient of this parameter with latitude is the ultimate driving force for our planetary circulations. The Nimbus 3 values for 1969 differ from earlier satellite measured values [1] in that the summer gradients are greater and less in the southern and northern hemispheres, respectively. This points out the possibility of interannual variation [1], now under further study. Interseasonal trends of zonal averages of the net radiation can be seen in the time-latitude section in Fig. 3. Here the area of radiative surplus migrates with sun's declination. Major surplus areas are the subtropics of both hemispheres; they do not present mirror images in the two hemispheres, a consequent in part of different land masses.

3.3. Geographical Variations of Radiation Budget

A zonally symmetric view of energy exchange between earth and space (Figs. 1-3) neglects significant longitudinal variations caused by semi-permanent circulation features and land masses even on the longest time-averaged periods [1]. The MRIR experiment allows detailed study of this variation and thus of the local radiation budgets. Fig. 4 depicts variations of the planetary albedo measurements during 1-15 July 1969. Bright features such as the Sahara desert, Indian monsoon, intertropical convergence zone, and regions of persistent stratus cloud can be noted by relatively high values of albedo. Portions of the subtropical ocean areas must have been virtually cloudfree; they have albedos measured as low as 10%.

3.4. Implications regarding Atmospheric Transport Processes

Over a time period (for example, annual) when all energy storage in the land, oceans and atmosphere is negligible, the measured radiation budget represents the local energy budget of an earth-atmosphere column. In this case an integration from pole to pole of the net energy excess or deficit in each column allows derivation of the net horizontal energy transport required by the atmosphere and oceans combined. The magnitude of this transport is a measure of the "vigor" of the fluid circulation. Fig. 5 shows the transport requirements inferred with these assumptions from the Nimbus 3 measurements, from the earlier satellite measurements [1], and from pre-satellite [5] and recent [8] calculations. The calculation results [6, 8] are based on relatively simple radiative transfer methods applied to imperfectly known climatological descriptions of atmospheric conditions.

In the northern hemisphere, as may be expected from § 3.2, both measurement sets indicate that more energy is transported than was believed before the satellite measurements. For the southern hemisphere the satellite data from Nimbus 3 depart from both earlier measurements and recent calculations. In general, however, both satellite data sets as well as the very recent cal-

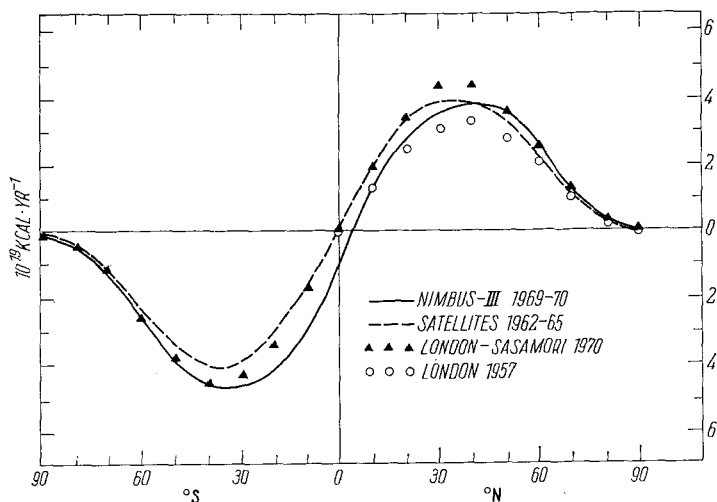


Fig. 5. Comparison of required energy transport by atmosphere and oceans as inferred from satellite measurements from earlier satellites [1] (— — —) and Nimbus 3 (—) and from calculations before satellites [7] (○) and after satellites [8] (▲).

culations [8] are in agreement that the poleward transport of energy by atmospheric and oceanic circulation is stronger (by 15–20%) than was previously believed.

4. Summary and Conclusions

Results of the Nimbus 3 radiation data confirm the long-term planetary scale measurements of radiation budget from earlier satellites of a warmer and darker planet, with a more active horizontal circulation thus required. Inter-annual variations of the radiation budget and its components at various scales need further investigations based on satellite experiments which should be considered to consist of more than ten years duration and where the same evaluation methods are used and the solar constant is accurately tracked. Then relative changes of the budget might be observed, which are due to changes in the circulation patterns and, possibly also of the pollution of the system land-ocean-atmosphere.

Acknowledgments

We thank our colleagues at NASA for aid, particularly J. Barksdale and H. Powell. This research was partially supported by NASA Grant NGR-06-022-102 from the Laboratory for Meteorology and Earth Surveys, Goddard Space Flight Center, and by the contract WRK 189 from the Federal Ministry of Education and Science, Bonn, Germany.

References

- [1] T. H. VONDER HAAR and V. E. SUOMI, *J. Atmos. Sci.* **28**, 305 (1971).
- [2] E. RASCHKE and W. R. BANDEEN, *J. Appl. Met.* **9**, 215 (1970).
- [3] E. RASCHKE et al., *Space Research XI*, 661 (1971).
- [4] A. DRUMMOND, *Advanc. Geophys.* **14**, 1 (1970).
- [5] A. McCULLOCH, *Nimbus 3 User's Guide*, NASA 1969.
- [6] V. BOLDYREV and I. VETLOV, *Meteorol. i Gidrol.* **10**, 23 (1970).
- [7] J. LONDON, Final Report, Contract AF 19(122)-165, Dept. of Meteorology and Oceanography, New York University (1957).
- [8] J. LONDON and T. SASAMORI, *Space Research XI*, 639 (1971).

APPENDIX 2

**MEASUREMENTS OF THE ENERGY EXCHANGE
BETWEEN EARTH AND SPACE FROM
SATELLITES DURING THE 1960's**

by

T. H. VONDER HAAR

E. RASCHKE

MEASUREMENTS OF THE ENERGY EXCHANGE BETWEEN
EARTH AND SPACE FROM SATELLITES
DURING THE 1960's

by

T. H. Vonder Haar
E. Raschke

Support for this project was provided by:

Grant NGR-06-002-102

National Aeronautics and Space Administration

Atmospheric Science Paper No. 184

April, 1972

ii

ABSTRACT

MEASUREMENTS OF THE ENERGY EXCHANGE BETWEEN EARTH AND SPACE FROM SATELLITES DURING THE 1960's

The net radiation budget of the earth-atmosphere system can be obtained from satellite measurements of the infrared radiant emittance and reflected and scattered solar radiation along with a knowledge of the solar constant. During the 1960's experimental and operational meteorological satellites carrying thermistor bolometer sensors designed for this task were in orbit during about 60 months. Our paper presents a synopsis of results from these measurements including: a global planetary albedo of 30%, long-term global radiation balance within measurement accuracy (2-3%), the net equator-to-pole radiation gradients (and their variation) that drive our atmospheric and oceanic circulations, as well as selected measurements of radiation budget terms over particular geographical areas. Future satellite experiments are planned to allow measurements of higher precision and with better space and time sampling. However, the results thus far have provided a solid descriptive base for more detailed diagnostic studies, especially regarding the significance of observed interannual radiation budget variations and also the separate consideration of energetics of the atmosphere and the ocean.

iii

T. H. Vonder Haar
Colorado State University

E. Raschke
Ruhr-Universitat Bochum

MEASUREMENTS OF THE ENERGY EXCHANGE BETWEEN
EARTH AND SPACE FROM SATELLITES
DURING THE 1960's

I. Introduction

While atmospheric scientists have been interested in the global radiation budget for more than 100 years, measurements have been available only in the last twelve years. Earth-orbiting satellites provided the platform for radiation budget measurements; first experiments were flown on Explorer VII in 1959.

As in earlier days, our desire to study the radiation budget is high because:

- a) global climate is a result of the total energy exchange (by radiation) between our planet and space,
 - b) the large-scale atmospheric and oceanic circulations are forced fundamentally by the gradient of radiation exchange with space between pole and equator,
- and
- c) local area radiation budgets at the "top of the atmosphere" are in an important boundary condition for local and regional energetics that affect both the physical and biological processes in the region of interest.

In recent years, radiation budget measurements from satellites have also been recognized as important controls for checking the performance of numerical models of the atmosphere's circulation on a global scale.

Invited Paper M-70 presented at the Joint Meeting of the German Physical and Meteorological Societies, Essen, Sept.-Oct. 1971.
To be published in Annalen der Meteorologie, 1972.

Figure 1 shows a schematic diagram of the terms of the radiation budget of the earth-atmosphere system. Three terms are shown, with the net radiation or radiation budget, Q_n , as the residual of:

- $H_S(\lambda, \phi, t)$ - the direct irradiance of solar energy at $p = 0$
(computed from an assumed value of the solar constant, I_0 , $1.95 \text{ cal} \cdot \text{cm}^{-2} \cdot \text{min}^{-1}$)
- minus $W_S(\lambda, \phi, t)$ - solar energy reflected and scattered from
clouds, atmospheric gas and aerosol, and the
surface (measured from the satellite)
- minus $W_L(\lambda, \phi, t)$ - the infrared radiant emittance from clouds,
atmospheric constituents and the surface
(measured from the satellite)

All dimensions (as the solar constant) are energy per unit area and unit time. The functionals λ, ϕ, t refer to longitude, latitude and time. They serve to note the time and space scale dependence of the radiation budget; our schematic box could apply to a unit area at some location or to the entire global envelope. Note that the planetary albedo, A , is the ratio W_S/H_S .

Two basically different types of radiation budget experiments have been flown on U.S. satellites [SUOMI, et al. (1967), McCULLOCH (1969)]. They are shown in Figure 2 as:

- a) the medium resolution infrared radiometer; it has a narrow angle (5 degree) field of view, scanning capability by rotating a mirror, four infrared channels and one to measure the radiance of reflected solar radiation.
- and b) omnidirectional (2π steradian) sensors named the Wisconsin hemisphere or Wisconsin plate radiometers (cones provide special checks for these omnidirectional sensors); they always consist of matched pairs of black and white sensors, the former to measure all radiation (solar and infrared), the latter only the infrared.

Both types of experiments use the same radiation detectors, thermistor bolometers. All other experiment parameters (field-of-view, time constant, spectral response, and method of data reduction) differ. Furthermore, the basic radiation measurement (of the radiation budget parameters shown in Figure 1) for the scanning radiometer is radiance, while the omnidirectional sensors measure radiant power. Data reduction techniques (more complex for the scanning radiometer data) are employed to derive the desired values of $W_S(\lambda, \phi, t)$ and $W_L(\lambda, \phi, t)$. From the viewpoint of scientific use, either system should be acceptable for studying the earth's radiation budget. However, the more complex scanning radiometer system does provide radiation budget measurements at one order of magnitude finer on the space scale. Both experiments undergo absolute calibration before launch into space. In addition, the omnidirectional sensors are checked against the direct solar energy during each orbit; the scanning radiometer views a reference source of known temperature on the satellite. In this way, relative calibration in space is provided for all measurements by the Wisconsin experiment and for the infrared measurements from the scanning radiometer. Reflected solar radiance measurements from the latter are checked against regions on the earth such as deserts.

II. Results for the Entire Earth and for Latitude Zones

VONDERHAAR and SUOMI [1971] have discussed results from satellite experiments in orbit before 1967. RASCHKE and BANDEEN [1970] have discussed two-and-one-half months of 1966 scanning radiometer data in detail. Both of these references cite numerous previous papers dealing with both the methods of data reduction and special studies using the radiation budget measurements. The present paper discusses all of the measurements available thus far, including those acquired from NIMBUS-III in 1969 and 1970.¹

Table 1 summarizes the measurements of the annual and seasonal radiation budget of the entire planet. First value is infrared radiant emittance, W_L ; followed by planetary albedo (A). Accuracy estimates for the results of the U.S. experiments are plus-or-minus one unit of the least significant digits shown; this yields relative measurement accuracies of about 3%.

For the annual case, both the earliest satellite data set (1962-66) and the most recent (1969-70) show that our earth-atmosphere system has a planetary albedo of 29-30%, outgoing infrared radiation to space averaging $0.34 \text{ cal} \cdot \text{cm}^{-2} \cdot \text{min}^{-1}$, and net global radiation balance (within measurement accuracy) when the solar constant is $1.95 \text{ cal} \cdot \text{cm}^{-2} \cdot \text{min}^{-1}$. The infrared emission is equivalent to a black-body temperature of (255°K), higher than the value estimated by LONDON [1957] before the

¹ See also Raschke, et. al. (1971), Vonder Haar, et. al. (1972, and Raschke, et. al. (1972) for a more detailed discussion of the Nimbus III measurements.

TABLE 1

GLOBAL RADIATION BUDGET			
	SATELLITES 1962-1966	NIMBUS-III 1969-70	METEOR-II 1969-70
M A M	.33 (30%)	.35 (29%)	.37
J J A	.34 (26%)	.35 (28%)	.37
S O N	.34 (28%)	.35 (28%)	.37
D J F	.33 (31%)	.34 (29%)	.35
ANNUAL	.34 (30%)	.34 (29%)	.36
ANNUAL NET RADIATION	.00	.00	—

4 (A)

satellite experiments. Also, our planet is darker than was previously believed; it has a lower albedo than the early value of 35%. Recall that these results have now been obtained from two different types of satellite experiments, thus giving further assurance of the accuracy of both data sets.

Seasonal variation of the planetary radiation budget is small. A very small tendency for a brighter and colder planet during the period December - May is seen in both sets of U.S. data. Infrared experiments on METEOR satellites in 1969-70 (BOLDYREV and VETLOV [1970]) also detected a slightly colder earth during the Northern Hemisphere winter.

The annual case is especially interesting when we relax the space scale and consider the satellite measurements gathered into averages for each specific latitude zone. Figure 3 shows the resulting mean meridional profiles for (a) the satellite measurements, 1962-66, (b) NIMBUS-III results and (c) the estimates by LONDON in pre-satellite days¹. As in the global case (Table 1) the satellite sets show general agreement even though they were not obtained during the same years. All measurements differ strikingly from the estimates of planetary albedo in the tropics. The darker planet noted previously is due primarily to a lower albedo in the region 0 - 30°N than was previously believed. Apparently, the calculations of LONDON and others more than ten years ago used over-estimates of opaque (reflecting) cloud amount in the tropics. Separate evidence for this has been noted by VONDERHAAR and HANSON [1969]. They found that the measured solar radiation reaching the surface in the tropics is greater than all previous estimates.

¹ BOLLE [1971] compares the satellite measurements of VONDERHAAR and SUOMI [1971] ((a) above) with very recent, new estimates by LONDON and SASAMORI [1970]. The new estimates are now in much better agreement with the measurements.

Infrared radiation to space is measured to be slightly greater than was calculated at all latitudes. The significance of the overall differences between measurements and earlier calculations is seen in Figure 4. Here, the net energy gain or loss of two earth-atmosphere zones is shown for the annual time period (horizontal lines) and for mean seasonal conditions (shaded bar, I=DJF). LONDON's results for the annual case are also shown. In the region $0 - 10^{\circ}\text{N}$ much more energy ($1.5 \times 10^{16} \text{ cal} \cdot \text{min}^{-1}$) is gained during the year than was previously estimated. At polar regions the old and new values are much closer, giving the same depiction as would have been inferred from Figure 3: more energy gained by our atmosphere and oceans at low latitudes, the need for increased poleward energy transport, slightly increased energy loss to space throughout the mid-latitudes.

Most of the energy gain is to the tropical oceans. Thus, the required increase in poleward transport must be accomplished by either direct sensible heat flux by the oceans, or increased air-sea energy exchange followed by energy transport in the atmosphere through some combination of the sensible, potential and latent energy mechanisms. On a seasonal basis, the energy gain and loss shown in Figure 4 varies in the expected relative pattern. Note, however, that a small net energy gain is measured over the North polar cap during summer. This energy, together with that advected from lower latitudes combines to allow the warming of air and melting of surface snow and ice characteristic of that season.

III. Measured Variation of the Radiation Gradient from Equator to the Poles

In the previous section we have seen the results and hypotheses that

are based on consideration of the satellite radiation budget measurements over a long time scale (5-6 years). Of special interest also are the measured values in specific seasons and their interannual variation. Figure 5 displays a simple index, $\Delta R_{N_E/P}$, used as a first look at the fundamental net radiation gradient between equator and pole. On the very longterm this gradient depicts the thermal forcing of our earth-atmosphere system; values of the mean annual gradient for both the northern and southern hemispheres are shown as horizontal lines in Figure 4. They are nearly the same, with the northern hemisphere slightly larger.

The same figure shows mean seasonal values (dots) and the range of gradients measured from satellites in specific seasons (range bars). In both hemispheres the gradient is least in summer and greatest in fall, with the most abrupt change between these two seasons. Mean winter values are less than those of fall due to a gradient reversal in polar regions not considered by our simple index. Therefore, the fall and winter values should be considered practically the same in the mean.

Measured variation had been the least in Northern Hemisphere winter, greatest in Northern Hemisphere summer during the 1962-66 period shown in Figure 5. Recent values of this same gradient measured from NIMBUS-III during 1969-70 fell within the range bars in all seasons and in both hemispheres except during Northern Hemisphere winter. This re-emphasizes the need for a continuing program of radiation budget measurement so that we may measure and study the full natural variation of the radiation gradient.

On the time scale of a specific season, one cannot expect a direct relation between the radiation gradient measured from satellites and the resulting atmospheric circulation. Whereas, this would be the case

on Mars, our oceans and hydrologic cycle provide other mean to release energy into the atmosphere and often operate out of phase with each other and with the radiative forcing from space.

Nevertheless, as an illustration of the potential equivalent variations of radiation gradient we have constructed the simple linear example shown in Figure 6. Here the mean summer and winter values of the thermal wind (V_T)¹ are used with the corresponding mean values of radiation gradient index (from Figure 5) to derive the linear relation. Mean values of gradient measured over the southern hemisphere are noted by the arrows, they would indicate a lesser range of the mean V_T in that hemisphere. Shaded areas denote the range of measured gradient in all summers and winters and the equivalent range of circulation activity. Research now underway will study the actual physical and dynamical relations between the satellite measurement of radiation resulting from atmospheric conditions and the subsequent circulations forced, in part, by the radiative energy exchange. The grossly oversimplified illustration in Figure 6 serves as a reminder that this application of the satellite measurements can proceed in parallel with an increasingly polished description of "mean" conditions.

IV. High Frequency Time and Space Changes in the Earth's Radiation Budget

This section is included to present the reader with examples of the radiation budget measurements from satellites on time and space scales sufficient to consider the local and regional energetics. The higher frequency data from the scanning radiometer is emphasized. Most results

¹ Northern Hemisphere from 20°-70°N between the levels 1000 and 300mb.

are recent ones from NIMBUS-III; they are described in detail in RASCHKE et al [1972] .

Figures 7a, 7b, and 7c denote time-latitude sections from pole-to-pole during April, 1969 - February 1970. They show the monthly course of outgoing infrared radiation, W_L ; planetary albedo, A ; and net radiation, Q_N , in each latitude zone.

Geographical variations of the same radiation measurements are shown for the period 1-15 July 1969 in the set of figures 8a, 8b and 8c. Here the high area resolution of the NIMBUS-III experiment can be used to examine radiation patterns characteristic of the tropical convergence zone, sub-tropical desert regions and special areas of cloudiness in mid-latitudes during these 15 days.

A final example of the geographical variation of radiation to space is seen in Figure 9 . Based on measurements from nine seasons with the low area resolution Wisconsin sensors, we see here the natural range of the seasonal values of infrared emittance to space. As in the case of the interannual radiation gradients, more study of these results is now in order. Some features, such as the large range of values over the Indian monsoon sector, can be interpreted with little difficulty. Questions are posed, however, by the maxima of range in the tropical eastern Pacific and by the minima near the British Isles. The latter might be due to persistent cirriform cloudiness.

V. Summary

During the 1960's, radiation budget measurements from satellites have allowed quantitative study of the global energetics of our atmosphere-

ocean system. A continuing program is planned, including independent measurement of the solar constant. Thus far, the measurements returned from two basically different types of satellite experiments are in agreement on the longterm global scales where they are most comparable. This fact, together with independent estimates of the accuracy of measurement from each system, shows that we now measure the energy exchange between earth and space better than it can be calculated.

Examples of application of the radiation budget data were shown. They can be related to the age-old problem of climate change, to the basic question of the thermal forcing of our circulation systems, and to the contemporary problems of local area energetics and computer modeling of the atmosphere.

ACKNOWLEDGEMENTS

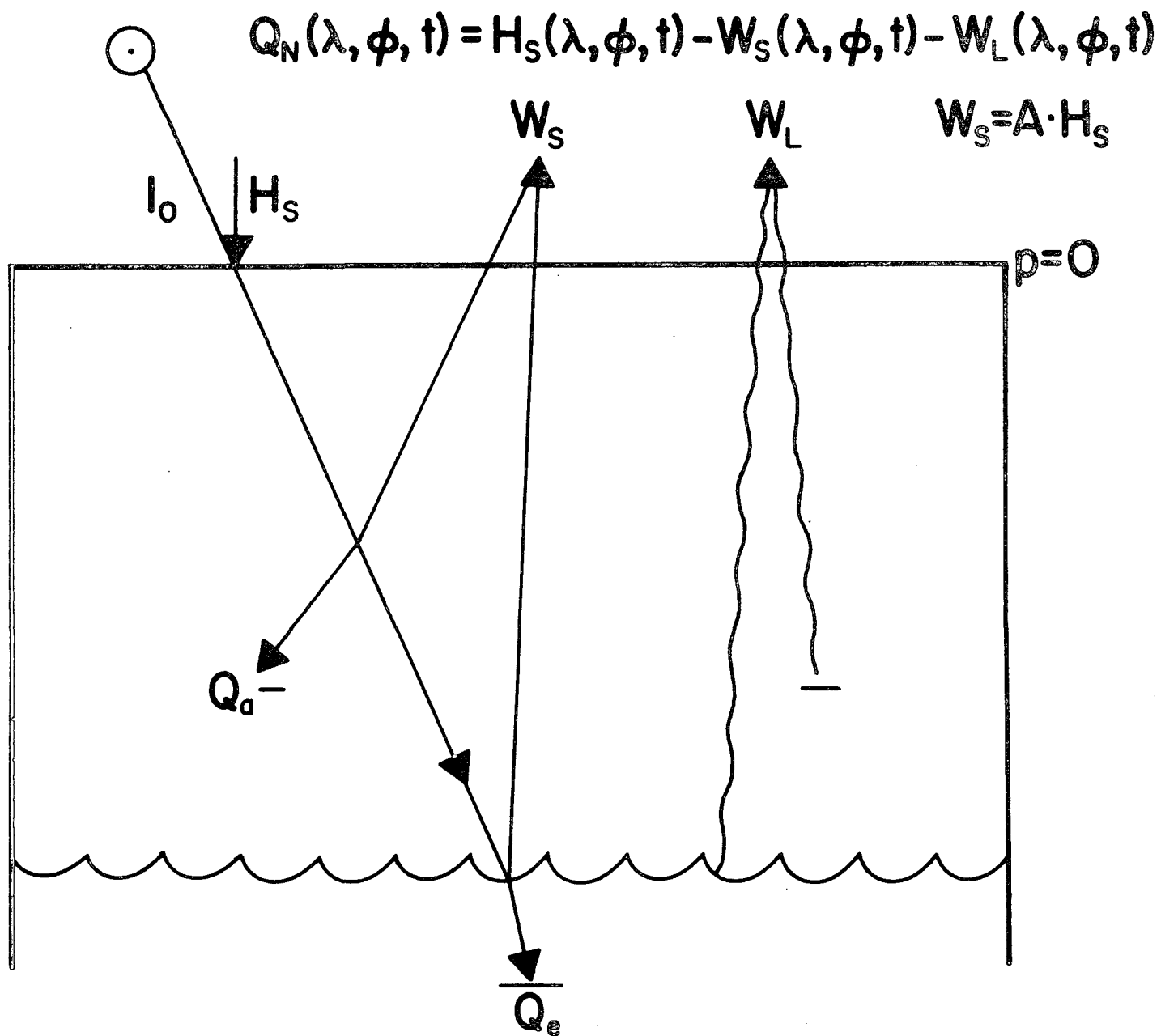
This research has been supported by the Laboratory for Meteorology and Earth Sciences, Goddard Space Flight Center, NASA, under Grant NGR-06-002-102 and with aid from contract WRK 189 from the Federal Ministry of Education and Science, Bonn, Germany.

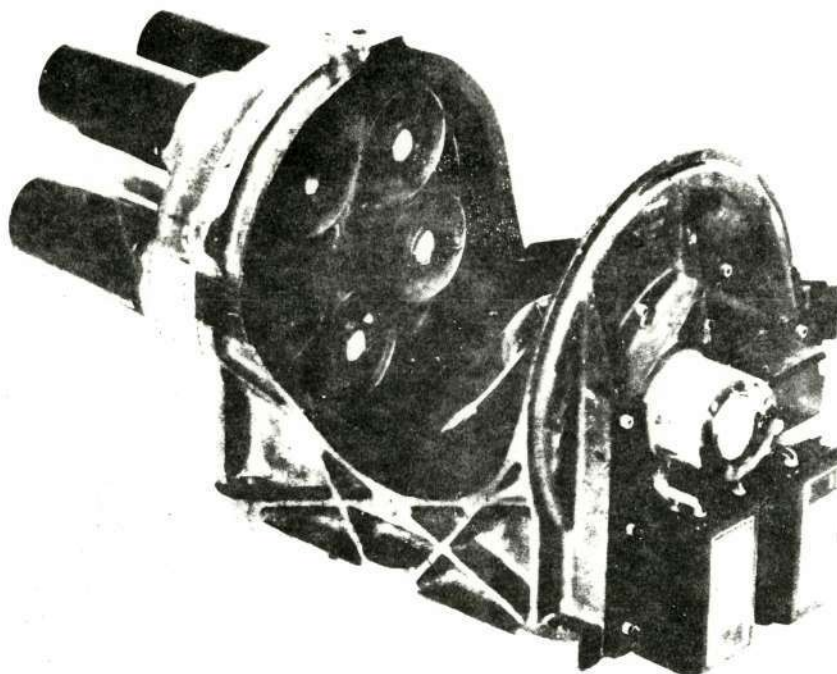
REFERENCES

- Boldyrev, V. and I. Vetlov, 1970: Met. and Hydrol., 10, 23.
- Bolle, H., 1972: Strahlungshaushalt nach satelliten messungen, Annalen de Meteorologie (in press).
- London, J., 1957: A study of the atmospheric heat balance. Final Report, Contract AF 19(122)-165, Dept. of Meteorology and Oceanography, New York University, 99 pp.
- London, J. and T. Sasamori, 1971: Radiative energy budget of the atmosphere. Space Research XI, Springer-Verlag, Berlin.
- McCulloch, A., 1969: The medium resolution infrared radiometer (MRIR) experiment, The NIMBUS-III Users Guide, NASA, GSFC
- Raschke, E., and W. R. Bandeen, 1970: The radiation balance of the planet earth from radiation measurements of the satellite NIMBUS II. J. Appl. Meteor., 9, 215-238.
- Raschke, T. H. Vonder Haar, W. Bandeen and M. Pasternak, 1971: The radiation balance of the earth-atmosphere system during June and July 1970 from NIMBUS-III radiation measurements. Some preliminary results. Space Research XI, Springer-Verlag, Berlin.
- Raschke, E., T. H. Vonder Haar, W. R. Bandeen, and M. Pasternak, 1972: The radiation balance of the earth-atmosphere system from NIMBUS-III radiation measurements (15 April 1969 - 3 February 1970). NASA Tech Note, in preparation.
- Raschke, E., and T. H. Vonder Haar, 1971: Climatological studies of the Earth's radiation and its variability with measurements of the satellite NIMBUS-III. (Paper presented at Symposium on Phys. and Dynam. Climat., Leningrad, 16-20 May 1971).
- Suomi, V. E., K. J. Hanson and T. H. Vonder Haar, 1967: The theoretical basis for low-resolution radiometer measurements from a satellite. Annual Report, Grant WBG-27, Dept. of Meteorology, University of Wisconsin, 79-100.
- Vonder Haar, T. and K. Hanson, 1969: Absorption of solar radiation in tropical regions. J. Atmos. Science, 26, 4, 652-655.
- Vonder Haar, E. Raschke, M. Pasternak and W. Bandeen, 1972: The radiation budget of the earth-atmosphere system as measured from the NIMBUS-III satellite (1969-70), Space Research XII, Springer, Verlag (in press).
- Vonder Haar, T. and V. Suomi, 1971: Measurements of the earth's radiation budget from satellites during a five-year period Part I: Extended time and space means. J. Atmos. Sci., Vol. 28, No. 3, April 1971, pp. 305-314.

LIST OF FIGURES

1. Schematic depiction of the radiation budget of an earth-plus-atmosphere column.
2. View of the radiation budget sensors flown on U.S. satellites during the 1960's.
3. The annual values of infrared radiant emittance, W_L , (top); and planetary albedo, A , (bottom) along a mean meridional cross-section as measured from satellites during 1962-66 (solid) and from Nimbus III 1969-70 (dash); and as calculated by LONDON (1957) (dot).
4. Energy gain and loss in latitude zones as measured from satellites (after VONDER HAAR and SUOMI, 1971).
5. Values of the index of radiation gradient from equator to pole in both the Northern and Southern hemispheres (see text) (after VONDER HAAR and SUOMI, 1971).
6. Illustration noting the potential (indirect) relation between radiation gradient, as measured from satellites and the circulation of the atmosphere.
7. Time-latitude sections of (a) planetary albedo, (b) outgoing long-wave (infrared) radiation and (c) net radiation, as measured from the Nimbus III satellite during April 1969 - February 1970.
8. Maps of the geographical distribution of (a) planetary albedo, (b) outgoing infrared radiation, and (c) net radiation as measured during 16-30 June, 1969, from the Nimbus III satellite (after RASCHKE and VONDER HAAR, 1971).
9. Geographical variation of the range of mean seasonal infrared radiation lost to space as measured from the first generation meteorological satellites of the United States.

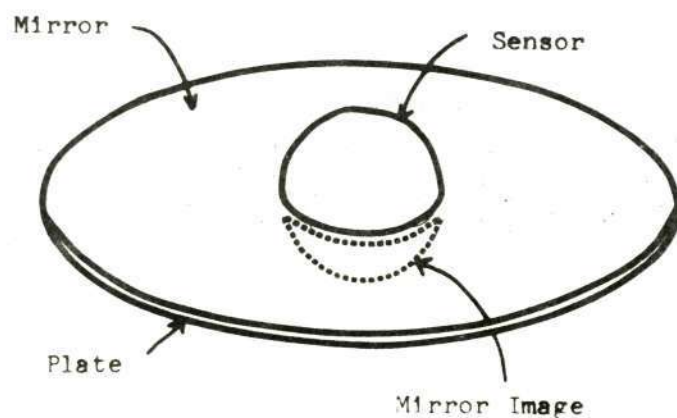




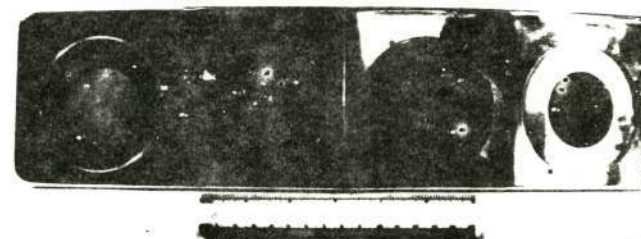
Reproduced from
best available copy.

THE MEDIUM RESOLUTION INFRARED RADIOMETER

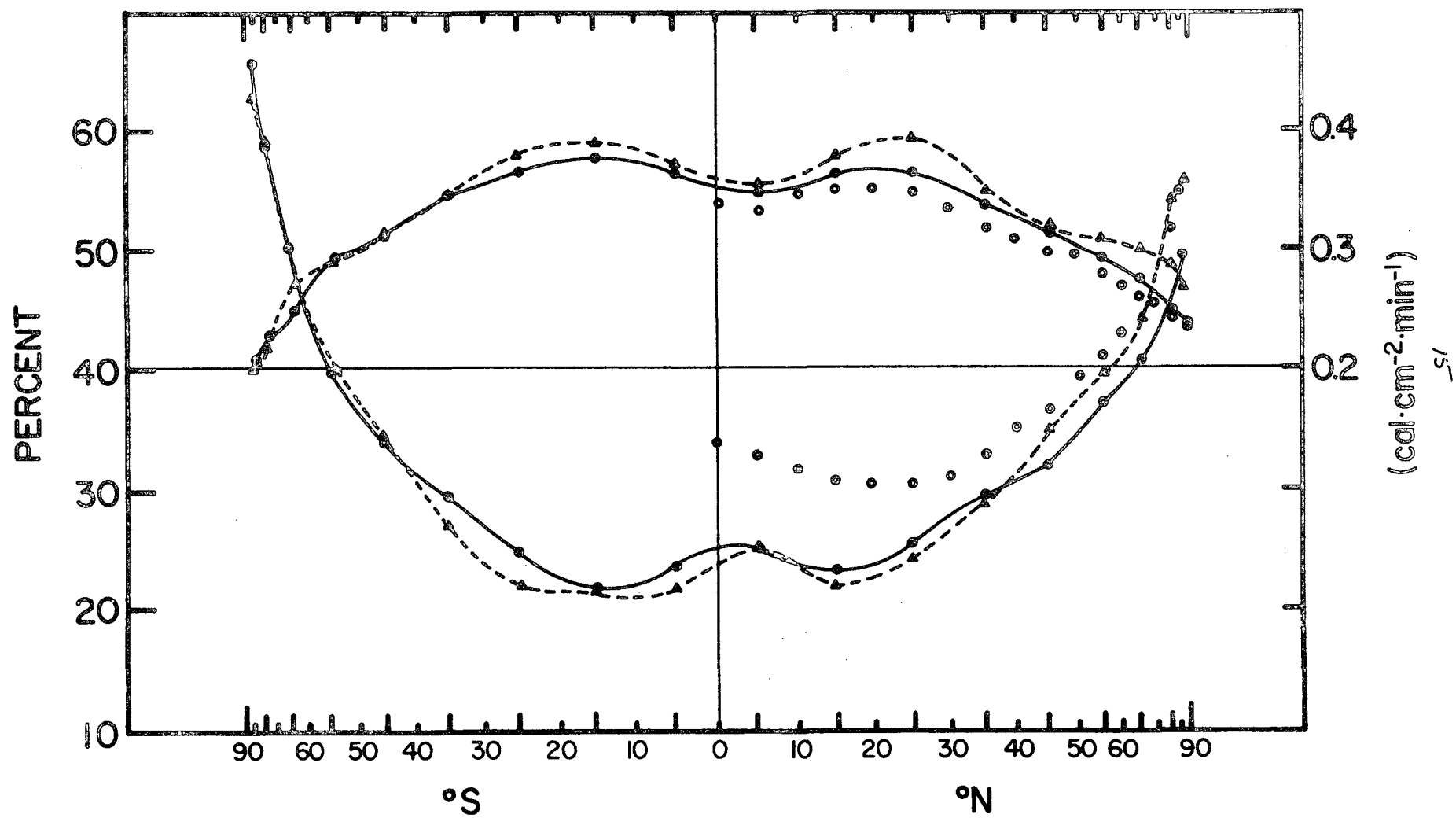
14

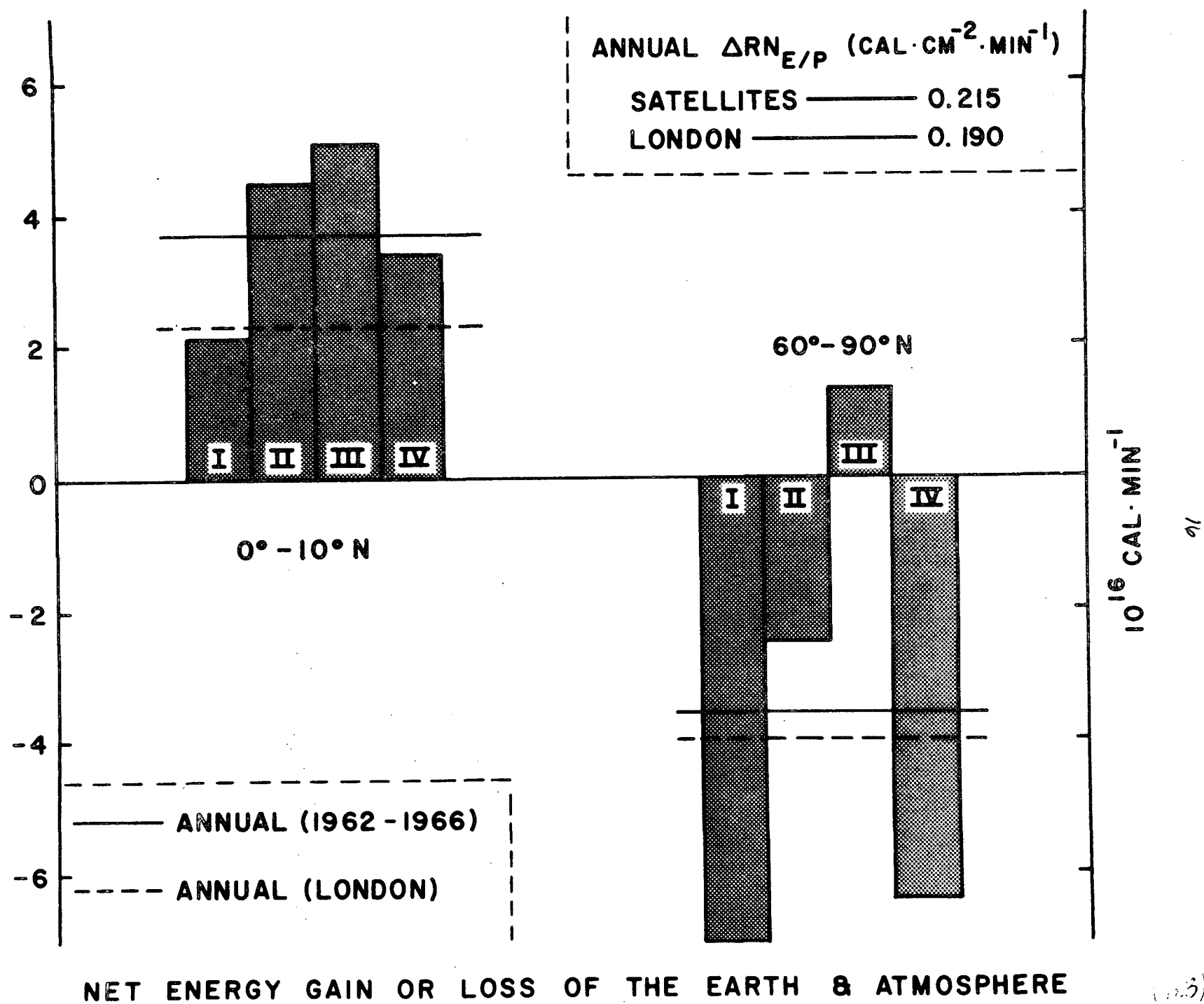


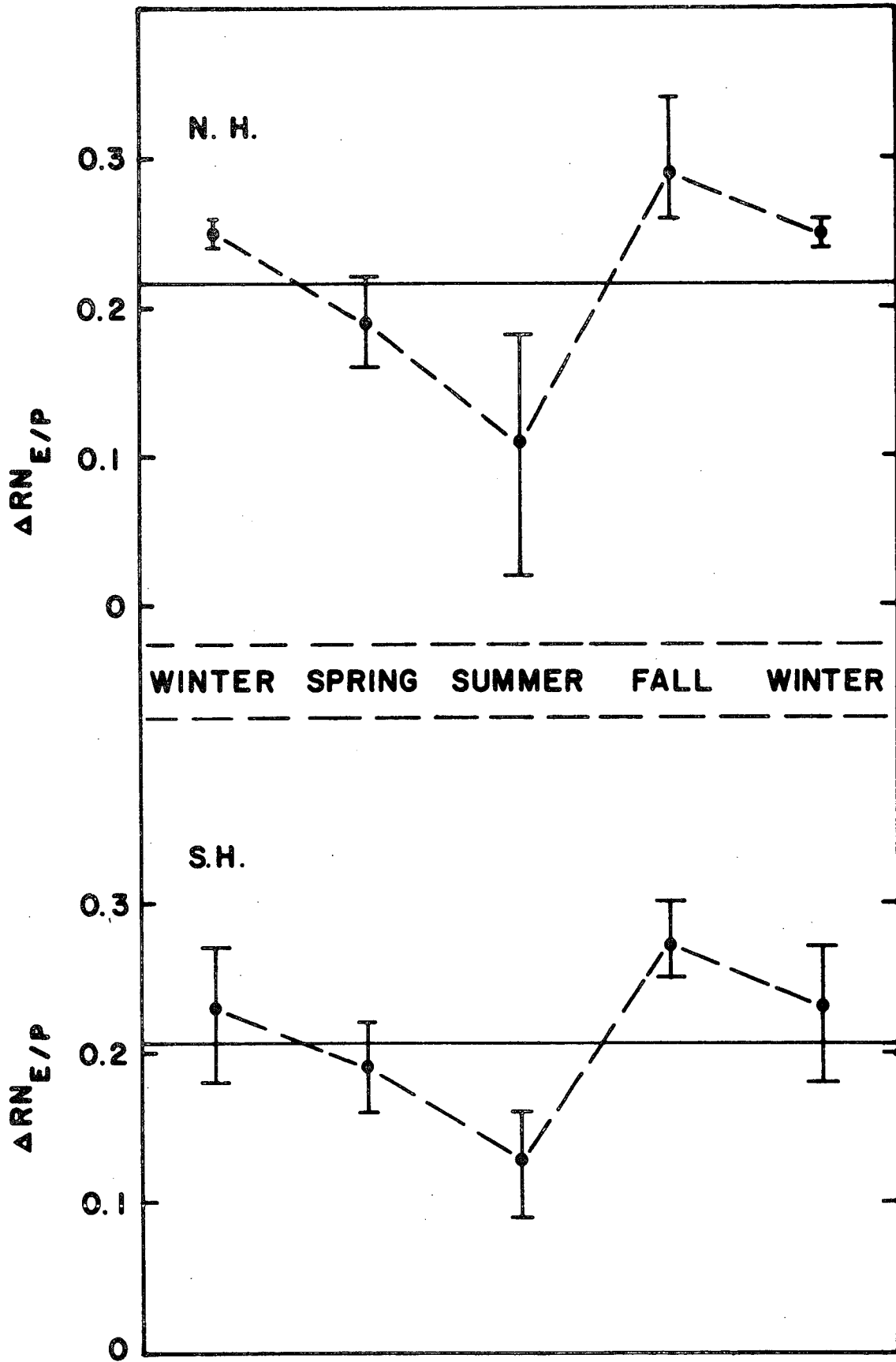
WISCONSIN HEMISPHERE RADIOMETER

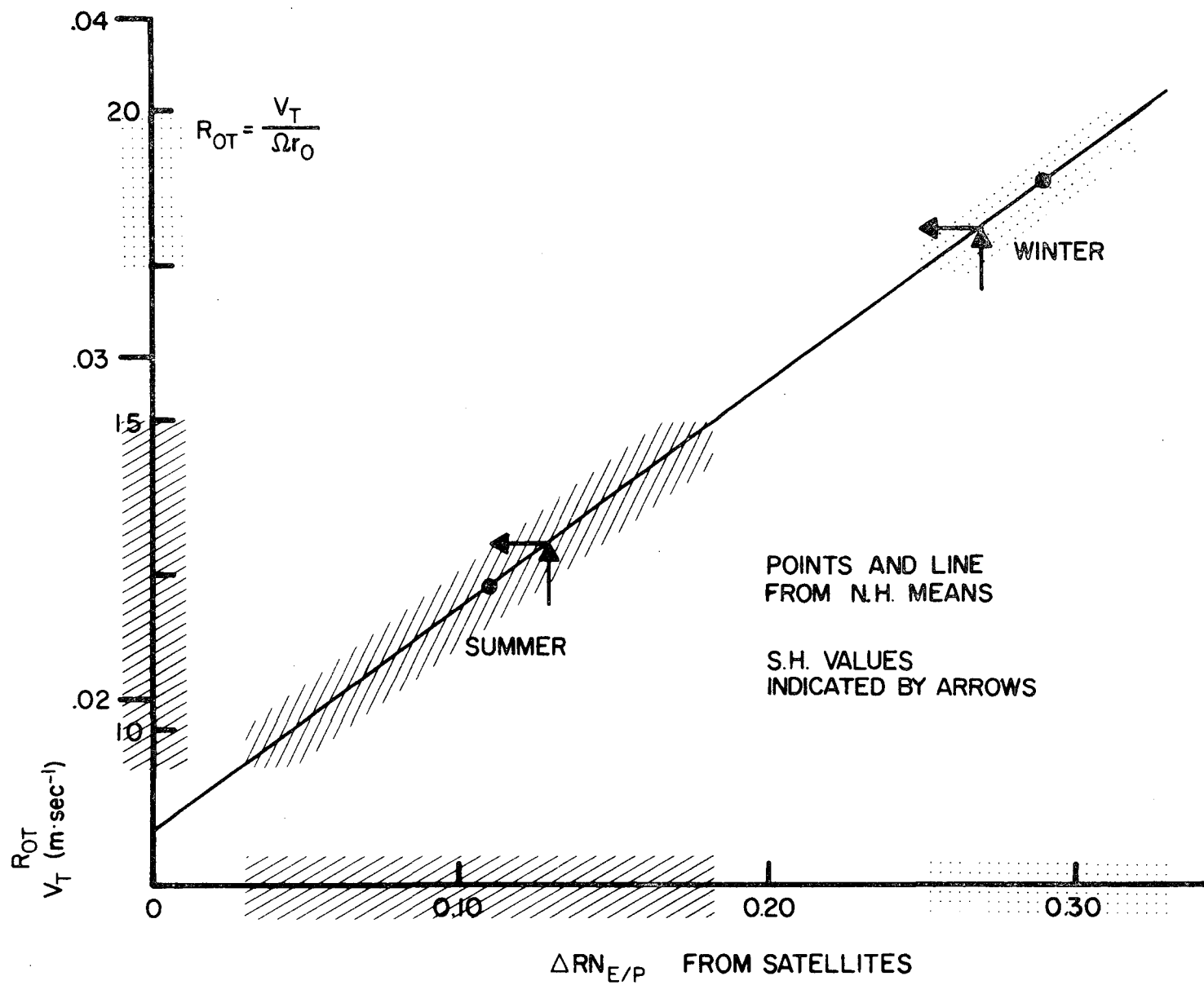


WISCONSIN FLAT-PLATE AND CONE RADIOMETERS

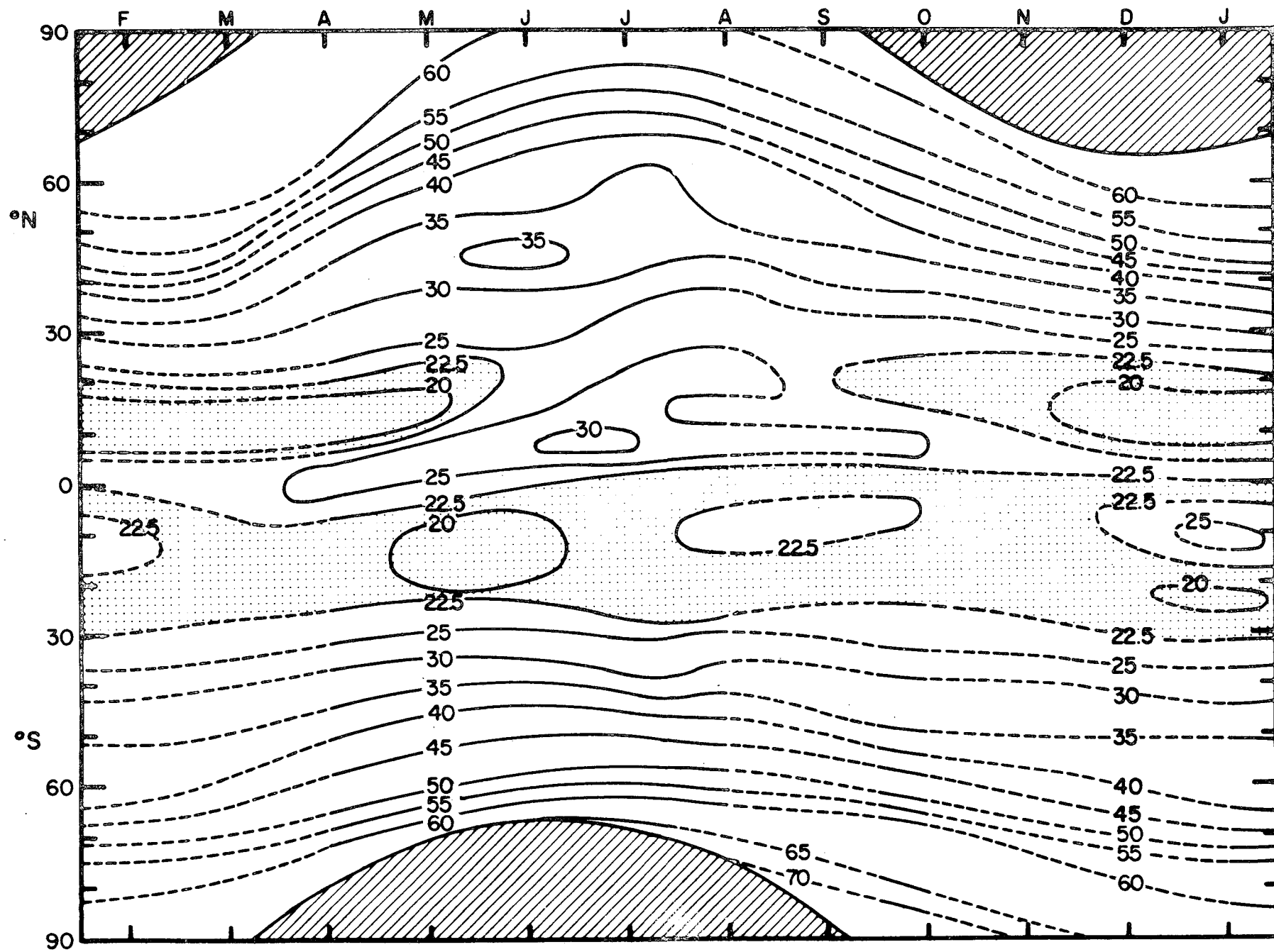


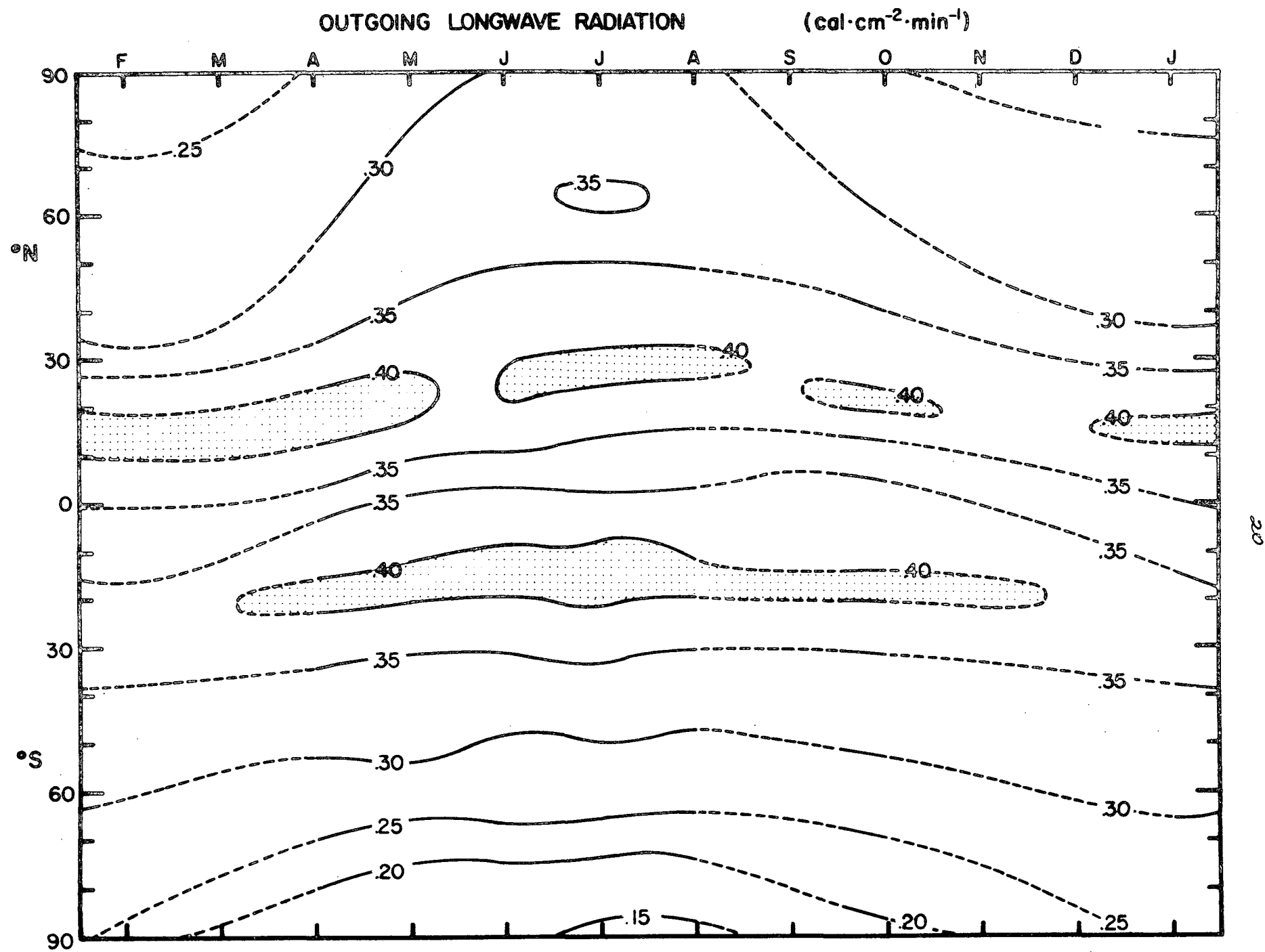


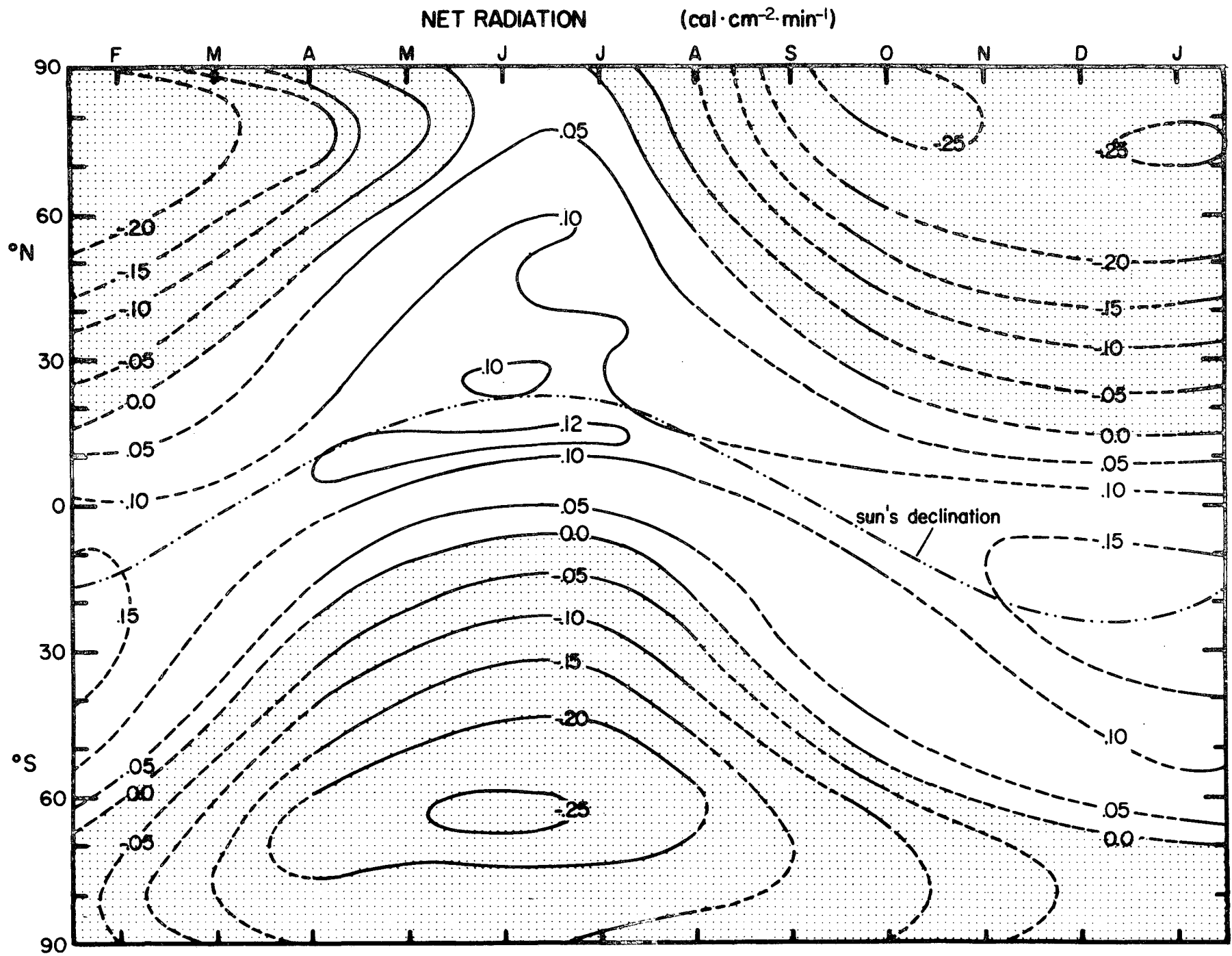




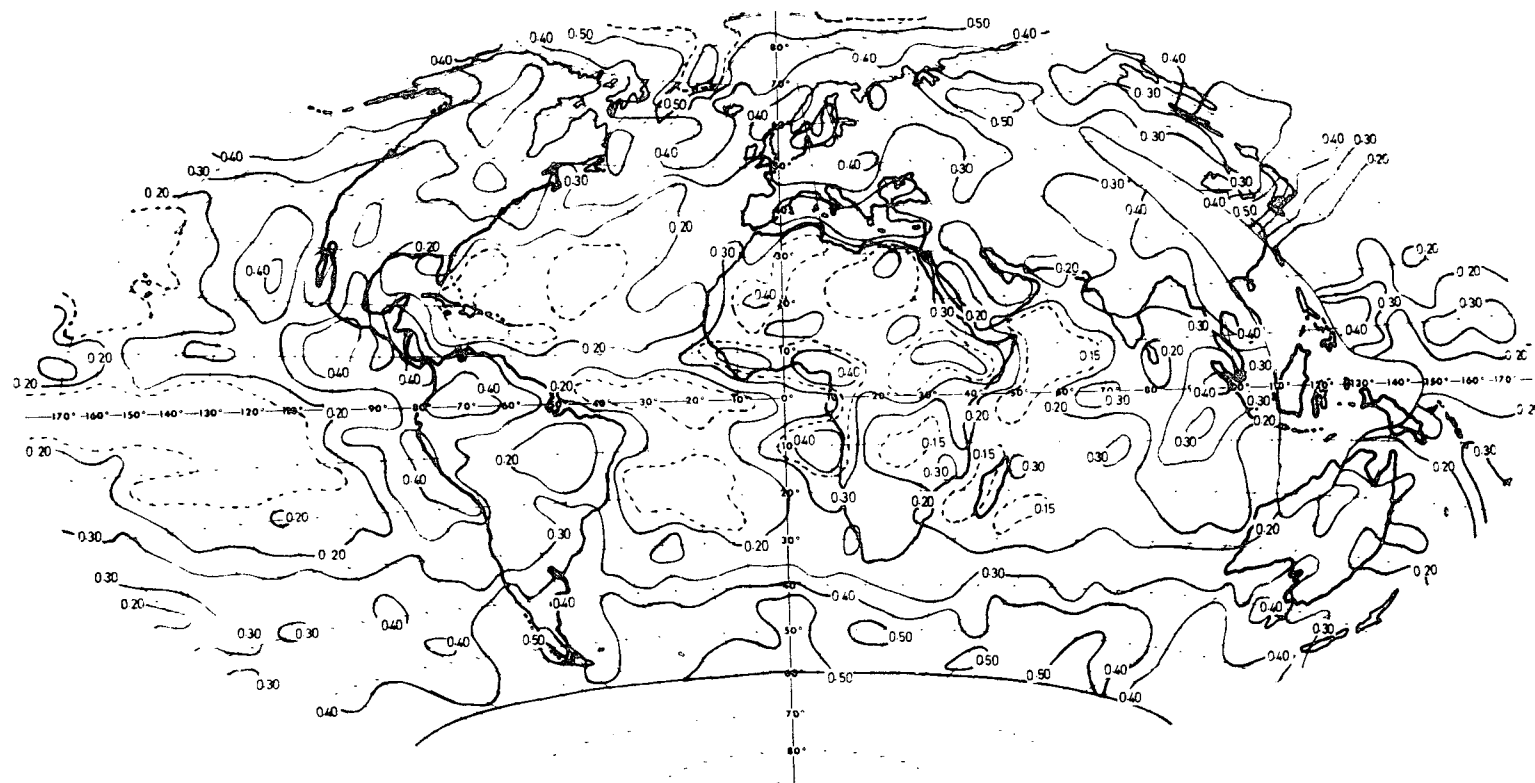
ALBEDO (percent)





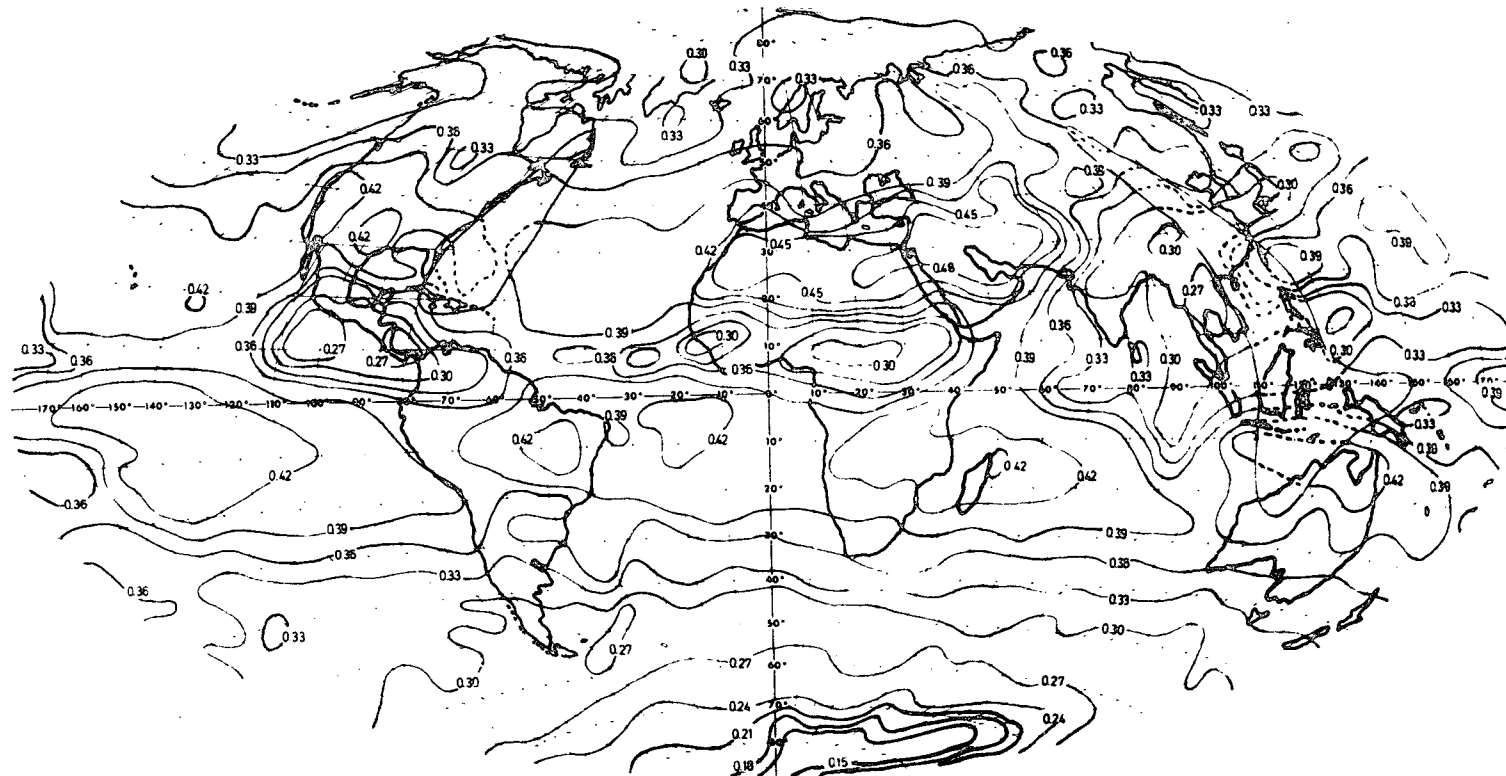


ALBEDO
NIMBUS III: 1-15 JULY 1969



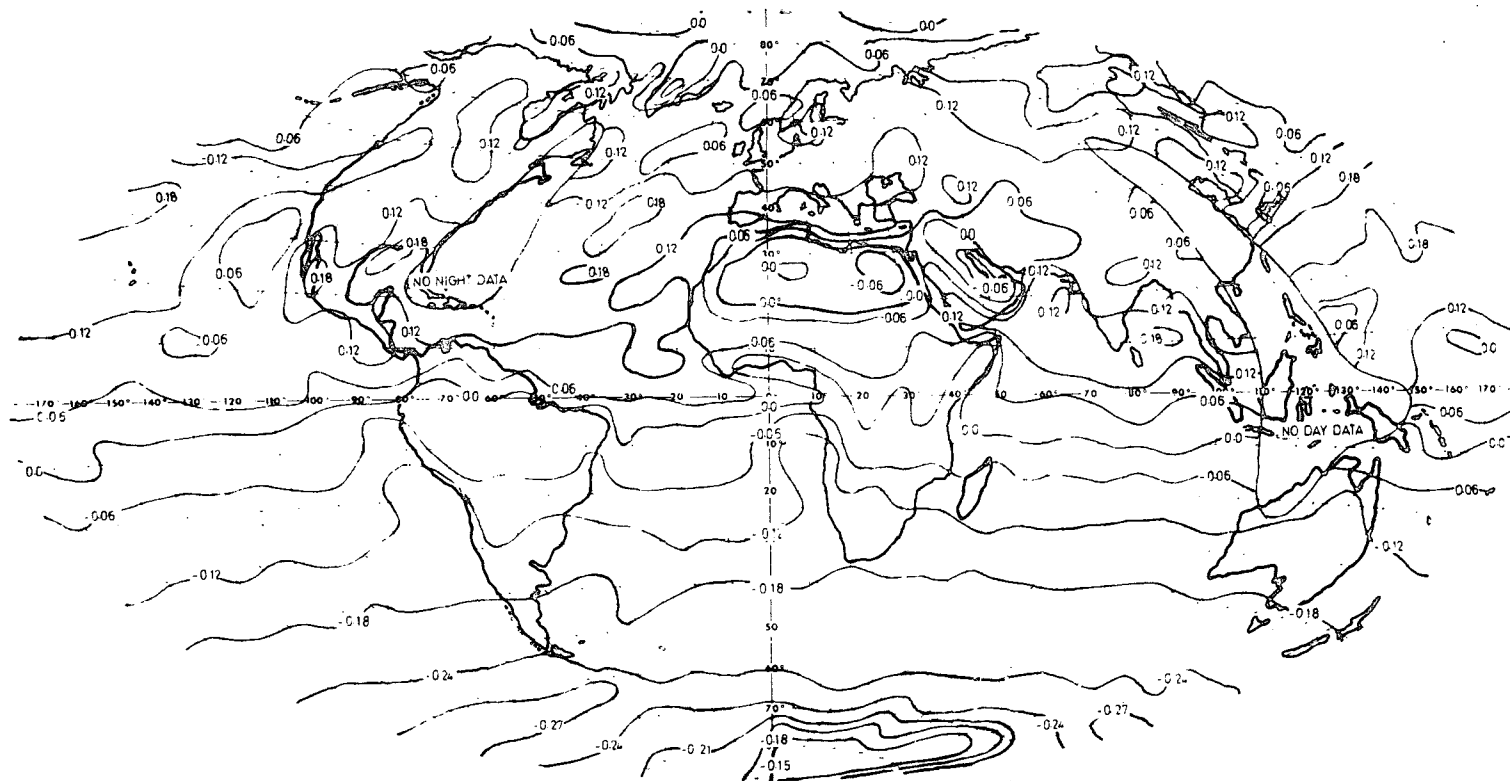
OUTGOING LONGWAVE RADIATION
(cal cm⁻² min⁻¹)

NIMBUS III 1-15 JULY 1969

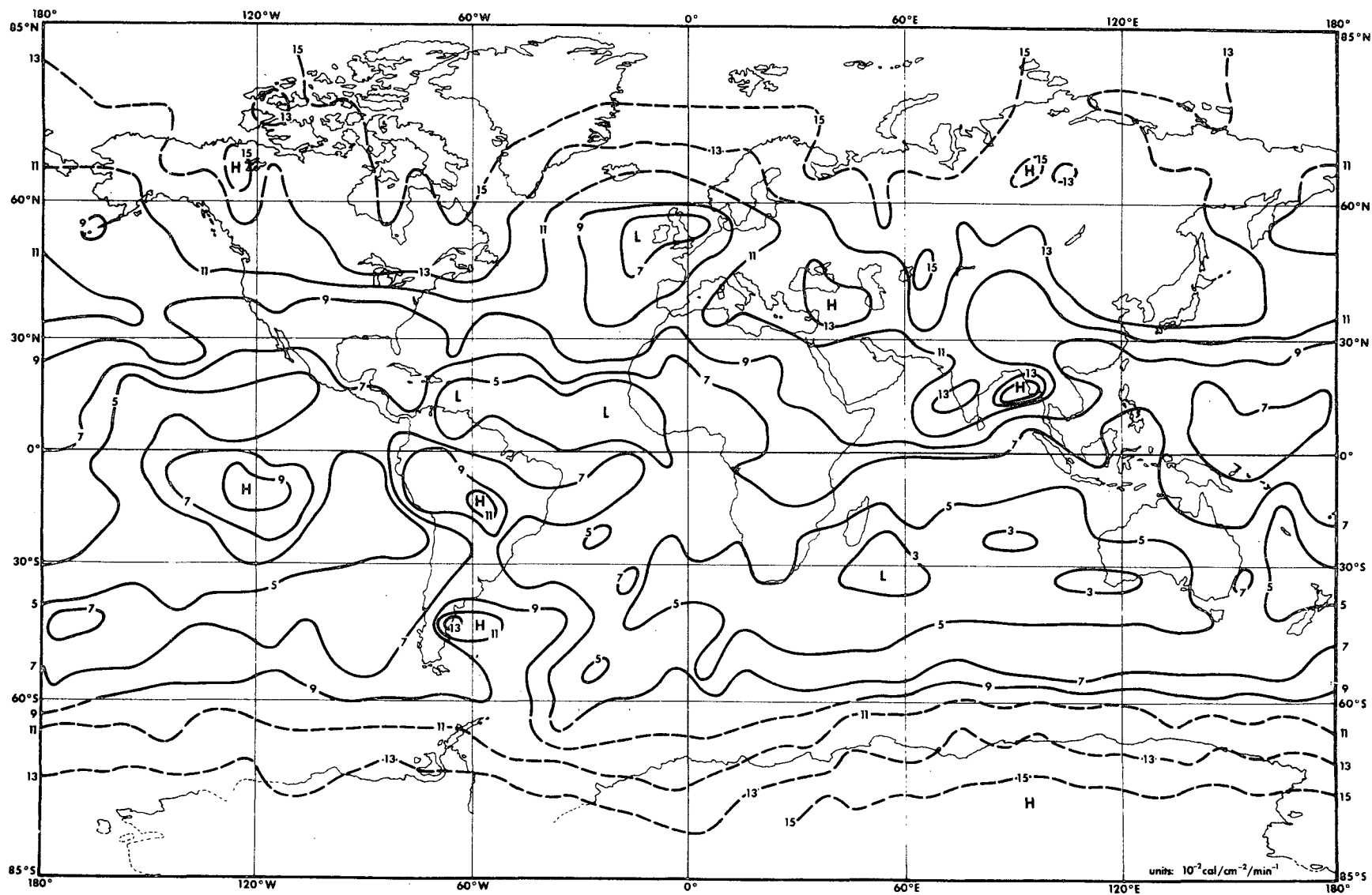


RADIATION BALANCE ($\text{cal cm}^{-2} \text{ min}^{-1}$)

NIMBUS III: 1-15 JULY 1969



RANGE OF TOTAL INFRARED RADIATION MEASURED FROM SATELLITES (1963-1965)



25

Published in NOV, 1972
issue of Solar Energy

Ordered 100 reprints
\$250 (#1973)
- from letter Aug 31, 72

SE. 136 P.1

MEASUREMENTS OF SOLAR ENERGY REFLECTED BY THE EARTH AND ATMOSPHERE FROM METEOROLOGICAL SATELLITES

T. VON DER HAAR,* E. RASCHKE,† W. BANDEEN‡ and M. PASTERNAK‡

(Received 17 May 1971)

Abstract—Sensors carried on the first and second generation meteorological satellites (TIROS, NIMBUS, ESSA), during the 1960's were designed to measure solar energy reflected and scattered by the earth and its atmosphere. From many months of data, a global planetary albedo of 30 per cent has been measured. Only small seasonal variations are detected on the global scale. However, much more solar energy is apparently absorbed in tropical regions than was previously believed. Application of these measurements to the total radiation and energy budgets provides a new insight into atmospheric energetics. In addition, the measurements allow quantitative study of the mean solar energy input at geographical locations, as well as temporal variations from that mean.

Résumé—Des dispositifs installés à bord des satellites météorologiques de 1^{re} et 2^e génération (TIROS, NIMBUS, ESSA) au cours des années 1960 étaient destinés à mesurer l'énergie solaire réfléchie et dispersée par la terre et par son atmosphère. A partir de mesures faites pendant plusieurs mois un albedo planétaire global de 30% a été mesuré. Seules quelques faibles variations saisonnières ont pu être détectées à l'échelle globale. Cependant, bien plus d'énergie solaire est absorbée dans les régions tropicales que l'on imaginait auparavant. L'application de ces mesures à la radiation totale et aux budgets d'énergie offre un nouvel aspect de l'énergie atmosphérique. De plus, les mesures permettent l'étude quantitative de la puissance moyenne de l'énergie solaire dans les régions géographiques et des variations avec le temps de cette moyenne.

Resumen—Los sensores que viajaron en los satélites meteorológicos de primera y segunda generación (TIROS, NIMBUS, ESSA) durante los años 1960 estaban destinados a medir la energía solar reflejada y dispersada por la Tierra y su atmósfera. A partir de los datos correspondientes a muchos meses de investigación, se ha determinado un albedo planetario global del 30%. Sólo se detectan pequeñas variaciones estacionales en la escala global. Sin embargo, parece ser que la absorción de energía solar en las regiones tropicales es mucho mayor de lo que se creía ser antiguamente. La aplicación de estas medidas a la radiación total y a los presupuestos de energía presenta un nuevo concepto de la energética atmosférica. Además, las medidas permiten el estudio cuantitativo de la admisión media de energía solar en lugares geográficos, así como variaciones temporales a partir de dicha media.

INTRODUCTION

DURING the 1960's sensors carried on near-earth satellites provided the first measurements of energy exchange between earth and space. Beginning with the TIROS-type and extending into the NIMBUS (experimental) and ESSA (operational) series, radiation budget measurements have allowed study of the basic forcing function that drives the circulation of our atmosphere and ocean.

The terms of the radiation budget are shown in Fig. 1., and include:

$$RN_{EA} = I_0(1.0 - A) - H_L$$

With RN the net radiation; I_0 the incident solar radiation at the "top of the atmosphere" (derived from knowledge of the solar constant* and astronomical parameters); A , the

*Colorado State University;

†University of Bochum.

‡Goddard Space Flight Center, NASA

*A solar constant of $1.95 \text{ cal. cm}^{-2} \text{ min}^{-1}$ is used throughout this paper except when another (2.00) is explicitly noted.

MARKED PROOF
THE EUROPEAN PRINTING
CORPORATION LTD. DUBLIN
25 AUG 1972
EASE RETURN MARKED PROOF

A read x A-3

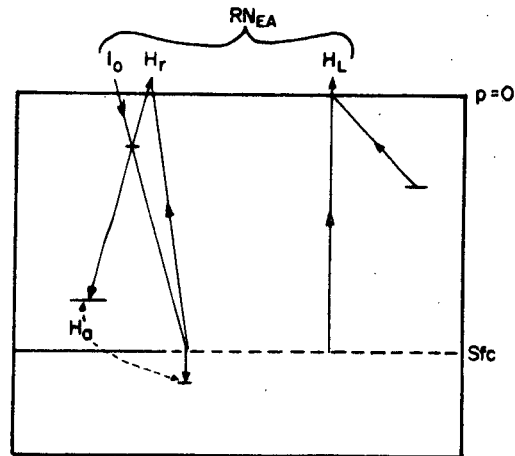


Fig. 1. Schematic depiction of terms of the radiation budget of the Earth-atmosphere system. *l.c.*

planetary albedo (ratio of total solar energy scattered and reflected by the atmosphere, clouds and earth surface, H_r , to the incident solar energy, I_0); and H_L the infrared energy emitted by the Earth-atmosphere system. Dimensions are energy per area per time except albedo, a percentage. The equation may be applied at all time and space scales. Expansion of the solar energy terms is simply

$$I_0(1.0 - A) = I_0 - H_r = H_a,$$

with H_a the amount of solar energy absorbed in the Earth and atmosphere.

l.c. This paper includes results of measurements from the first and second generation satellites during 1962–1966[1] and also preliminary data from the NIMBUS-III experiment. The latter has been described for Nimbus-II by Raschke and Bandeen[2]. Together, the two references contain citations of many other papers describing the satellite experiments and data, too numerous to cite in this article. The other papers discuss the detectors (thermistor bolometer), accuracy estimates (2–3 per cent on the global scale), time and space sampling bias (especially diurnal sampling problems from experiments on Sun-synchronous satellites), ground resolution and smoothing, as well as data reduction procedures. The period of data used in this paper included 39 months during the years 1962–1966; then a seasonal sample during 1969 from NIMBUS-III. Some measurements obtained in the late 1960's have not yet been totally processed and new experiments are planned for future spacecraft. As will be seen, comparisons between different experiments show a consistent picture of the large-scale energy exchange between earth and space. On smaller space and time scales the variability (as expected) is greater; examples of these measurements are also included in the present paper.

SOLAR ENERGY IN THE RADIATION BUDGETS OF THE ENTIRE PLANET AND OF LATITUDE ZONES

Table 1 depicts the global radiation budget measurements from satellites. The i.r. term, H_L , is followed by the planetary albedo measurement, A , in parentheses. Annual

Table 1. Global radiation budget

	Satellites 1962-1966	NIMBUS-III 1969-70
MAM	0.325 (30%)	0.326 (29%)
JJA	0.335 (26%)	0.335 (29%)
SON	0.342 (28%)	0.329 (29%)
DJF	0.333 (31%)	0.320 (28%)
Annual	0.336 (30%)	0.328 (29%)
Preliminary		

values from the 1962-1966 data set agree well with more recent results from NIMBUS-III. They both show that our planet is:

(a) warmer and darker (higher infrared emission and lower albedo) than was previously estimated;

(b) in net radiation balance with space (to within measurement accuracy).

A very small seasonal variation in these mean values shows that the earth as a whole is slightly colder and brighter during the period December-May. Radiation from the Antarctic region would favor this seasonal effect.

A comparison of mean zonal averages of H_i , H_o , and A are shown in Fig. 2. Here we see the classic profile of more energy absorbed than emitted in equatorial regions

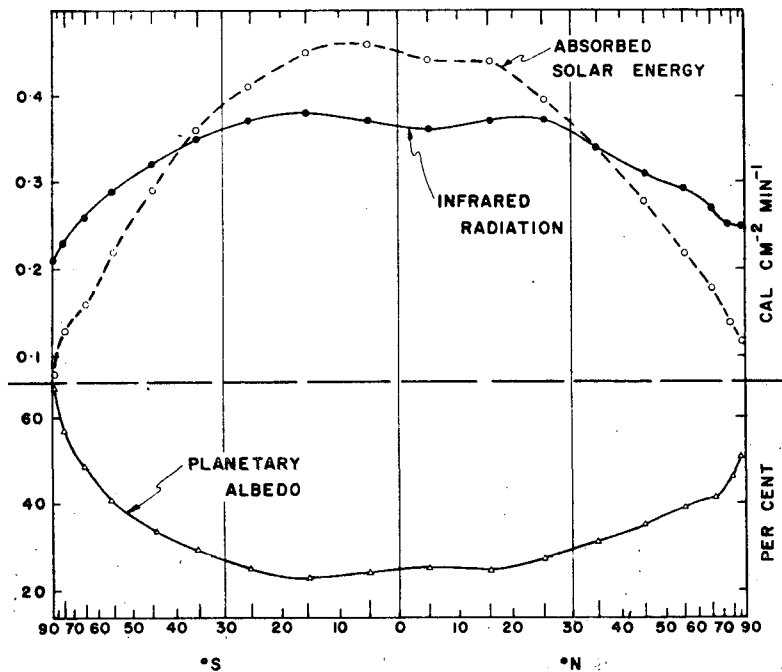


Fig. 2. Mean meridional profiles (averages within latitude zones) of components of the earth's radiation budget measured during the period 1962-1966. The abscissa is scaled by the cosine of latitude. (After Von der Haar and Suomi [13])

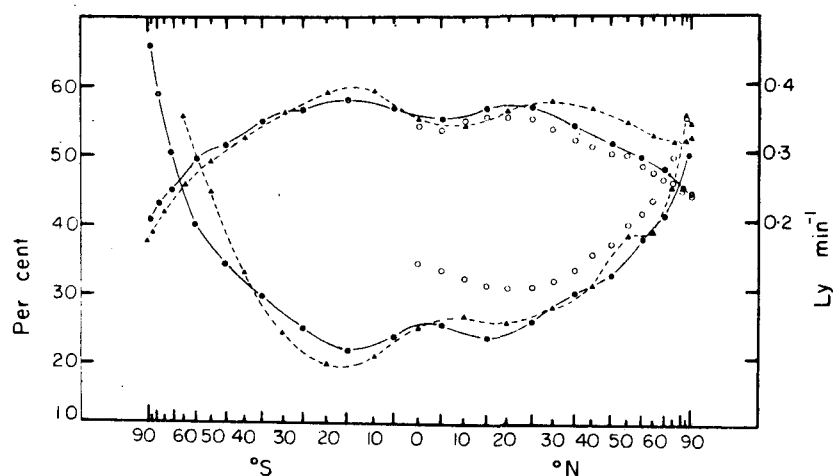


Fig. 3. Mean meridional profiles of outgoing infrared radiation (ly. min^{-1} , upper portion) and planetary albedo (percent). Dashes joined by solid circles, mean 1963-1965, dashes joined by solid triangles, July 1966 from NIMBUS-II; open circles, mean annual calculations by London [3].

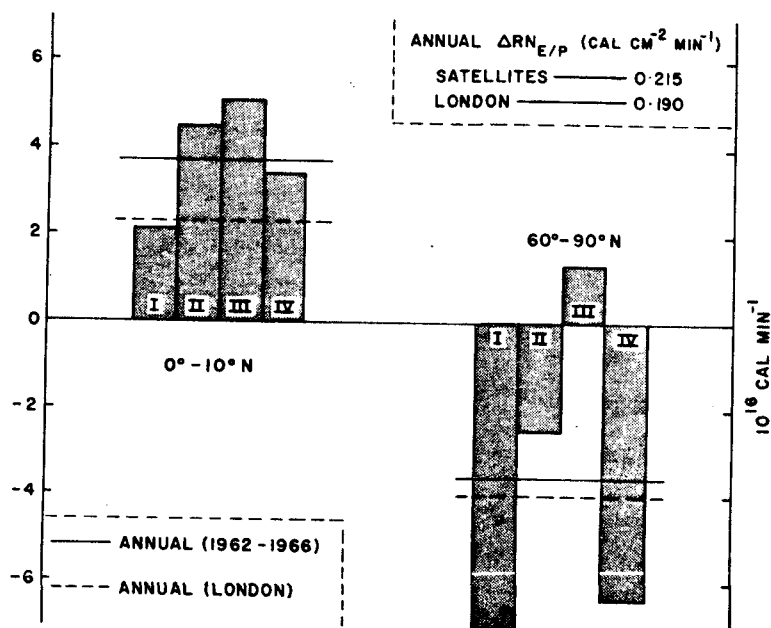


Fig. 4. Mean annual and seasonal energy exchange with space, measured from satellites during 1962-66, for two latitude zones. Bar graph represents seasonal values (I = Dec., Jan., Feb.; II = Mar., Apr., May; etc.). $\Delta R_N / \Delta P$ is the net radiation gradient between equator and pole (after Von der Haar and Suomi [1]).

and more lost than gained at higher latitudes. Variation in this equator-to-pole gradient of net radiation, $RN = H_a - H_l$, is of great interest in atmospheric and oceanic energetics.

As known, the measured solar energy absorption varies with latitude more than the infrared emission. An unexpected result, however, is depicted in Fig. 3, where first generation satellite measurements and results from NIMBUS-II are compared with the earlier, extensive computations by London[3]. Here, we find that the tropical regions especially have a lower albedo than was previously believed. This being the region of great insolation, the result shows that the additional energy being absorbed in our global system is primarily being absorbed in the tropics. Von der Haar and Hanson[4] have further found that most of the extra energy is absorbed in the oceans.

A closer look at two latitude zones of nearly equal surface area is shown in Fig. 4. The mean net energy gain or loss is displayed by season and for the yearly case London's annual values are 35 per cent less than measured in the 0-10°N zone; about the same near the poles*. The large differences in one region are compensated by generally greater measured infrared loss to space throughout the middle latitudes (see Fig. 3). More energy absorbed in the tropics implies a more vigorous circulation (atmospheric, oceanic or both) than was previously thought.

GEOGRAPHICAL VARIATION OF THE SOLAR ENERGY REFLECTED TO SPACE AND ABSORBED IN THE EARTH-ATMOSPHERE SYSTEM

We have seen that satellite measurements of solar energy absorption on global and planetary scales differ from what was previously believed. Relaxing the space scale another dimension, we note the mean annual geographical variation of absorption, H_a , in Fig. 5. The magnitude of the absorption is based on a solar constant of 2.00 ly min^{-1} . Similar maps for the other radiation budget terms are given in Von der Haar and Suomi[1]. Figure 5 shows a smoothed pattern since all daily and seasonal variations of cloudiness and most surface variations are included in the mean map (in addition, the low resolution satellite sensors cannot resolve more than 10° square areas). H and L labels denote relative magnitudes for each latitude zone. The greatest absorption of solar energy occurs near the mouth of the Amazon river and in the Central Pacific; the least over the South Pole. Sub-tropics of the southern hemisphere gain slightly more than the same regions in the north, due both to a lower albedo and to greater mean insolation. Major atmospheric (the summer monsoon) and surface (Sahara desert) features can be discerned. Comparison with the climatological maps of Budyko, Geiger and others will be the subject of future work.

Figure 6 allows study of the geographical scale during a shorter time period and with a higher resolution sensor. Here the preliminary NIMBUS-III i.r. data are used to display a higher frequency pattern of energy (infrared) loss to space. The infrared and solar energy maps are complementary in that they contain independent information and are not mirror images. Longitudinal differences in the tropics are striking; see for example the highly emitting Arabian region and the low i.r. energy from the deep high cloud systems of the neighboring Indian monsoon. The tropical convergence zones in the Atlantic and Pacific are apparent. West of Central America a broad band of clouds are noted by the low infrared measurements.

*Just recently, London and Sasamori[5] have performed new calculations which are in much closer agreement with measurements from satellites.

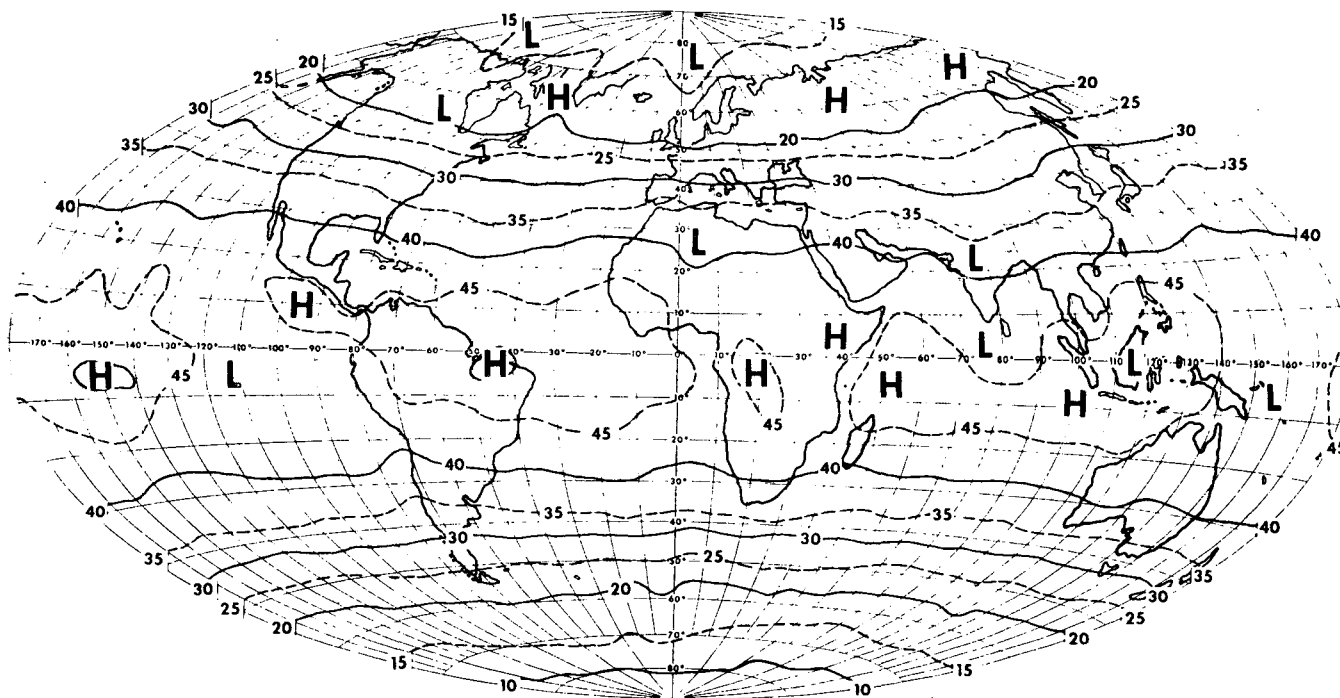
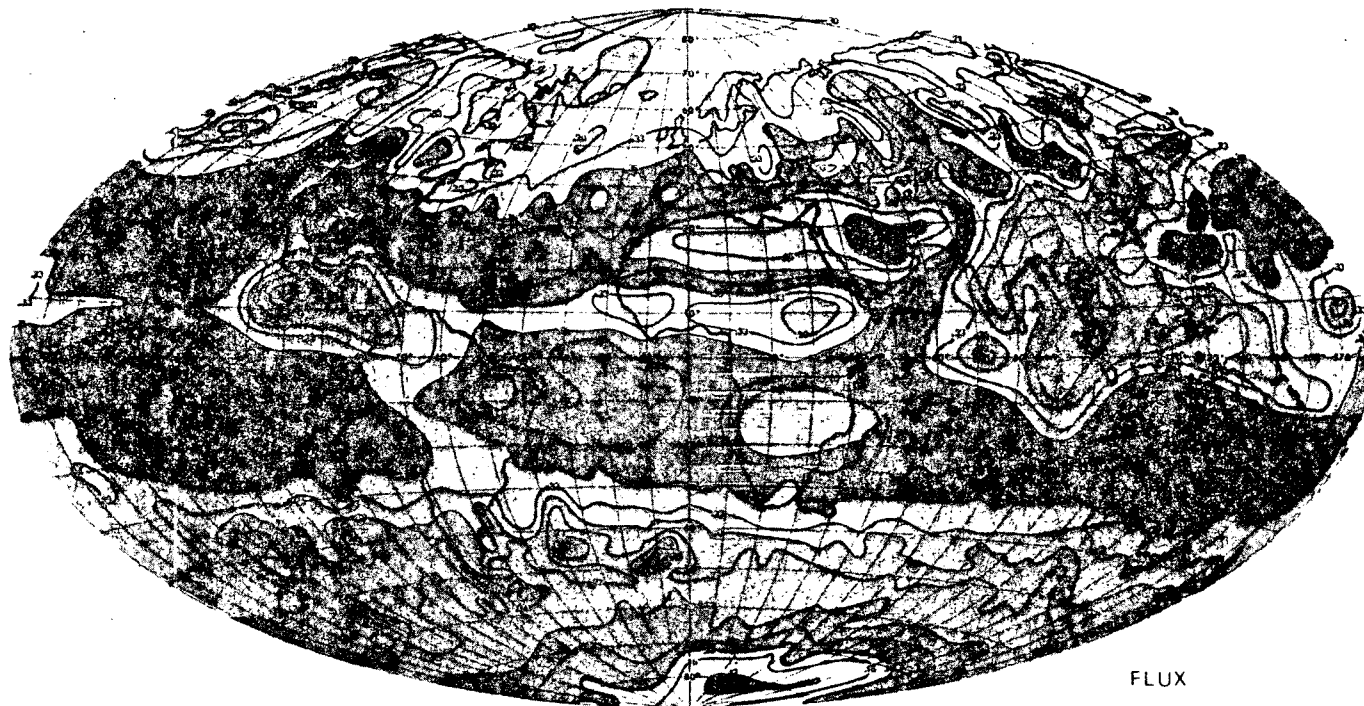


Fig. 5. Mean annual map of solar energy absorbed by the earth and atmosphere.
1962-1965 (10^{-2} cal/cm $^{-2}$ min $^{-1}$).

36135
P.6

T. VON DER HAAR *et al.*

TOTAL OUTGOING LONG-WAVE RADIATION Ly min
 NIMBUS III $10\text{-}11\ \mu$ primarily, also $20\text{-}23\ \mu$, $6\text{-}7\text{-}0\ \mu$ and $15\text{-}16\ \mu$ channels.
 JULY 1-15, 1969






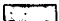
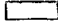

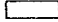

FLUX			
0.11-0.12		0.30-0.36	
0.12-0.18		0.36-0.42	
0.18-0.24		0.42-0.48	
0.24-0.30		0.48-0.49	

Fig. 6. Preliminary results from the NIMBUS-III satellite showing the variation of outgoing infrared (long-wave) radiation (1-15 July 1969).

36135
p.7

Measurements from meteorological satellites

Reproduced from
best available copy.

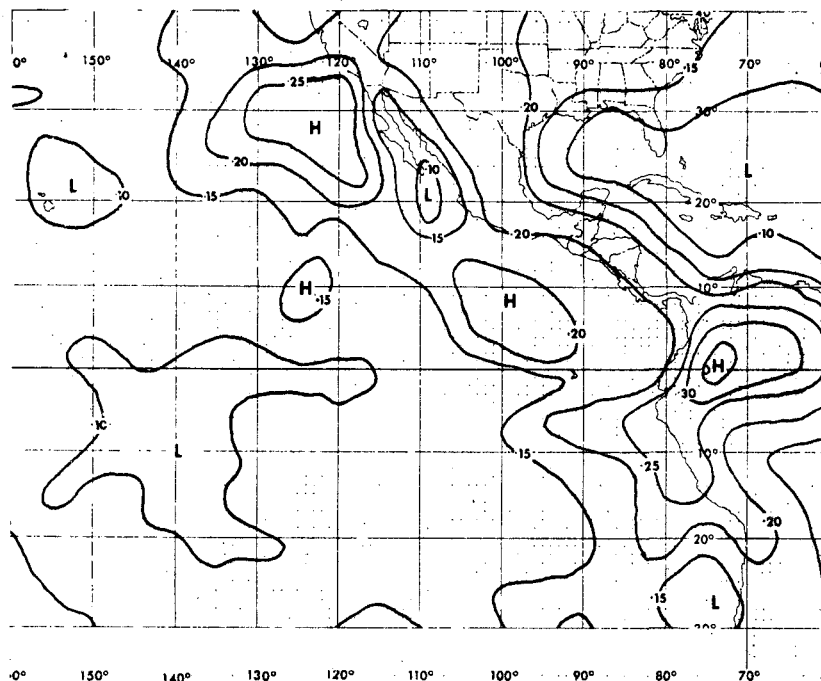


Fig. 7. Minimum daily values of albedo based on preliminary measurements from the NIMBUS-III satellite during time period shown. (1-15 July, 1969)

On the same time scale (15 days) Fig. 7 shows measured minimum values of planetary albedo, A , over a section of the western hemisphere tropics. Minimum (daily) albedo maps would depict land-ocean differences if cloud cover were completely random. It is not, and two regions show this on Fig. 7. One, over the ocean west of Baja California, undoubtedly denotes the presence of persistent stratiform cloud cover. The other, centered near 10°N, 100°W coincides with the marked minimum on the infrared map. It must represent persistent high and middle clouds, but the reason that this part of the convergence zone is so active at this time needs further study. East and north of a strong gradient of minimum albedo, the Gulf of Mexico and Western Atlantic show minimum albedo value of 10 per cent or slightly less. Hawaii does the same, indicating at least one cloud-free day during the 14 considered for the map.

stratiform

To aid the study of solar energy measurements from satellites, Fig. 8 shows the relative dispersion of albedo (ratio of standard deviation to the mean) for the same area and time as Fig. 7. Both the stratus and middle cloud regions mentioned above show low dispersion, reinforcing our estimate of persistence. Conversely, portions of the convergence zone in the central Pacific, as well as the Gulf of Mexico and other local areas have high dispersion. Southwestern United States and Central Mexico have small relative dispersions in daily albedo for this summer sample. Where possible, the dispersion maps will be compared with station observations to aid meteorological interpretation. However, we have demonstrated the complementary value of simultaneous infrared and solar energy measurements as well as the added value of special derivatives from these data. A matched set allows display and study of the energy exchange with space and its interaction with cloud and surface features.

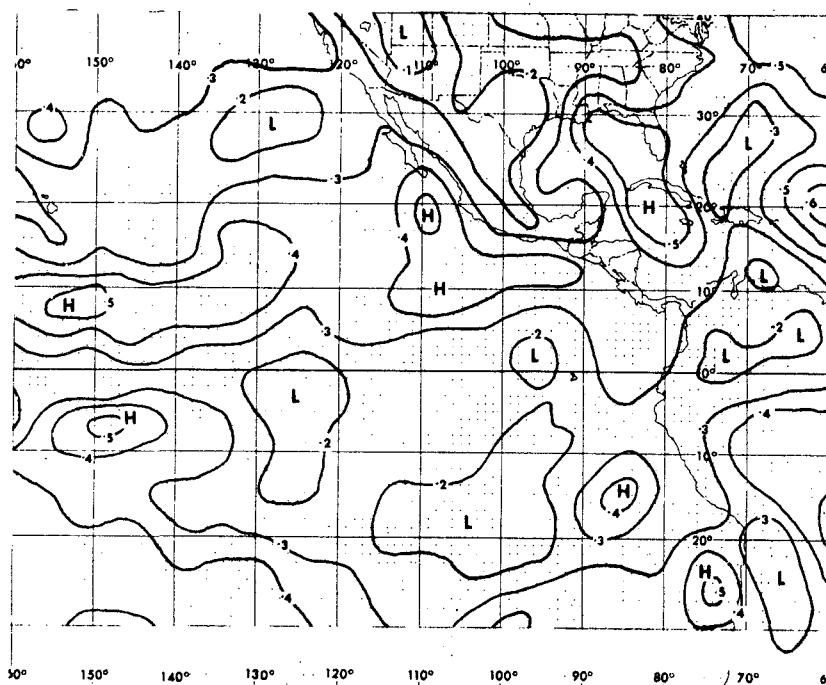


Fig. 8. As Fig. 7 for values of Relative Dispersion (%) of Albedo.

Since it is not possible to discuss in detail all the satellite measurements in map form, Table 2 presents a qualitative summary of seasonal variations of planetary albedo, A, maxima, and minima. Final versions of the maps from which these were extracted will be published after final orbit processing and data checks. Some entries in the table show a seasonal progression (e.g., the Brazil-Columbia locations). West and northwest Mexico appear in the minima column during three seasons of 1969-1970; Parts of Brazil and India alternate between the extremes.

* i.e.,
l.e.

Measured extremes of planetary albedo over land areas*
(40°N-40°S)

	Maxima	Minima
April 1969	Central China/Japan South Central Asia	South India Western Mexico
July 1969	North Brazil/Columbia India/Southeast Asia Colombia/Peru Equatorial Africa	East Australia East Mediterranean Central Brazil South Africa
October 1969	South China Colombia Equatorial Africa	Northwest Mexico Southwest Arabia Florida
January 1970	Midwest United States Central Brazil South Central Asia	South India West Africa Western Mexico

* Excluding major desert regions

Table 2

SUMMARY

We have learned a great deal about the energy exchange between our planet and space from the measurements acquired from satellite platforms. Atmospheric scientists now study the interannual variation of this energy exchange and its role in atmospheric energetics. They also desire to study ocean response to the energy separate from that of the atmosphere and also the longterm problem of climate change. It is hoped that this brief paper has demonstrated the high importance of the solar energy terms of the radiation budget as well as shown that the satellite data can complement the many ground-based observations for research and engineering studies.

measurements

REFERENCES

- [1] T. H. Von der Haar and V. E. Suomi, Measurements of the earth's radiation budget from satellite during a five-year period. Part I: Extended time and space means. *J. Atmos. Sci.* **28**, 305-314 (1971).
- [2] E. Raschke and W. R. Bandeen, The radiation balance of the planet earth from radiation measurements of the satellite Nimbus II. *J. Appl. Met.* **9**, 215-238 (1970).
- [3] J. London, A study of the atmospheric heat balance. *Final Report, Contract AF19(122)-165*, Dept. of Meteorology and Oceanography, New York University, 99 pp.
- [4] T. H. Von der Haar and K. J. Hanson, Absorption of solar radiation in tropical regions. *J. Atmos. Sci.* **26**, 652-655 (1969).
- [5] J. London and T. Sasamori, Radiative energy budget of the atmosphere. *Space Research XI*, Springer-Verlag, Berlin (1971).
- [6] T. H. Von der Haar and V. E. Suomi, Satellite observations of the earth's radiation budget. *Science* **163**, 667-669 (1969).

satellites

THESIS

DISTRIBUTION AND PARAMETERIZATION OF ABSORPTION OF
SOLAR RADIATION IN THE ATMOSPHERE

Submitted by
Patrick H. Downey

In partial fulfillment of the requirements
for the degree of Master of Science
Colorado State University
Fort Collins, Colorado
August 1972

ABSTRACT

DISTRIBUTION AND PARAMETERIZATION OF ABSORPTION OF
SOLAR RADIATION IN THE ATMOSPHERE

A year of satellite and surface observations from 1969-1970 are combined to determine spatial and temporal variations of atmospheric absorption of solar radiation. Most of the additional energy available to the earth-atmosphere system, due to lower values of global earth-atmosphere albedo than previously estimated, is added to the oceans in tropical latitudes and to the atmosphere in extratropical latitudes. Two parameters, cloud cover and optical pathlength are used in a step-wise multiple linear regression program to parameterize atmospheric absorption of solar radiation.

Patrick H. Downey
Department of Atmospheric Science
Colorado State University
Fort Collins, Colorado 80521
August, 1972

Preceding page blank

ACKNOWLEDGEMENTS

Special thanks are extended to Dr. Thomas H. Vonder Haar for his guidance and suggestions which made this research possible.

The many hours of work by Vicki Brant, Paula Brant, Lyn Koch and Patty Frease in preparing this thesis are deeply appreciated.

I also wish to thank Steven Lassman for the tremendous programming assistance rendered to this thesis.

This research was supported by the National Aeronautics and Space Administration under Grant NGR 06-002-12.

TABLE OF CONTENTS

	<u>page</u>
ABSTRACT	iii
ACKNOWLEDGEMENTS	iv
LIST OF FIGURES.	vii
LIST OF TABLES	viii
1.0 Introduction.	1
2.0 Calculation of Solar Radiation Absorption	4
2.1 Irradiance at the Upper Boundary	6
2.2 Reflected Radiation at the Upper Boundary.	6
2.3 Irradiance at the Ground	6
2.4 Irradiance Reflected at the Ground	8
2.5 Accuracy of Measurements	10
3.0 Cloud Cover and Water Vapor as Parameters	16
3.1 Opaque Cloud Cover Data Availability and Reduction	17
3.2 Calculation and Distribution of Optical Pathlength	17
3.3 Space and Time Restrictions.	18
4.0 Distribution of the fraction of incident sunlight re- flected to space, the fraction of incident sunlight ab- sorbed in the atmosphere, the fraction of incident sun- light absorbed at the surface and the transmissivity of the atmosphere in the tropics	25
4.1 Distribution of the fraction of incident sunlight reflected to space, the fraction of incident sun- light absorbed in the atmosphere and the fraction of incident sunlight absorbed at the surface on a global scale	29
4.2 Seasonal variations of the fraction of incident sunlight reflected to space, the fraction of in- cident sunlight absorbed in the atmosphere and the fraction of incident sunlight absorbed at the surface.	30

	<u>page</u>
4.3 Distribution of the fraction of incident sunlight reflected to space, the fraction of incident sunlight absorbed in the atmosphere and the fraction of incident sunlight absorbed at the surface	34
4.4 Solar Heating Rate	35
5.0 Parameterization Scheme Using Regression Techniques. . .	40
5.1 Data Analysis.	41
5.2 Results of the Parameterization Scheme	43
5.3 Results from the U. S. Network	44
6.0 Conclusions and Recommendations	47
REFERENCES	50

APPENDIX A

Processing of ESSA 9 brightness data into a study of global cloud cover.

LIST OF FIGURES

<u>Figure</u>	<u>Page</u>
2.0-1 Symbols for irradiance bounding the atmosphere and absorption of radiation in the atmosphere	4
2.2-1 Albedo measurements from Nimbus 3, January 21 - February 3, 1970	7
2.3-1 Ratio of annual values of Q_g estimated by Geiger to those found by this study	9
2.5-1 Graphical solution of the most probable error in dQ_a . .	13
2.5-2 Graphical solution of the most probable error in dQ_a . .	14
2.5-3 Graphical solution of the most probable error in dQ_a . .	15
3.2-1 Values of optical pathlength in cm, April 1969.	19
3.2-2 Values of optical pathlength in cm, July 1969	20
3.2-3 Values of optical pathlength in cm, October 1969.	21
3.2-4 Values of optical pathlength in cm, January 1970.	22
4.2-1 Seasonal variations in albedo and absorption on a global scale	31
4.2-2 Seasonal variations in albedo and absorption in Europe. .	32
4.2-3 Seasonal variations in albedo and absorption in South America	33
4.4-1 Solar heating rate over the U. S. during October 1969 . .	37
4.4-2 Solar heating rate with latent effects over the U. S. during October 1969	39

LIST OF TABLES

<u>Table</u>	<u>Page</u>
3.4-1 Nimbus 3 Data Availability	23
4.0-1 Tropical continental vs. tropical oceanic values of the fraction of incident sunlight absorbed in the atmosphere, the fraction of incident sunlight absorbed at the surface, the fraction of sunlight reflected to space and the transmissivity of the atmosphere	27
4.0-2 Tropical zonal average of the fraction of sunlight re- flected to space, the fraction of sunlight absorbed in the atmosphere and the fraction of sunlight absorbed at the surface	29
4.1-1 Tropical vs. global values of the fraction of sunlight reflected to space, the fraction of sunlight absorbed in the atmosphere and the fraction of sunlight absorbed at the surface	30
5.3-1 Statistical analysis of the regression program over the U. S. network.	45
5.3-2 Correlation matrices from May 16-31, August 1-15 and October 3-17, 1969 and January 21-February 3, 1970 . .	46

1.0 INTRODUCTION

Previous estimates of a globally integrated value of the absorption of solar energy in the atmosphere have been made by Gabites (1950), London (1957) and Sellers (1965). These estimates were in good agreement showing 17-18% absorption by the atmosphere and a global albedo of 34-36%. However, these estimates were made prior to the acquisition of reliable satellite measurements of reflected solar radiation.

Vonder Haar (1968), using recent satellite data, has shown the earth's albedo to be close to 30%, a deviation of 4-6% from previous estimates. Hence, one would suspect an error in previous calculations of the absorptivity of the atmosphere or the earth's surface or both.

More recent studies by Vonder Haar and Hanson (1969), Hanson, et. al. (1967) and Hanson (1972) have concentrated on spatial variations and dependence of absorption on precipitable water, but only in selected geographical locations such as the central Pacific and the U.S.

This study is designed to look at only a small part of the heat and energy budget of the earth atmosphere system in detail. Future studies may utilize these solar energy results in conjunction with the other components of the radiation and energy balance equations.

In particular, the purpose of this study is to combine recent satellite measurements of reflected solar radiation from the Medium Resolution Infrared Radiometer (MRIR) on Nimbus 3 with a global network of surface albedo and actinometric measurements to determine the spatial and temporal distribution of atmospheric absorption of solar energy. In addition, a two parameter model will be established to determine the relationship between solar radiation absorption in the atmosphere, precipitable water and opaque cloud cover.

Results will serve three purposes:

- 1) Energy budget studies may be updated with the aid of the global value and variations of atmospheric absorption found in this study by using the most recent satellite observations. Whether solar irradiance enters the atmospheric energy cycle directly or latently determines the response time of the atmosphere to the solar forcing function. For special reasons, results from the tropical regions will be of interest to the meteorologist and oceanographer alike since the absorption at the earth's surface (which is primarily oceanic in tropical latitudes and therefore a latent energy source) is obtained as a complement to atmospheric absorption. The results of this study may help define more clearly the role of ocean currents in transporting energy poleward to maintain the heat balance of the earth-atmosphere system.
- 2) Absorption over the sparsely populated regions of the world is unknown because of the lack of an actinometric and surface observation network. Because of the large data sample and wide range of locations included in this study, generalization of the results may hopefully be extended to regions of the world having poor surface data networks.
- 3) Parameterization of solar energy absorption, in terms of parameters that can be remotely sensed on a global scale by satellites will

allow continuing study of this important process. Furthermore, the same parameters being available within current numerical models, allows additional use of the results of this study.

With these goals in mind, sections dealing with the data used will be followed, first by the diagnostic results, then by the results dealing with the parameterization of solar energy absorption.

2.0 CALCULATION OF SOLAR RADIATION ABSORPTION

Fritz, et. al. (1964) have developed a method of determining solar absorption in the atmosphere which combines satellite and surface measurements. As illustrated in Fig. 2.0-1, Q_o and Q_r are the values of solar irradiance incident and reflected from the top of the atmosphere. Likewise, Q_g and Q_s are values of solar irradiance incident and reflected from the earth's surface. When combined, these irradiance terms define the absorption in the atmosphere, Q_a , as:

$$Q_a = Q_o - Q_g + Q_s - Q_r \quad (1)$$

dividing equation (1) by Q_o yields:

$$\frac{Q_a}{Q_o} = \frac{Q_o}{Q_o} + \frac{Q_s}{Q_o} - \frac{Q_g}{Q_o} - \frac{Q_r}{Q_o} \quad (2)$$

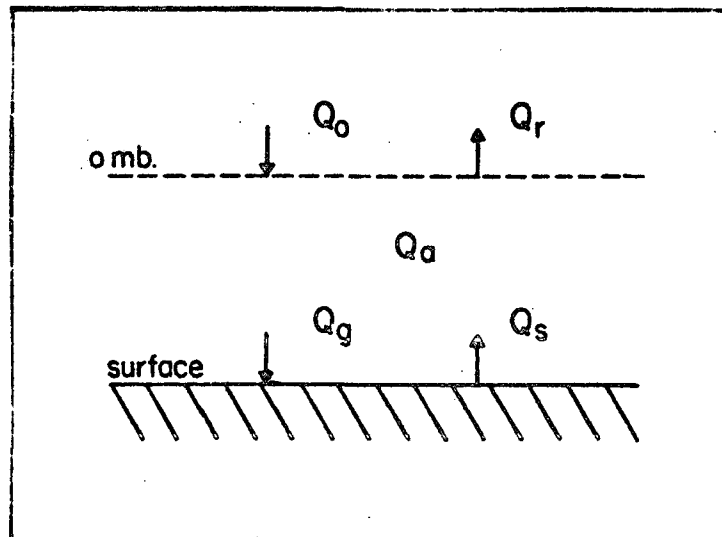


FIGURE 2.0-1 - Symbols for irradiance bounding the atmosphere and absorption of radiation in the atmosphere.

We may now define:

$q_a = \frac{Q_a}{Q_o}$, the fraction of incident sunlight absorbed in the atmosphere,

$q_r = \frac{Q_r}{Q_o}$, the fraction of incident sunlight reflected to space,

$q_g = \frac{Q_g}{Q_o}$, the transmission of the atmosphere,

$\alpha = \frac{Q_s}{Q_g}$, the surface albedo,

$q_e = q_g(1-\alpha)$, the fraction of incident sunlight absorbed at the surface.

Equation (2) may now be written as:

$$q_a = 1 + \frac{Q_s}{Q_o} \cdot \frac{Q_g}{Q_g} - \frac{Q_g}{Q_o} - q_r \quad (3)$$

since $\frac{Q_s}{Q_g} = \alpha$, equation (3) is equivalent to:

$$q_a = 1 - q_g(1-\alpha) - q_r \quad (4)$$

or, rearranging:

$$1 = q_a + q_e + q_r \quad (5)$$

which is a statement of the conservation of short wave radiant energy.

Clearly, the sunlight reaching the top of the atmosphere is either reflected to space by the earth, atmosphere and clouds, absorbed by the atmosphere or absorbed at the surface.

2.1 Irradiance at the Upper Boundary

The irradiance at the upper boundary of the atmosphere, Q_o , can be calculated from:

$$Q_o = I_s (r_m/r)^2 \cos \zeta \quad (6)$$

I_s , the solar constant, is $1.95 \text{ cal/cm}^2 \text{ min}$, r_m and r are the mean and actual earth-sun distances; and ζ is the solar zenith angle at the subsatellite point at the time of observation.

2.2 Reflected Radiation at the Upper Boundary

The outward irradiance at the upper boundary, Q_r , was obtained from Nimbus 3 MRIR measurements of sunlight reflected to space by the earth, atmosphere and clouds. Techniques used in reducing the measurements have been discussed by Raschke, et. al. (1972). Q_r/Q_o is known as the albedo of the earth atmosphere system. Figure 2.2-1 is an illustration of albedo measurements made by Nimbus 3 from January 21 - February 3 1970.

2.3 Irradiance at the Ground

The irradiance at the ground, Q_g , was taken from actual observations of all actinometric stations in the World Meteorological Organization (WMO) network. This network represents more than 350 reporting

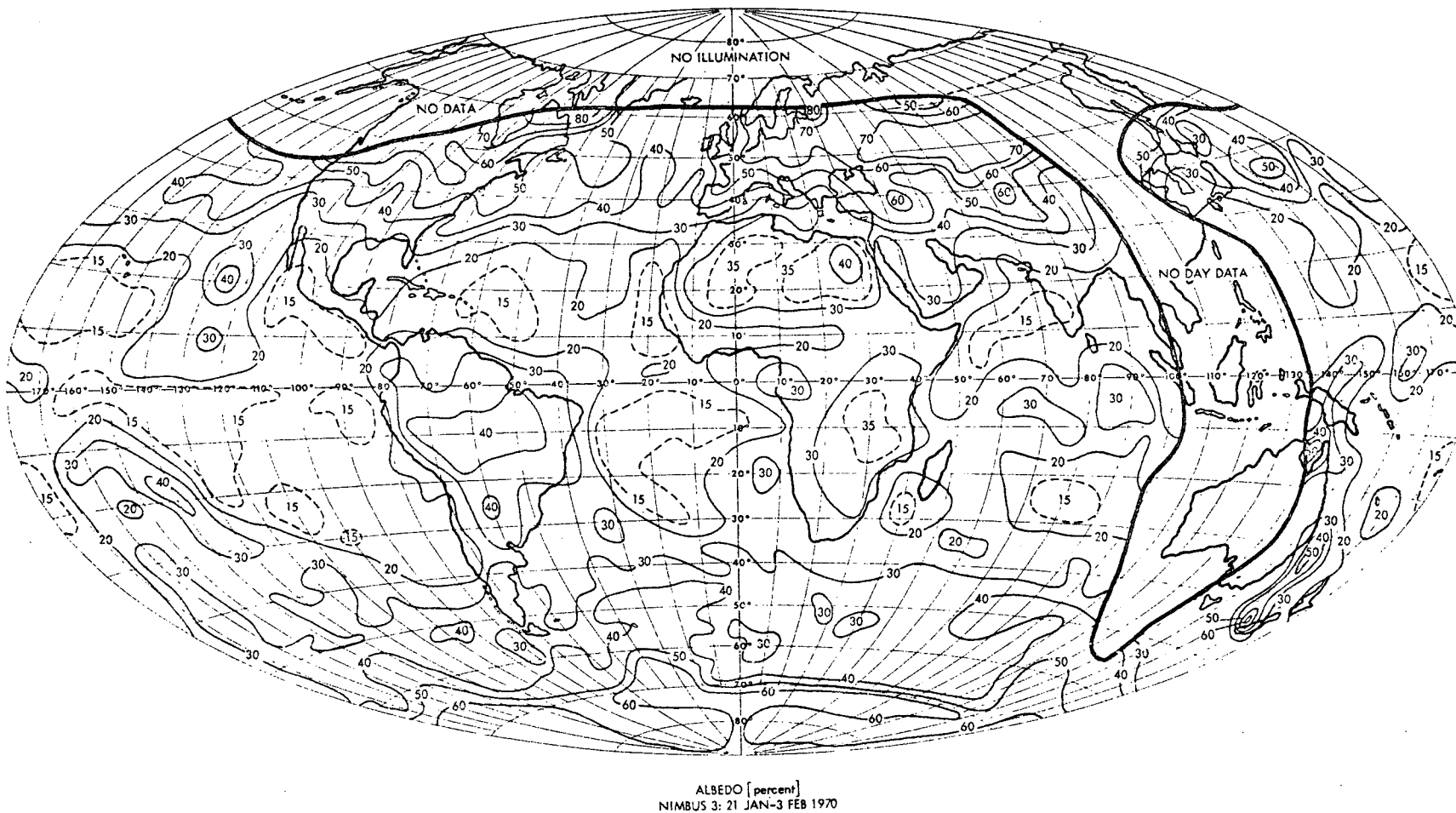


FIGURE 2.2-1 Albedo measurements from Nimbus 3, January 21 - February 3, 1970.

stations from over 50 countries. Figure 2.3-1 depicts the ratio of annual values of Q_g estimated by Geiger (1963) to those found by this study, over randomly selected portions of the globe. Geiger's values are based in part on measurements of radiation over long periods of time, and also from relationships of air turbidity, cloudiness and the height of the sun.

2.4 Irradiance Reflected at the Ground

The irradiance reflected at the ground, Q_s , was obtained as the product of irradiance at the ground and the surface albedo. Over the U.S., surface albedo was taken from data compiled by Kung, et. al. (1964). Over the remainder of the globe surface albedo was specified in reference to Posey and Clapp (1964) and with the aid of Nimbus 3 minimum albedo maps.

The data compiled by Posey and Clapp over the U.S. was consistently lower than the data obtained by Kung, et. al. (1964) thus prompting a 3% correction factor to be added to the Posey and Clapp albedo values less than 20%. This was applied world-wide.

The few surface values greater than 20% were more in line with the data gathered by Kung, et. al. (1964) and Nimbus 3 minimum albedo maps, hence no corrections were applied to the Posey and Clapp data for surface albedo above 20%.

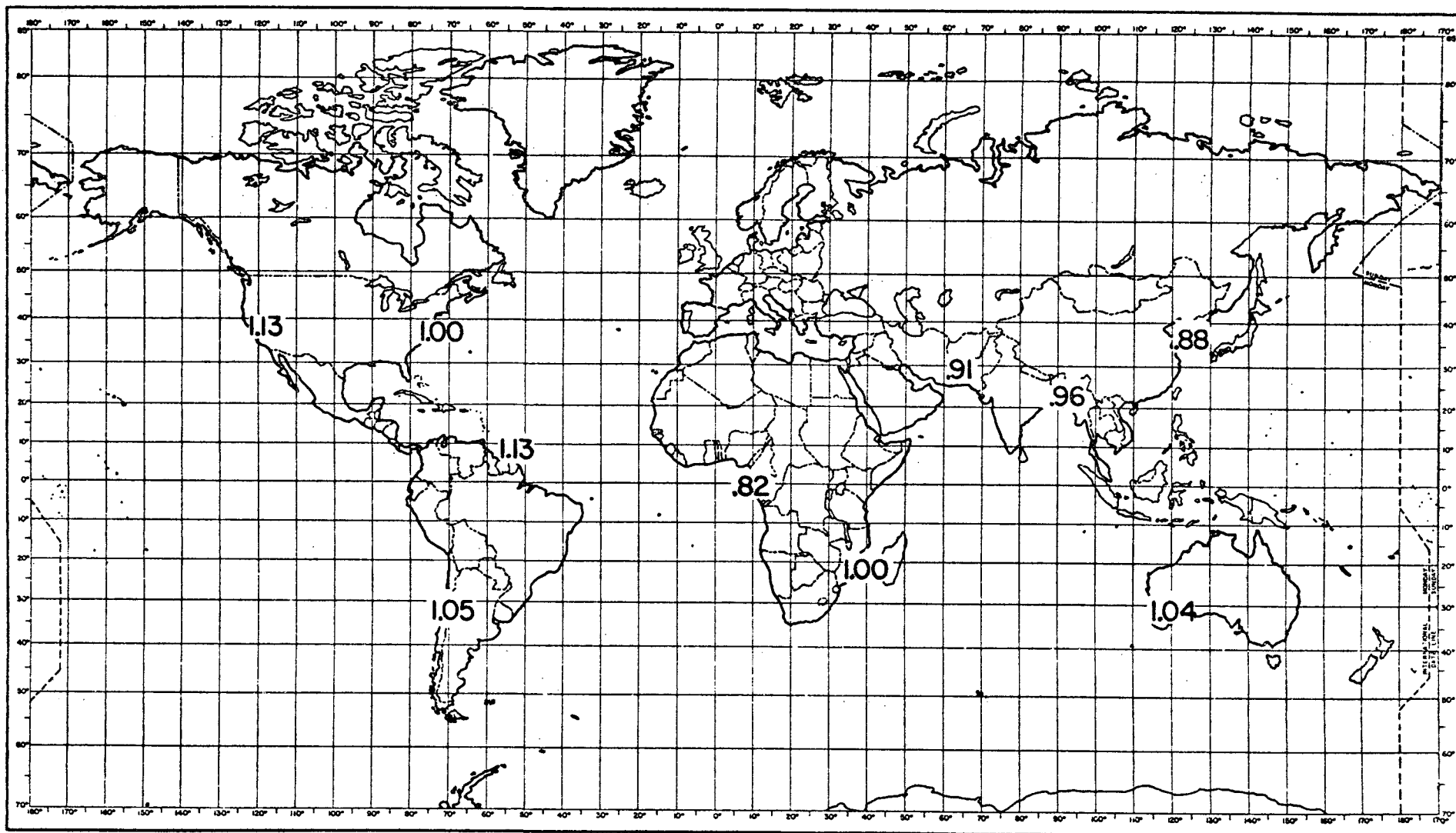


FIGURE 2.3-1 Ratio of annual values of Q_g estimated by Geiger to those found by this study.

2.5 Accuracy of Measurements

Accuracy of the individual measurements will determine the validity of the whole study so a careful error analysis must be undertaken.

Raschke, et. al. (1972) have placed the random error of radiance measurements on all MRIR channels at $\pm 1-2\%$. Relative calibration of measurements of the reflected solar radiance were made over cloud free areas of the deserts of North Africa and Arabia. The results showed no systematic increase or decrease of reflectances during the entire life span of the Nimbus 3 MRIR. Assuming that absolute calibration before launch was accurate and that there are only small processing errors, we may then place a relative bias error of $\pm 5\%$ on values of Q_T .

Errors in the measurement of surface albedo should not be large. Kung, et. al. (1964) estimated no more than a 4% absolute error in their measurements over North America. A similar error would be probable in the combined data of Posey and Clapp (1964) and the Nimbus 3 minimum albedo maps.

Actinometric measurements pose the largest problem due to the large number and varying types of instruments in use and the large number of calibration standards in the WMO network. Hanson, et. al. (1972) have shown the Eppley pyranometers in the U.S. to be consistently erroneous since 1954 by 3.5-10.5% due to initial calibration. These errors have been corrected and factors for instrument degradation with time in the U.S. have also been applied in accordance with a study made by Case (1972), so that the actinometric data used in the U.S. should show an error of no more than 2%. For other portions of the world,

Vonder Haar and Hanson (1969) have suggested a relative systematic error of 3% in well calibrated instruments, but Sellers (1965) has indicated a relative error no better than 5-10% in certain instruments.

Since:

$$Q_s = Q_g \alpha \quad , \quad (7)$$

where α is the surface albedo. Equation (1) may then be written as:

$$Q_a = Q_o - Q_g + Q_g \alpha - Q_r \quad . \quad (8)$$

When factored, equation (8) is equivalent to:

$$Q_a = Q_o - Q_g(1-\alpha) - Q_r \quad . \quad (9)$$

By differentiating equation (9) one may obtain values of the maximum absolute error in Q_a :

$$dQ_a = dQ_o - dQ_g + Q_g d\alpha + \alpha dQ_g - dQ_r \quad (10)$$

where dQ_o is assumed to be negligible.

Of more interest to this study is the most probable absolute error (.6745) in Q_a . Computations have been made for varying absolute errors in Q_g and Q_r with a constant error in α , to determine the most probable error in dQ_a . Figures 2.5-1 through Figure 2.5-3 illustrate the graphical solution of the most probable absolute error in dQ_a .

During May 1969, Little Rock, Arkansas had a surface albedo = .15, $Q_g = 500 \text{ ly day}^{-1}$, $Q_r = 275 \text{ ly day}^{-1}$ and as calculated from this study, $Q_a = 235.6 \text{ ly day}^{-1}$. Maximizing the absolute error in each measurement we obtain $d\alpha = .05$, $dQ_g = 25 \text{ ly day}^{-1}$ and $dQ_r = 13.7 \text{ ly day}^{-1}$. Then the greatest absolute error in Q_a is 67 ly day^{-1} and the most probable error is 11.4 ly day^{-1} .

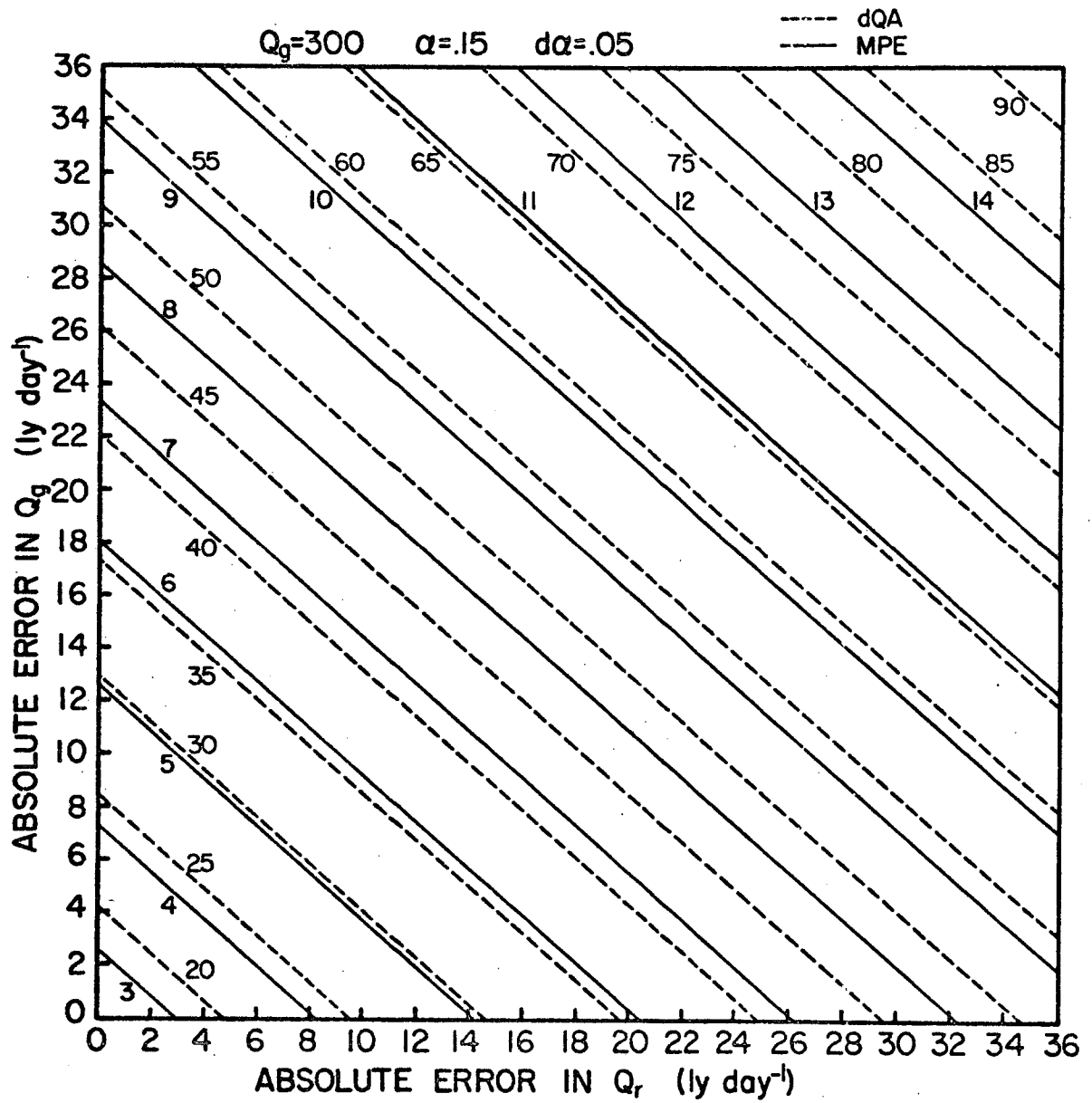


FIGURE 2.5-1 Graphical solution of the most probable error in dQ_a .

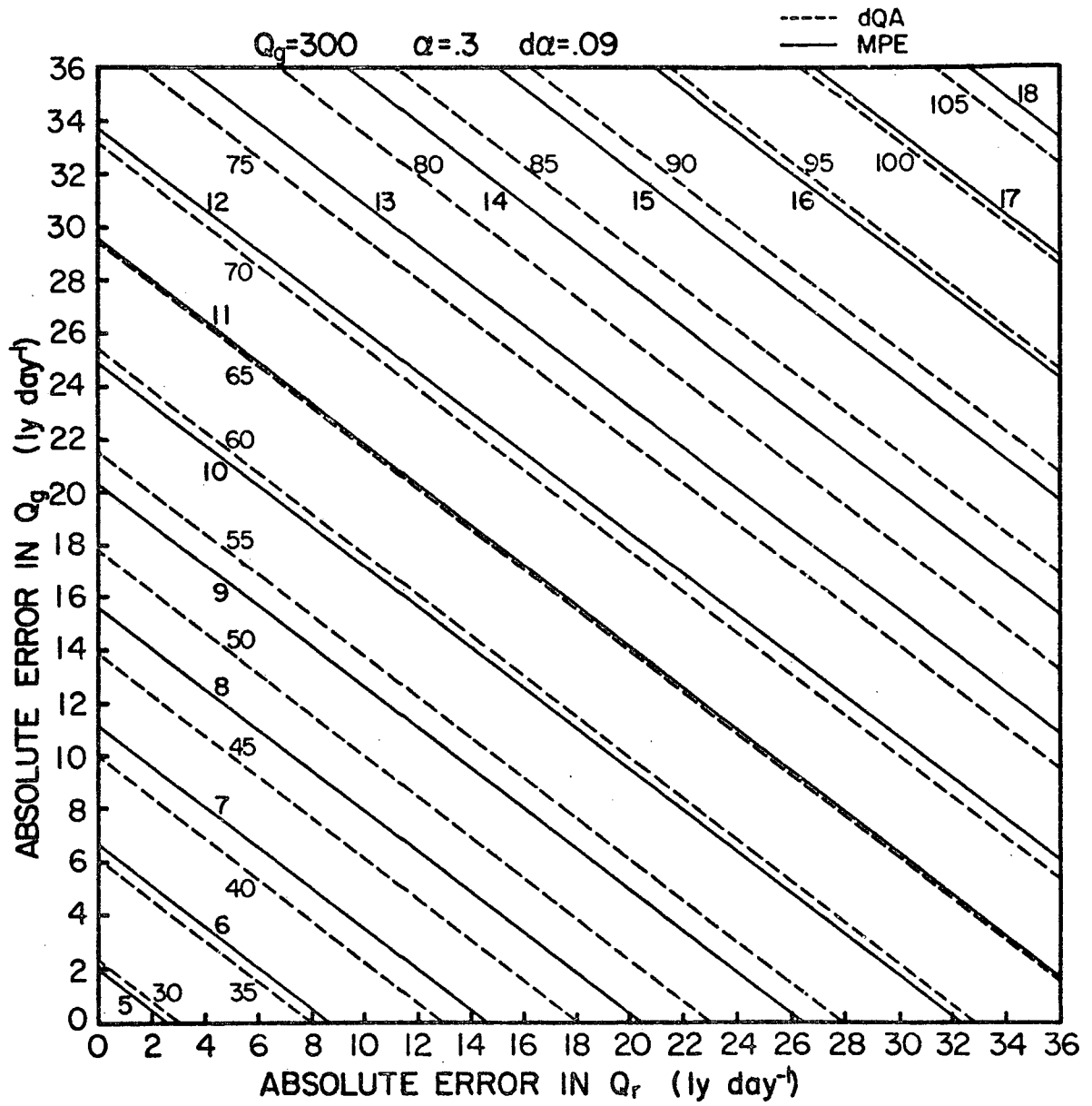


FIGURE 2.5-2 Graphical solution of the most probable error in dQ_a .

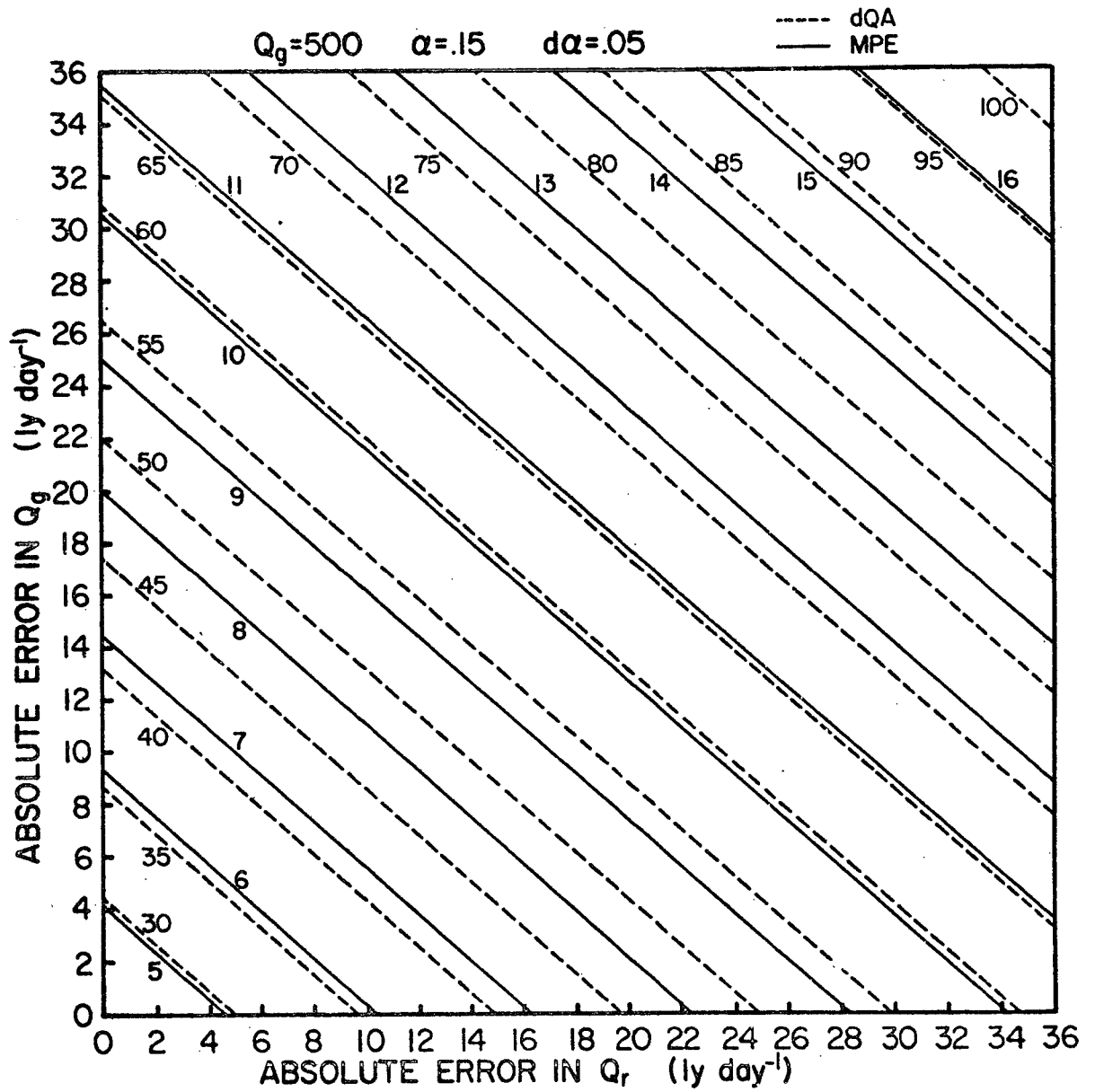


FIGURE 5.2-3 Graphical solution of the most probable error in dQ_a .

3.0 CLOUD COVER AND WATER VAPOR AS PARAMETERS

In order to make a realistic assessment of the magnitude and distribution of solar absorption, one must determine which parameters are of importance. Quinn, et al. (1969) found that in a test of several different meteorological parameters, the total opaque cloud cover provided the most reliable estimate of atmospheric transmission. Opaque clouds have high reflectance and substantial absorption would be expected within an opaque cloud both because of the liquid water (or ice) and because multiple scattering may greatly increase the effective water vapor pathlength.

Yamamoto (1962) has shown that absorption by water vapor is predominant in the lower troposphere being an order of magnitude larger than the carbon dioxide and oxygen absorption. In the upper troposphere, absorption by carbon dioxide and oxygen becomes more important but at the same time concentrations of these gases becomes nearly constant thus providing a poor input into this study which is concerned with variable atmospheric parameters.

Studies by Cox et al. (1972) have demonstrated that haze (a concentration of aerosols, which may be dilute solutions of NaCl or water coated dust particles) may absorb solar energy directly or cause a longer path through the absorbing gaseous constituents by scattering. However, due to the difficulty in measuring this variable it was not considered in this study.

It should be clear then why spatial and temporal variations in opaque cloud cover and water vapor are the primary parameters needed for development of this solar absorption model.

3.1 Opaque Cloud Cover Data Availability and Reduction

The magnitude of absorption by clouds is dependent on cloud depth and density and on the zenith angle of the sun. This presents a formidable task for a cloud cover parameterization since present meteorological satellites do not sense clouds three dimensionally. The best approach to the problem on a global scale with the present state of the art is to consider opaque cloudiness as related to thick cloudiness and disregard density (dropsizes distribution and liquid water content). Over the time scales considered here, (semi-monthly periods) the zenith angle of incident solar energy plays a lesser role in absorption.

Such a cloud study was accomplished using data from ESSA 9 during the same time period as Nimbus 3. For a detailed description of this study, see Appendix A.

3.2 Calculation and Distribution of Optical Pathlength

As mentioned earlier, water vapor is a major absorber of solar irradiance particularly in the lower troposphere. The water equivalent of a column of unit cross sectional area extending from the surface to the top of the atmosphere is known as precipitable water. Given any sounding for a station, the precipitable water may be found from equation (11):

$$u = \frac{1}{g} \int_{\text{sfc}}^{300 \text{ mb}} w \, dp \quad (11)$$

where g is the gravitational acceleration at the earth's surface, w is the mixing ratio of water vapor and p is the atmospheric pressure. Note that the integration was only carried out to 300 mb as the amount of water vapor above 300 mb is negligible.

Since solar irradiance usually enters the atmosphere on a slant path, we must define the optical pathlength, u^* , as:

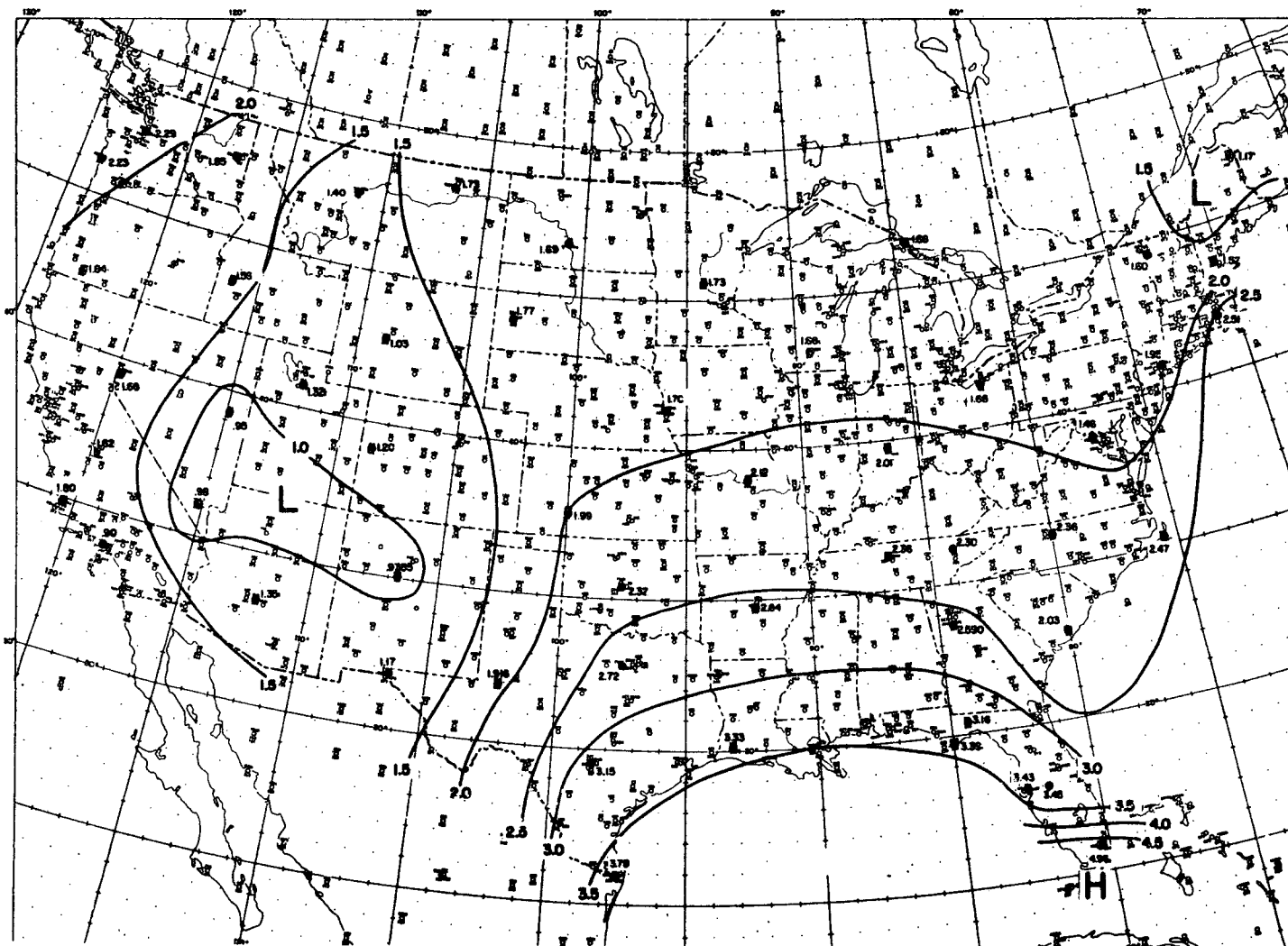
$$u^* = u \cdot \sec \zeta \quad (12)$$

Values of u^* (in cm) for the months of April, July and October 1969, and January 1970 (representative of the four seasons), are shown in Figs. 3.2-1 through 3.2-4. Marked seasonal variations in absolute magnitude can be seen with maximum values in July and minimum values in January. Although values of precipitable water are very low in the winter, values of u^* are high due to the large zenith angle during this season.

Positioning of the maximum and minimum values of u^* is nearly constant with time, exhibiting minimum values in the Great Basin and a general ridging over the Mississippi Valley

3.3 Space and Time Restrictions

Although ESSA 9 vidicon data and surface actinometric values are available for nearly all days in 1969, the Nimbus 3 data is limited to specific time periods. Hence the data sample used in the development portion of this study corresponds to the 10 individual Nimbus 3 15-day



FIGURES 3.2-1 Values of optical pathlength in cm. April 1969

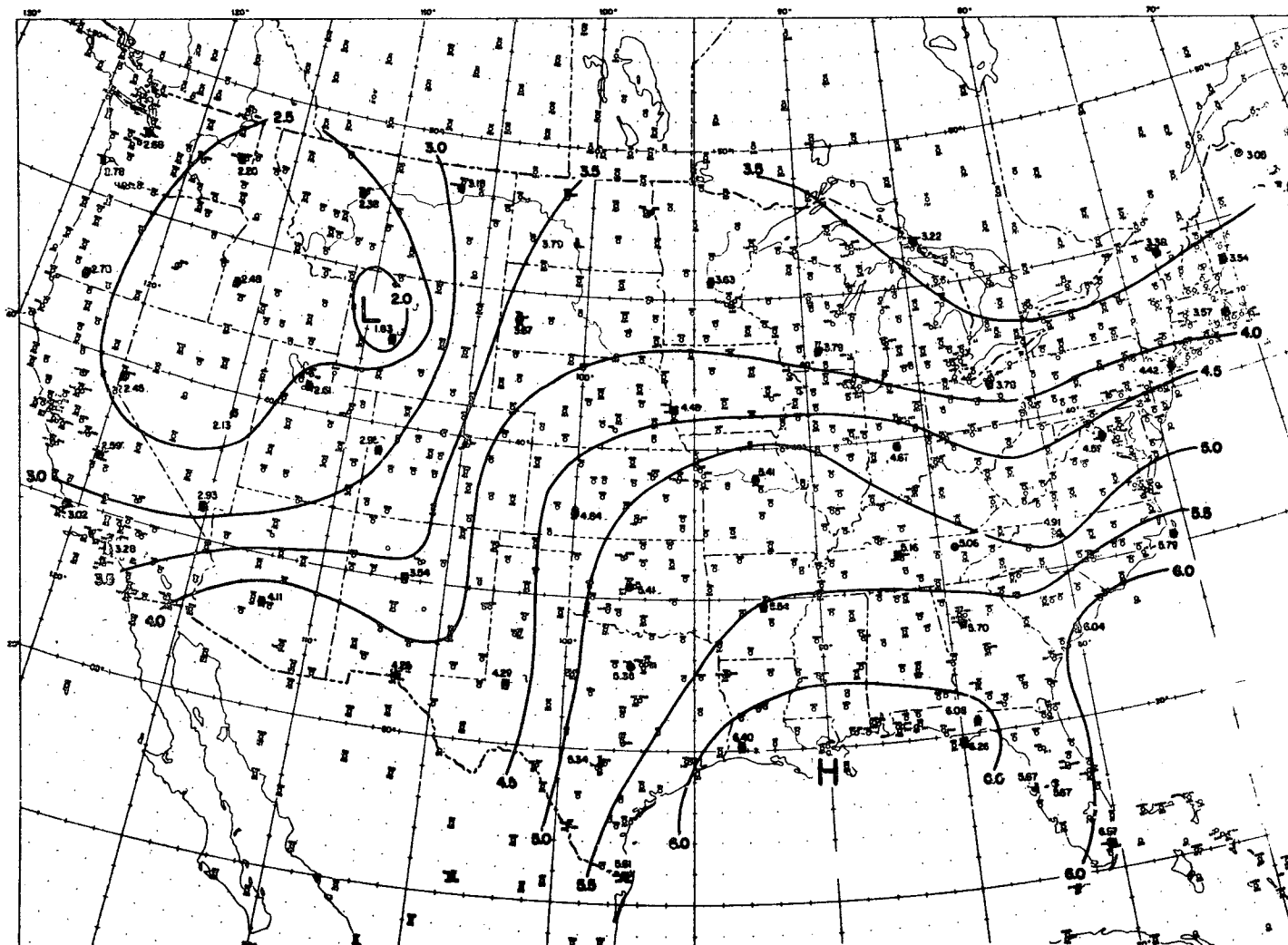


FIGURE 3.2-2 Values of optical pathlength in cm. July 1969

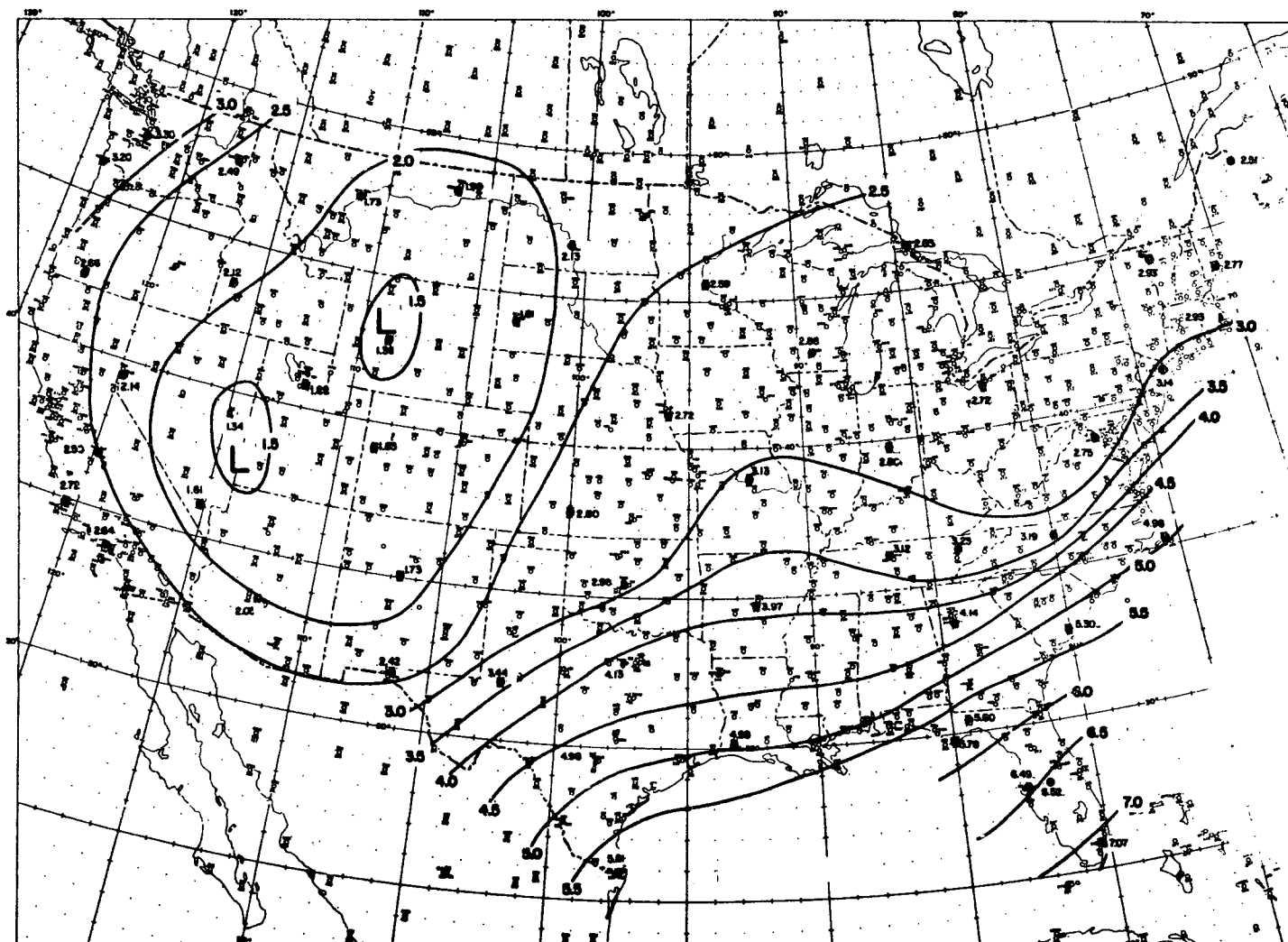


FIGURE 3.2-3 Values of optical pathlength in cm. October 1969

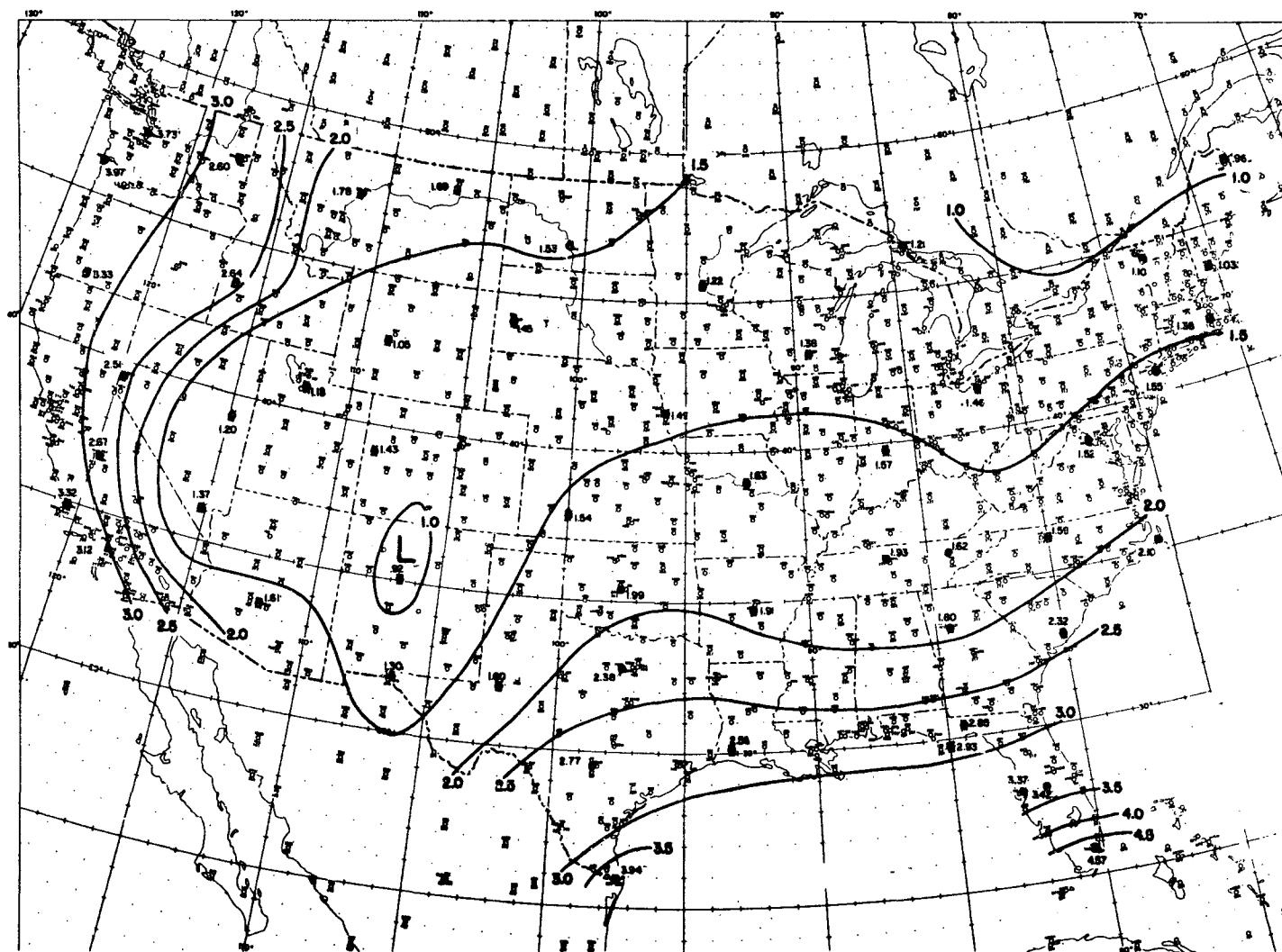


FIGURE 3.2-4 Values of optical pathlength in cm. January 1970

periods listed in Table 3.4-1. This does not preclude an extension of the results of this study to other time intervals as one of the primary goals of this study is to develop a general relationship between atmospheric absorption of solar radiation and the independent variables (precipitable water and opaque cloud cover).

TABLE 3.4-1

Nimbus 3 Data Availability

15-30 April	1969	1 -15 July	1969
1 -15 May	1969	16-31 July	1969
16-31 May	1969	1 -15 August	1969
1 -15 June	1969	3 -17 October	1969
16-30 June	1969	21 January -	
		3 February	1970

Mean monthly soundings are available through the United States Department of Commerce (1969-70) for all upper air stations in the United States. Precipitable water as calculated from these mean monthly soundings is assumed to represent the 15-day periods also.

Spatial limitations are imposed by the extent of the world actinometric network and by high surface albedo. In regions of high albedo, the ESSA 9 vidicon cannot distinguish between background and cloud cover. As a result Greenland and the deserts of North Africa and Saudi Arabia have been deleted from this study as have locations poleward of 58° in all seasons. In the northern hemisphere winter, snow and ice make a study of this type impractical north of 42° .

An areal division of the WMO actinometric network was thought to be advantageous for this study so that general regression equations for the world relating q_T , u^* and opaque cloud cover may be compared at different geographical areas. Accordingly, the globe was divided into four regions; the U.S. (because all reporting stations use Eppley pyranometers), South America (because all reporting stations use Robitzch bimetallic actinographs), portions of Europe (which use the Robitzch bimetallic actinograph), and the remaining stations (which use a wide variety of instruments relative to the sample size). Unfortunately it was found that Italy, which is part of the European division, reported consistently low measurements with respect to the other countries in this division. This prompted application of a correction factor of 15%, which was applied to all Italian reporting stations in all months.

This areal division of the globe is a tenuous one to say the least since 2 of the 4 division utilize the Robitzch bimetallic actinograph which has poor response characteristics and as Sellers (1965) has pointed out, a relative error no better than 5-10% for the measurement of Q_g .

4.0 DISTRIBUTION OF q_r , q_a , q_e and q_g IN THE TROPICS

Previous studies of the absorption, transmission and albedo in the tropics have been quite general giving results of only a zonal average of q_r , q_a , q_e and q_g . After a study by Vonder Haar and Hanson (1969) which demonstrated that the oceanic portions of the tropics absorb more energy than previously estimated, it is pertinent to consider whether a distinction between oceanic and continental regions should be studied prior to compiling a zonal average of absorption values.

This study is heavily biased with continental stations (60 continental vs 5 island stations in the region $20^{\circ}\text{N} - 20^{\circ}\text{S}$). Thus, a scheme had to be developed to estimate q_e , q_a and q_r over the oceanic portion of the tropics in order to compare our work with many of the earlier generalized results.

Using an equation for the radiation balance of the earth's surface we can write:

$$R = Q_g(1-\alpha) + I_{\downarrow} - I_{\uparrow} \quad (13)$$

where R is the radiation balance, and $I_{\downarrow}(I_{\uparrow})$ is longwave radiation lost (gained) by the atmosphere. By partitioning land and ocean surfaces in a latitude belt and using the relationship:

$$Q_e = Q_g(1-\alpha) \quad , \quad (14)$$

and the assumption that $I_{O\downarrow} = I_{L\downarrow}$ we may arrive at:

$$(R_O - R_L)_{\phi} = Q_{eO} - Q_{eL} - I_{O\uparrow} + I_{L\uparrow} \quad (15)$$

where the subscripts ϕ , 0 and L refer to latitude, ocean and land. A further check on the validity of the assumption that $I_0^\dagger = I_L^\dagger$ could be made by comparison with the energy balance equation over the oceanic and continental portions of the tropics. Rearranging:

$$Q_{e0} = (R_0 - R_L)_\phi + Q_{eL} + I_0 - I_L \quad (16)$$

Fortunately, Budyko (1963) has computed the radiation balance, R , using climatological estimates of cloud cover to determine Q_g , and distinguished between oceanic and continental surfaces in all latitude belts. Since the albedo of the earth-atmosphere system in the tropics is lower than previous estimates, we may assume that his values of R are too low. Equation (16), however, uses the difference $(R_0 - R_L)_\phi$ and hence should still be valid for the purposes of this calculation.

From Budyko's calculations, the tropical values of $(R_0 - R_L)_T$ is $4.5 \times 10^4 \text{ ly yr}^{-1}$. Although Budyko does not explain why there is a land-sea difference we may assume that it is due both to values of surface albedo which are much larger over land than ocean, and to any cloud cover differences. Approximating infrared losses by the Stephan Boltzman law:

$$W = \sigma T^4 \quad (17)$$

where W is radiant emittance, T is temperature and σ a constant equal to $1.17 \times 10^{-7} \text{ ly day}^{-1} \text{ K}^{-4}$, one can compute $I_0^\dagger - I_L^\dagger$. Using values of T_0 and T_L of 300°K and 304°K after Riehl (1954), $I_0^\dagger - I_L^\dagger$ was found to be $-2.0 \times 10^4 \text{ ly yr}^{-1}$. From this study, Q_{eL} was found to be $13.7 \times 10^4 \text{ ly yr}^{-1}$ which gives Q_{e0} , the residual, a value of $16.2 \times 10^4 \text{ ly yr}^{-1}$. Then $q_{e0}/q_{eL} = (16.2 \times 10^4)/(13.7 \times 10^4) = 1.18$.

Hence the amount of surface absorption over the oceanic portion of the tropics is calculated to be 18% greater than absorption over the continental regions. This needs verification, but will be used hereafter.

Vonder Haar (1972), using data from 5 years of satellite measurements, places the mean annual oceanic albedo in the tropics at 23% and that of the land areas at 26%. If this absolute difference of 3% is subtracted from the continental value of albedo found in this study (28%), one can arrive at the values given in Table 4.0-1.

TABLE 4.0-1

	Continental Measured (1969)	Oceanic Calculated (1969)	Canton Island ¹ (1955-1966)	Wake Island ¹ (1955-1966)
q_a	.25	.20	.18	.13
q_e	.47	.55	.61	.60
q_r	.28	.25	.21	.27
q_g	.55	.59	.64	.63

¹Calibration and degradation errors have been applied to the original data to arrive at the values at these stations.

For purposes of comparison, oceanic measurements made by Vonder Haar and Hanson (1969) have been included. The results from the oceanic calculations qualitatively resemble the measurements made by Vonder Haar and Hanson.

The small tropical island sample size and the large aperiodicity with which they reported in 1969 precludes a comparison of the calculated values with the actual tropical oceanic data sample used in this study.

The ocean-representative calculations were based on the assumption that $I_{O\downarrow} - I_{L\downarrow} = 0$ which deserves a closer look. Longwave counter radiation in the cloud free case is a function of water vapor content, which under normal circumstances would be larger over the oceans. If this were the case, equation (16) would become:

$$Q_{e0} = (R_O - R_L)_\phi + Q_{eL} + I_{O\uparrow} - I_{L\uparrow} - I_{O\downarrow} + I_{L\downarrow} \quad (18)$$

This would have the effect of lowering Q_{e0} .

Swinbank (1963), on the basis of measurements made in Australia and in the Indian Ocean, concluded that counter radiation can be estimated to a high degree of accuracy from the surface temperature alone. Since the continental surface area in the tropics would be warmer than the oceanic surface a good portion of the day, Q_{e0} would become larger.

When clouds, which are effective back radiators, are taken into account, we can see that the trade cumuli (predominant over the oceans) would have the effect of increasing $I_{O\downarrow}$. Therefore the net effect would be $I_{O\downarrow} > I_{L\downarrow}$ which means that calculations made in this study for oceanic q_e are slightly too high, and for oceanic q_a too low.

Previous tropical zonal averages given by London (1957) placed q_r at 34%, q_a at 18% and q_e at 48%. Assuming the tropics are 80% oceanic, a weighting scheme may be applied to the results of this study in order to obtain a "zonal" average which may be compared to London's values. The weighted zonal values from this study are compared to those of London in Table 4.0-2.

TABLE 4.0-2 Tropical zonal average of q_r , q_a and q_e

	London (1957)	Downey (1972)
q_r	.34	.25
q_a	.18	.21
q_e	.48	.54

Now we can clearly see the effect of the additional solar energy (9%) available due to a lower albedo in the tropics. Most of the additional energy received is realized in a 6% increase of surface absorption. From Table 4.0-1 it is evident that this increased surface absorption takes place primarily in the oceanic portion of the tropics.

4.1 Distribution of q_r , q_a , and q_e on a Global Scale

The method of partitioning the oceanic and continental regions discussed in section 4.0 is not applicable on a global scale because of the wide variation in land-sea temperature differences poleward of 20° . Nevertheless, continental comparisons on a global scale may be made with the continental tropics.

Table 4.1-1 makes a comparison of q_r , q_a , and q_e throughout the world and tropics. Most striking is the difference in surface absorption as the tropical continental surface absorption exceeds globally averaged surface absorption by 3%. The small variation in atmospheric absorption should also be noted. Values of q_r used by London and Sasamori (1971) are 3% higher than the values found by this study and

also by Vonder Haar (1968). Results from this study indicate that the lower global albedo is accounted for by a corresponding increase in q_a .

TABLE 4.1-1 Tropical vs. global values of q_r , q_a and q_e

	q_r	q_a	q_e	
Tropics	28	25	47	(Downey, 1969)
Global	30	26	44	(Downey, 1969)
Global	33	22	45	(London and Sasamori, 1971)

4.2 Seasonal Variations of q_r , q_a and q_e

Figure 4.2-1 shows the march of seasonal variations in albedo and absorption on a global scale. Most striking is the inverse relationship between albedo and q_a (which will be looked at in detail in section 5.1).

As expected q_r was a maximum in the winter and a minimum in the fall. Downey, et. al. (1972), using ESSA 9 brightness data found that global cloudiness was a minimum in the summer of 1969 and not the fall as the albedo values indicate. Perhaps the reason lies in the degradation of the ESSA 9 sensor during May, June and July 1969, which would have the effect of decreasing the number of cloudy days during the summer.

These global seasonal averages mask some of the variations in the networks comprising the global sample. Figures 4.2-2 and 4.2-3 show that significant variations in q_r , q_a and q_e from the global means do indeed occur. It is felt that these regional variations are due to space and time variations of cloud cover or water vapor.

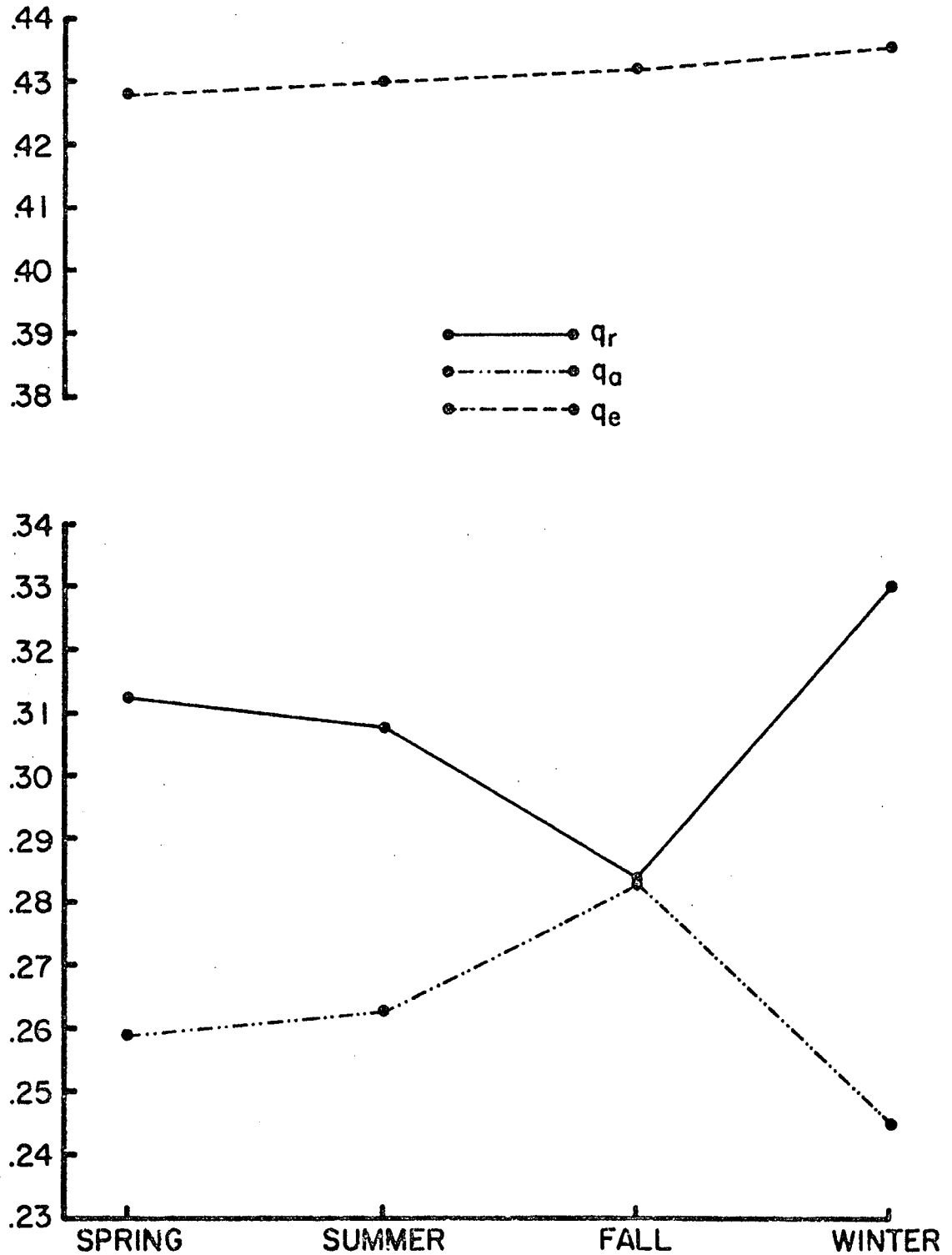


FIGURE 4.2-1 Seasonal variations in albedo and absorption on a global scale. Seasons reckoned to the northern hemisphere.

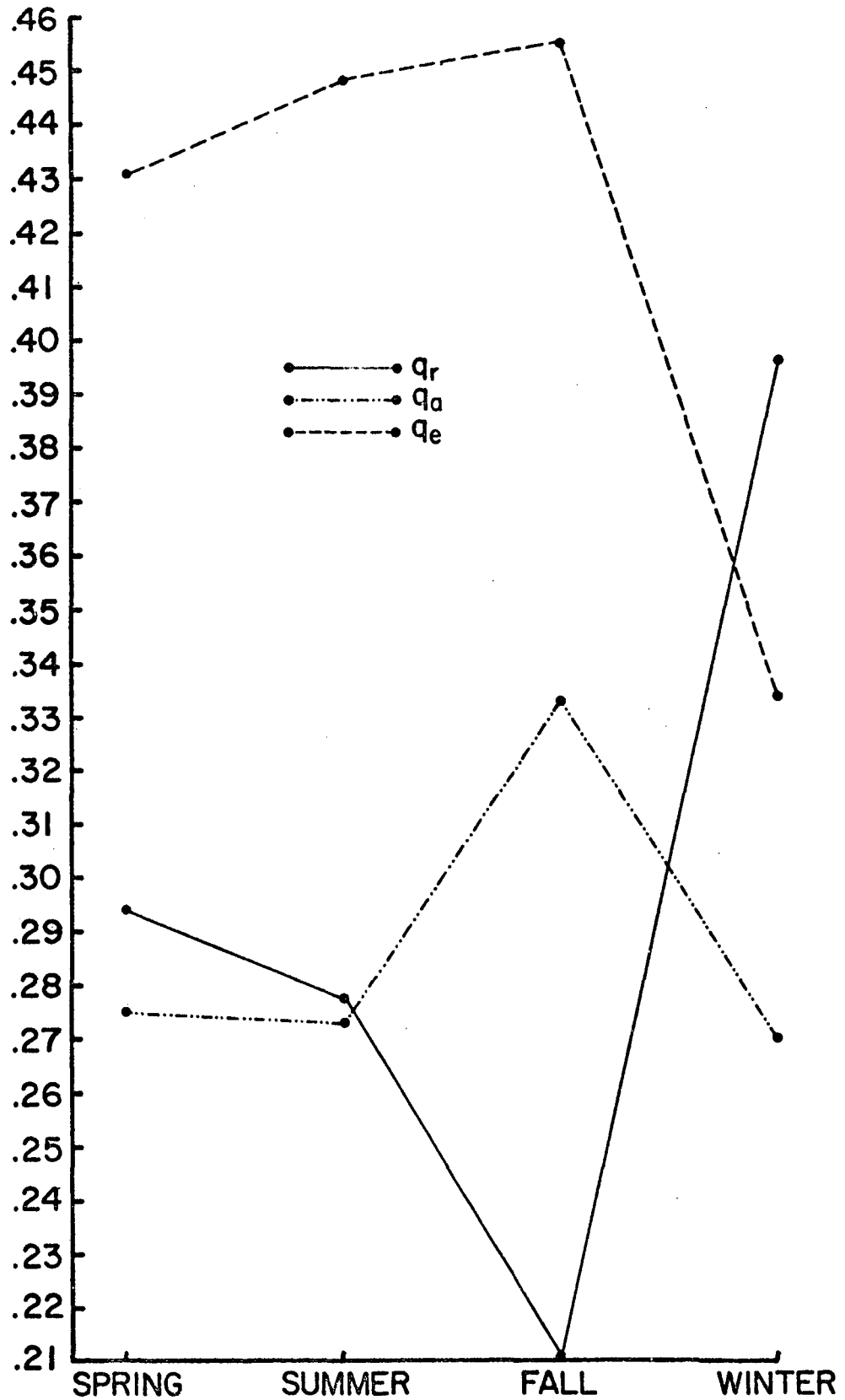


FIGURE 4.2-2 Seasonal variations in albedo and absorption in Europe. Seasons reckoned to the northern hemisphere.

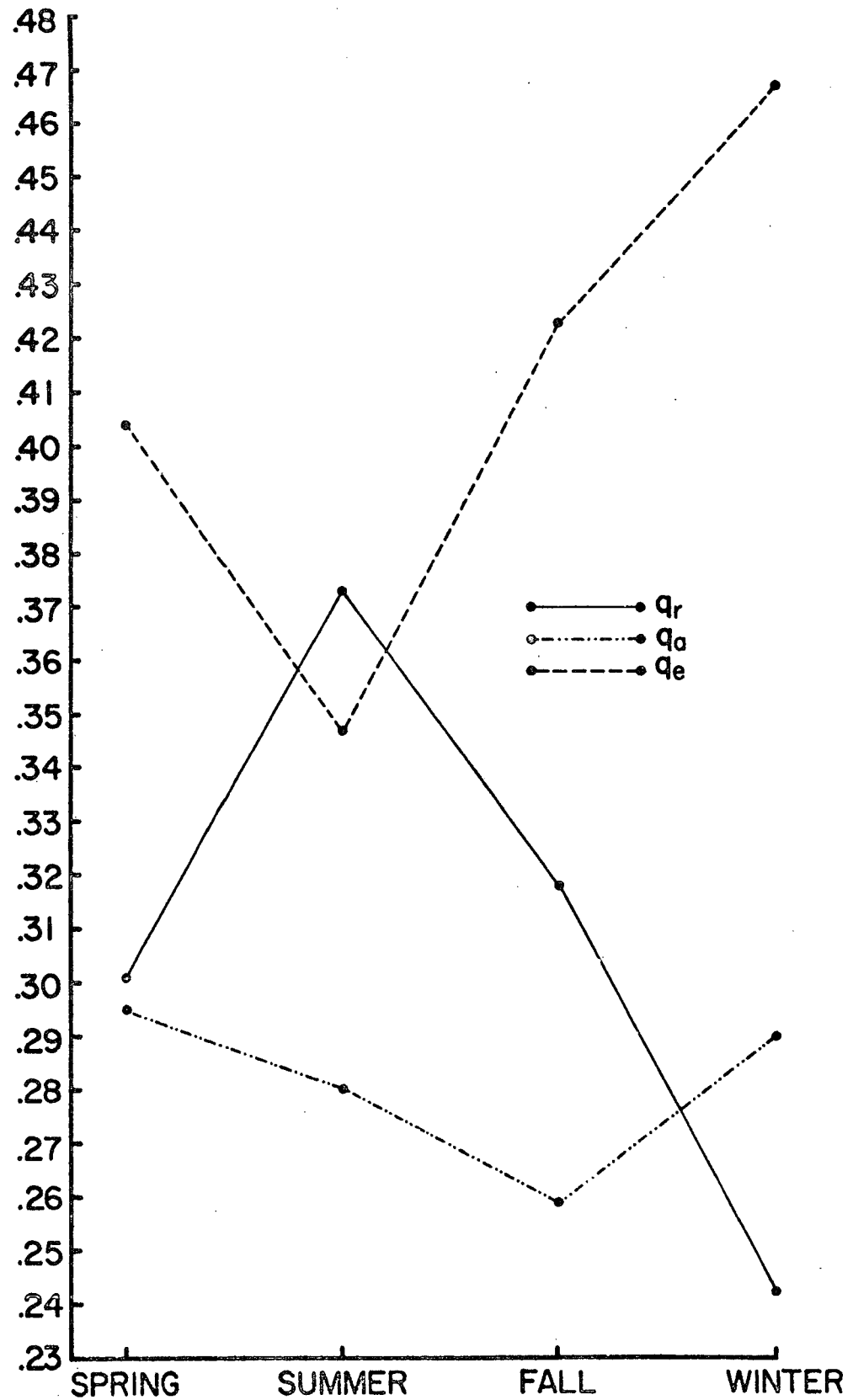


FIGURE 4.2-3 Seasonal variations in albedo and absorption in South America. Seasons reckoned to the northern hemisphere.

4.3 Distribution of q_r , q_a and q_e over the U. S.

Since most studies of solar energy absorption and reflection have concentrated on the U.S. network, comparisons may be made to determine any temporal differences.

The results of this study for June 1969 closely resemble those of Hanson (1971) during June 1966. A minimum in albedo was found by both studies in the southwest and southeast portions of the U.S. However, Hanson found a minimum (.34) in the northeastern U.S., while this study found minimum values of albedo (.27). There was also a discrepancy in the Great Lakes region where Hanson found a minimum (.28) and this study found a high flat gradient (.38). These differences are related to variations in the synoptic pattern over the country.

Values of q_e were similar in the southwest and Gulf of Mexico where both studies reported maximum values of surface absorption, but in the Great Lakes area this study found a minimum (.36) while Hanson found a maximum (.50). These differences were to be expected in light of the large variance in albedo in this region during the two years. Most of the pyranometer data used by Hanson was not corrected for either calibration or degradation errors (not available at the time of his work), hence his values of q_e are slightly too high and correspondingly, his values of q_a are too low.

Absorption in the atmosphere showed minimum values in the Great Basin and northern plains with maxima in the southeast and northeast. In the southwestern coastal area this study found a maximum in q_a (.36) due to slightly lower q_e found in this study in this area. Hanson found a flat gradient with values of q_a near .19.

Hanson, et. al. (1967) did another study over the U. S. with data from the spring of 1962. A marked similarity exists in the values of albedo between the 1962 study and the values found in April 1969. High albedo is present in both studies across the northern tier of states with a minimum in the southwest.

Atmospheric absorption is a minimum in the dry Great Basin in both studies and is a maximum in the moist southeast. Absorption at the surface is at a minimum in the northwest and south central U. S., and a maxima is present in the southwest in both studies.

4.4 Solar Heating Rate

Using the atmospheric absorption results we may obtain an atmospheric heating rate due to absorption of solar irradiance only.

The net heat gain or loss due to absorption of solar energy may be represented as $Q_o \cdot q_a$ which has units of energy area⁻¹ time⁻¹. Taking the difference in absorption between the top of the atmosphere and the surface, we get $\frac{\Delta Q_o \cdot q_a}{\Delta Z}$ with units of energy area⁻¹ time⁻¹ height⁻¹ which is equivalent to energy volume⁻¹ time⁻¹. Multiplying by ρ^{-1} (density) yields $\frac{1}{\rho} \frac{\Delta Q_o \cdot q_a}{\Delta Z}$ in units of energy time⁻¹ mass⁻¹.

The first law of thermodynamics may be written:

$$dh = c_p dT - \alpha dp \quad (13)$$

where h is energy added per unit mass, c_p (.240 cal g⁻¹ °K⁻¹) is specific heat at constant pressure and α is ρ^{-1} . If an isobaric process is assumed, $\alpha dp = 0$ and:

$$dh = c_p dT \quad (14)$$

Dividing equation (14) by dt yields:

$$\frac{dh}{dt} = c_p \frac{dT}{dt} = \frac{1}{\rho} \frac{\Delta Q_o \cdot q_a}{\Delta Z} \quad (15)$$

Using the hydrostatic equation:

$$\Delta P = -\rho g \Delta Z \quad (16)$$

where P is pressure, and the conversion:

$$1 \text{ mb} = 10^3 \text{ dynes cm}^{-2}, \quad (17)$$

we may say:

$$\Delta Z = \frac{\Delta P}{10^3 \rho g} \quad (18)$$

substituting into equation (15):

$$\frac{dT}{dt} = \frac{g}{c_p} \frac{\Delta Q_o \cdot q_a}{\Delta P 10^3} \text{ (}^\circ\text{C/day)} \quad (19)$$

An example of the solar heating rate over the U. S. during October 1969 is shown in Figure 4.4-1. For comparison, an average annual tropical heating rate was computed and found to be 1.08°C/day compared to an average annual heating rate over the U. S. of $.83^\circ\text{C/day}$.

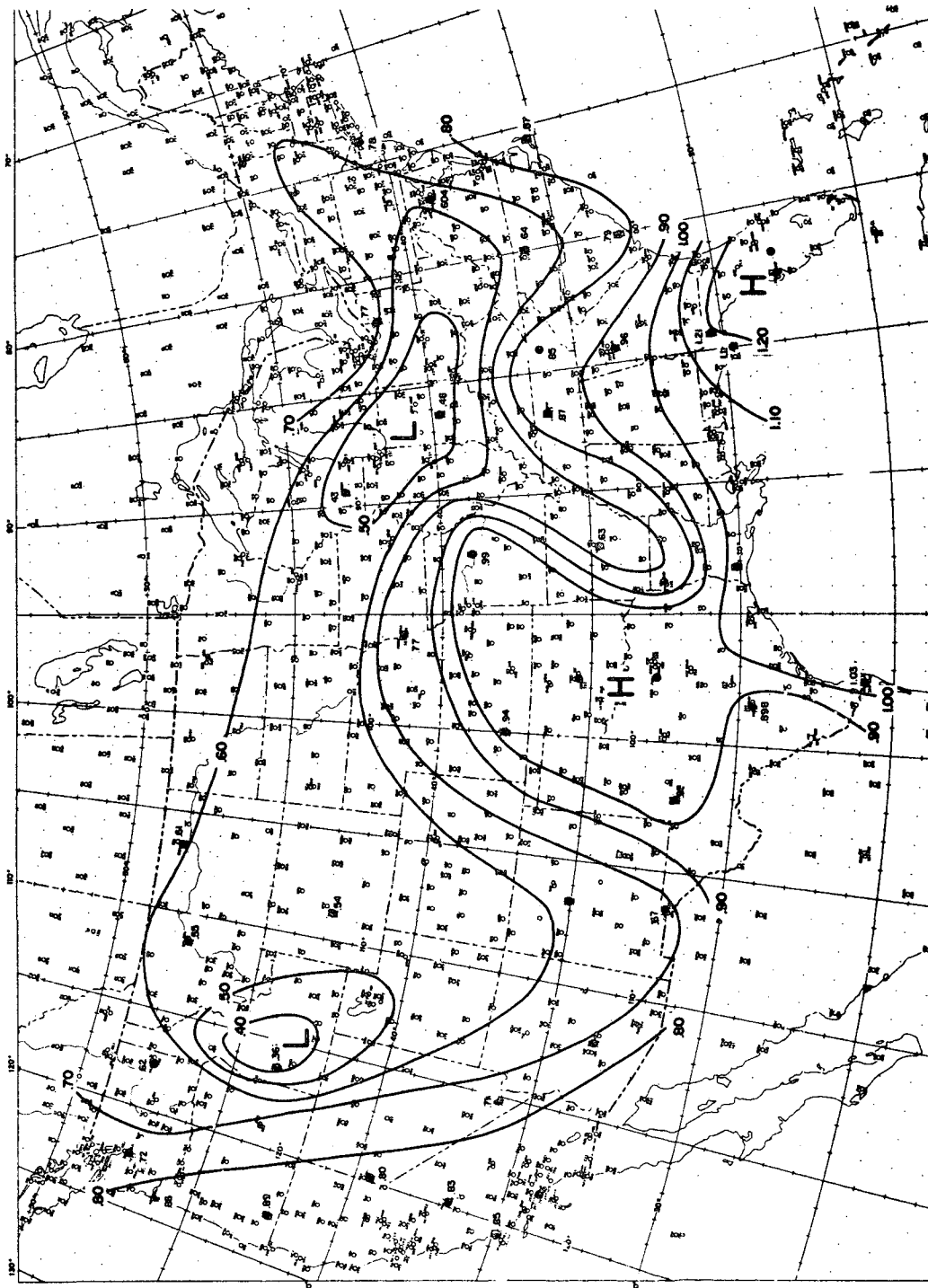


FIGURE 4.4-1 Solar heating rate over the U.S. during October 1969 in $^{\circ}\text{C}/\text{day}$.

These heating rates are not actually observed, however, Almost as fast as the energy is absorbed, it is either transferred vertically by longwave radiation and conduction or used to evaporate water so that the net result is an atmosphere that acts as a radiational sink. As Gray (1972) has pointed out, the atmosphere cools at the rate of $1.2^{\circ}\text{C}/\text{day}$.

Knollenberg (1972) has shown that a considerable portion of solar insolation in cloudy regions is used not for sensible heating but for latent purposes resulting from radiational cooling of the cloud layer. Figure 4.4-2 shows the solar heating rate for October 1969 with latent effects taken into account. It is assumed for computational purposes that the clouds in October had a mean temperature of 0°C .

Using equation (19), the average heating rate may also be computed for an oceanic volume. A tropical oceanic layer 100 meters deep would warm by absorption of solar energy at the rate of $.017^{\circ}\text{C}/\text{day}$ while a layer 1 cm deep would warm $170^{\circ}\text{C}/\text{day}$. This tremendous sensible heat source is used primarily for evaporation and hence latently heats the atmosphere.

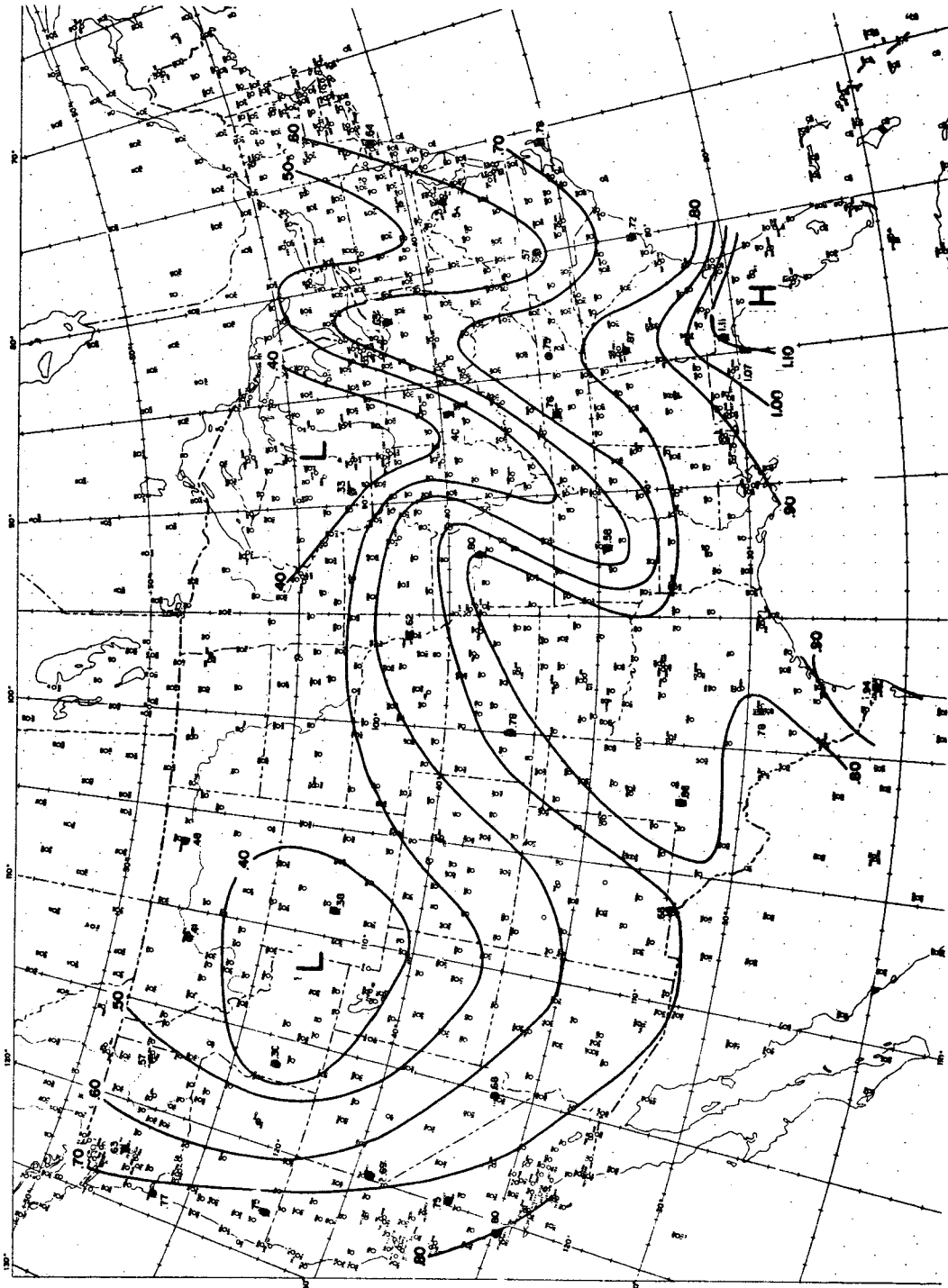


FIGURE 4.4-2 Solar heating rate with latent effects over the U.S. during October 1969 in $^{\circ}\text{C}/\text{day}$.

5.0 PARAMETERIZATION SCHEME USING REGRESSION TECHNIQUES

Parameterization of solar radiation absorption was formulated using a stepwise, least squares, multiple linear regression program with cloud cover and optical pathlength as independent variables (predictors) and atmospheric absorption as the dependent variable (predictand). Albedo (q_r) was also used as a predictor but only in the sense of providing a check on the cloud cover-albedo correlation.

The basic stepwise regression program, a library routine on the Colorado State University (CSU) CDC 6600 computer, was developed at U.C.L.A. (Dixon, 1970) and later slightly refined by the Statistical Laboratory at CSU. This program searches the data to find the best initial correlation among parameters and initializes the regression equation. At each succeeding step, a new independent variable, which makes the greatest reduction in the sum of squares, is added to the regression equation. Before each step an F test is applied to determine whether the additional variable is significant to the 95% confidence level, and if it is not, the regression program is terminated.

As each parameter is brought into the equation an r value (known as the multiple correlation coefficient) is determined. r^2 is defined as the fraction of total variance of q_a which is contributed by its regression on the independent variables. A value of zero gives no correlation between q_a and the predictors whereas a value of 1 means that all the sample points lie exactly on the regression line. Another statistical measure of confidence given by this program is the standard error of estimate, S , which is a measure of the residual scatter about the regression line.

5.1 Data Analysis

A statistically valid analysis of the results of the stepwise multiple linear regression program is dependent on a careful understanding of the extent and limitations of the data set used. Due to the scarcity of u^* data on a global basis, only albedo and cloud cover are available as predictors over most of the world. In these regions albedo is generally brought into the stepwise regression equations first, but this is to be expected from the relationship:

$$q_a = 1 - q_r - q_e \quad (20)$$

The fact that q_r is generally selected on the initial step of the regression is really insignificant since cloud cover and albedo are so closely correlated. In fact, the predictor chosen second generally adds little or nothing to r^2 , due to the near equivalence of cloud cover and q_r . Since satellite measurements of cloud cover are available during more previous years than measurements of albedo, the equality of their use in this study is significant for the study of other time periods.

Results of the parameterization scheme carried out over the U.S. network will be important for two reasons:

- 1) Values of Q_g are known to be highly accurate,
- 2) This is the only network where u^* was also compiled as an independent variable.

Since this ideal data is available with values of u^* included, we wish to know if u^* is the primary variable affecting absorption of solar

radiation. If this is the case, q_a will be a maximum when incoming solar irradiance "sees" the entire optical pathlength available. One may hypothesize that in regions of opaque cloudiness (high q_r), the effect of u^* would be minimal and atmospheric absorption low. Conversely, in clear regions (low q_r) u^* should be the dominant predictor, therefore q_a should be high.

Looking only at areas of the U.S. with greater than 25% opaque cloud cover during the four seasons (sample size 35), albedo was the best predictor accounting for an r^2 of .55. u^* was next in importance but provided an increase of only .04 in r^2 . Cloud cover was brought into the regression equation last and accounted for no increase in r^2 . This was to be expected in light of the relationship between cloud cover and albedo discussed above. Clearly u^* had little effect in the cloudy regions of this data set and with q_r a maximum, q_a is a minimum (.23).

In the clear regions (those areas with an albedo of .25 or less) cloud cover was brought into the regression equation first with an associated r^2 of .29. This may seem surprising at first because u^* was thought to be correlated best with q_a , but in this case study u^* and cloud cover were almost equally correlated with q_a . u^* was brought into the regression equation on the second step, providing an increase in r^2 of .26. Albedo was then brought into the equation and as expected only slightly raised r^2 . Here we can see that as hypothesized, with q_r a minimum, q_a is a maximum (.296).

We may conclude that u^* is an important predictor in the clear areas of the U.S. because it substantially raised r^2 and lowered the

standard error of estimate from .05 to .04. In cloudy regions the effect of u^* was overshadowed by the influence of cloud cover. The inverse relationship between q_r and q_a has been explained in terms of the importance of u^* in clear areas.

5.2 Results of the Parameterization Scheme

Over other regions of the world where there are two predictors of atmospheric absorption, q_r and cloud cover, three facts become immediately obvious:

- 1) Cloud cover and q_r are insignificant as predictors in the tropics. The maximum value of r^2 was .33 and for all time periods combined r^2 reached only .11. Outside the tropics, values of r^2 as high as .91 have been found, and for all time periods, all stations combined outside of the tropics, r^2 reached .28, more than twice the value found in the tropics. (As noted in section 4.1, the results apply exclusively to land areas).
- 2) The areal division of the world into networks has demonstrated that the parameterization of solar radiation absorption is a space problem and not a time problem. Time variations appear to be quite constant but the spatial differences far outweigh any temporal variations. The U.S. network produced the highest values of r^2 , followed closely by the European network. In contrast to these networks are the tropical and South American divisions which had consistently low values of r^2 .
- 3) One general equation will not effectively describe the parameterization of atmospheric absorption. When all stations from all time periods were combined, r^2 reached only .22 while S was rather high at .06. During the individual time periods with all stations throughout the world combined, r^2 fared only slightly better. These results are in line with the wide spatial variations cited above.

5.3 Results from the U.S. Network

Table 5.3-1 gives the results of the parameterization in the U.S., which was the best of all networks. N is the sample size, P is the parameter selected in each step and cc represents cloud cover. Note the play between the predictors entered as the first parameter into the stepwise regression. q_r was selected 4 times, cloud cover 4 times and u^* twice. u^* was significant in April and July but only practically significant in January and October. Reasons for the wide variation in importance of u^* are not immediately obvious but can be explained with the use of Table 5.3-2 which gives the correlation matrix for several time periods. During October and January even though u^* had a good positive correlation with q_a , q_r had a higher negative correlation and hence was brought into the regression equation on the first step. Obviously if q_r was deleted, u^* would be brought into these two time periods on the first step.

From Table 5.3-1 we see a large increase in r^2 between the first and second step during May 16-31. This would normally not be expected in light of the discussion in section 5.1, but the correlation matrix for May 16-31 (Table 5.3-1) explains why this anomaly occurred. Theoretically and in practice throughout this study, both cloud cover and q_r demonstrate a negative correlation with q_a . Clearly the positive correlation between cloud cover and q_a is out of line, making any parameterization scheme dubious.

August 1-15 was an anomalous time period throughout the globe and is certainly reflected in the U.S. network. Reference can be made to Table 5.3-2 which gives the correlation matrix for this time period which shows almost no correlation between the predictors and q_a .

		r^2	N	S	P
April	15-30	.26	39	.05	u*
		.38		.05	cc
		.51		.04	q _T
May	1-15	.16	38	.05	cc
		.36		.04	q _T
May	16-31	.15	34	.05	cc
		.53		.04	q _T
June	1-15	.58	42	.05	q _T
		.73		.04	cc
June	16-30	.23	44	.05	q _T
		.42		.04	cc
July	1-15	.23	49	.05	u*
		.28		.04	q _T
		.49		.04	cc
July	16-31	.15	52	.04	cc
		.32		.04	q _T
August	1-15	.05	49	.05	cc
		.14		.05	q _T
October	3-17	.40	33	.05	q _T
		.61		.04	cc
		.63		.04	u*
January 21 - October 3		.68	35	.05	q _T
		.77		.04	u*
		.80		.04	cc

TABLE 5.3-1 STATISTICAL ANALYSIS OF THE REGRESSION PROGRAM
OVER THE U.S. NETWORK

May 16-31 1969				
	cc	u*	q _r	q _a
cc	1.00	0.00	0.64	0.39
u*		1.00	0.00	0.00
q _r			1.00	-0.22
q _a				1.00

August 1-15 1969				
	cc	u*	q _r	q _a
cc	1.00	0.00	0.78	0.23
u*		1.00	0.00	0.00
q _r			1.00	-0.01
q _a				1.00

October 3-17 1969				
	cc	u*	q _r	q _a
cc	1.00	-0.46	0.78	-0.21
u*		1.00	-0.54	0.42
q _r			1.00	-0.63
q _a				1.00

January 21 - February 3 1970				
	cc	u*	q _r	q _a
cc	1.00	-0.35	0.85	-0.57
u*		1.00	-0.57	0.71
q _r			1.00	-0.83
q _a				1.00

5.3-2 CORRELATION MATRICES FROM MAY 16-31, AUGUST 1-15 AND OCTOBER 3-17, 1969 AND JANUARY 21-FEBRUARY 3, 1970.

6.0 CONCLUSIONS AND RECOMMENDATIONS

It is well known that the energies driving the atmospheric circulation against frictional dissipation are produced by a non-homogeneous spatial distribution of the atmospheric heat sources and sinks. The primary cause of such a spatially non-homogeneous heating field in the atmosphere is the net radiative warming in lower latitudes and the net cooling in the higher latitudes in the earth-atmosphere system. Therefore knowledge about the distribution of any one part of the radiation budget in the earth-atmosphere system will be helpful in determining the entire radiation budget. This study has concentrated on solar irradiance, an often overlooked portion of the heat and energy balance of the earth-atmosphere system.

In addition to meteorological and oceanographic applications, results may also be used by biologists, botanists and agriculturalists as Gates (1972) has pointed out. Gates found that many plants and animals have an upper and lower threshold as to the amount of solar radiation they can absorb. Habitation restrictions would be imposed if these limits were exceeded in a particular geographic area.

In line with these applications this study found surface absorption of solar irradiance was 18% (relative) greater over the oceanic portion of the tropics than over the continental regions. This adds significantly to the role of the oceans in maintaining the heat balance of the earth-atmosphere system. Due to lower values of tropical albedo, both atmospheric and surface absorption values are higher than the zonal averages given by London (1957). Also of interest is the inverse relationship between q_r and q_a .

Results of the parameterization scheme indicate:

- 1) u^* is indeed an important predictor in clear regions.
- 2) the parameterization of solar radiation absorption is a space problem and not a time problem
- 3) both cloud cover and q_r are insignificant predictors in the tropics
- 4) one general equation will not effectively describe the parameterization of solar radiation absorption

Hanson (1972) reviewed several methods of parameterizing Q_G :

- A) The use of long term mean irradiance provided a reasonable parameterization scheme only on a time scale of a year.
- B) The use of surface observed cloud cover provides a slightly better parameterization scheme on the shorter time scales. Hanson estimates that the numerous and differing formulae for parameterizing Q_g from surface observed cloud cover are due primarily to time scale variations.
- C) The use of satellite data to parameterize Q_g was tested on only a monthly time scale but was considerably better than methods a and b on the same time scale.

One may conclude that indeed the satellite parameterization scheme on intermediate time scales is the best available. It would be interesting for future studies to compare parameterization schemes of surface observed cloud cover with those of satellite observed cloud cover.

Hanson et al. (1967) and Hanson (1972) have also looked at a parameterization scheme using q_a as the dependent variable and u^* as the dependent variable. The results were encouraging and demonstrated a logarithmic relationship. This study employed only a linear regression scheme allowing no transgenerations. Future studies should take into consideration the logarithmic parameterization scheme.

Other studies of this type could be enhanced by securing more tropical island and ship data. If the current island network is inadequate then more actinometric stations should be established.

The parameterization scheme has definite potential for further research especially over the U. S. and Europe; this being the case, u^* data should be secured over Europe and run with 1972 data.

In the near future meteorological satellites will provide real-time cloud cover, albedo and water vapor profiles. Studies may then proceed on the meso-scale and synoptic level on a daily time scale and perhaps enhance short and long term weather forecasting.

REFERENCES

- Booth, A. L. and Taylor, V. R., 1968: Meso-scale archive and products of digitized video data from ESSA satellites. ESSA TM NESCTM-9, National Environmental Satellite Center, Suitland, Maryland.
- Budyko, M. I., 1963: Atlas teplovogo balansa. Gidrometeorologicheskoe Izdatel'skoe, Moskow.
- Case, R.: Personal communication.
- Cox, S. K., Vonder Haar, T. H., Hanson, K. J. and Suomi, V., 1972: Measurements of absorbed shortwave energy in a tropical atmosphere. Solar Energy, Vol. 14.
- Dixon, W. J., 1970: Biomedical computer programs. University of California publication in Auto. Comp., No. 2.
- Downey, P. H., Lassman, S. J. and Vonder Haar, T. H., 1972: A study of extreme and persistent cloudiness based on satellite observations (1969-1970), Colorado State University Tech. Report.
- Fritz, S., Krishna Rao, P., and Weinstein, M., 1964: Satellite measurements of reflected solar energy and the energy received at the ground. Jour. Atmos. Sci., 21, pp. 141-151.
- Gabites, J. F., 1950: Seasonal variations in the atmospheric heat balance. ScD. thesis, Massachusetts Institute of Technology.
- Gates, D. M., 1972: Man and His Environment: Climate, Harper and Row.
- Geiger, R., 1963: Total Annual Shortwave Radiation (map), Darmstadt, Germany.
- Gray, W. M., 1972: The magnitude and character of the radiation induced vertical circulation of the Troposphere. Conf. on Atmos. Rad., AMS.
- Hanson, K. J., 1971: Studies of cloud and satellite parameterization of solar irradiance at the earth's surface. Proceedings of the Miami Workshop on Remote Sensing, U. S. Department of Commerce.
- Hanson, K. J., Hickey, J. and Scholes, W.: A report on the pyranometer calibration program of the U. S. Weather Bureau, ESSA and NOAA 1954-1972. In publication.
- Hanson, K. J., Vonder Haar, T. H. and Suomi, V. E., 1967: Reflection of sunlight to space and absorption by the earth and atmosphere over the U. S. during Spring 1962. Mon. Wea. Rev., 95, 6, pp. 354-362.

- Knollenberg, R. G., 1972: On radiational cooling computations in clouds. Jour. Atmos. Sci., 29, 1, pp. 212-214.
- Kung, E. C., Bryson, R. A., and Lenschow, D. H., 1964: Study of a continental surface albedo on the basis of flight measurements and structure of the earth's surface cover over North America. Mon. Wea. Rev., 92, 12, pp. 543-563.
- London, J., 1957: A study of the atmospheric heat balance. Final Report, Contract AF 19(122)-165, College of Engineering, New York University.
- London, J. and Sasamori, T., 1971: Radiative energy budget of the atmosphere. Sp. Res. IX, Akademik-Verlag, Berlin.
- Miller, D. B., 1971: Global atlas of relative cloud cover 1967-70. U. S. Department of Commerce, Washington, D. C.
- Posey, J. W. and Clapp, P. F., 1964: Global distribution of normal surface albedo. Geof. Inter., 4, 1, pp. 33-48.
- Quinn, W. H., Burt, W. V. and Pawley, W. M., 1969: A study of several approaches to computing surface insolation over tropical oceans. Jour. Appl. Met., 8, 2, pp. 205-212.
- Raschke, E., Vonder Haar, T. H., Bandeen, W. R. and Pasternak, M.: The radiation balance of the earth-atmosphere system from Nimbus 3 radiation measurements (15 April 1969 - 3 February 1970). In publication.
- Riehl, H., 1954: Tropical Meteorology. McGraw-Hill Publishing Co.
- Sellers, W. D., 1965: Physical Climatology. University of Chicago Press.
- Swinbank, W. C., 1963: Longwave radiation from Clear Skies. Quart. Jour. Roy. Met. Soc., 89, pp. 339-348.
- Vonder Haar, T. H., 1968: Variations of the Earth's Radiation Budget. Meteorological Satellite Instrumentation and Data Processing, Final Scientific Report on NASw-65 1958-1968, University of Wisconsin, pp. 31-107.
- Vonder Haar, T. H., 1972: Natural Variation of the Radiation Budget of the Earth-Atmosphere System as Measured from Satellites. In publication.
- Vonder Haar, T. H. and Hanson, K. J., 1969: Absorption of Solar Radiation in Tropical Regions. Jour. Atmos. Sci., 26, 4, pp. 652-655.

Yamamoto, Giichi, 1962: Direct Absorption of Solar Radiation by
Atmospheric Water Vapor, Carbon Dioxide and Molecular Oxygen.
Jour. Atmos. Sci., 19, 2, pp. 182-188.

APPENDIX A

ESSA 9 was launched February 26, 1969 by the National Aeronautics and Space Administration (NASA) into a nearly circular, sun-synchronous polar orbit at an average altitude of 910 statute miles above the earth's surface. The orbit is inclined at 102° (retrograde) to the equatorial plane with an equatorial crossing of approximately 1430 L.

The original vidicon data tapes compiled by the National Environmental Satellite Service (NESS) (3 days of data per tape) were reduced in area resolution during processing for economic reasons. Digitized data from ESSA 9 was resolved each day into two 4096 X 4096 matrices, which present polar stereographic views of both Northern and Southern hemispheres. A 64 X 64 submatrix of this full resolution data corresponds to a Numerical Weather Prediction (NWP) grid. Thus, there are 4096 NWP grid squares per hemisphere. The term "meso-scale" (often used in the literature) refers to an 8 X 8 submatrix of the NWP grid square and hence has an area 1/64 of an NWP grid. Meso-scale data covers a 512 X 512 square grid per hemisphere which has a resolution that varies from 16 nautical miles at the equator to 32 nautical miles at the poles. Each meso-scale grid originally contained 64 data points with integral values from 0 (darkest) to 14 (brightest), representing a measure of the brightness of clouds, background, or a composite of both. The original brightness data with a range 0-14, was reduced at NESS, into 5 equal classes from 1-5, thus achieving a three fold reduction in dynamic range prior to processing by CSU. Space reduction was achieved by combining the frequency distributions of 16 meso-scale

data grid points, thus providing a $\frac{1}{4}$ NWP grid mesh resolution (190 km at 60°N) for the present study. In a $\frac{1}{4}$ NWP there are 1024 data points (the population of the new frequency distribution).

Those interested in a description of the tape format of the satellite data should consult Booth and Taylor (1968) Downey et al. (1972) discuss in detail the quality of the compressed data tapes.

Miller (1971) converted brightness data to octas of cloud cover through the simple weighting scheme shown below:

Orig. Bright- ness Range	Class	Contribution to total cloud amount	Weights	
			October-May	June-Sept.
0, 1, 2	1	0%	0	0
3, 4, 5	2	25%	2	2.5*
6, 7, 8	3	88%	7	7.5*
9, 10, 11	4	100%	8	8
12, 13, 14	5	100%	8	8

* The summer and winter weights were applied according to the hemispheric season.

When applied to several years of ESSA data, this weighting scheme yields reasonable results for total cloud amount. However, the scheme is not effective for determining opaque cloud cover because it weights clouds with low albedo (class 2). The values used in this study to determine opaque cloud cover are listed in the following table:

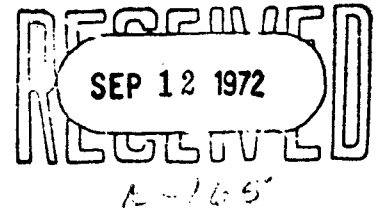
Orig. Brightness Range	Class	Contribution to total cloud amount	Weights ¹
0, 1, 2	1	0%	0
3, 4, 5	2	25%	0
6, 7, 8	3	100%	1
9, 10, 11	4	100%	2
12, 13, 14	5	100%	3

¹Cloud cover in this study is not determined on an octal, but rather a percentage basis.

Of the numerous weighting schemes tried, this weighting scheme displayed the highest correlation between albedo and opaque cloud cover.

Comparisons of the resultant cloud cover have been made with minimum albedo maps from Nimbus 3 to determine whether background noise (surface albedo) will bias the nephanalysis. As it turns out, with the weighting scheme above, the output yields results only for an equivalent albedo $\geq 35\%$. Thus, the only background problem exists in areas covered with ice and snow and the North African deserts.

More checks were made to determine the quality of the output by comparison with Nimbus 3 albedo maps, Miller's weighted output, actual surface observations over the United States, and actual cloud photographs. The results were encouraging and verified the fact that this weighting scheme gives a satisfactory correlation between brightness and opaque cloud cover.



NEW ESTIMATE OF ANNUAL POLEWARD ENERGY TRANSPORT
BY NORTHERN HEMISPHERE OCEANS

by

Thomas H. Vonder Haar
Department of Atmospheric Science
Colorado State University
Fort Collins, Colorado

and

Abraham H. Oort
Geophysical Fluid Dynamics Laboratory/NOAA
Princeton University
Princeton, New Jersey

Accepted For Publication in
J. Phys. Ocean. April, 1973 issue

ABSTRACT

Recent measurements of the earth's radiation budget from satellites, together with extensive atmospheric energy transport summaries based on rawinsonde data, allow a new estimate of the required poleward energy transport by northern hemisphere oceans for the mean annual case. In the region of maximum net northward energy transport (30-35°N), the ocean transports 47% of the required energy ($1.7 \times 10^{22} \text{ cal} \cdot \text{yr}^{-1}$). At 20°N, the peak ocean transport accounts for 74% at that latitude; for the region 0-70°N the ocean contribution averages 40%.

1

Poleward energy transport by ocean currents plays an important role in climate on earth and has been a subject of study for many years. Bryan (1962) provides a synopsis of the estimates based on surface heat budget studies (Budyko (1958), Albrecht (1960), Sverdrup (1957)). In addition, he demonstrates a method for oceanic transport calculations based on hydrographic data as an extension of earlier work by Jung (1952). The inadequacies of the former method are shown by Bryan to result primarily from the fact that the transport is calculated as a small residual of two large quantities, the net radiation gain of the ocean surface and the net energy loss (to the atmosphere) due to latent and sensible heat exchange. Unfortunately, global availability of hydrographic data is probably not yet extensive enough to use the second technique for global ocean transport estimates; an additional difficulty is the ambiguity in the choice of reference level.

The present study uses a third, indirect approach based entirely upon measurements. Satellite data on the net radiation budget of the earth-atmosphere system (Vonder Haar and Suomi, 1971) are now available over sufficient time periods (data from the years 1962-1970 are used in this study) to allow a firm estimate of the "mean annual" energy exchange between earth and space. In addition, rawinsonde data from the MIT General Circulation Library for the 5-year period May 1958 through April 1963 give a matching data set for which Oort (1971) has calculated the energy transport in the atmosphere.

The energy balance for a polar cap north of a certain latitude, $\phi^{\circ}\text{N}$, can be written in the following form (compare Starr, 1951):

$$\partial E / \partial t = AT + OT + RF + HF \quad (1)$$

where $\frac{\partial E}{\partial t}$ = rate of change with time of the total energy in a polar cap north of latitude ϕ^0_N . The important components of the total energy are the internal energy, potential energy, latent heat and kinetic energy of the atmosphere, ocean and cryosphere (snow and ice) contained in the polar cap.

AT = atmospheric energy flux into polar cap across latitude ϕ^0_N (area S1)

$$= \int_{S1} \int \rho (c_v T + gz + Lq + c^2/2 + p/\rho) v \, dx \, dz$$

OT = oceanic energy flux into polar cap across latitude ϕ^0_N (area S2)

$$= \int_{S2} \int \rho (c'_v T + gz + c^2/2 + p/\rho) v \, dx \, dz$$

RF = net radiational flux into polar cap at top of the atmosphere (area S3)

$$= \int_{S3} \int Q \, dx \, dy$$

HF = energy flux into polar cap at the surface of the solid earth (area S4)

$$= \int_{S4} \int Q' \, dx \, dy$$

Other symbols used are:

c = wind (current) velocity

$c_v (c'_v)$ = specific heat at constant volume in atmosphere (ocean)

g = acceleration resulting from gravity

L = heat of condensation

P = pressure

q = specific humidity
 Q = net flux of radiation at top of atmosphere
 Q' = net flux of energy at surface of solid earth
 T = temperature
 v = northward component of wind (current)
 z = height
 ρ = density

For a period of a year the energy storage in the atmosphere-ocean-cryosphere system $(\partial E/\partial t)$ ¹ and the energy exchange with the solid earth (HF) are probably small compared to the remaining terms on the right-hand side of (1) and will be neglected. Thus, on a mean annual basis we assume an approximate balance of the following form:

$$AT + OT + RF = 0 \quad (2)$$

From satellite measurements we have an estimate of the net radiational heating (RF) which under the assumptions used in deriving (2) must be equal to the net northward energy flow into the polar cap. The atmospheric measurements supply an estimate of AT . Therefore the oceanic transport (OT) can be computed from (2) as a residual. Figure 1 shows the total energy flux from radiation requirements (RF), the atmospheric flux (AT) and the deduced oceanic flux as a function of latitude. The numerical values are presented in Table 1. Sellers (1965) values for atmospheric (AT_s) and oceanic (OT_s) transports based on the most recent surface energy budget estimates (including Budyko's (1963) estimates) are also tabulated.

¹) Variability in ocean energy storage, presently under study in terms of temperature anomalies, is not well known but most probably lies within the error limits of this study.

The atmospheric energy flux was computed for 5 different years. This enabled us to estimate the error of the 5-year mean value of AT by calculating the standard deviation of the mean $S = \sigma(X)/(N-1)^{1/2}$, where $n = 5$. Twice the standard deviation of the mean indicates the 95% confidence limit and we assume that the instrument plus sampling error of the atmospheric transport is not larger than this value. Error estimates are tabulated in Table 2. From Vonder Haar (1968) and Vonder Haar and Suomi (1971), error analysis of the satellite measurements showed a maximum probable bias error of $\pm 0.01 \text{ cal} \cdot \text{cm}^{-2} \cdot \text{min}^{-1}$ in mean annual zonal values of the net radiation, Q . The cumulative effect of such an error in the required transport (RF) values derived from the satellite measurements increases equatorward from the beginning point of integration at $\phi = 90^\circ \text{N}$ (Table 2). The law of propagation of independent errors was used to obtain the estimate of error in the derived ocean transport $E_{\text{OT}} = (E_{\text{RF}}^2 + E_{\text{AT}}^2)^{1/2}$. This error is indicated by the shading in Fig. 1.¹

Between $10\text{--}50^\circ \text{N}$ latitude the ocean transports derived in the present study are significantly greater than those previously derived. In the region of maximum net northward energy transport by the ocean-atmosphere system ($30\text{--}35^\circ \text{N}$), the ocean transports 47% of the required energy ($1.7 \times 10^{22} \text{ cal yr}^{-1}$). At 20°N , the peak ocean transport accounts for 74% at that latitude; for the region $0\text{--}70^\circ \text{N}$ the ocean contribution averages 40%. Both the absolute magnitude of the ocean transport and the relative role of the oceans significantly exceed earlier estimates.

¹The error shown for the tropics and subtropics results primarily from the cumulative satellite error. It is definitely a worst case estimate for this region since independent information (Vonder Haar and Suomi (1971) from measurements, London and Sasamori (1971) from calculations) show no net energy transport required across the equator. Thus, our transport integration could begin at 0° rather than 90° .

The total transport value, RF , derived directly from satellite measurements is also greater than earlier (pre-satellite) estimates (Houghton, 1954). Vonder Haar (1968) pointed out that the increased required energy transport stemmed primarily from a lower albedo in tropical regions than was estimated before satellite data became available. Vonder Haar and Hanson (1969) showed that the increased net gain of energy in the tropics was corroborated by the few available measurements of direct solar energy reaching the tropical ocean surfaces. In fact, they showed that the extra energy entering the tropical zones was primarily absorbed in the oceans. Independent checks of the satellite values (1962-1966) on the annual scale have just recently been possible using Nimbus 3 radiation budget measurements during 1969-1970 (Vonder Haar, et. al. (1972), Raschke, et. al. (1972)). These data, from a totally different radiometer system, confirm the earlier satellite results of a lower planetary albedo (0.29 - 0.30), an increased net energy gain and an increased required transport. In addition, the atmospheric transport values used in this study are somewhat smaller than earlier values compiled by Sellers (1965) (see Table 1). Thus, the absolute value of ocean transport must be greater since the overall requirement is greater and the atmosphere transports less.

These new ocean values show that not only the absolute amount, but also the relative role of the oceans is greater than previously believed. They are shown to transport on the average 40% of the total required. Peak net transport values for the ocean ($20^{\circ}N$) apparently exceed the flat atmospheric maxima between $30-50^{\circ}N$. Location of the ocean peak is the same as Sellers has shown, but the transport value is more than 50% larger. Note that the curves indicate the need for a small net northward energy transport across the equator by the oceans.

In recent years large numerical models have been used to simulate the circulation of the atmosphere and the ocean. As they pass from the development phase they offer great promise for numerical experimentation. A measure of their representativeness is gained by comparison of their computed values of basic circulation parameters with the observed values. Comparison of the recent values of ocean transport computed in a joint ocean-atmosphere model run for the annual case (Bryan (1969); Manabe (1969)) shows that the total northern hemisphere transport calculated by the model is less than the results of this study (but in agreement with previously accepted values). Furthermore, the latitude of maximum transport by oceans was calculated in the model to be about 38°N , which is not in agreement with our results or any others. Wetherald and Manabe (1972) have recently run another joint atmosphere-ocean model in which seasonal variations of insolation were allowed. Reduced snow cover in the high latitude summer lessened the annual gradient of net radiation to space and also the meridional transport of energy by ocean currents. Thus, this recent experiment caused the ocean value to deviate even further from our result. At this point it should be mentioned that the models presently used to simulate the combined atmosphere-ocean system are highly idealized and cannot be expected to give very reliable results for the ocean transport. For example, in the model horizontal sub-grid scale and vertical mixing strongly affect the oceanic heat transport. Unfortunately, it is not known what value one should use for the mixing coefficient.

In summary, the estimates of ocean transport obtained in the present study are greater than previously believed; are derived from two new extensive data sets that have been checked and will be continuously

updated in the years to come; and are timely in view of the renewed interest in the influence of the ocean on weather and climate. Our results suggest that air sea interaction in mid-latitudes may be even more significant than presently acknowledged.

Acknowledgements

This research has been sponsored in part by NASA Grant NGR 06-002-102 and NSF Grant GA-31588. We thank our colleagues for their stimulating reviews and discussion.

References

- Albrecht, F., 1960: Jahreskarten des Wärme- und Wasserhaushaltes der Ozeane. (Annual charts of the heat and water balance of the oceans). Berichte Deutscher Wetterdienst, 9, 66, pp. 3-19, Germany
- Budyko, M. I., 1958: The heat balance of the earth's surface. (Teplovoi balans zemnoi poverkhnosti, 1956), N. A. Stepanova, Translator, U.S. Weather Bureau, Washington, D. C., 259 pp.
- Budyko, M. I., 1963: Atlas of the heat balance of the globe (in Russian). Moscow, Hydrometeorological Service, 69 pp.
- Bryan, K., 1962: Measurements of meridional heat transport by ocean currents. Jour. Geo. Res., 67, 9, pp. 3403-3414.
- Bryan, K., 1969: Climate and the ocean circulation: III. The ocean model. Mon. Wea. Rev., 97, 11, pp. 806-827.
- Houghton, H. G., 1954: On the annual heat balance of the Northern Hemisphere J. Meteor., 11, 1, pp. 1-9
- Jung, G. H., 1952: Note on the meridional transport of energy by the oceans. J. Marine Research, Sears Foundation, 11, 2, pp. 139-146.
- London, J. and T. Sasamori, 1971: Radiative energy budget of the atmosphere. Space Res. XI. Akademie-Verlag, Berlin, 1, pp. 639-649.
- Manabe, S., 1969: Climate and the ocean circulation: II. The atmospheric circulation and the effect of heat transfer by ocean currents. Mon. Wea. Rev., 97, 11, pp. 775-805.
- Oort, A. H., 1971: The observed annual cycle in the meridional transport of atmospheric energy. J. Atmos. Sci., 28, 3, pp. 325-339.
- Raschke, E., T. H. Vonder Haar, M. Pasternak and W. R. Bandeen, 1972: The radiation balance of the earth-atmosphere system from Nimbus 3 radiation measurements (16 April 1969 - 3 February 1970). NASA Tech. Note (in press).
- Sellers, W. D., 1965: Physical Climatology. The University of Chicago Press, 272 pp.
- Starr, V. P., 1951: Applications of energy principles to the general circulation. Compendium of Meteorology, Boston, Amer. Meteor. Soc., pp. 568-574.
- Sverdrup, H. U., 1957: Oceanography. Handbuch der Physik, 48, Akademie-Verlag, Berlin, pp. 608-670.

Vonder Haar, T. H., 1968: Variations of the earth's radiation budget. Ph.D. thesis, Dept. of Meteorology, Univ. of Wisconsin, 118 pp.

Vonder Haar, T. H., 1972: Natural variation of the radiation budget of the earth-atmosphere system as measured from satellites. Preprint Volume, Conference on Atmospheric Radiation, Fort Collins, Colorado, August, pp. 211-220.

Vonder Haar, T. H. and Hanson, K. J., 1969: Absorption of solar radiation in tropical regions. J. Atmos. Sci., 26, 4, pp. 652-655.

Vonder Haar, T. H. and V. E. Suomi, 1971: Measurements of the earth's radiation budget from satellites during a five-year period. Part I: Extended time and space means. J. Atmos. Sci., 28, 3, pp. 305-314.

Vonder Haar, T. H., E. Raschke, M. Pasternak and W. R. Bandeen, 1972: The radiation budget of the earth-atmosphere system as measured from the Nimbus-III satellite (1969-70). Space Res. XII, Akademie-Verlag, Berlin (in press).

Wetherald, R. T. and S. Manabe, 1972: Response of the joint ocean-atmosphere model to the seasonal variation of the solar radiation. Mon. Wea. Rev., 100, 1, pp. 42-59.

TABLE 1: POLEWARD ENERGY TRANSPORT IN THE NORTHERN
HEMISPHERE FOR THE MEAN ANNUAL CASE

Lat.	RF ¹⁾	AT ²⁾	OT	AT _S ³⁾	OT _S ³⁾	OT/RF
90°N	0	0	0	0	0	----
80	0.32	0.37	-0.05	0.25	0	----
70	1.14	1.10	0.04	1.18	0.09	3.5%
60	2.15	2.11	0.04	2.14	0.26	2 %
50	3.10	2.24	0.86	2.82	0.57	28 %
40	3.76	2.20	1.56	3.10	0.79	41 %
30	3.88	2.03	1.85	2.60	1.15	48 %
20	3.49	0.91	2.58	1.34	1.19	74 %
10	2.14	0.72	1.42	0.42	0.81	66 %
EQ	0.33	0.13	0.20	-0.07	-0.16	60 %
10°S	-1.54	-1.44	-0.10	-0.66	-1.00	6.5%
(Values x 10 ²² cal·yr ⁻¹ ; minus indicates net southward transport)						

1) The values of RF are slightly different from those reported by Vonder Haar and Suomi (1971), since the measurements from the 13 seasons of that study have been augmented by 4 more measurement seasons (see Vonder Haar, 1972).

2) The values of AT are slightly different from those reported earlier by Oort (1971). The present values represent the mean of 5 years analyzed separately. In the earlier study the same 5-year data set was analyzed but as one sample.

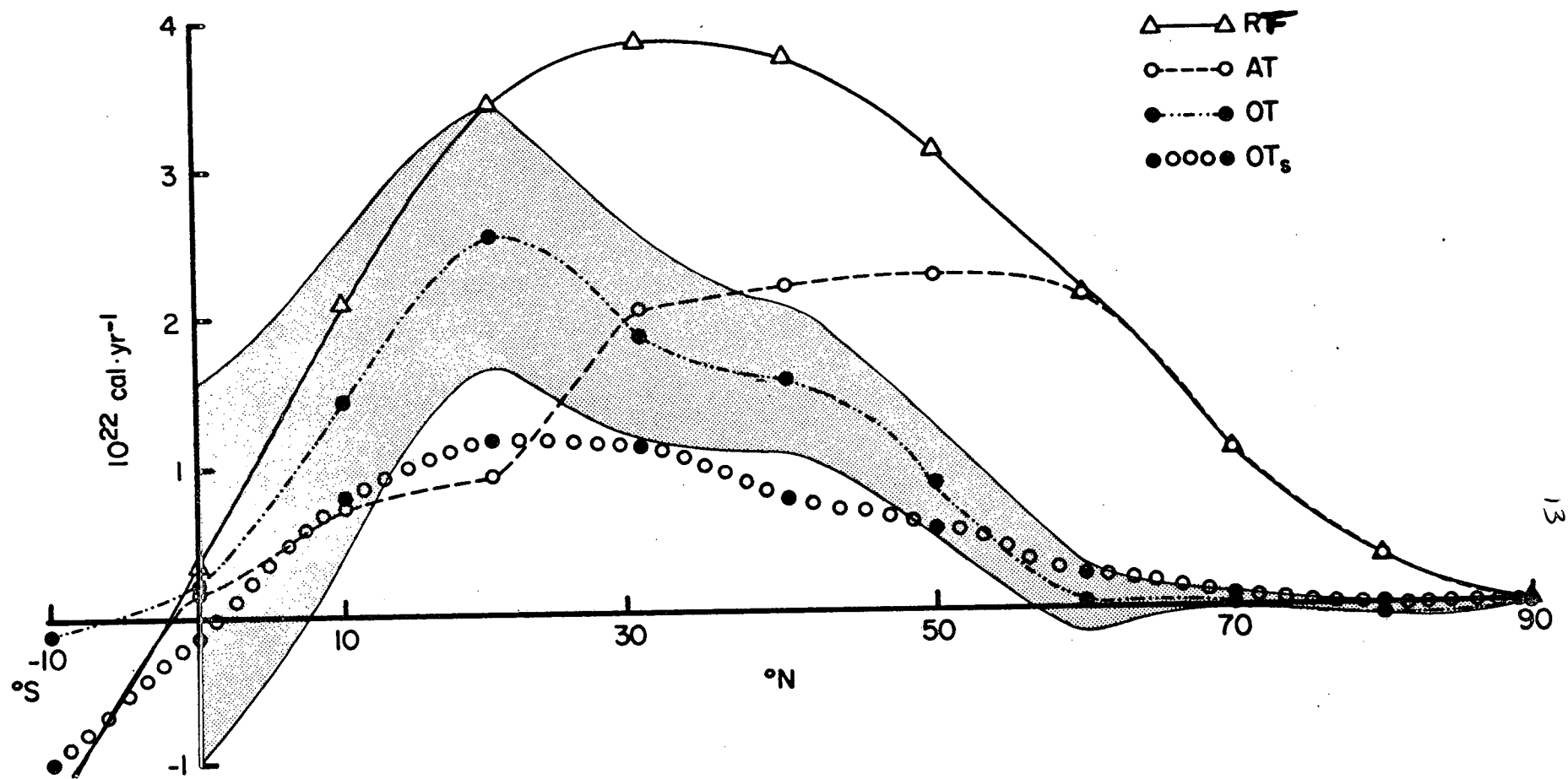
3) Values of AT and OT as given by Sellers (1965).

TABLE 2: PROBABLE ERROR IN MEASUREMENTS AND ESTIMATES OF POLEWARD ENERGY TRANSPORT IN THE NORTHERN HEMISPHERE FOR THE MEAN ANNUAL CASE (10^{22} cal yr $^{-1}$)

Lat.	E_{RF}	E_{AT}	E_{OT}
90°N	----	----	----
80	±0.02	±0.12	±0.12
70	±0.08	±0.06	±0.10
60	±0.18	±0.10	±0.21
50	±0.32	±0.16	±0.34
40	±0.48	±0.10	±0.49
30	±0.67	±0.16	±0.68
20	±0.88	±0.08	±0.88
10	±1.10	±0.12	±1.10
EQ	±1.33	±0.10	±1.33
10°S	±1.56	±0.24	±1.58

Figure Legend

1. Variation of net energy transport with latitude over the northern hemisphere. RF , total required energy transport inferred from satellite measurements; AT , measured energy transport by the atmosphere; OT , ocean energy transport derived from the present study; OT_S , ocean energy transport according to Sellers (1965). Uncertainty in the OT values is denoted by the shading. Minus values indicate net transport to the south.



NATURAL VARIATION OF THE RADIATION BUDGET OF THE EARTH-ATMOSPHERE SYSTEM AS MEASURED FROM SATELLITES

Thomas H. Vonder Haar

Colorado State University
Fort Collins, Colorado 80521

1.0 INTRODUCTION

The earth's radiation budget has been a subject of study and estimation for more than a century. Beginning with pioneering experiments on the Explorer-7 satellite, a continuing experimental program has been designed to measure the budget, the energy exchange between earth and space. The global budget determines climate on earth. Pole-to-equator gradients of the energy exchange force the planetary scale circulation of our atmosphere and oceans. Local area (geographic scale) radiation budget measurements allow study of regional energetics and the resulting physical and biological response.

There was an evident need for the satellite measurements and they have satisfied many of the initial scientific goals regarding the mean or steady-state magnitude of the energy exchange between earth and space. Vonder Haar (1968) and Vonder Haar and Suomi (1969, 1971) have reported on results for the mean annual and seasonal cases at space scales $> 10^6 \text{ KM}^2$ based on measurements during five years (1962-1966). They found that the earth was warmer and darker (planetary albedo $A=30\%$) than previously thought. Global radiation balance within measurement accuracy of $\pm 3\%$ was found for the mean annual case and occasionally even for individual seasons. The tropical regions were especially noted to have a lower albedo than believed in pre-satellite days. Additional energy transport by the atmosphere and/or oceans was apparently required to handle the increased energy "load" on our earth-atmosphere system.

Others, including Winston (1967) and Raschke and Bandeen (1970), discussed short spans of data (weeks, seasons) from satellite experiments having space resolution at the synoptic scale (10^4 - 10^6 KM^2). As yet, satellite measurements of radiation budget at the mesoscale ($< 10^4 \text{ KM}^2$) are not available.

Recently, a new set of radiation budget measurements have been obtained at the synoptic scale from an experiment on the NIMBUS-3 satellite. They provide the first data on the annual course (1969-70) of radiation budgets of synoptic-scale regions. When averaged over latitude zones and the entire earth (Vonder Haar, et. al., 1972; Raschke, et. al., 1972) these NIMBUS-3 data independently verify the global and planetary scale annual radiation budget of Vonder Haar and Suomi noted above.

Thus, after more than ten years of intermittent experiments: (a) the required information regarding the mean annual and seasonal radiation budget is in hand¹ and being used by the scientific community, and (b) a significant set of accurate (5%) measurements of radiation budget at the regional scale is available.

The purpose of the present study is to use the same body of data that provided the mean radiation budget results to study the natural time and space variations from that mean state. With this effort, it will be possible to move closer toward an understanding of the interrelation of the earth's radiation budget and its fluid circulations.

Using measurements acquired during the 17 seasons noted in Table 1, the paper will include:

1. A review of the annual and seasonal, global and hemisphere, radiation budgets and their observed time-variations.
2. A study of the mean annual radiation budgets of latitude zones and,
 - a) the interannual (time variation) of these parameters,
 - b) the space variation of the zonal averages with respect to land vs. ocean.
3. Consideration of the natural variation of radiation budget in the mixed space-time domain at three "frequency" modes:
 - a) "low frequency" variations as measured at the $> 10^6 \text{ KM}^2$ space scale during individual seasons (90-day periods),
 - b) "middle frequency" variations as measured at a grid size between 10^2 and 10^3 KM over time periods of days and weeks,
 - c) "high frequency" variations at space scales $< 10^4 \text{ KM}^2$ and over time periods of hours.

Of course, most of the radiation budget data available thus far can only be used for the low frequency study so it shall be emphasized. Each frequency mode can be used to examine atmospheric circulation phenomena in resonance or up or down scale in the space-time domain.

¹with the important exception that global and zonal radiation budget data of very high accuracy (1%) and high precision needed to study climate change has not been acquired.

4. Two special applications of satellite radiation budget measurements conclude the paper:

- joint use of satellite, balloon and surface radiation measurements to examine the total steady-state radiation budget of the deep tropics,
- combination of northern hemisphere energy transport requirements measured by satellites with circulation parameter measurements within the atmosphere to derive the poleward energy transport required of northern hemisphere oceans.

TABLE 1: RADIATION BUDGET MEASUREMENTS USED IN THE PRESENT STUDY

MAM 1962	JJA 1965
JJA 1963	Oct. 1965
SON 1963	July 1966
DJF 1963/64	Dec. 1966
MAM 1964	April 16-30 1969
JULY 1964	July 16-31 1969
SON 1964	Oct. 3-17 1969
DJF 1964/65	Jan. 20-through
MAM 1965	Feb. 3 1970

2.0 RADIATION BUDGET PARAMETERS AND SOURCE OF SATELLITE DATA

On any time or space scale the radiation budget, or net radiation:

$$Q_N(\lambda, \phi, t) = H_S(\lambda, \phi, t) - W_S(\lambda, \phi, t) - W_L(\lambda, \phi, t) \quad (1)$$

with H_S the insolation, W_S and W_L the radiant energy per area and time leaving the region (ϕ, λ) due to reflected and scattered solar energy and emitted infrared (longwave) energy, respectively. Units are $\text{cal} \cdot \text{cm}^{-2} \cdot \text{min}^{-1}$. Note that A , the planetary albedo is W_S/H_S . H_S is derived from a knowledge of the solar constant. The value $1.95 \text{ cal} \cdot \text{cm}^{-2} \cdot \text{min}^{-1}$ was used throughout this study.

For the zonal average annual case the product $Q_N(\phi, \text{annual})$ ($a(\phi)$) may be integrated from pole to pole to obtain the required poleward energy transport of the earth-atmosphere system:

$$RT(\phi, \text{annual}) = \int_{\phi=90^\circ\text{S}}^{\phi=90^\circ\text{N}} Q_N(\phi, \text{annual}) a(\phi) d\phi \quad (2)$$

where $a(\phi)$ is the area of each latitude zone.

As seen in Table 1, 17 seasons between March 1962 and February, 1970 have radiation budget measurement coverage from satellites. All were U.S. satellites; those prior to 1966 often termed the "first generation" meteorological satellites (TIROS-type), those in more recent years the "second-generation" NIMBUS and ESSA type. Eventually, it is hoped that additional measurements acquired from ESSA-type satellites (low resolution sensor data not yet processed to final form) will expand coverage in the period 1967-71.

All radiation detectors in the satellite experiments were thermistor bolometers. The sensors and data reduction techniques are described in the references cited in Sec. 1.0. Accuracy estimates are 2-3% for the longterm global and zonal averages, about 5% for the other data sets. As will be noted further in the text, the severest potential unaccounted bias may be due to the diurnal variations of the radiation budget. At geographic locations where this may be expected to occur, measurements must be interpreted with care (see the references).

3.0 TIME VARIATION OF THE GLOBAL AND HEMISPHERIC RADIATION BUDGETS

Vonder Haar and Suomi (1969) first noted that the planetary albedo, A , was measured to be 29-30% in contrast with the then accepted value of 35% for the mean annual case. They also found the same albedo for both the Northern and Southern Hemispheres. The hemispheres independently, and the earth as a whole, were also in radiation balance to within measurement accuracy ($\pm 0.1 \text{ cal} \cdot \text{cm}^{-2} \cdot \text{min}^{-1}$).

The mean measured values of Q_N presented in Table 2 are the same (± 0.1) as derived by Vonder Haar and Suomi from 13 seasons. For the first time the natural variation (17 seasons) of Q_N for the total earth and for the northern and southern hemispheres is also shown. Of course, the natural variation of the earth and hemispheres for the annual case is not yet known, but presumed to be within the noise level of results available thus far. Precise instruments now under design will fill this data gap, important for the study of climate change. The annual course of net radiation can be readily detected from existing measurement and is seen to be in phase with the annual variation of insolation at these largest space scales. Note that while neither hemisphere has been observed in radiative equilibrium over a seasonal period, the entire globe has been in balance at least once in each season. In fact, this has been observed for 50% of all seasons of record with the exception of MAM, the northern Spring. Why doesn't the global radiation budget have a greater variation with season? Is such fast response due to features of the earth's surface or the atmospheric circulation? How do the two radiation budget components, W_S and W_L , contribute to compensation on a global scale? The observed variations stimulate further study of these questions.

NATURAL VARIATIONS OF NET RADIATION OF THE EARTH ATMOSPHERE SYSTEM

	ANNUAL	SEASONAL				
		DJF	MAM	JJA	SON	
GLOBAL	$0 \pm ()$	$+0.2 \pm 0.2$	$+0.1 \pm 0.3$	0.0 ± 0.3	$+0.1 \pm 0.2$	
N	$0 \pm ()$	-0.9 ± 0.3	$+0.5 \pm 0.3$	$+1.0 \pm 0.3$	-0.4 ± 0.2	
S	$0 \pm ()$	$+1.1 \pm 0.2$	-0.3 ± 0.2	-0.9 ± 0.2	$+0.6 \pm 0.1$	

($\text{cal} \cdot \text{cm}^{-2} \cdot \text{min}^{-1}$)

TABLE 2

4.0 NATURAL VARIATION OF THE RADIATION BUDGET OF LATITUDE ZONES

The curve in Figure 1 shows the measured mean annual net radiation as a function of latitude as well as the mean budget compiled separately for the land areas and ocean regions of each zone. Note that the ocean regions consistently gain more energy in the tropical one-half of the earth than do the land areas. Poleward of 30° latitude in both hemispheres the difference in net radiation between land and ocean is less striking.

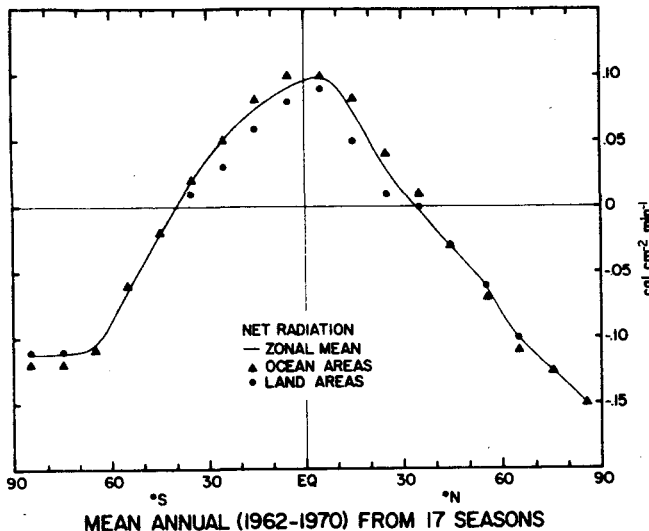


FIGURE 1

The abrupt change of radiation gradient over the Antarctic cap is overemphasized on this figure since the abscissa is not scaled by the area of each zone. Nevertheless, satellite observations in the southern winter and late fall have shown a complete reversal of gradient that has led to the mean annual result shown. The effect arises during polar night when, in the absence of insolation, the relatively warmer zone of $60-70^\circ$ emits more energy to space than the pole itself, thus placing the Q_N minimum near 70° . A similar occurrence has been measured over the Arctic, but it is weaker and apparently masked in the annual summary by the strong direct gradient at other times of the year. These net radiation gradient reversals need further study concerning their impact on the regional circulation. For example, since the Antarctic is a region where the ocean and atmosphere are decoupled, and where latent heat effects are minimized, one would expect a very direct relation between radiation gradient and atmospheric circulation. Reversal of the gradient affects the net atmospheric cooling of the Antarctic atmosphere. A relative warming (Sasamori, et. al., 1971) in contrast to subpolar latitudes would destroy potential energy available for conversion to drive the atmospheric polar circulation. The time of establishment, magnitude and persistence of this gradient reversal has been and can continue to be measured from satellites.

Other aspects of the zonal mean net radiation curve are similar to those discussed by Vonder Haar and Suomi (1971). Recently, new calculations by London and Sasamori (1971) show closer agreement with the satellite measurements than the earlier work of London (1957).

Figure 2 continues the display of measured variations of net radiation, in this case inter-annual variations of the pole-to-equator net radiation gradient expressed as the simple difference in measured values at equator and pole. For each hemisphere the horizontal line notes the mean difference value; dots the seasonal mean range; bars the observed variation during the 13 seasons presented by Vonder Haar and Suomi, and; triangles the values measured during four more seasons from NIMBUS-3. Except for northern Winter the NIMBUS values all fall within the natural range observed previously. The cloud and circulation situation that gave rise to this apparent anomaly is under study. Furthermore, did the stronger gradient give rise to increased poleward energy transport in January 1970? or in subsequent months? Again, measurement and study of variations of the radiation budget give rise to questions that would never be noticed in a study confined only to mean values.

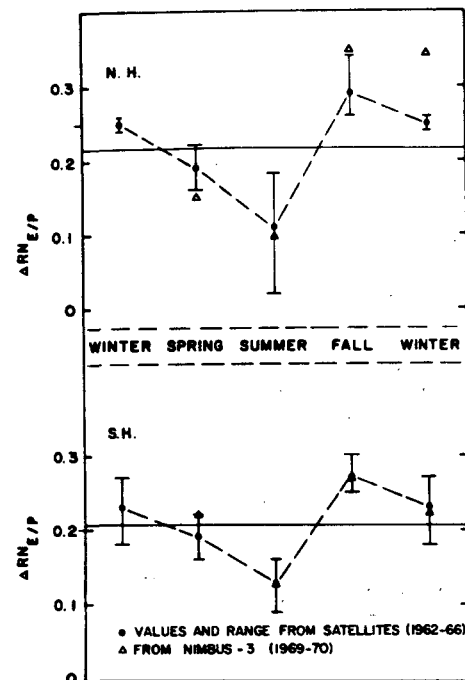


FIGURE 2

As noted in Sec. 2.0, the net radiation changes depend on the variation in planetary albedo and emitted longwave radiation. Mean annual profiles for latitude zones and for ocean and land areas are shown in Figure 3. We see here that the increased net radiation gain over ocean regions results primarily from the albedo being lower than the zonal average. This space variation of land vs. ocean zonal albedo is portrayed in more detail in Figure 4 where mean seasonal profiles are shown. Note that the greater albedo over land areas has a strong north-south excursion in phase with the magnitude of insolation. Thus, apparently land heating effects play a significant role in the albedo, and, thence, net radiation budgets of tropical regions, a role that may be out of proportion to the relative area they occupy.

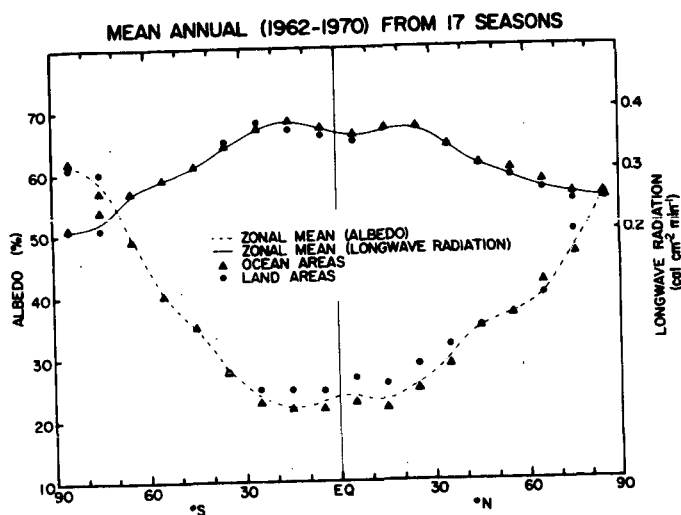


FIGURE 3

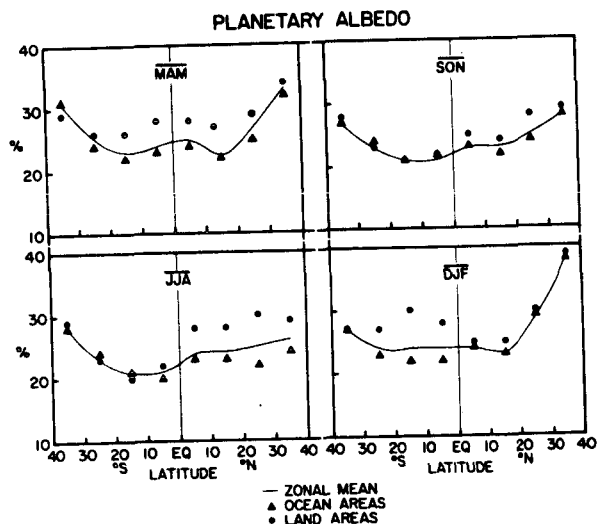


FIGURE 4

Time variation of the zonal albedo and longwave radiation profiles was studied by computing the relative dispersion of the parameters in each zone based on the 17 seasons of measurement¹. Figure 5 displays the input data for the study of time variations of W_L in the form of a time-latitude section. Such a section also shows the annual cycle of infrared radiation to space and interannual variation within latitude zones.

The relative dispersion is the standard deviation divided by the mean (the annual values of Figure 3). Longwave radiation to space was remarkably invariant. Relative dispersions of W_L

¹ poleward of 60° latitude no relative dispersion were calculated because the samples were too small.

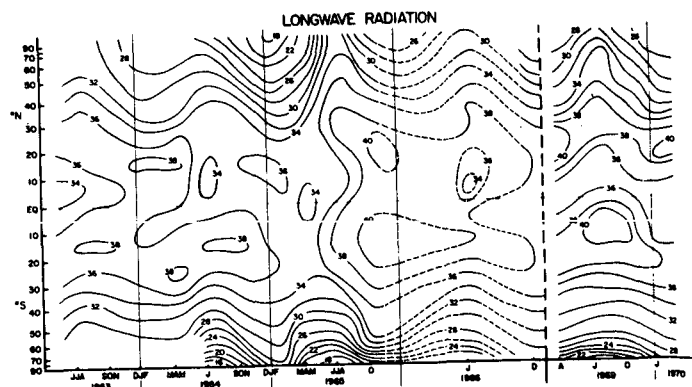


FIGURE 5

ranged from 6% at 30°S to 12% in the zone 40-60°N. The average value over 85% of the earth area was less than 10%. Do the oceans provide the stabilization of outgoing longwave radiation? Does the formation of cloud compensate for land surface heating? In contrast to W_L , relative dispersion of albedo is always greater in each latitude zone. The quasi-global average is about 25%, and values of 25-30% dominate from 20°S to 60°N, the region of most global land mass. Minimum relative dispersion for zonal albedo is 16% at 40-50°S.

This first study of the natural variation of the zonal radiation budget of the earth has indicated that land areas, both near the south pole and in the tropics, play a significant role in variations of radiation budget that affect the planetary scale circulation. Whether the land masses themselves or the cloud systems' influence (including monsoons), play the major role as perturbation mechanisms is the subject of continued study.

5.0 NATURAL VARIATION OF THE EARTH'S RADIATION BUDGET IN DISTINCT FREQUENCY MODES

Before proceeding with the use of measurements from satellites to study the time and space variation of the radiation budget, it is useful to recall that the physical processes and observed conditions within our earth-atmosphere system can be orderly classed in certain frequency modes of the mixed space-time domain. For example, in Table 2, the as yet unmeasured variation of the global annual radiation budget would appropriately be termed the study of very low frequency (VLF) variations.

Rigorous scale analysis is not the purpose of this paper, but the satellite observations on hand and those to be acquired in the near future are conducive to the arbitrary assignment by scale to the following frequency modes:

1. The LF region to be studied at the planetary scale with measurements available at a grid mesh of $10^3 \times 10^3$ km and at a seasonal (90-day) time base.
2. MF or synoptic scale region that requires a grid size approaching $10^2 \times 10^2$ km and a time set of daily observations.

3. The HF mode that allows investigation of the mesoscale ($<10^4 \text{ km}^2$) radiation budget on an intra-daily or hourly basis.

In any of the modes, the radiation budget parameter, X , can be expressed in terms of its time and longitude (space) variations using the notation of Reiter (1969):

$$X = [X]_{(\lambda,t)} + ([X]_{(\lambda)})_{(t)} + [X]_{(\lambda)} + (X)_{(\lambda,t)} \quad (3)$$

Brackets refer to the average value of a parameter, parentheses to the departure from the average and the subscripts in parentheses indicate the ordinates (time or longitude) along which the averages or departures are computed.

5.1 Study of the Planetary Scale, Low Frequency Mode Variation of the Earth's Radiation Budget

Objectively analysed base maps of net radiation $Q_N(\lambda, \phi, \text{annual})$ and planetary albedo $(\lambda, \phi, \text{annual})$ are given in Figures 6a and 6b. We wish to study the LF variations about these mean cases. The annual maps have been discussed by Vonder Haar and Suomi (1971). Kondratyev and Dyachenko (1971) have compared these maps with others that had been calculated using climatological data. They found moderately good agreement between the relative radiation budget patterns and noted the systematic differences discussed earlier in this paper. Note the relative minima of net radiation over the Sahara (here an actual net loss occurs), the Australian sector, northeast China and the South American region. The greatest net gain of energy occurs west of Malaya. The zonality of albedo pattern is interrupted by the Eurasia and North American continents at midlatitudes, but shows increase of albedo poleward. However, equatorward of 30° latitude relative high values of albedo are found over western South America, Libya, the Congo, southeast Asia and eastern New Guinea. Low values occur for this mean annual case over the central Atlantic and Pacific and northwest of Australia.

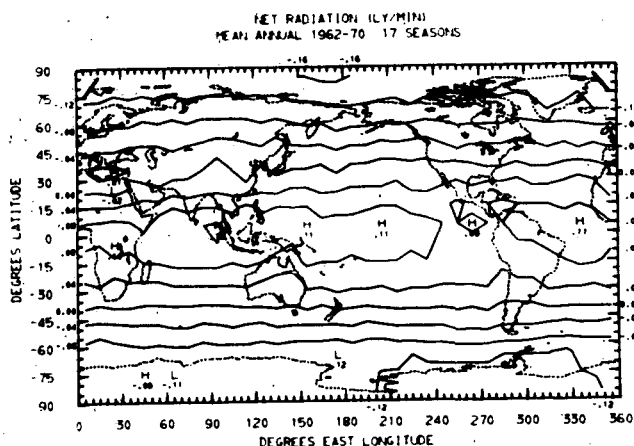


FIGURE 6a

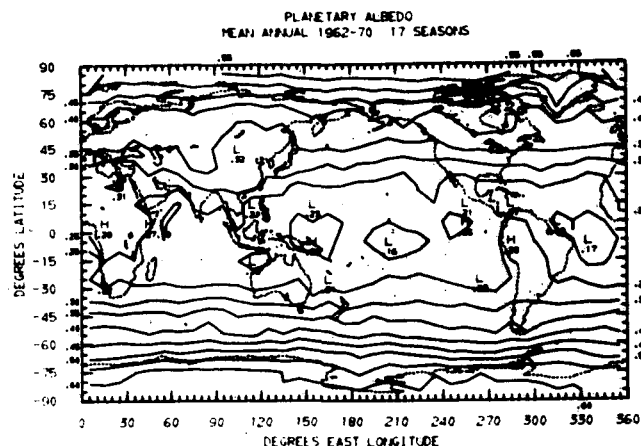


FIGURE 6b

Use of equation (3) to examine the natural LF variation of radiation budget parameters shows that four terms should be studied:

- a) the mean annual zonal values (discussed in sec. 4, Figures 1 and 3),
- b) the time variations (relative dispersion) about the zonal means (sec. 4 and Figures 2, 4 and 5),
- c) the longterm mean value of departure of the radiation budget at a grid point from the zonal average, and
- d) the time variation of the departure of the grid point value from the zonal average.

The latter two parameters, $[X]_{(\lambda)}_{(t)}$ and $(X)_{(\lambda,t)}$ are discussed in the remainder of this section concerning the LF variations.

Figure 7 presents the deviation of net radiation values from the zonal average using the 17 season data set to remove situations peculiar to only one year. The map presents the location of significant deviations far better than the mean annual map (Fig. 6a). For example, the extent of the South American minimum, masked previously by the general north-south variation of net radiation, is now evident and extensive. The maximum gain area of the Bay of Bengal is highlighted, as are equally great deviations in the subtropical North Atlantic. The Libyan minima is seen to extend to the east and west.

The magnitude of intrazonal net radiation gradient is as strong in some sectors as the more well-known north-south gradient. Just as the latter forces poleward energy transport, intrazonal (east-west) circulations that might arise, for example, in the tropics and subtropics of 60°W to 90°E should be the subject of study, perhaps with the aid of numerical models.

As a prelude to discussion of the space and time perturbation term, the following paragraph shows the spatial distribution of time variation of radiation budget, $(X)_{(t)}$.

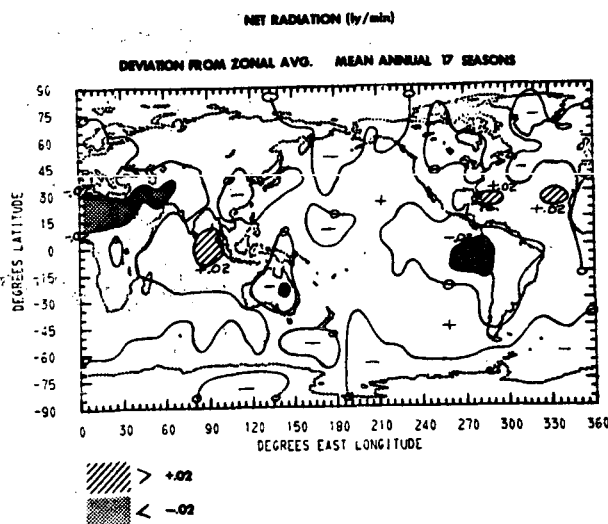


FIGURE 7

Planetary albedo was noted to have a very high mean relative dispersion for the latitude zones 60°N-20°S. Figure 8 shows the locations of the most pronounced variability. For the entire quasi-globe ($\pm 60^\circ$) the greatest variation is found centered at 5°S, 110°W. This is the site where the "double-ITCZ" has been observed on satellite photographs. Great relative dispersion is also found over the Amazon basin, where a well-known rain/dry season markedly changes the cloud pattern. Aside from the entire belt of low albedo variation in the southern hemisphere, the region of Tibet and the North Atlantic do not change albedo appreciably from season to season.

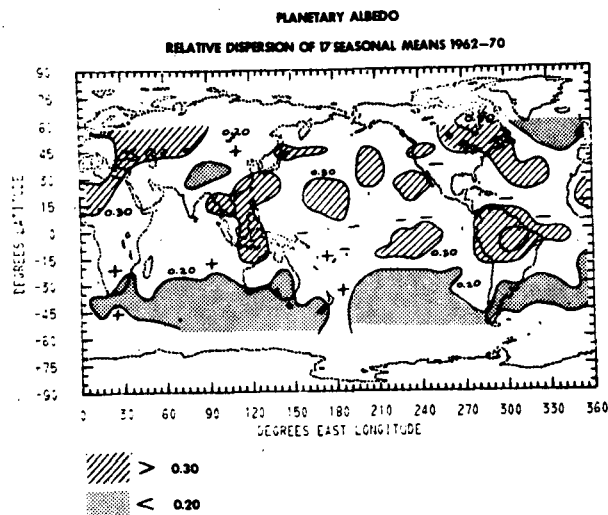


FIGURE 8

Deviation of relative dispersion of the long-wave radiation from the zonal mean is seen in Fig. 9. A striking example of greater than average variation occurs in the band extending from southern Russia, across the summer monsoon region towards New Guinea and ending north of New Zealand. Regions of lower than average variability of outgoing longwave radiation are prevalent in the subtropics of the western hemisphere. Use of these measured natural variations to highlight anomalous regions will allow study of the radiation physics and circulations situations that cause them.

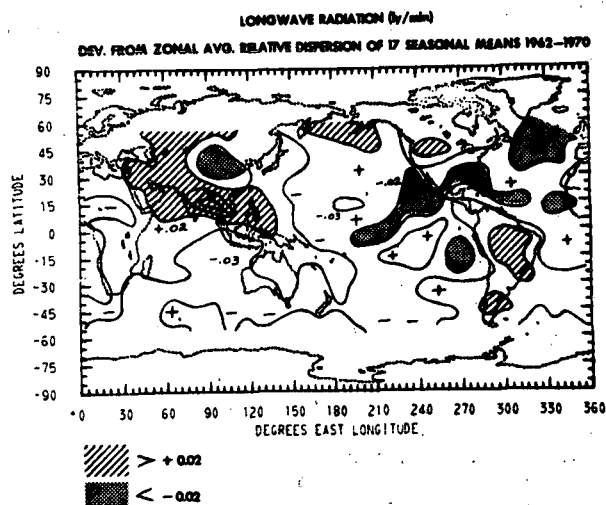


FIGURE 9

Satellite observations have been used above to exemplify all aspects of the space and time variation of the earth's radiation budget in the low frequency mode.

5.2 Natural Variations of Radiation Budget at the Middle Frequency Mode (Synoptic Scale)

As noted in the Introduction, a much smaller amount of radiation budget measurements are available to study the MF mode of natural variation. Most of this data was obtained from the NIMBUS-3 radiation budget experiment. From sun-synchronous orbit, it was possible to obtain radiation measurements twice each day over most of the earth's surface. When gathered into 15-day, semi-monthly data sets they may be used to study the synoptic scale radiation budget as seen in Figures 10a and 10b. Here $[(W_L)_{(\lambda)}]_{(t)}$ and $[(Q_N)_{(\lambda)}]_{(t)}$ from 1-15 July 1969 are shown. As expected, longwave radiation from the Sahara region exceeds the zonal mean and contributes to the negative anomaly of net radiation at the same time. Less than average W_L is noted at 15°N, west of Central America, marking persistent high and middle clouds during the 15 days. For net radiation, less than zonal average values are found over the stratus southwest of California and near the coast of south west Africa over the convective cloud region of Columbia. The Gulf of Mexico gains more energy than the norm during these fifteen days.

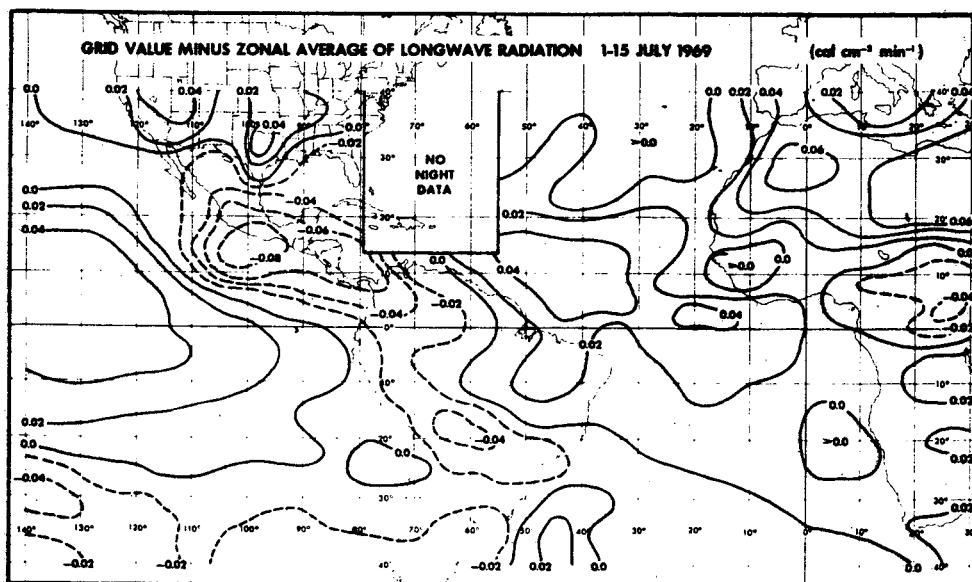


FIGURE 10a

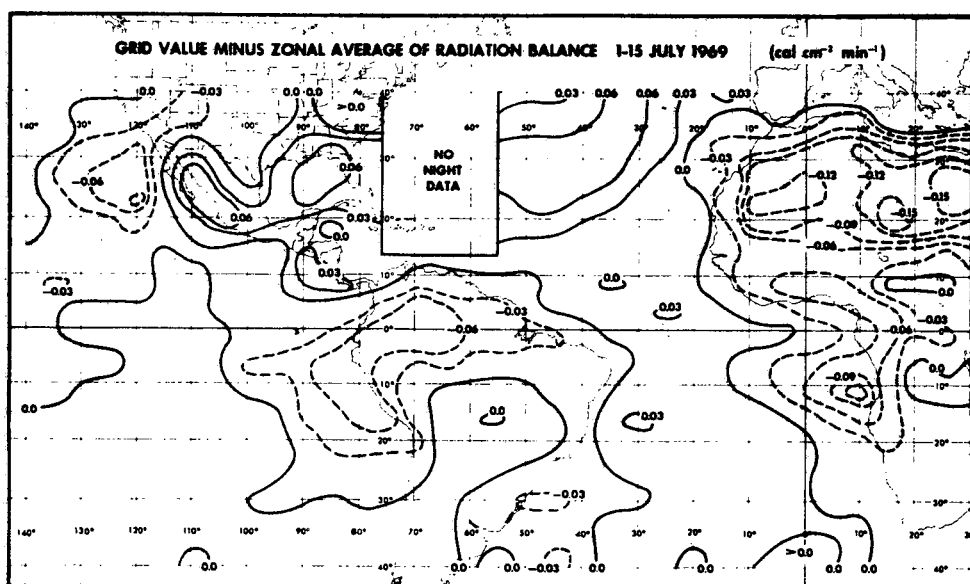


FIGURE 10b

Many additional studies of the radiation budget variation at the MF mode can aid the study of atmospheric energetics on the regional scale.

5.3. High Frequency Variation of Radiation Budget at the Mesoscale

Although some NIMBUS-3 data have been used over the BOMEX array, their time sampling is poor and space resolution too coarse to allow true mesoscale radiation budget studies. Some improvement in space

scale will be possible using the scanning radiometer data obtained from experiments on the operational meteorological satellites. However, it will remain for the high resolution geosynchronous satellite measurements (in both short and longwave channels) to allow study of the HF mode of natural variation of radiation budget.

Geosynchronous satellite data will provide high frequency measurements of the diurnal variation of energy exchange with space that affects atmospheric processes and thermal forcing at the surface of the

earth. Some preliminary results regarding the natural diurnal variation of radiation budget were obtained years ago from a composite of TIROS-4 satellite data during MAM, 1962. Figure 11 shows the results which indicate a semi-diurnal variation of radiation budget parameters over the total area 50° latitude. The primary maximum (minimum) of albedo (longwave radiation) occurs at 1500-1700 local time. A secondary minimum of W_L may be seen just before dawn. Could this represent the effect of the often discussed cloudiness maxima over the oceans? Vertical bars note the daytime nodal crossing times of second generation meteorological satellites. These preliminary results of diurnal variation show that NIMBUS data may be more free of temporal sampling bias.

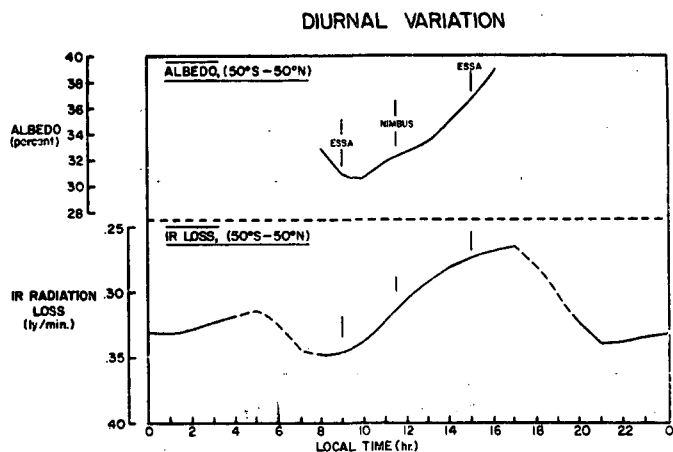


FIGURE 11

Figure 12 shows that the diurnal variation of radiation budget is greatest in subtropical latitudes.

These results and further studies of the high frequency, mesoscale variations of radiation budget will be greatly aided by measurements from geosynchronous-satellites. Many local scale atmospheric processes can then be examined.

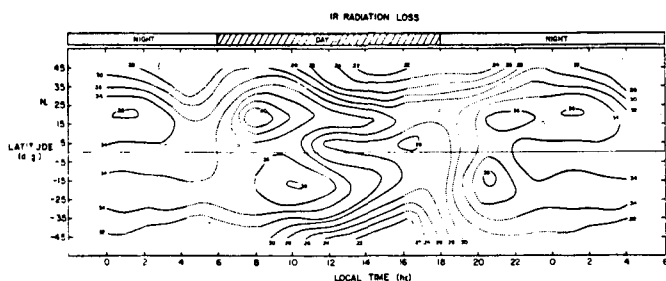


FIGURE 12

6.0 SPECIAL APPLICATION OF RADIATION BUDGET MEASUREMENTS

6.1 Total Radiation Budget of the Zone $0-20^\circ\text{N}$

A great deal of study is presently being directed toward the energetics of the tropics and their inter-relation with midlatitude circulation. The

GARP Atlantic Tropical Experiment (GATE), the Central African Project (CAP) and other major efforts are directed toward the study of these regions. It is appropriate to update our information on the steady state radiation exchange in this area, both as a background for other work and with the realization that certain radiation processes may play key roles in the energetics of the tropics.

As noted in section 2.0, the satellite measurements have shown that the tropics are warmer and darker than previously believed (until 1968). With this lower planetary albedo in mind, Vonder Haar and Hanson (1969) used the few available measurements of solar energy reaching the earth's surface in the tropics to find that most of the additional solar energy entering the earth-atmosphere system was being absorbed in the tropical oceans.

Figure 13 contrasts the newly compiled radiation budgets of the surface, the atmosphere, and the earth-plus atmosphere based on measurements, with the calculated values generally accepted in pre-satellite years. In addition to the complete solar energy portion of the budget noted above, measurements of the net infrared cooling of the tropical atmosphere reported by Cox (1971) were used with the satellite measurements of W_L to complete the IR budget. The greater net cooling of the atmosphere contrasts with the increased net energy gain of the surface. Aside from sensible heat exchange at the interface, the major remaining term in the local energetics of the atmosphere is warming resulting from cumulus convection. Here, radiation budget considerations have led us to one of the central issues of present-day atmospheric science. The mechanism for convective initiation, mode of energy addition to the tropical atmosphere and the method of conversion and transport of energy to poleward latitudes is bounded and shaped by the energy available via the radiation budget. Can further study of the variation of radiation budget assist the present day effort to improve our understanding of tropical circulation? Yes, much will be gained from the satellite measurements.

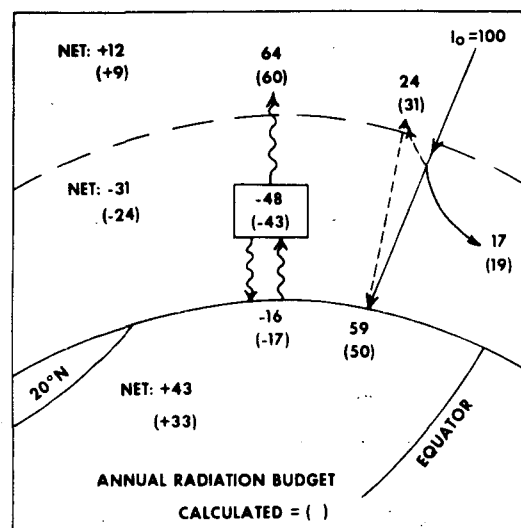


FIGURE 13

6.2 Energy Transport Requirements for Northern Hemispheric Oceans

As shown by equation (2) the total net poleward energy transport for the mean annual case can be determined solely from satellite measurements. Since it was found that more energy had to be transported than previously assumed, it was natural to investigate the possible mechanisms. In addition, Vonder Haar and Hanson had shown that the bulk of the increased solar energy absorption occurred in the oceans.

With the aid of 20 seasons of measurements carefully compiled from the northern hemisphere rawinsonde network, Oort (1971) has been able to independently measure the net poleward energy transport (all forms) by the atmosphere. Figure 14 shows the required total energy transport RT, and the measured mean annual atmospheric transport, AT. The difference between these values at each latitude zone yields an estimate of the ocean energy transport, OT. This value, OT, cannot be measured directly, nor calculated without stringent assumptions.

The curve ΔF is a contemporary estimate of ocean energy transport from Sellers (1965). The new value, OT, derived with the aid of satellite data has nearly the same latitude variation as the old curve. However, the magnitude of ocean transport in the northern hemisphere has been apparently underestimated. The ocean transport reaches a maximum at 20°N with a value that equals the maximum atmospheric transport by waves at mid-latitudes. Overall, about 40% of the poleward transport of energy can now be attributed to the ocean. Vonder Haar and Oort (1972) discuss this topic in more detail.

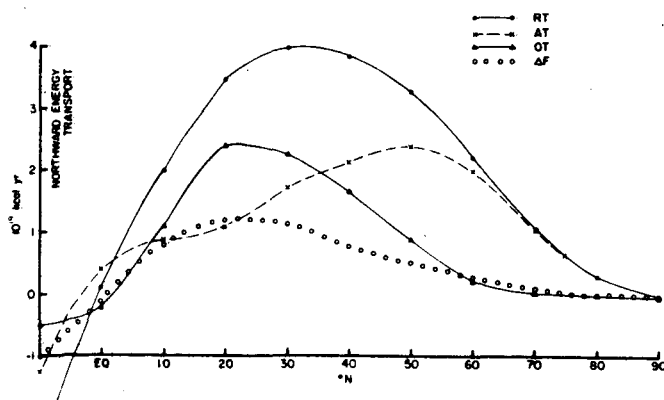


FIGURE 14

SUMMARY

This paper has shown that satellite measurements of the natural variation of radiation budget offer many opportunities for scientific inquiry. Data available at the present time (17 seasons) have been used to thoroughly examine the low frequency mode (planetary scale) of variation in the mixed space-time domain. Examples and discussion have included the important aspects of variation at three other modes: very low

frequency (global climate), middle frequency (synoptic scale), and high frequency (mesoscale). For the first and last of these three, new measurements from new sensors will be needed. The synoptic scale can be studied well with newly available NIMBUS data.

Studies of natural variation of radiation budget at all scales are a necessary portion of present-day research on the energetics of the atmosphere and ocean, as evidenced by two examples discussed briefly in this paper.

ACKNOWLEDGEMENTS

All who contributed to the success of the many satellite radiation budget experiments deserve great credit. Mr. James Ellis, Mr. Steve Lassman and Miss Lyn Koch aided with this manuscript. Support for the research was provided by GRANT NGR-06-002-102 from the National Aeronautics and Space Administration.

REFERENCES

- Cox, S., 1971: Cirrus clouds and the climate. *J. Atmos. Sci.*, 28, 8, pp. 1513-1515.
- Kondratyev, K. and L. Dyachenko, 1971: Comparison of satellite and calculation charts for the earth's radiation budget. *Space Research XI*, Akademie-Verlag, Berlin, 651-660.
- London, J., 1957: A study of the atmospheric heat balance. *Final Report*, Contract AF 19(122)-165, Dept. of Meteorology and Oceanography, New York University, 99 pp.
- London, J. and T. Sasamori, 1971: Radiative energy budget of the atmosphere. *Space Research XI*, Springer-Verlag, Berlin.
- Oort, A., 1971: The observed annual cycle in the meridional transport of atmospheric energy. *J. Atmos. Sci.*, 28, 3, 325-339.
- Raschke, E., T. H. Vonder Haar, W. R. Bandeen, and M. Pasternak, 1972: The radiation balance of the earth-atmosphere system from NIMBUS-III radiation measurements (15 April 1969 - 3 February 1970). *NASA Tech. Note*, in preparation.

- Raschke, E. and T. H. Vonder Haar, 1971: Climatological studies of the Earth's radiation and its variability with measurements of the satellite NIMBUS-III. (Paper presented at Symposium on Phys. and Dynam. Climat., Leningrad, 16-20 May 1971).
- Sasamori, T., J. London and D. Hoyt, 1971: Radiation budget of the southern hemisphere, NCAR Ms. No. 71-100.
- Vonder Haar, T., 1968: Variations of the earth's radiation budget. Ph.D. thesis, Department of Meteorology, The University of Wisconsin.
- Vonder Haar, T. and K. Hanson, 1969: Absorption of solar radiation in tropical regions. J. Atmos. Sci., 26, 4, 652-655.
- Vonder Haar, T. and V. Suomi, 1969: Satellite observation of the earth's radiation budget. Science, 163, 667-669.
- Vonder Haar, T. and V. Suomi, 1971: Measurements of the earth's radiation budget from satellites during a five-year period. Part I: Extended time and space means. J. Atmos. Sci., 28, 3, pp. 305-314.
- Vonder Haar, E., Raschke, M. Pasternak and W. Bandeen, 1972: The radiation budget of the earth-atmosphere system as measured from the NIMBUS-III satellite (1969-70), Space Research XII, Springer, Verlag (in press).
- Winston, J. 1967: Zonal and meridional analysis of 5-day averaged longwave radiation data from TIROS-IV over the Pacific sector in relation to the Northern Hemispheric circulation. J. Appl. Meteor., 6, 453-463.

THESIS

INTERANNUAL VARIATIONS IN THE EARTH'S
RADIATIVE BUDGET AND THE GENERAL CIRCULATION

Submitted by

James S. Ellis

In partial fulfillment of the requirements

for the Degree of Master of Science

Colorado State University

Fort Collins, Colorado

August, 1972

INTERANNUAL VARIATIONS IN THE EARTH'S RADIATIVE BUDGET
AND THE GENERAL CIRCULATION

The north-to-south gradient of net radiation, as determined from 35 months of satellite data, and parameters defining the intensity of the general circulation are brought together for the first time to investigate interrelationships in their year-to-year variations. An error analysis of the net radiation gradient is presented to attest to its validity. Parameterization of the atmosphere is accomplished through the zonal index, thermal wind and the eddy and zonal components of available potential and kinetic energies.

Statistical correlations indicate that, overall, interannual variations in the gradient of net radiation and the general circulation are out of phase by three months. However, for selected extreme variations, there are no apparent phase differences.

James Stephen Ellis
Atmospheric Science Department
Colorado State University
Fort Collins, Colorado 80521
August 1972

Preceding page blank

ACKNOWLEDGEMENTS

The author wishes to thank Dr. Thomas H. Vonder Haar for his patience and guidance and also Mr. Glenn W. Brier for his advice. Special thanks are extended to Charlene Polifka for computer programming, Vicki Brant for assistance in data reduction, Lyn Koch and Paula Brant for typing the manuscript, Dana Wooldridge for the graphic art, and to others, all of whom graciously gave of their time and skill.

The author is also indebted to the National Center for Atmospheric Research for a grant of their computing facility resources. This research was supported by NASA Grant No. NGR 06-002-12.

TABLE OF CONTENTS

	<u>page</u>
ABSTRACT	iii
ACKNOWLEDGEMENTS	iv
LIST OF FIGURES.	vii
LIST OF TABLES	ix
1.0 Introduction.	1
2.0 Radiation Data Analysis	3
2.1 Available Data	3
2.2 Net Radiation Gradient	5
2.2a Procedure.	6
2.2b Gradient Analysis.	7
2.3 Error Analysis	14
2.3a Bias Error	14
2.3b Other Error.	18
2.4 Diurnal Effects.	19
3.0 General Circulation and the Gradient of Net Radiation	23
3.1 Zonal Index.	23
3.2 Thermal Wind	25
3.3 Energetics	26
3.3a Available Potential Energy	30
3.3b Kinetic Energy	34
3.4 Quantitative Comparison.	36
4.0 Analysis of Results	43
4.1 Gradient and Circulation	43
4.1a Periodicity in Data.	44
4.1b 3 Month Lag.	48

	<u>page</u>
4.2 Interhemisphere Comparison	51
4.3 Gradient and Cloudiness.	54
5.0 Summary and Conclusions	56
REFERENCES	58

LIST OF FIGURES

<u>Figure</u>		<u>Page</u>
1	Northern hemisphere monthly net radiation gradient (solid curve) and gradient of solar insolation (dashed curve) from 5N to 65N	8
2	Southern hemisphere monthly net radiation gradient (solid curve) and gradient of solar insolation (dashed curve) from 5S to 65S.	9
3	Northern hemisphere seasonal net radiation gradient (solid curve) and gradient of solar insolation (dashed curve) from 5N to 55N	11
4	Southern hemisphere seasonal net radiation gradient (solid curve) and gradient of solar insolation (dashed curve) from 5S to 55S	12
5	Net radiation bias error for infrared and albedo bias errors in the same direction.	16
6	Net radiation bias error for infrared and albedo bias errors in opposing directions	17
7	Diurnal variation in albedo and infrared radiation from TIROS 4 for April (after Vonder Haar and Hanson; see Vonder Haar, 1968)	20
8	Diurnal variation in albedo and infrared radiation from Nimbus 3 and ESSA 7 for April fitted with TIROS 4 profiles	21
9	Northern hemisphere monthly zonal index from 35N to 55N on a 700 mb surface (solid curve); mean monthly zonal index based upon a 9 year average (dashed curve)	24
10	Annual cycle of the net radiation gradient (ΔR_N) and the thermal wind (V_T) based upon a 9 year average from 1963 to 1971.	27
11	Northern hemisphere thermal wind for the layer 1000 mb to 300 mb from 20N to 70N (solid curve); mean monthly thermal wind based upon a 9 year average (dashed curve).	28
12	Northern hemisphere zonal available potential energy in the mixed space-time domain for the layer 850 mb to 200 mb from 20N to 90N (solid curve); mean monthly zonal available potential energy based upon a 9 year average (dashed curve)	32
13	Northern hemisphere eddy available potential energy in the mixed space-time domain for the layer 850 mb to 200 mb from 20N to 90N (solid curve); mean monthly eddy available potential energy based upon a 9 year average (dashed curve)	33

	<u>page</u>
14 Northern hemisphere zonal kinetic energy in the mixed space-time domain for the layer 850 mb to 200 mb from 20N to 90N (solid curve); mean monthly zonal kinetic energy based on a 9 year average (dashed curve)	35
15 Northern hemisphere eddy kinetic energy in the mixed space-time domain for the later 850 mb to 200 mb from 20N to 90N (solid curve); mean monthly eddy kinetic energy based on a 9 year average (dashed curve)	37
16a Correlation coefficients of interannual variations with the general circulation parameters leading (-months) and lagging (+months) the net radiation gradient. . . .	40
16b Correlation coefficients of interannual variations with the general circulation parameters leading (-months) and lagging (+months) the net radiation gradient. . . .	41
17 Temporal distribution of the net radiation gradient with the annual cycle removed ($\Delta RN'$)	45
18 Spectrum analysis of general circulation parameters: smoothed spectrum (solid line), unsmoothed spectrum (dashed line)	47
19 Ocean storage curve for selected latitudes of the northern hemisphere (taken from data of Newell et al., 1969)	49
20 Correlation between interannual variations in net radiation gradient (black bars) and zonal available potential energy (light bars) with 3 months lag and no lag. . . .	50
21 Correlations between interannual variations in net radiation gradient (black bars) and zonal kinetic energy (light bars) with 3 months lag and no lag	52
22 Temporal comparison between interannual variations in the net radiation gradient of the northern hemisphere (solid line) and the southern hemisphere (dashed line)	53

LIST OF TABLES

<u>Table</u>		<u>page</u>
1	Available radiation data: TIROS 4 (T4), TIROS 7 (T7), Experimental (EX), Nimbus 2 (N2), Nimbus (N3), ESSA 3 (E3), ESSA 7 (E7) and ITOS 1 (I1).	4
2	Range of interannual variations in zonally average monthly net radiation at gradient latitudes ($\text{cal cm}^{-2}\text{min}^{-1}$). . .	13
3	Diurnal variations in net radiation ($\text{cal cm}^{-2}\text{min}^{-1}$). . .	19
4	Summary table of qualitative comparison between inter-annual variations in the net radiation gradient and the general circulation parameters	38

1.0 INTRODUCTION

Measurements from radiation sensors on earth orbiting satellites have allowed a study of the spatial distribution and the temporal variations in the radiative characteristics of the earth-atmosphere system. This information is fundamental to gaining a better understanding of the energy input to our oceanic and atmospheric circulation.

The net radiation budget (RN) is defined as the total incoming solar energy minus the sum of the outgoing scattered, reflected, and emitted energies which are measured at the top of the atmosphere.

The purpose of this report is to investigate the interannual variations in the north-to-south net radiation budget distribution and the relationship of these variations to the general circulation of the atmosphere.

The north-to-south net radiation budget distribution can be represented to a first approximation by the net radiation gradient (ΔRN), i.e., the north-to-south difference in the net radiation budget. Vonder Haar and Suomi (1969) first discussed the pole-to-equator ΔRN as a simple measure of the radiative forcing on the global circulation. The magnitude of ΔRN reflected the seasonal north-to-south migration of the sun's path on the earth but, more important were the interannual differences in the seasonal values of ΔRN (Vonder Haar and Suomi, 1971). These differences are most probably indirectly related to the year-to-year variations in the strength of the general circulation of the atmosphere through complex energy exchange mechanisms. This study is an attempt to detect related changes in the general circulation and to gain a better understanding of the feedback mechanisms.

The procedure will be to compute monthly values of ΔRN and then to compare them with general circulation parameters. Parameterization of the atmosphere has been accomplished to some degree by computing the zonal index, the thermal wind, and the potential and kinetic energies.

2.0 RADIATION DATA ANALYSIS

2.1 Available Data

The radiation data used in this study comprise the most complete set of reduced data available to data from radiation experiments on earth orbiting satellites, excluding only data which does not include both albedo and infrared measurements. The data are for 36 months and 5 additional seasons which together intermittently span 10 years from 1962 to 1971 (Table 1).

Discussion on the data reduction can be found in the following references: TIROS 4, TIROS 7, EXPERIMENTAL (Vonder Haar, 1968), Nimbus 2 (Raschke, 1968; Raschke and Bandeen, 1970), ESSA 3 preliminary results (MacDonald, 1969), Nimbus 3 (Raschke, et al., 1972), ITOS 1 preliminary results (Smith, 1972), and ESSA 7 (MacDonald, 1970 and 1972).

Data from 1962 through 1965 are the same as that used by Vonder Haar (1968) except for an adjustment in the solar constant from $2.00 \text{ cal cm}^{-2} \text{ min}^{-1}$ to $1.95 \text{ cal cm}^{-2} \text{ min}^{-1}$ (the solar constant used throughout this study). Half of the data (17 continuous months) are from the Wisconsin low resolution plate sensors flown on an experimental satellite. The remainder of the data were collected by the following sensors: medium resolution scanning radiometers on TIROS 7, Nimbus 2, and Nimbus 3; Wisconsin low resolution hemispheres on TIROS 4, and Wisconsin flat plate radiometers on ESSA 3, ESSA 7, and ITOS 1.

Five seasonal sets of data from the TIROS satellites were included to extend the data set back to 1962. Large gaps in the longitudinal

TABLE 1: Available radiation data: TIROS 4 (T4), TIROS 7 (T7), Experimental (EX), Nimbus 2 (N2), Nimbus 3 (N3), ESSA 3 (E3), ESSA 7 (E7) and ITOS 1 (I1).

Months	Year										No.
	1962	1963	1964	1965	1966	1967	1968	1969	1970	1971	
J				EX				E7	N3		3
F				EX				E7			2
M				EX				E7			2
A				EX				N3,E7			2
M				EX	N2			N3		I1	4
J				EX	N2			N3			3
J			EX	EX	N2			N3			4
A			EX	EX				N3			3
S			EX	EX							2
O			EX	EX			E7	N3			4
N			EX	EX			E7				3
D			EX		E3		E7				3
Seasons											
DJF		T7	EX		E3		E7	N3			
MAM	T4		T7	EX				E7,N3			
JJA		T7	EX	EX	N2			N3			
SON		T7	EX	EX			E7	N3			

NOTE: The DJF season is assigned the year of the respective December.

average limited the temporal resolution to seasons for complete longitudinal coverage.

2.2 Net Radiation Gradient

The net radiation gradient (ΔRN) is the north-to-south difference in the zonally averaged (latitudinal average) net radiation budget.

The net radiation budget (RN) at the top of a column extending from the surface to the top of the atmosphere (30 km) is defined precisely as:

$$RN = I_o (1 - A) - RL \quad (1)$$

where:

I_o = the solar irradiance on the top of the column determined by the solar constant $1.95 \text{ cal cm}^{-2} \text{ min}^{-1}$.

A = the albedo - the ratio of outgoing scattered and reflected solar flux at the top of the column to I_o .

RL = the outgoing longwave radiation (emitted radiation) at the top of the column.

Each term of Eq. (1) is a function of both space and time.

The net radiation gradient was taken between latitudes 5° and 65° for the monthly data:

$$\Delta RN = RN_5 - RN_{65} \quad (2)$$

and between 5° and 55° latitudes for the seasonal data:

$$\Delta RN = RN_5 - RN_{55} \quad (3)$$

2.2a Procedure

Data prior to 1966 were gridded every 10° latitude and 10° longitude from 85° north latitude to 85° south latitude. The higher resolution data after 1965 were averaged to obtain the same gridding. Net radiation was computed at each grid point using the albedo, long-wave radiation, and solar insolation components. The net radiation gradient was computed from the zonally averaged net radiation budget for each data set.

Equation (2) was used to compute the net radiation gradient from the monthly data sets. The equatorward limit was selected at 5 degrees rather than the equator since it required no interpolation on the basic grid; interpolation at the equator would have required averaging over the zone 5°N to 5°S , where intertropical convergence zone migrates north and south during the course of a year.

The poleward limit was set at 65° rather than 85° because of the data coverage; ten monthly data sets had no data at 85°N , however, only four data sets had missing data at 65°N . Of these four sets, three had data both north and south of 65°N (October 1964, October 1965, and February 1965). The net radiation at 65°N could not be evaluated directly on these three occasions because the reflected energy was near the noise level of the signal. These three points were therefore, indirectly evaluated by interpolation using meridional profiles of the same months for other years. The zonally averaged net radiation 65°N for the fourth data set (September 1964) was extrapolated using the meridional profile for September 1965. Similarly, for the gradient in the southern hemisphere, three August values were interpolated and June 1966 value was extrapolated to 65°S .

Equation (3) was used to compute the net radiation gradient for the seasonal data. Since the TIROS data did not extend poleward of 55°N and 55°S latitude, the gradient was taken across the 55° to 5° latitude band. In addition, all monthly data were averaged into seasons so that a gradient comparison could be made.

2.2b Gradient Analysis

Monthly net radiation gradients (ΔRN) are presented in Figures 1 and 2 for the northern and southern hemispheres, respectively. The continuous solid curve traces the monthly mean gradient to show the intermonthly change in the gradient. The vertical lines with the horizontal bars followed by the year show the interannual variation in the monthly gradients. The continuous dashed curve traces the monthly gradient of incoming solar insolation (ΔI_0) taken over the same latitude belt. (Note that the scale of ΔI_0 - to the right of the graph - is different than the scale of ΔRN).

The net radiation gradient declines less rapidly from spring to summer than it rises from summer to fall - apparent in both hemispheres. This is attributed to higher surface and atmospheric temperatures during fall in the poleward latitudes. Smaller longwave radiative loss in the poleward latitudes and smaller net radiative gain near the equator at winter solstice appears in both hemispheres as a sharp drop in the gradient - December in the northern and June in the southern. The rise from December to January in the northern hemispheres is probably due to the large gradient in the January 1970 Nimbus 3 data which was not available in December 1969, and is thus a consequence of the data set.

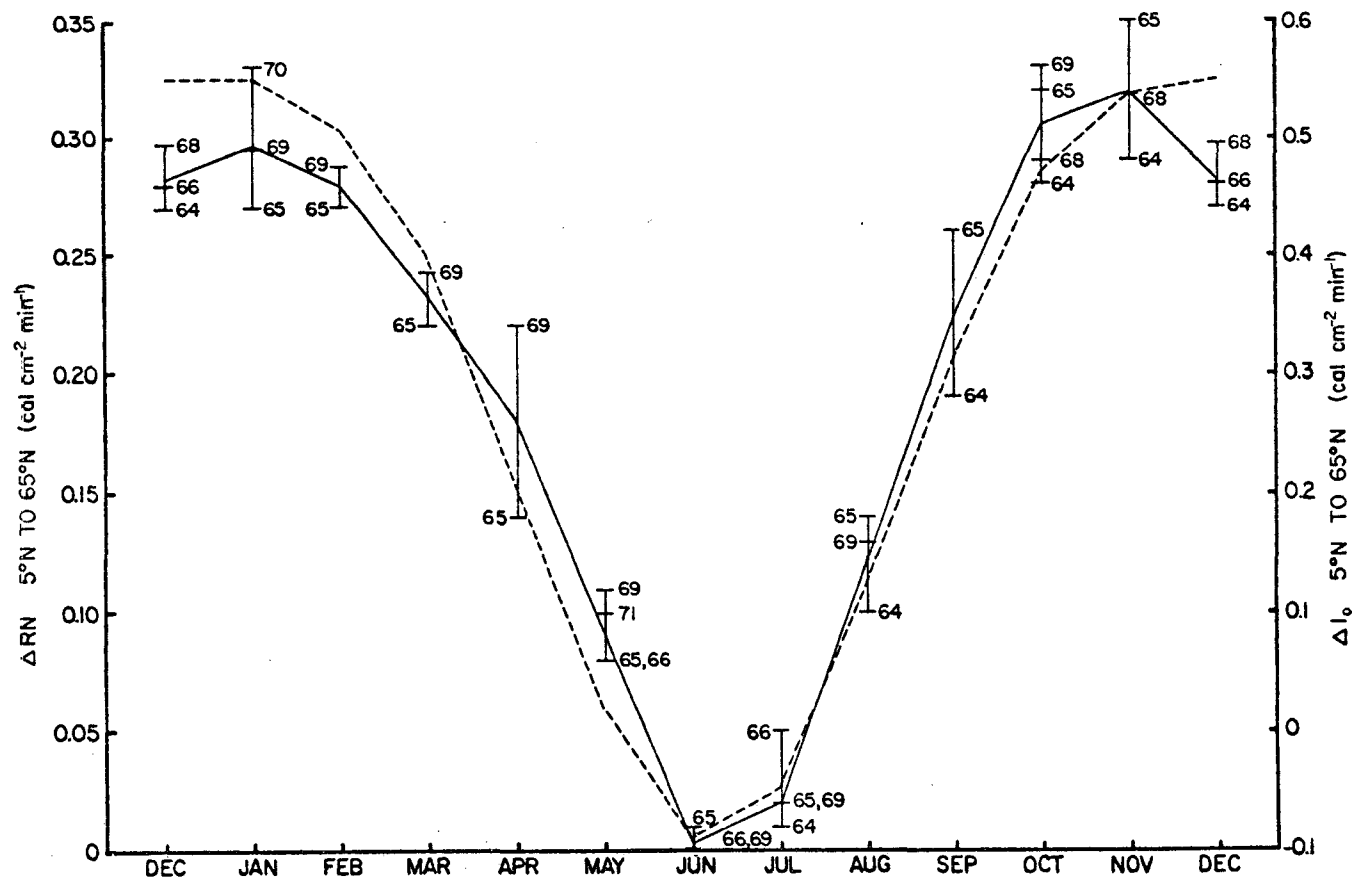


FIGURE 1. Northern hemisphere monthly net radiation gradient (solid curve) and gradient of solar insolation (dashed curve) from 5N to 65N.

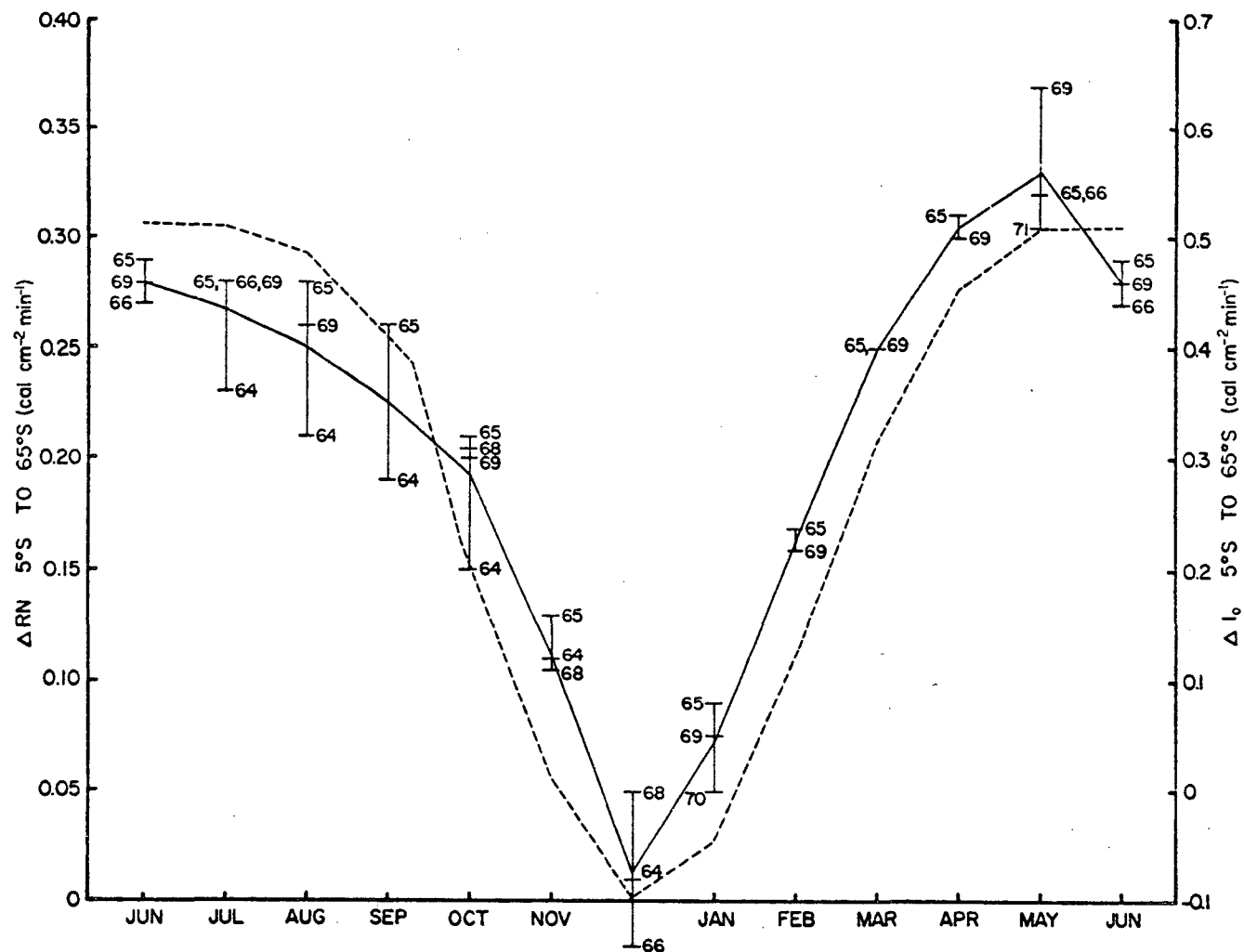


FIGURE 2. Southern hemisphere monthly net radiation gradient (solid curve) and gradient of solar insolation (dashed curve) from 5S to 65S.

Seasonal gradients appear in Figures 3 and 4 for the northern and southern hemispheres, respectively. A striking feature is the extremely sharp rise from summer to fall as compared to the moderate decline from spring to summer. This feature results primarily from the way the seasons are defined; the solstices and equinoxes do not fall in the center of the seasons but near the end of the first month in each season. Had the seasons been so defined to be centered on the equinoxes and solstices, then the profiles would have been near symmetrical except for a slight asymmetry as noted in the monthly profiles.

In both hemispheres the net radiation gradient is in phase with the gradient of solar insolation on both monthly and seasonal time scales. This does not exclude a phase shift for time scales less than a month. In addition, quite large year-to-year variations exist in the monthly and seasonal net radiation gradient - the primary concern of this study.

The range in the interannual variations in ΔRN and in RN at gradient latitudes are shown in Table 2. The range in the monthly RN variations is larger at 65N than at 5N latitudes and larger at 5S than at 65S latitudes. On the whole, the range is less at 65S than at 65N and less at 5N than at 5S. These relationships become most apparent by considering the average range for each which is also shown in the table. Therefore, the net radiation gradient is affected most by variations in net radiation at 65N for the northern hemisphere and at 5S for the southern hemisphere.

The next step is to establish through an error analysis that such variations in both ΔRN and RN are real and not data error.

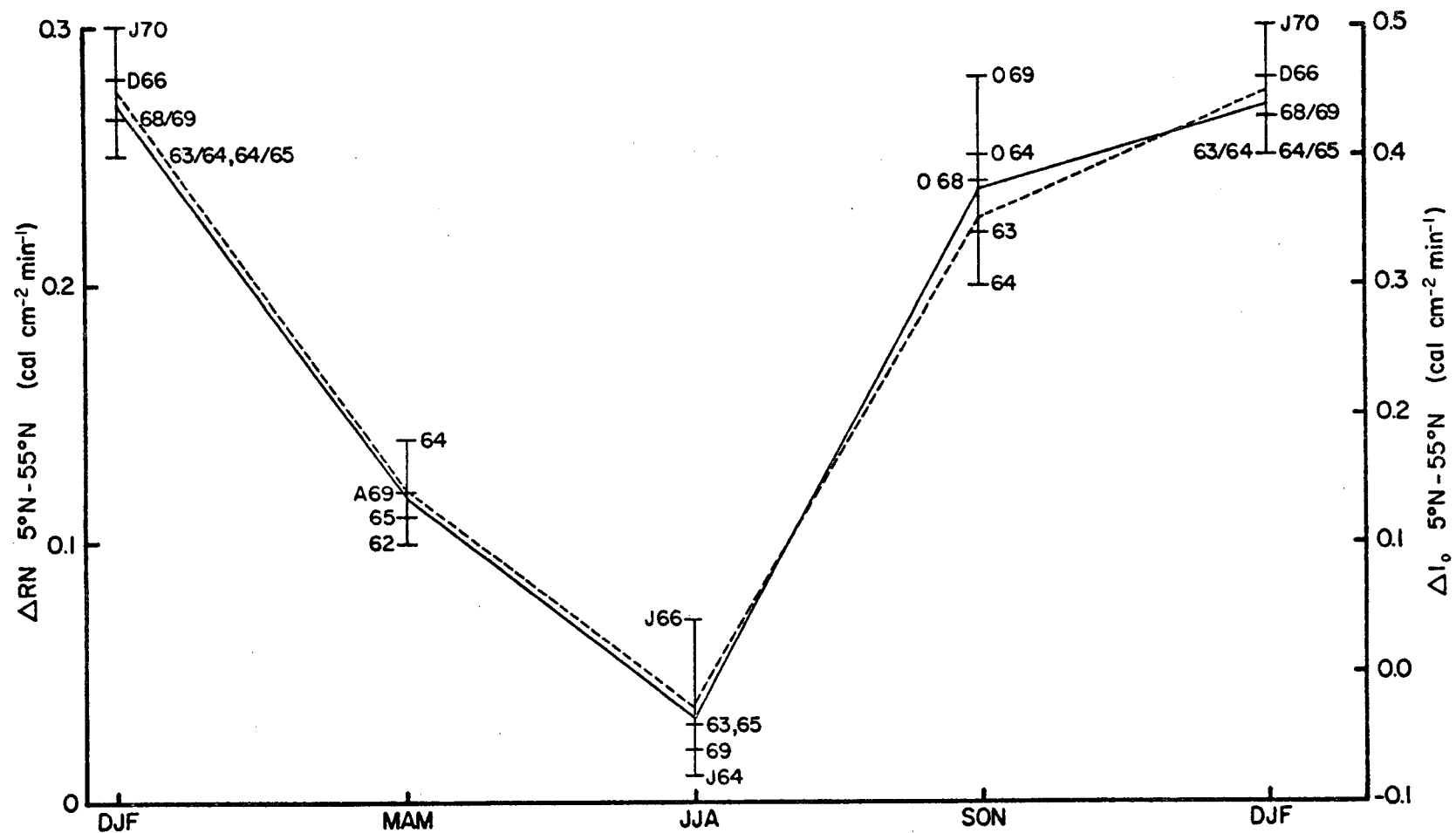


FIGURE 3. Northern hemisphere seasonal net radiation gradient (solid curve) and gradient of solar insolation (dashed curve) from 5N to 55N.

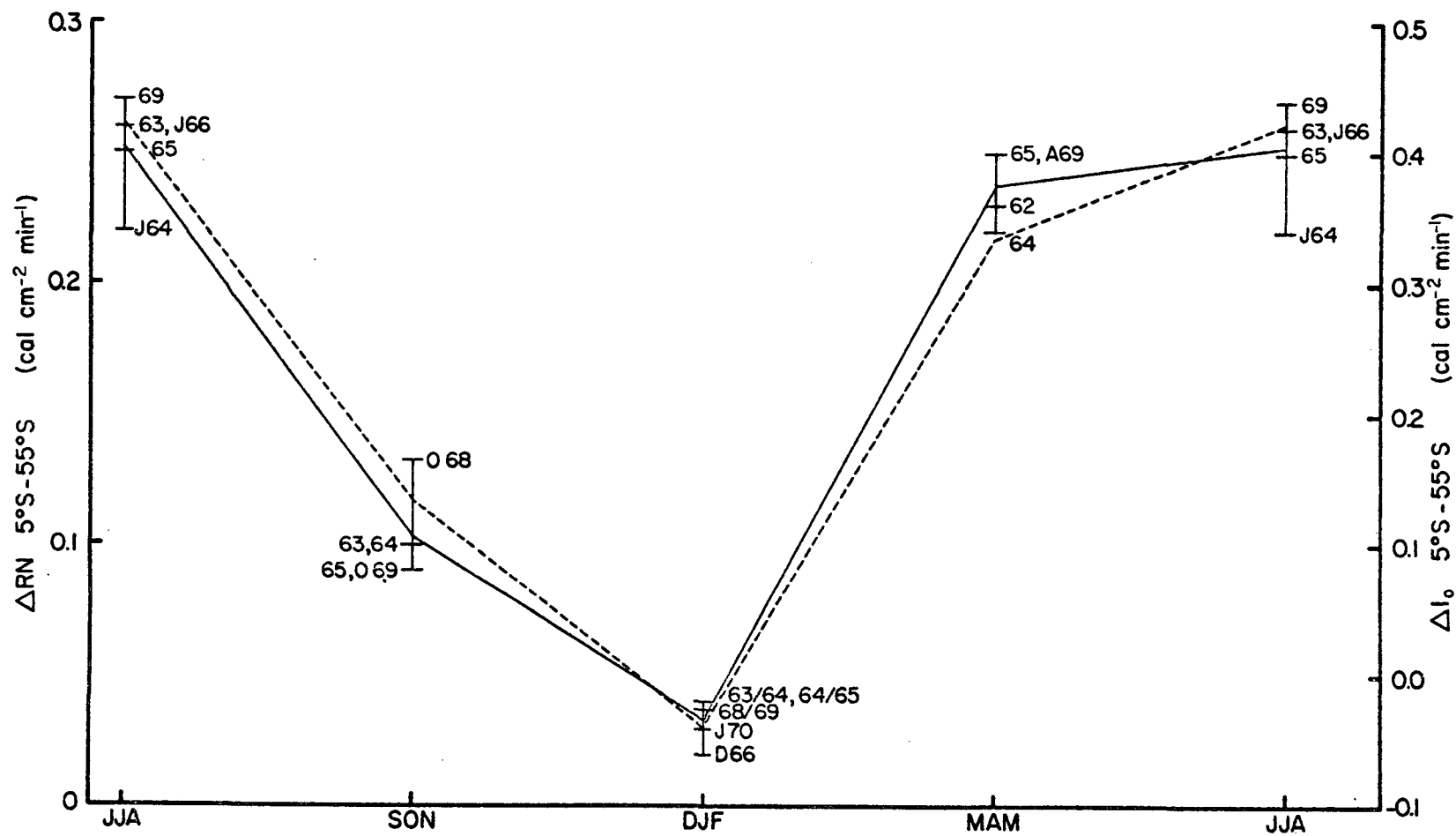


FIGURE 4. Southern hemisphere seasonal net radiation gradient (solid curve) and gradient of solar insolation (dashed curve) from 5S to 55S.

TABLE 2: Measured range of interannual variations in zonally averaged monthly net radiation at gradient latitudes ($\text{cal cm}^{-2} \text{ min}^{-1}$). (see TABLE 1 for sample size).

Months	Northern Hemisphere			Southern Hemisphere		
	5N	65N	ΔRN_{5-65}	5S	65S	ΔRN_{5-65}
JAN	.03	.05	.06	.04	.06	.04
FEB	.02	.04	.02	.02	.01	.01
MAR	.03	.06	.02	.04	.04	.00
APR	.03	.10	.08	.06	.03	.03
MAY	.08	.10	.03	.09	.08	.06
JUN	.05	.04	.01	.05	.04	.02
JUL	.04	.06	.06	.05	.06	.05
AUG	.05	.04	.04	.05	.05	.07
SEP	.02	.05	.07	.04	.03	.07
OCT	.02	.04	.05	.03	.05	.06
NOV	.02	.05	.06	.02	.01	.03
DEC	.03	.05	.03	.07	.00	.06
AVG	.035	.057	.044	.047	.038	.042

2.3 Error Analysis

The type of error which can occur in data measurement and reduction are bias and random errors.

2.3a Bias Error

Vonder Haar (1968) thoroughly discussed the bias errors in the data prior to 1966. He established a most probable absolute error of ± 1.0 percent and $\pm 0.01 \text{ cal cm}^{-2} \text{ min}^{-1}$ in the albedo and longwave components, respectively. (These are equivalent to relative error of 3 to 5 percent.)

The total relative bias error in the same components from the Nimbus 3 satellite has been estimated to be near 5 percent (Raschke, et al., 1972). An error discussion by MacDonald (1970) would place bias error for ESSA 3 and ESSA 7 within the same limits.

Detailed discussion on the magnitude of bias error in the Nimbus 2 and ITOS 1 data are not available. Indication from Raschke, et al. (1970) is that the error in the Nimbus 2 data may be near or within the 5 percent estimated for Nimbus 3. Bias error in the preliminary data from ITOS 1 are presumed to be within the same 5 percent level.

The maximum probable bias error has therefore been set at 5 percent for the albedo and longwave components.

The total bias error in the net radiation gradient can now be determined. Differentiating Eq. (2) we get:

$$d(\Delta RN) = d RN_5 - d RN_{65} \quad (4)$$

Substituting from Eq. (1) and assuming that the solar constant is known exactly we get:

$$d(\Delta RN) = (I_0 dA)_{65} - (I_0 dA)_5 + dRL_{65} - dRL_5 \quad (5)$$

We see that Eq. (5) is dependent upon the incoming solar insolation, a function of latitude and time, and the direction and magnitude of the bias error in albedo and longwave radiation.

There is no reason to suspect a sign change in dA or dRL with latitude so that dA will have the same sign at 5° as at 65° latitude and, similarly, for dRL . However, the error in albedo can be in the same or opposite direction of the error in longwave radiation. Eq. (5) has been used to calculate the bias error in the net radiation gradient for different months of the year with a ± 5 percent bias in each component. Actual data at both $5^\circ N$ and $65^\circ N$ were used in the computation.

The shaded area in Fig. 5 shows the monthly range in the net radiation gradient error when dA and dRL are of the same sign; a maximum of $\pm 0.014 \text{ cal cm}^{-2} \text{ min}^{-1}$ occurs in the winter months which is reduced to a range from zero to $\pm 0.004 \text{ cal cm}^{-2} \text{ min}^{-1}$ in the late spring and summer months. The other curves in the same figure show the bias error in the individual net radiation budgets at $5^\circ N$ and $65^\circ N$. The bias at $5^\circ N$ is relatively unchanging throughout the year. The bias at $65^\circ N$ goes from a minimum during winter to a maximum during summer months.

Figure 6 shows the bias error in the gradient and component radiation budgets when dA and dRL have opposing signs. The maximum bias in this case is $\pm 0.010 \text{ cal cm}^{-2} \text{ min}^{-1}$ which occurs in spring to early summer. A minimum of $\pm 0.02 \text{ cal cm}^{-2} \text{ min}^{-1}$ occurs in the winter months. The smallest overall bias error exists in this case.

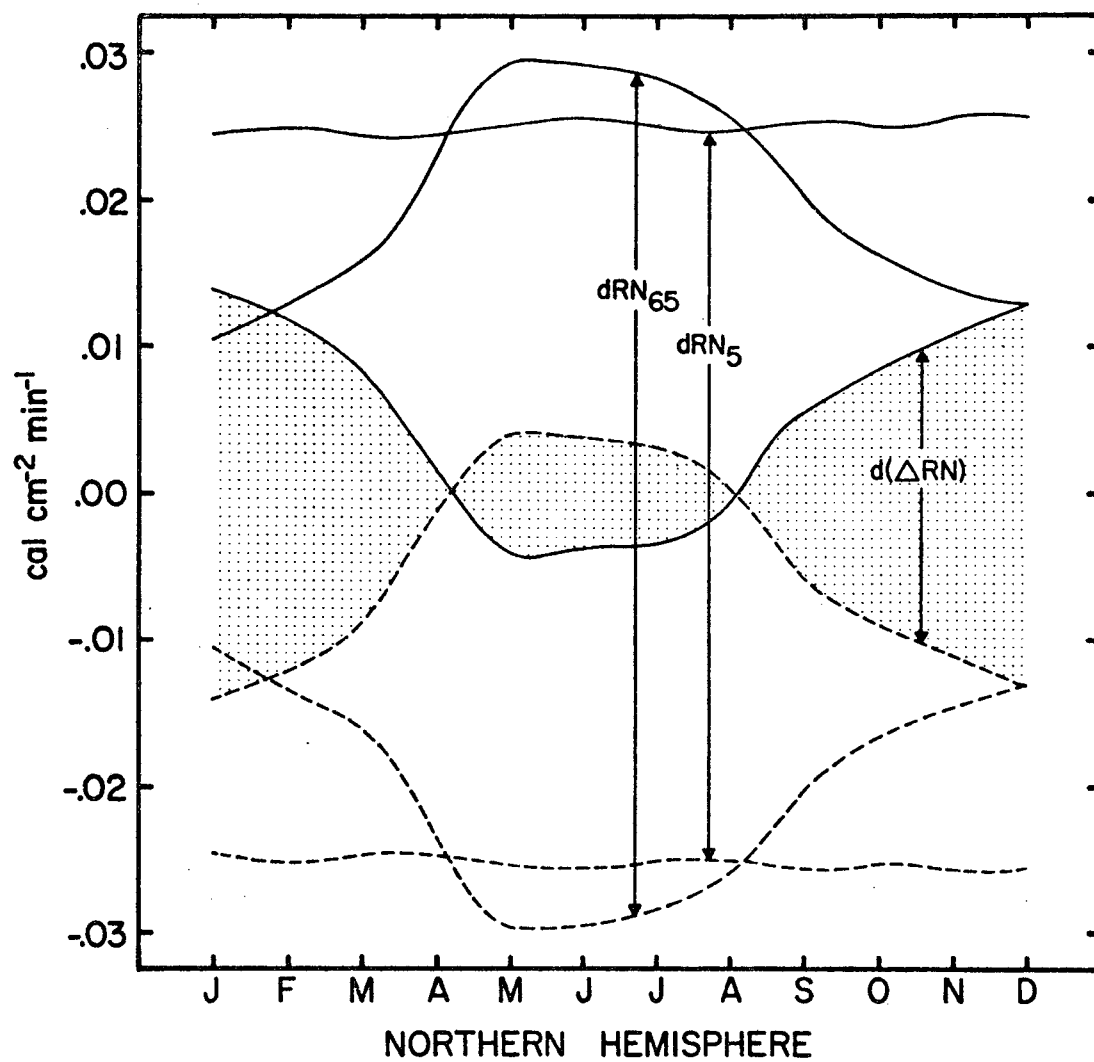


FIGURE 5. Net radiation bias error for infrared and albedo bias errors in the same direction.

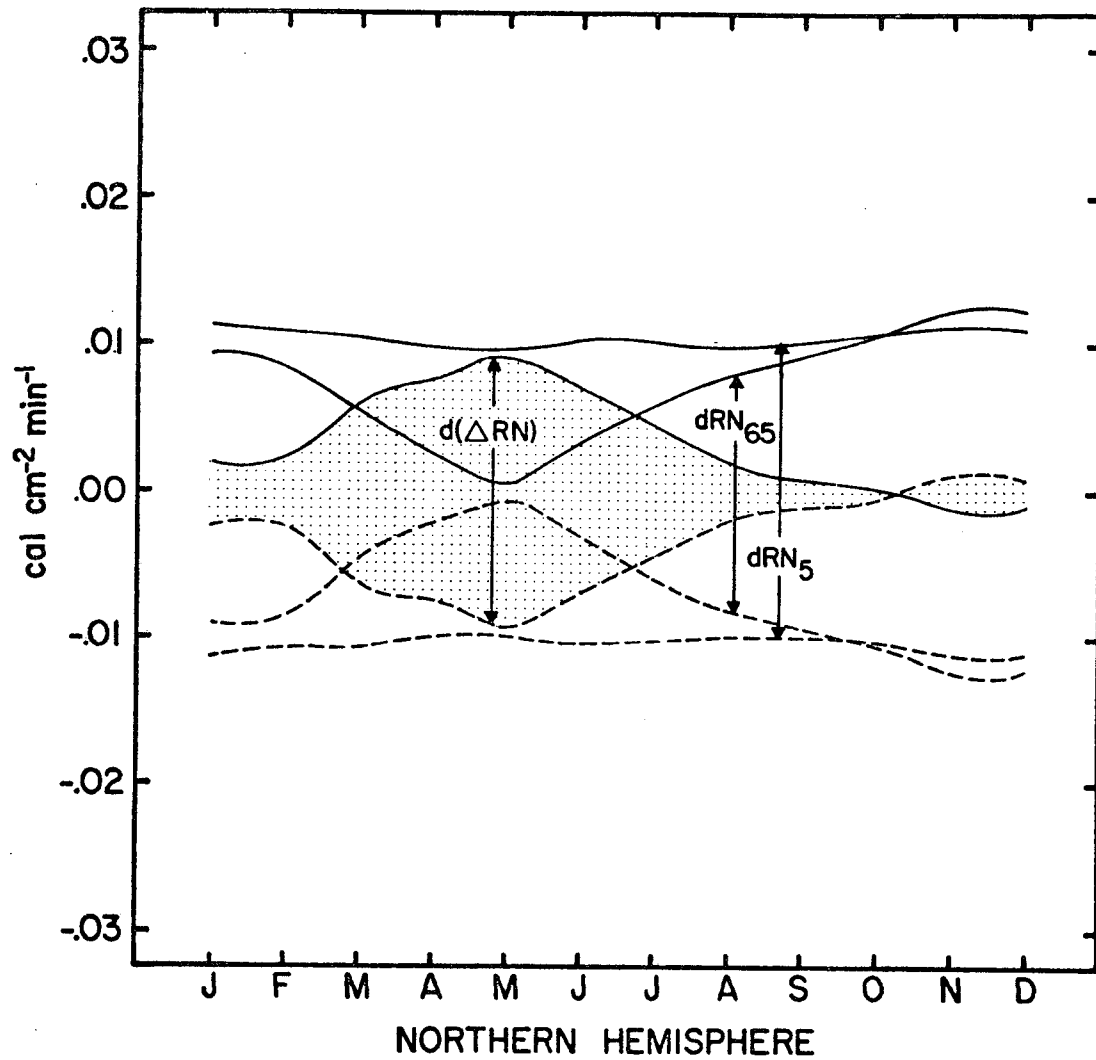


FIGURE 6. Net radiation bias error for infrared and albedo bias errors in opposing directions.

Previously, investigators have shown that dA and dRL are of opposite sign on the low resolution infrared radiometers on the experimental satellites. Thus, the bias error in the latter case applies to more than 75 percent of the data set.

Raschke, et. al. (1972) showed by use of a different reflectance model for reduction of Nimbus 3 data that the albedos over snow and ice ($A > 50\%$) were overestimated by as much as 15 percent by the reduction model applied to Nimbus 2. Overestimates by such a magnitude would show up as a positive bias error in the net radiation gradient for that data because of the large ice field in the polar regions. Such error is minimized in the winter months when the solar insolation is small and maximized in the summer months when the solar insolation is at its greatest. However, from late spring to middle fall the sensor sees very little ice at 65° . Thus, this bias falls within the previously computed bias error for the gradient.

2.3b Other Error

Error induced by uncertainty of the exact value of the solar constant affects each gradient equally. Hence, it does not change the relative interannual variation in the net radiation gradient and, therefore, can be neglected.

It is the opinion of this author that all random errors in time and space have been eliminated by using zonally averaged monthly mean and seasonally mean data.

2.4 Diurnal Effects

Earlier estimates of the diurnal variation in albedo and longwave radiation were made by Vonder Haar and Hanson (see Vonder Haar, 1968) for spring 1962, TIROS 4 data (Fig. 7). These preliminary results were compared to Nimbus 3 and ESSA 7 data from April 1969 which have approximate equator crossing times of 1130 and 1430 local, respectively (Fig. 8).

The absolute values in TIROS 4 albedo profiles had to be adjusted downwards by 5 to 8 percent to fit the new data. A profile at 65°N was also estimated from the new data. A good fit exists between the new data and the preliminary albedo profiles depicting diurnal variation. We see that the albedo drops from early morning to mid-morning and then rises into the afternoon at all latitudes.

The longwave data did not fit the preliminary longwave profiles nearly as well as the albedo data except at 5°N where a precise fit is again found. We see that a general decrease occurs in the longwave loss from early morning to afternoon.

The diurnal effect on the net radiation gradient for Nimbus 3 and ESSA 7 data in the month of April 1969 is shown in Table 3.

TABLE 3: Diurnal variations in net radiation ($\text{cal cm}^{-2} \text{ min}^{-1}$) measured during April 1969

SATELLITE	NET RADIATION BUDGET		GRADIENT
	5°N	65°N	
NIMBUS 3	0.12	-0.10	0.22
ESSA 7	0.10	-0.06	0.16

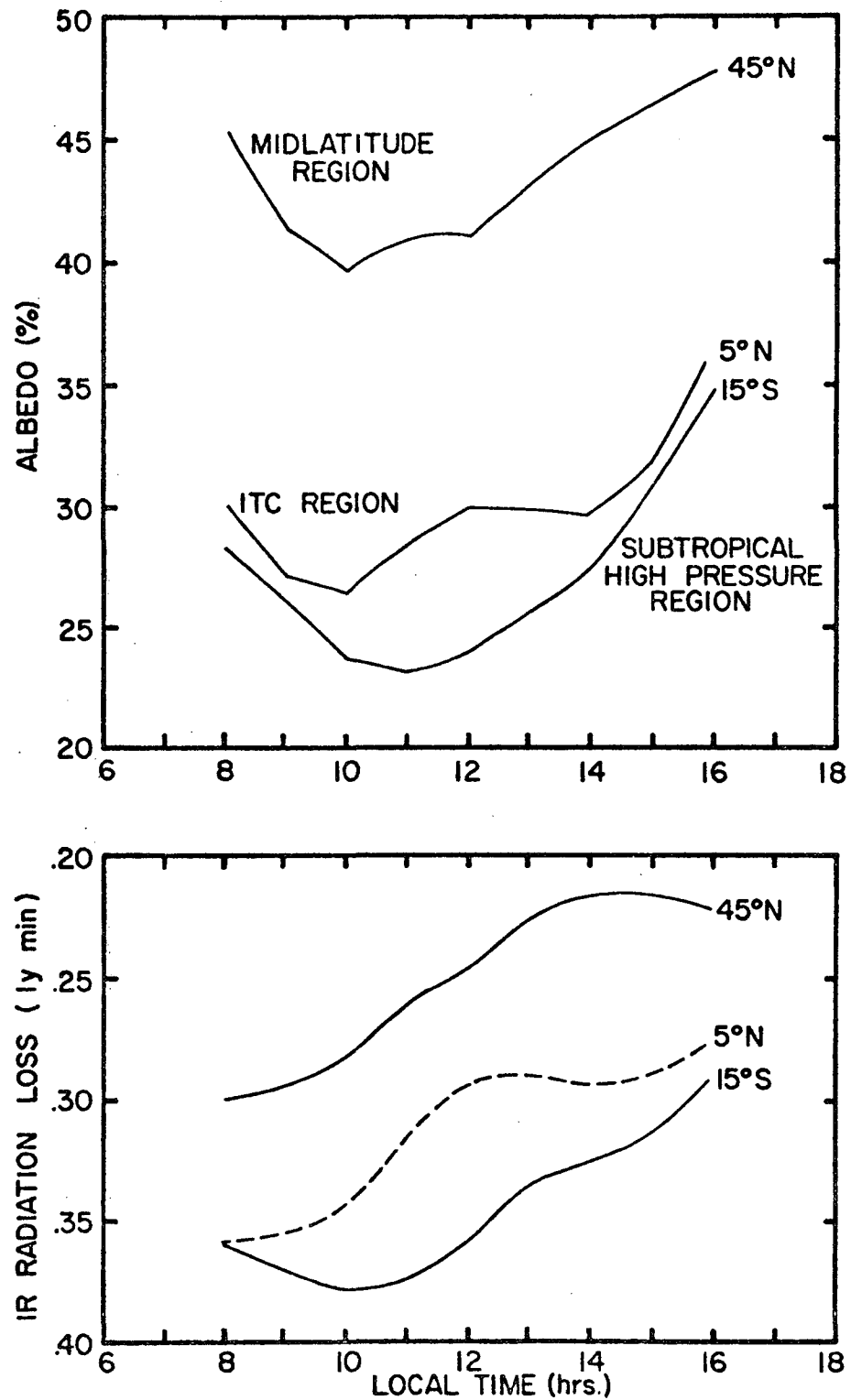


FIGURE 7. Diurnal variation in albedo and infrared radiation from TIROS 4 for April (after Vonder Haar and Hanson; see Vonder Haar, 1968).

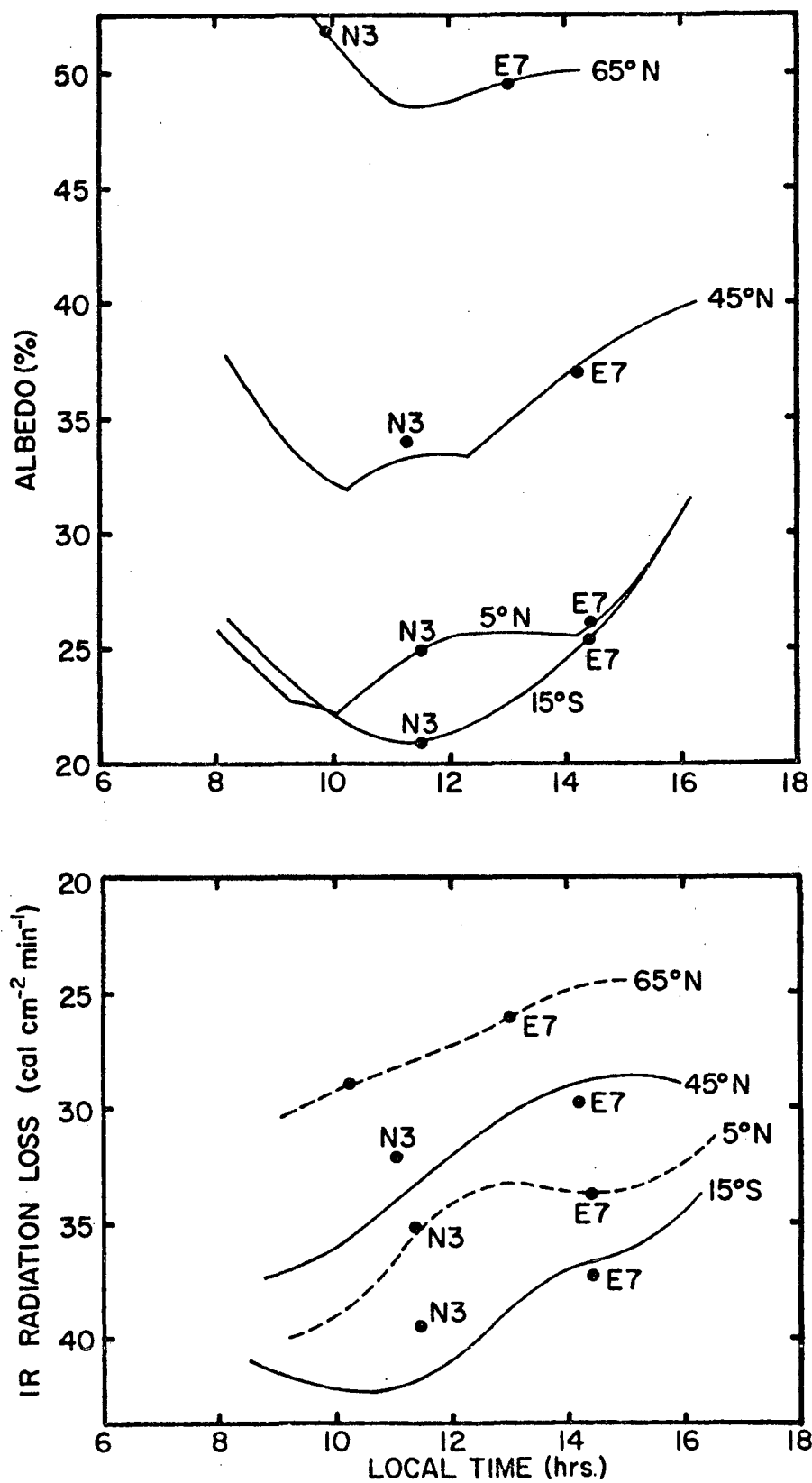


FIGURE 8. Diurnal variation in albedo and infrared radiation from Nimbus 3 and ESSA 7 for April fitted with TIROS 4 profiles.

The gradient near noon for Nimbus 3 data is $0.22 \text{ cal cm}^{-2} \text{ min}^{-1}$. The gradient drops from near noon to afternoon to the ESSA 7 value of $0.16 \text{ cal cm}^{-2} \text{ min}^{-1}$. This change of $0.06 \text{ cal cm}^{-2} \text{ min}^{-1}$ is well beyond the bias error which was computed to be $0.007 \text{ cal cm}^{-2} \text{ min}^{-1}$ for the month of April.

No adjustment have been made to the data in this study for the diurnal variation since the magnitude of its influence is not known for the other months of the year; it is certainly a function of the time of day, season and satellite orbital characteristics. Eventually the diurnal change will be measured for all seasons by experiments on geosynchronous satellites which have the capability to sample at all local times. One will then be able to adjust all of this earlier data for diurnal effects to get average daily radiation parameters and, hence, the gradient.

For the purpose of the study we will proceed with the knowledge that the net radiation gradient decreases from near noon to afternoon.

3.0 GENERAL CIRCULATION AND THE GRADIENT OF NET RADIATION

The intensity of the general circulation can be most quantitatively observed by parameterization of the atmosphere. Parameters selected for describing the atmosphere are: the zonal index, thermal wind, available potential energy, and kinetic energy. Each parameter was computed for each month of the 9 year period from January 1963 through October, 1971. Data for the computations were taken from the daily objective analysis of the National Meteorological Center (NMC).

3.1 Zonal Index

The zonal index (ZI) is the west-to-east component of the geostrophic wind taken across the 35°N to 55°N latitude band on a 700 mb surface. It has been described as a very stable index since its analysis over 20 years indicates typical fluctuations on the order of +5 percent (Kutzbach et al., 1968). Therefore, small changes in the index may infer significant changes in the general circulation.

Namias (1950) suggests that the zonal index is more of an indicator of the organization of the tropospheric circulation than a measure of its strength. The organization of the general circulation is indicated by low index (blocking patterns) and high index (zonal flow).

The zonal index shows the expected seasonal trend over the 9 year period (Figure 9). The dashed line represents the 9 year monthly averages and does not change from year to year. An interesting feature is the sharp decline in the index for February 1968 - low index. Examination of the tropospheric winds revealed the maximum winds to be above normal in strength but south of their normal position. Within the 35°N to 55°N latitude band the winds were more meridional than normal

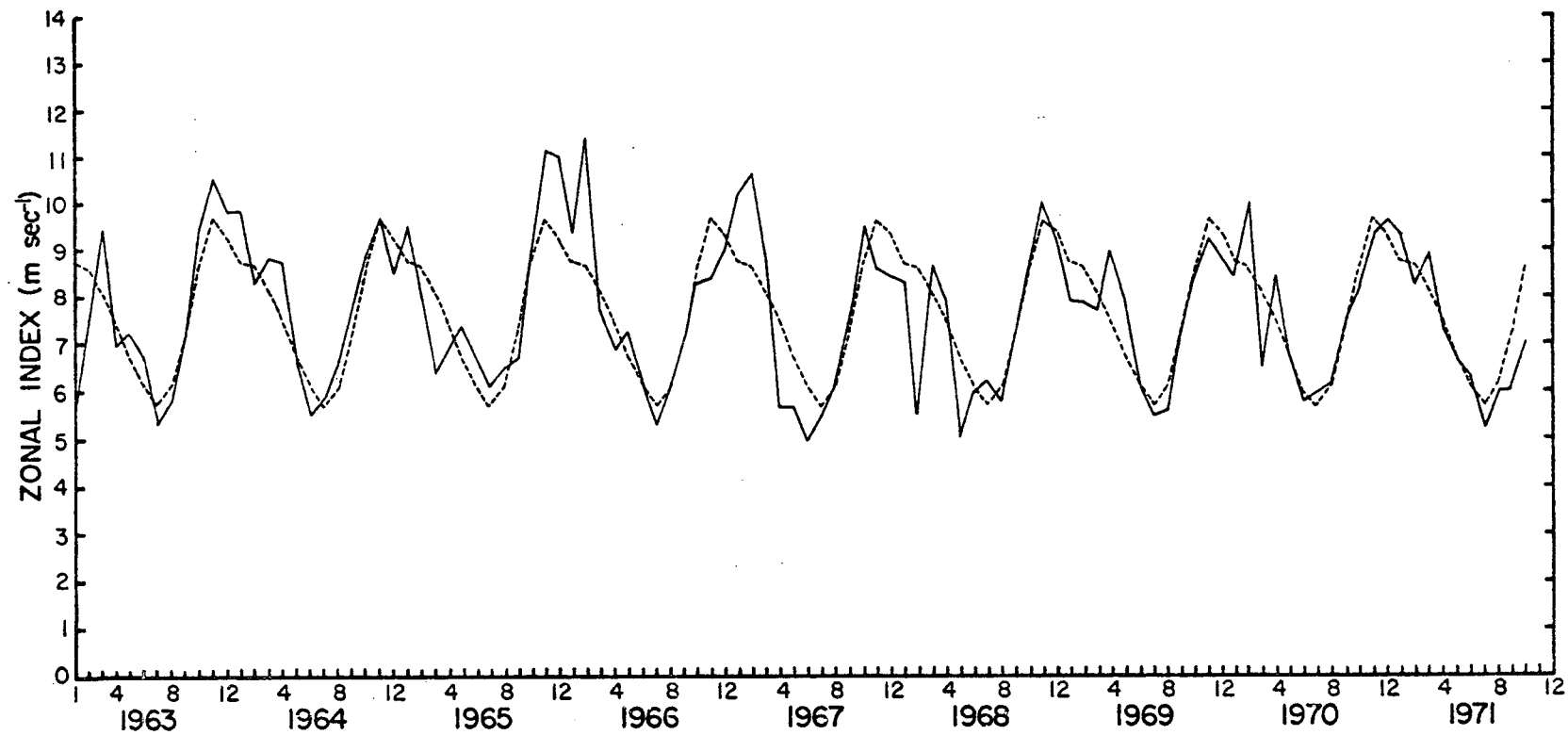


FIGURE 9. Northern hemisphere monthly zonal index from 35N to 55N on a 700 mb surface (solid curve); mean monthly zonal index based upon a 9 year average (dashed curve).

due to amplified troughs and ridges. The foregoing discussion points out that the index is not a good descriptor of the general circulation strength but may be, to a first approximation, a quantitative measure of the organization of the mid-latitude general circulation.

A notable feature is the above normal index for November, 1965 through February, 1966; it is approximately 20% higher than the mean indicating strong zonal flow. Other departures that may be significant are positive departures in winters 1963/64 and 1966/67 and negative departures in winter 1967/68 and spring to summer 1967.

A qualitative look at the net radiation gradient shows significantly stronger gradients in September through November 1965 than in the same months of 1964 (see Figure 1). However, the gradient and index may be inversely and neutrally related in winter 1963/64 and December 1966, respectively.

Also of interest is the November maximum in the mean zonal index profile which also appears in the mean net radiation gradient profile.

3.2 Thermal Wind

The thermal wind is defined as:

$$V_T = -\frac{g}{f} \frac{\partial}{\partial y} (\Delta Z)$$

where g is the acceleration due to gravity, f is the Coriolis parameter, $\frac{\partial}{\partial y}$ the north-to-south gradient from 20°N to 70°N , and ΔZ the thickness of the 1000 to 300 mb layer.

The thermal wind was selected as a parameter since the north-to-south thermal gradient, implicit in the thermal wind, is indirectly

related to the north-to-south difference in radiative energy. This indirect relationship evolves primarily from diabatic heating of the atmosphere through latent and sensible heat transfer from a radiatively heated or cooled earth's surface. Figure 10 shows that the thermal wind lags the net radiation gradient by 4 to 6 weeks, an apparent indirect relationship.

One would hope to see a relationship between the interannual variations of the net radiation gradient and the thermal wind since the two appear to be related on a month to month basis. Examination of the thermal wind (V_T) over the nine year period (see Fig. 11) reveals significant positive anomalies in the following periods: November 1965 through February 1966, July 1966, January and February 1967, March 1969, April 1970, and January and July 1971. Significant negative anomalies appear in winters 1963/64 and 1967/68. The periods for which the net radiation gradient are available (winter 1963/64, November and December 1965, July 1966, and March 1969) have anomalies in the gradient with the same sign as the anomalies in the thermal wind (see Figure 1).

Of course one can start with a gradient anomaly and look for a corresponding anomaly in the thermal wind. Large positive anomalies in the gradient for April 1969 and January 1970 are not reflected in the thermal wind.

3.3 Energetics

Interannual changes in the net radiation gradient not reflected in the intensity of the general circulation may, however, cause the atmosphere to operate in a different mode. By computing available

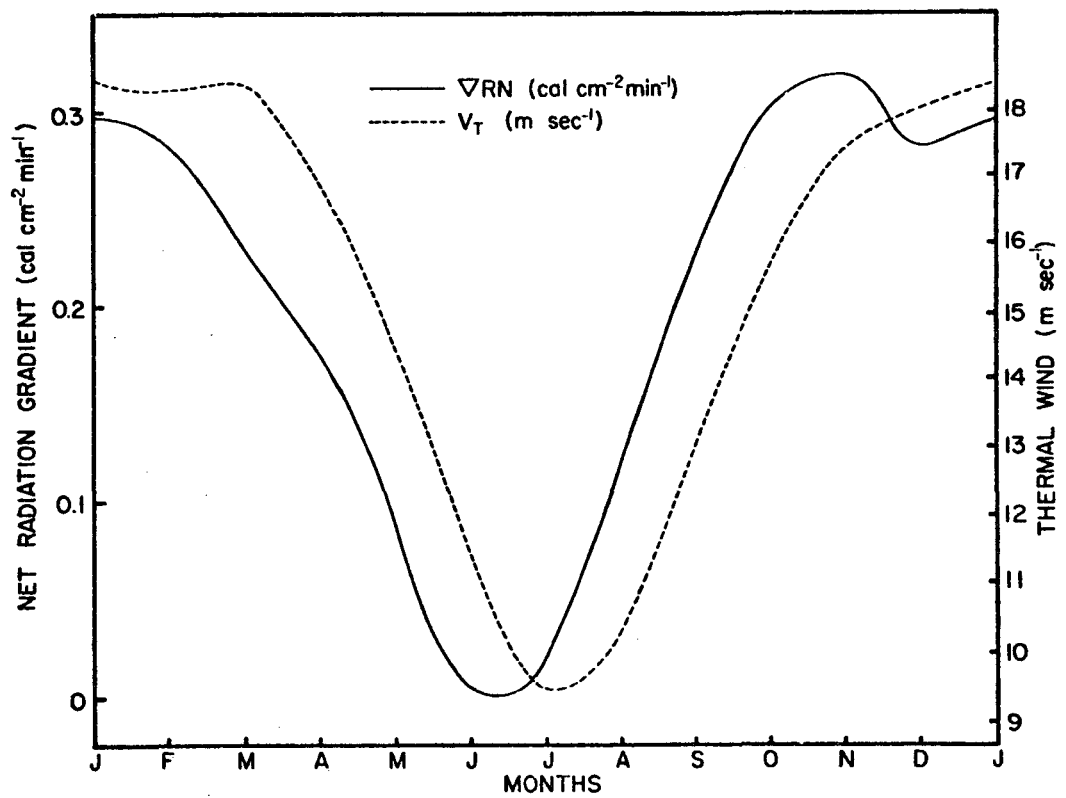


FIGURE 10. Annual cycle of the net radiation gradient (ΔRN) and the thermal wind (V_T) based on a 9 year average from 1963 to 1971.

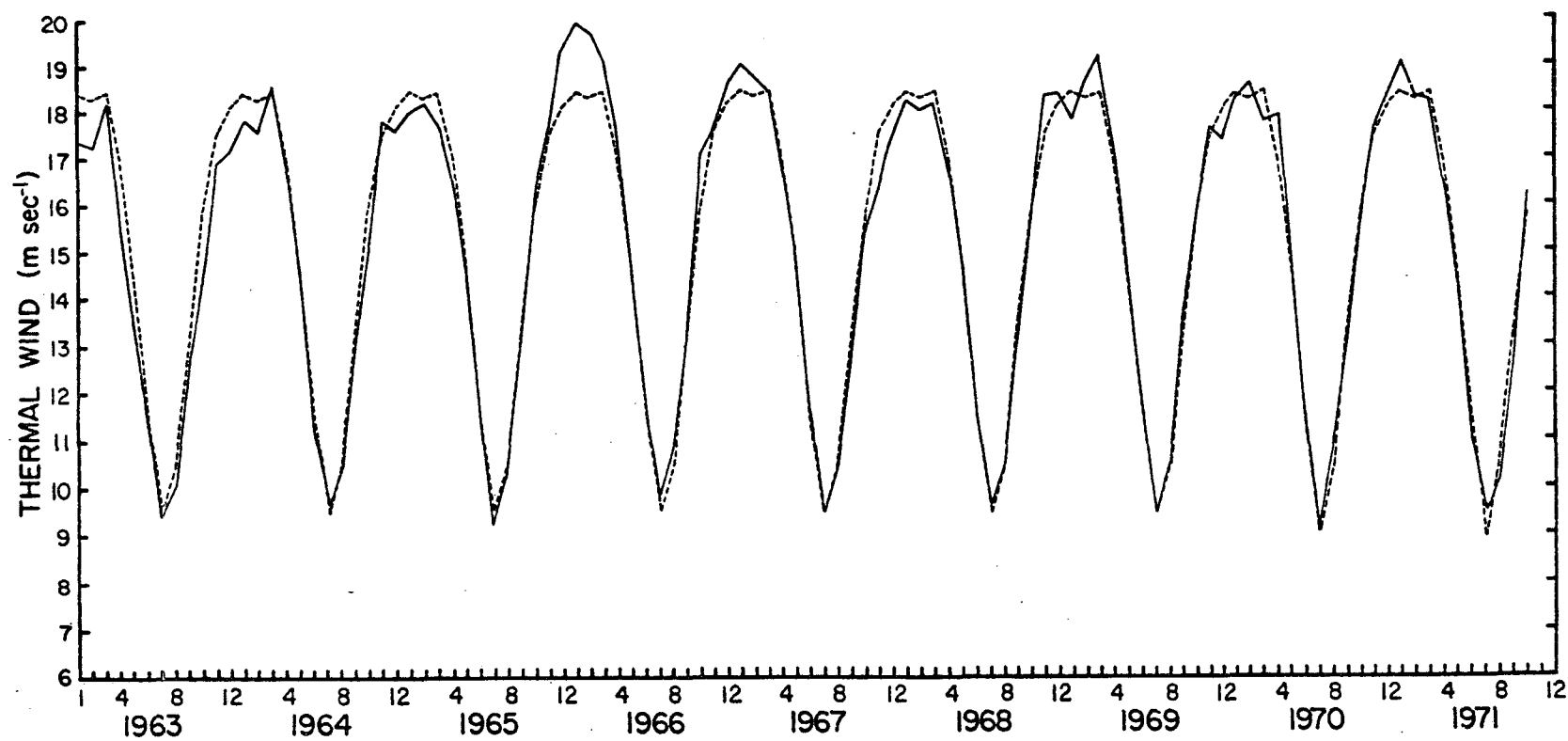


FIGURE 11. Northern hemisphere thermal wind for the layer 1000 mb to 300 mb from 20N to 90N (solid curve); mean monthly thermal wind based upon a 9 year average (dashed curve).

potential and kinetic energies which are partitioned into their zonal and eddy components one can observe the energy distribution between each component. A further refinement, which has not been done in this study, would be to compute the generation, conversion, and dissipation terms of the atmospheric energy cycle to see the actual mode of operation.

The relative distribution of energy between the zonal and eddy components is a function of the order used in computing space and time means. Oort (1964) discusses this thoroughly and establishes a set of equations for space, time, and mixed space-time domains. All computations in this study are within the mixed space-time domain. All integrations, taken over the mass of the atmosphere (trapezoidal method of integration was used), have limits from 850 to 200 mb and 20°N to 90°N . These limits were set because of data limitations in the NMC daily objective analysis. The zonal values were computed from the monthly mean data which included both the 00 and 12 GMT data. The eddy components were computed just from the daily 00 GMT data.

Symbology used in the equations is defined as follows:

p = pressure

p_0 = 850 mb in this study

T = temperature in degrees absolute

m = mass

θ = potential temperature

u, v = east-west and north-south wind components

R = gas constant

C_p = specific heat at constant pressure

$[X]$ = zonal average of X

X^* = deviation from zonal average of X

\bar{X} = time average of X

X' = deviation from time average of X

\tilde{X} = area average of X over a closed isobaric surface

X'' = deviation from area average of X

3.3a Available Potential Energy

Zonal and eddy available potential energy are defined in the mixed space-time domain as:

$$P_m = \frac{1}{2} C_p \int \gamma [\bar{T}]'^2 dm \quad (7)$$

and

$$P_e = \frac{1}{2} C_p \int \gamma [\bar{T}'^2 + \bar{T}^{*2}] dm, \quad (8)$$

respectively, with

$$\gamma = - \left(\frac{\theta}{T} \right)^2 \frac{R}{C_p p_o} \int_0^{p_o} \left(\frac{T}{\theta} \right) \frac{1}{p} \left(\frac{\partial \tilde{\theta}}{\partial p} \right) dp \quad (9)$$

Eq. (9) depends upon the mean static stability of the atmosphere; this is more apparent when γ is written in the form

$$\gamma = \frac{g}{C_p} (\Gamma_d - \bar{\Gamma})^{-1} \tilde{T}^{-1} \quad (10)$$

where Γ_d is the dry adiabatic lapse rate and $\bar{\Gamma}$ is the time mean lapse rate of the environment.

Eq. (9) can be used in the definition of available potential energy as:

$$\gamma = -k \left(\frac{\theta}{T} \right)^2 \quad (11)$$

where k is independent of pressure and time (Oort, 1964). The procedure used in this study was to compute k for each month of the 9 year period (106 values) and to use Eq. (11) in Eqs. (7 and 8).

Figures 12 and 13 show computed zonal (P_m) and eddy (P_e) available potential energies, respectively, for the 9 year period. Again, the dashed curve represents the average monthly values and does not change from year-to-year.

A large positive anomaly in P_m , approximately 12 percent of P_m , again appears in November 1965 through February 1966 as it had in the zonal index and thermal wind. Other anomalies that also appeared in the thermal wind are positive anomalies in January and February 1967, and February and April 1969, and a negative anomaly in winter 1967/68. As we shall see later, the mean available potential energy undergoes interannual variations in actual magnitude much larger than the three other energy terms.

The months for which radiation data were available (November 1965 and February and April, 1969) show corresponding variations in the net radiation gradient and P_m .

Eddy available potential energy shows instead of a positive departure from the mean in November 1965 through February 1966, a negative departure. Other features which stand out are the large positive departures in January 1963 and January through May 1967.

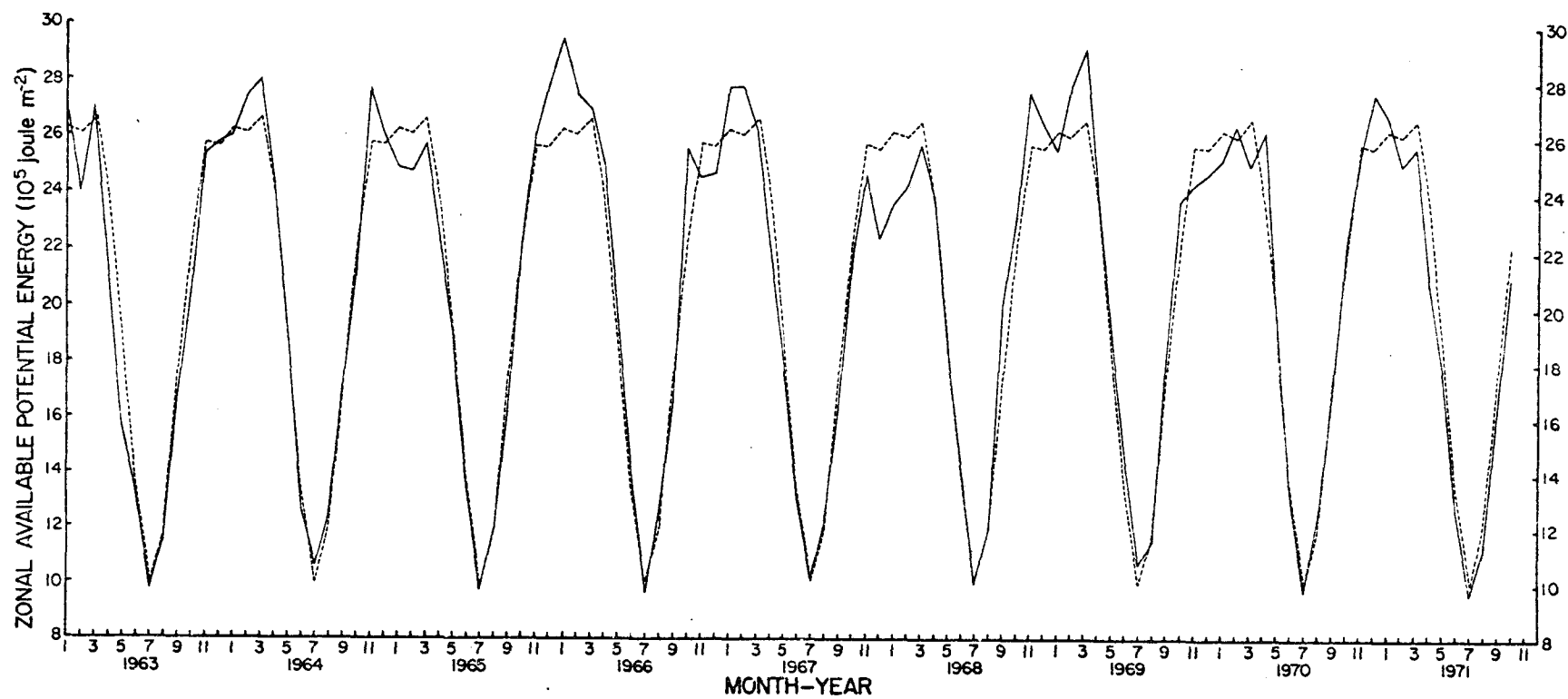


FIGURE 12. Northern hemisphere zonal available potential energy in the mixed space-time domain for the layer 850 mb to 200 mb from 20N to 90N (solid curve); mean monthly zonal available potential energy based upon a 9 year average (dashed curve).

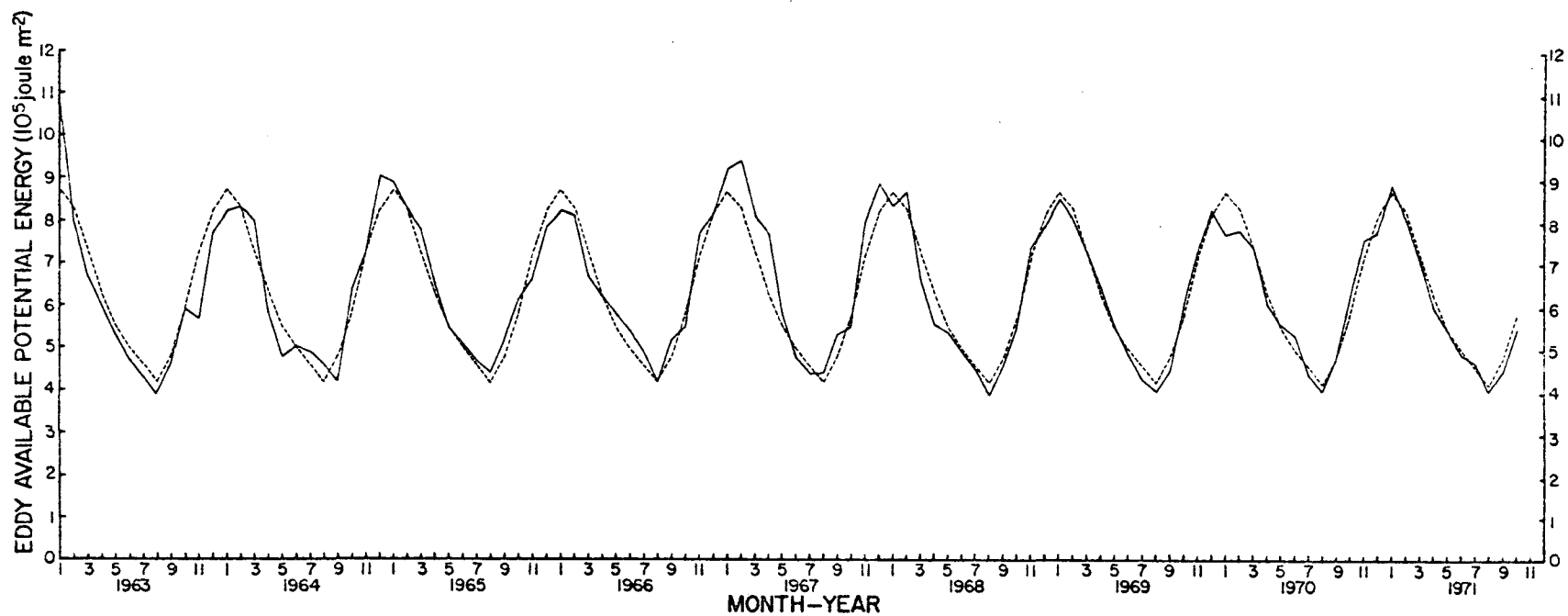


FIGURE 13. Northern hemisphere eddy available potential energy in the mixed space-time domain for the layer 850 mb to 200 mb from 20N to 90N (solid curve); mean monthly eddy available potential energy based upon a 9 year average (dashed curve).

However, no satellite data is available for these periods. The negative departure from November 1963 through January 1964 is in agreement with the net radiation gradient for the seasons SON 1963 and DJF 1963 (see Figure 3).

3.3b Kinetic Energy

Zonal and eddy kinetic energy are defined in the mixed space-time domain as:

$$K_m = \frac{1}{2} \int ([\bar{u}]^2 + [\bar{v}]^2) dm \quad (12)$$

and

$$K_e = \frac{1}{2} \int [\bar{u}'^2 + \bar{v}'^2 + \bar{u}^{*2} + \bar{v}^{*2}] dm, \quad (13)$$

respectively. Geostrophic winds were computed for this study since the actual winds in the NMC objective analysis were not available for the entire 9 year period. Because of the geostrophic approximation, the second term in Eq. (12) involving the zonal average of the meridional wind is zero. The latitudinal limits in the integration are also reduced to 22.5°N and 87.5°N .

The large positive anomaly which appeared in the other parameters for November 1965 through February 1966 again appears in K_m (Fig. 14). The similarity of the interannual variations between K_m and the other parameters stops here. Another striking feature, the largest anomaly in K_m , is the large positive anomaly in January 1970. This anomaly in K_m agrees with the large positive anomaly in the net radiation gradient in January 1970. Likewise, the negative anomaly in K_m for November 1964 through February 1965 agrees with the negative anomaly in the gradient of net radiation for the same period.

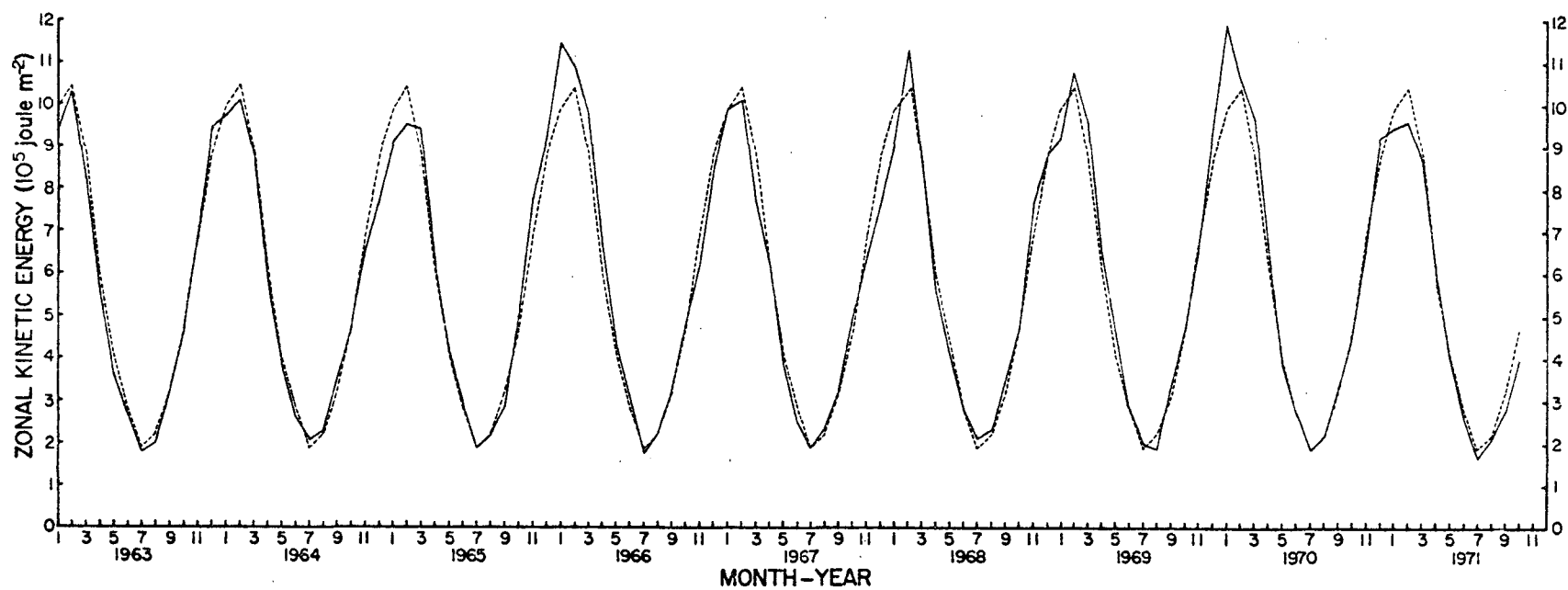


FIGURE 14. Northern hemisphere zonal kinetic energy in the mixed space-time domain for the layer 850 mb to 200 mb from 20N to 90N (solid curve); mean monthly zonal kinetic energy based on a 9 year average (dashed curve).

The large positive anomaly in winter 1965/66 apparent in the other parameters is slightly negative in K_e (Fig. 15). Comparing K_m and K_e one can conclude, to a first approximation, that the interannual variations in K_m and K_e are inversely related. Of course this is an expected result; given a constant total kinetic energy, then an inverse relationship will exist between the mean and eddy components. This is a particular case which illustrates that given slight variations in impulse, the atmosphere may not respond with a change in its total energy but may only change its mode of energy transformation.

The foregoing qualitative discussion brought out that relationships between the interannual variations of the gradient and the general circulation parameters are apparent for the cases when variations in either one or both are very large. The relationship is summarized in Table 4. A positive sign indicates that the variations in the net radiation gradient and the general circulation parameters are of the same sign; a negative sign indicates that they are of opposite sign and a zero indicates that one of the variables does not deviate from the mean.

3.4 Quantitative Comparison

Correlation coefficients were computed between each of the general circulation parameters. The annual cycle was first removed from the data so that only interannual variations in the monthly values were compared. There were 106 samples of each parameter.

The results showed the best correlations of 0.68 and 0.67 between the thermal wind (V_T) and zonal available potential energy (P_m) and between eddy kinetic (K_e) and eddy potential energies (P_e),

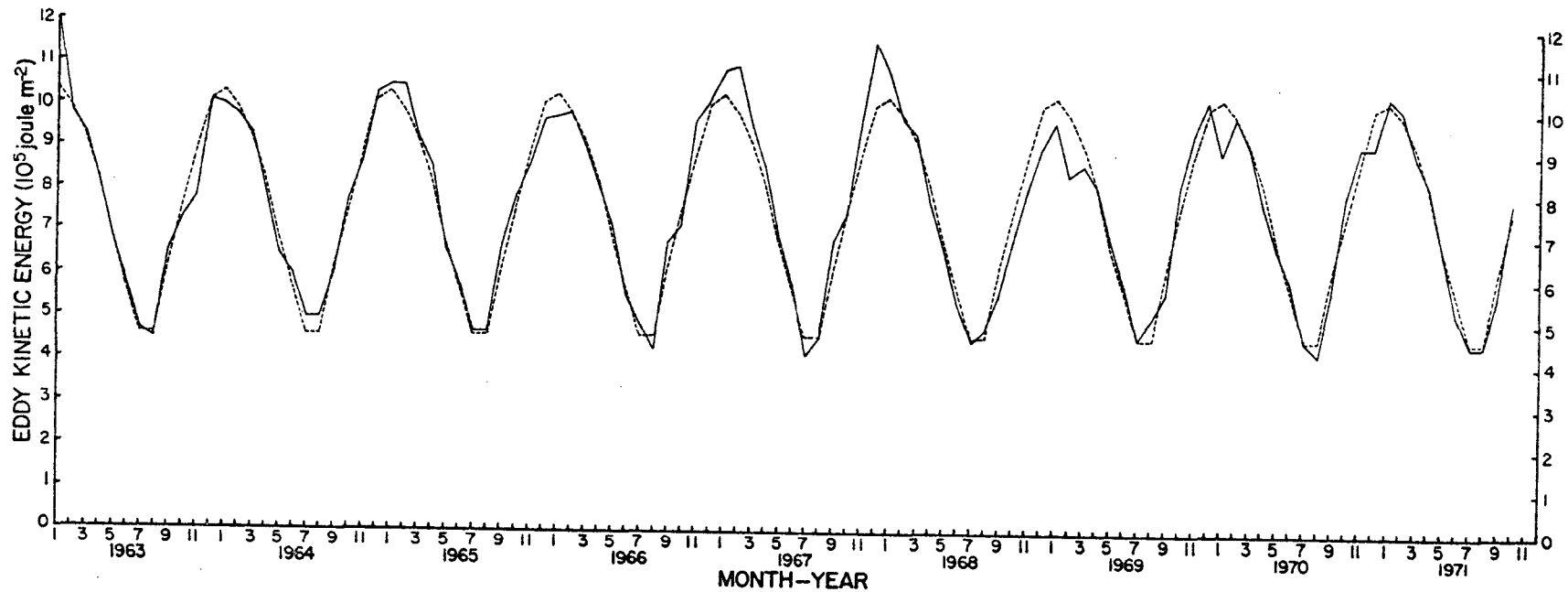


FIGURE 15. Northern hemisphere eddy kinetic energy in the mixed space-time domain for the later 850 mb to 200 mb from 20N to 90N (solid curve); mean monthly eddy kinetic energy based on a 9 year average (dashed curve).

TABLE 4: Summary table of qualitative comparison between interannual variations in the net radiation gradient and the general circulation parameters.

Parameter	J	F	M	A	M	J	J	A	S	O	N	D
ZI	-65 066 069 070	+65 -69	+65 -69	+65 +69	-65 +69	+65	065	+65	-65	+65	+65	066
V _t	+65 +69 -70	+65 +69	+65 +69	+69			+66			+65	+65 065	+64 066 +68
P _m	+65 -70	+65 +69	+65 +69	+65 +69			-64 069			+65 -68 +69	-64 +65 068	065 066 +68
P _e	-70									-65	-65	-64 -65
K _e	-65 069 -70	-65 -69	-69		-71		-64			-65 +68	-65 068	-68
K _m	+65 +70	+65								+65	+64 +65	+64

respectively. The high correlation between V_T and P_m is explainable in the fact that both parameters are a measure of the north to south atmospheric temperature difference. The large positive correlation between K_e and P_e is not so easily explained, but is directly dependent upon energy generation, dissipation and conversion rates. A correlation of -0.47 was found between the interannual variations of zonal kinetic and eddy kinetic energies which demonstrates to some degree the inverse relationship between the zonal and eddy components. A somewhat unexpected result was the lack of correlation between the interannual variations in the zonal kinetic energy and the zonal index. This again probably relates to the fact that the zonal index may be a better descriptor of the organization rather than the intensity of the general circulation.

Correlations coefficients were computed between the gradient of net radiation and the general circulation parameters with the annual cycle removed. The correlations were based on a sample size of 35 which require correlations larger than 0.335 and 0.430 to be significant at the 5 and 1 percent levels, respectively. The monthly means used to remove the annual cycle from the general circulation parameters were established from the same months which were used to remove the annual cycle from the net radiation gradient. In this respect, the interannual variations from both sets of data will be compared using input data from the same months.

The results are shown in Figures 16a and 16b. The computations were made with the net radiation gradient lagging the circulation parameters by 1 to 12 months (shown as a minus lag) and with circulation

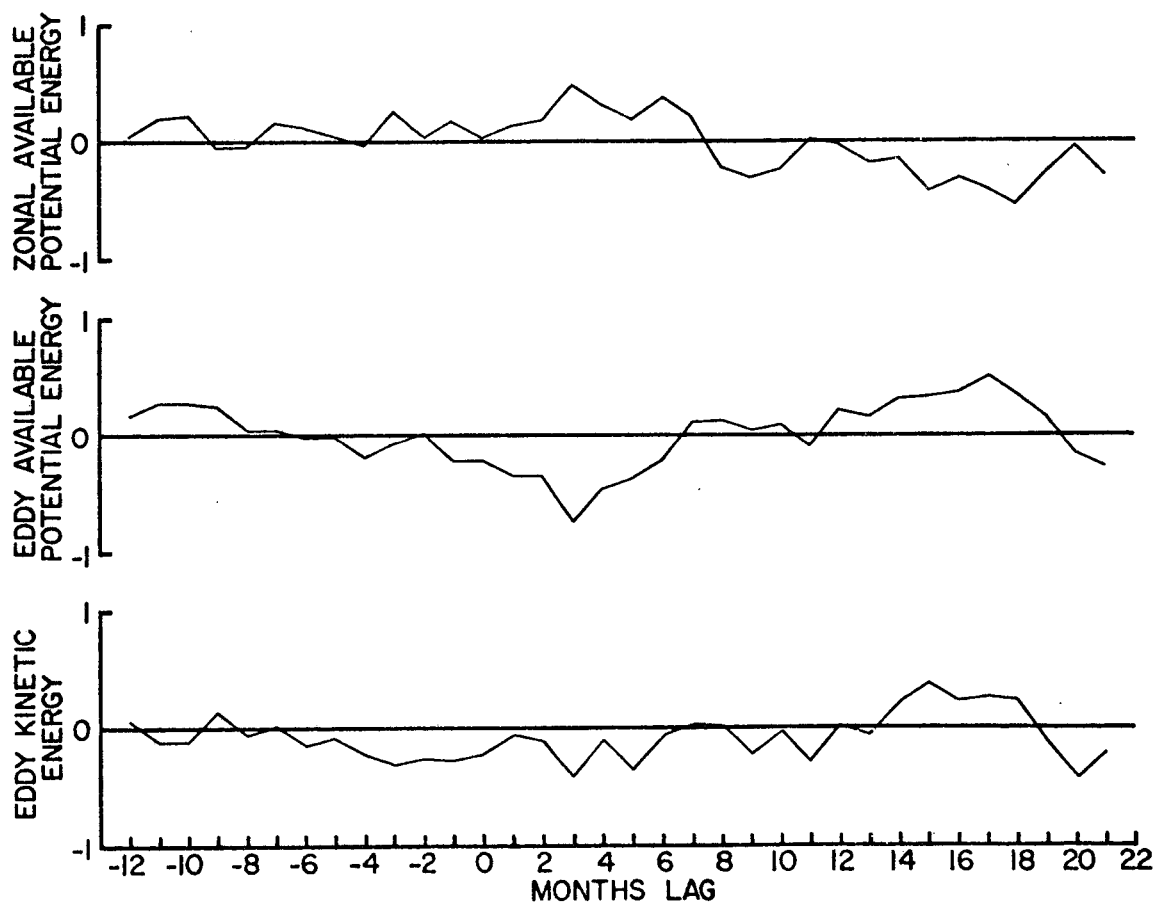


FIGURE 16a. Correlation coefficients of interannual variations with the general circulation parameters leading (-months) and lagging (+months) the net radiation gradient.

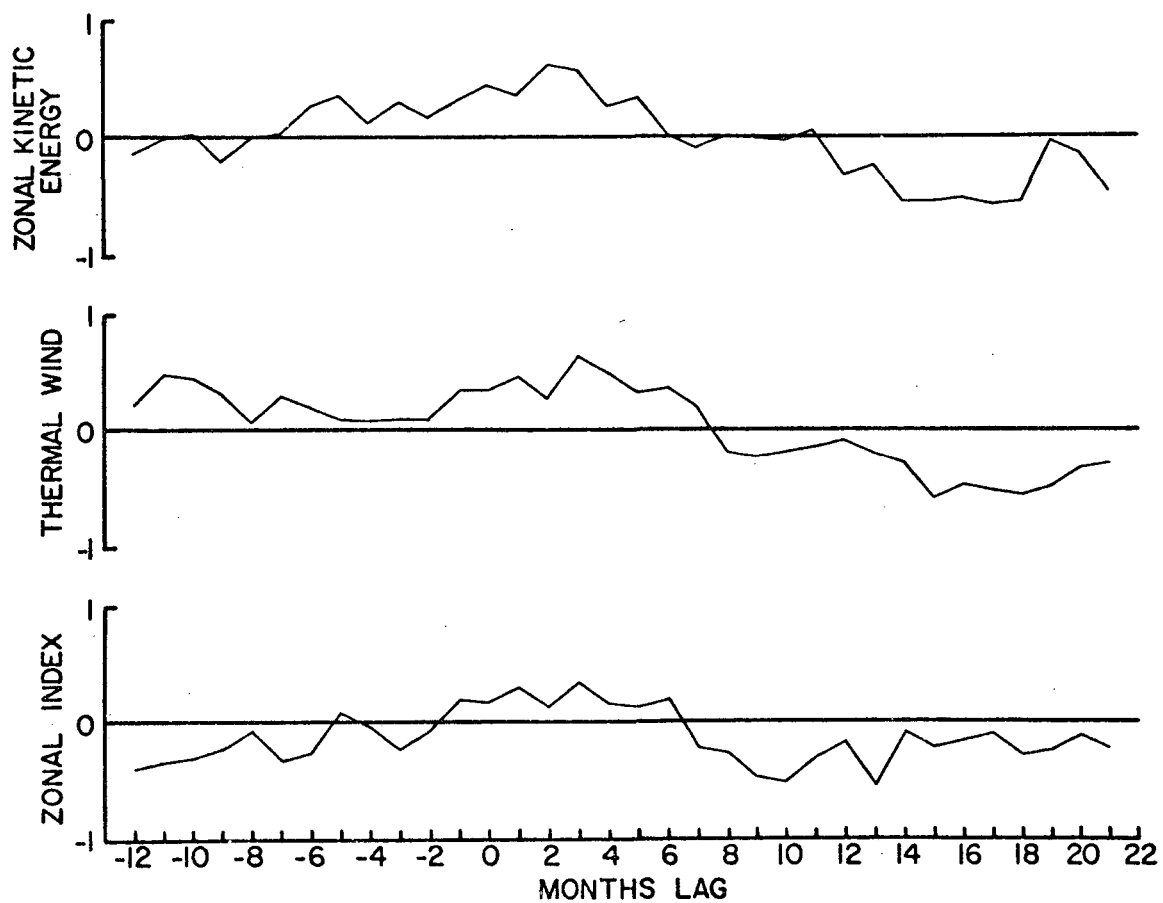


FIGURE 16b. Correlation coefficients of interannual variations with the general circulation parameters leading (-months) and lagging (+months) the net radiation gradient.

parameters lagging the net radiation gradient by 1 to 21 months (shown as a positive lag).

Excluding the zonal index, the best correlations appear with positive lags of 2 to 4 months. For the most part, these correlations are centered about a 3 month lag. Other correlations which are significant appear at 15 to 18 months lag with signs opposite of those at 3 months lag. These correlations have an average lag at 17 months.

Scanning the complete graph another general inflection in the curves appears at 9 to 10 months lead (-lag), especially prominent in the thermal wind and eddy potential energy. Going from crest to crest or trough to trough one sees that the wavelength is 26 to 27 months in length. Finding a wave in the correlations and especially a wavelength of 26 to 27 months was totally unexpected.

The lag relationship of the wave indicates that the general circulation parameters lead the net radiation gradient by 9 to 10 months or lag it by 3 months. Because of this wave, in contrast to the appearance of just one major peak in the correlation, no cause and effect relationship can be established.

Peak positive and negative correlations in the seasonal data were not as well defined--a most probable effect resulting from a smaller sample size (18) and averaging the data into seasonal values. For this reason, the interannual variations in the seasonal data will not be pursued any farther.

4.0 ANALYSIS OF RESULTS

4.1 Gradient and Circulation

Interannual variations in the net radiation gradient are indirectly caused by variations in the general circulation. Variations in the general circulation affecting the gradient are primarily manifested in cloudiness. For an example, decrease in middle and low cloudiness in the tropics contributes to a stronger north-to-south net radiation gradient.

Going one step farther, one should expect changes in the net radiation gradient to feed back into the general circulation. Knowing the time constant for the feedback may be important to long range weather prediction since the primitive equation models are presently limited to 10-14 day predictions.

It takes on the order of 4 to 6 weeks for the atmospheric temperature structure to respond to seasonal changes in the net radiation gradient as evidenced by the thermal wind lag. Also, there is an apparent 3 month response time between year-to-year differences in the net radiation gradient and the circulation parameters. Of course, this is based on an assumption that the two are related. In addition, there are a number of cases when a qualitative inspection showed that no apparent lag relationship existed between the year-to-year variations in the two.

A question to be answered is why the apparent cycle in correlations with a near 26 month period and why the initial 3 month lag in the circulation behind the gradient or, looking at it another way, why a 9 month lag in the gradient behind the general circulation.

4.1a Periodicity in Data

The cycle with approximately a 26 month period as seen in the correlation coefficients must result from a similar cycle in either one or both of the data sets used in the correlation.

With some imagination, one can fit a sine curve with approximately a 26 month period to a time series of the interannual variations in the monthly net radiation gradient ($\Delta RN'$) (Fig. 17). A definite increase is apparent in $\Delta RN'$ from early fall 1964 to winter 1965/66. This same general trend, but not as well defined, appears in early fall 1968 to the latter part of 1969 and is just two wavelengths downstream from the earlier trend. Therefore, the $\Delta RN'$ data will tend to correlate with any other data set which contains a 26 month period when certain lags are introduced.

Could this cycle be indicative of the 26 month or quasi-biennial cycle? The temporal distribution of $\Delta RN'$ did not definitely show the cycle but indicated that one may be present. Data is needed in 1967 and early 1968 so that, at least, the existence of one wave might be verified. Future measurements by satellites will enable us to draw valid conclusions concerning the presence of a 26 month oscillation in the data.

If the quasi-biennial cycle is in $\Delta RN'$, then it is most likely in the interannual variations in tropospheric cloudiness since cloudiness is the primary modifier of $\Delta RN'$. That it is in the tropospheric cloudiness is supported by the fact that it has been found in the temporal distribution of tropical precipitation (Garstang, 1967).

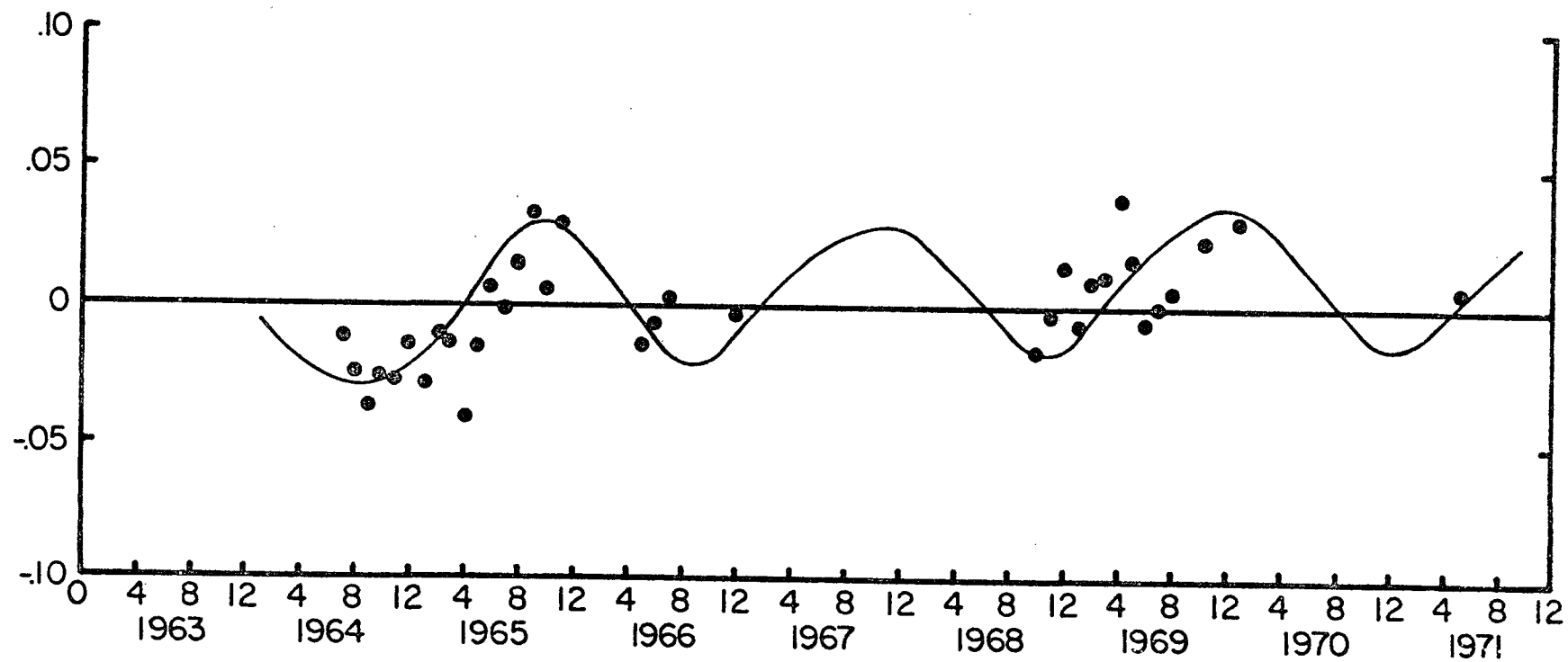


FIGURE 17. Temporal distribution of the net radiation gradient with the annual cycle removed ($\Delta RN'$).

A wave with a 26 month period must exist in the general circulation parameters since no well defined wave was found in the $\Delta RN'$. Such periodicity has been found in the mid-latitude troposphere by investigation of the sea level zonal index (Brier, 1969), in surface temperature (Landsberg et al., 1963), and 500 mb angular momentum transport (Miller, et al., 1967). Many studies indicate a dominating role of winter months in the 26 month oscillation (see Reiter, 1969).

To determine if such a wave exists in the general circulation data with the annual cycle removed--which was intercompared with the satellite measurements--a power spectrum analysis was performed on each 9 year data set. The first 11 harmonics representing periods of 108 months to 9.8 months are shown in Figure 18. One would expect to see a relatively large percent variance for the fourth harmonic (27 months period) if the quasi-biennial oscillation is in the data. Indeed, such large variance is seen in the smoothed spectrum (solid curve) for eddy available potential energy--the same parameter which had the most distinguishable 26 month cycle in the correlation coefficients (Fig. 16a). The smoothed spectrum does not show the 27 month periodicity nearly as well in the other parameters. However, the unsmoothed spectrum (dashed) shows a peak in the variance at 27 months periodicity in all parameters but the zonal index and zonal kinetic energy. The predominate variance in zonal kinetic energy and the thermal wind is with a periodicity on the order of 54 months rather than 27 months. In all, the two eddy parameters show a 27 month periodicity best.

The spectrum for zonal kinetic energy shows a minimum of variance at 27 months but the correlation coefficients showed a well

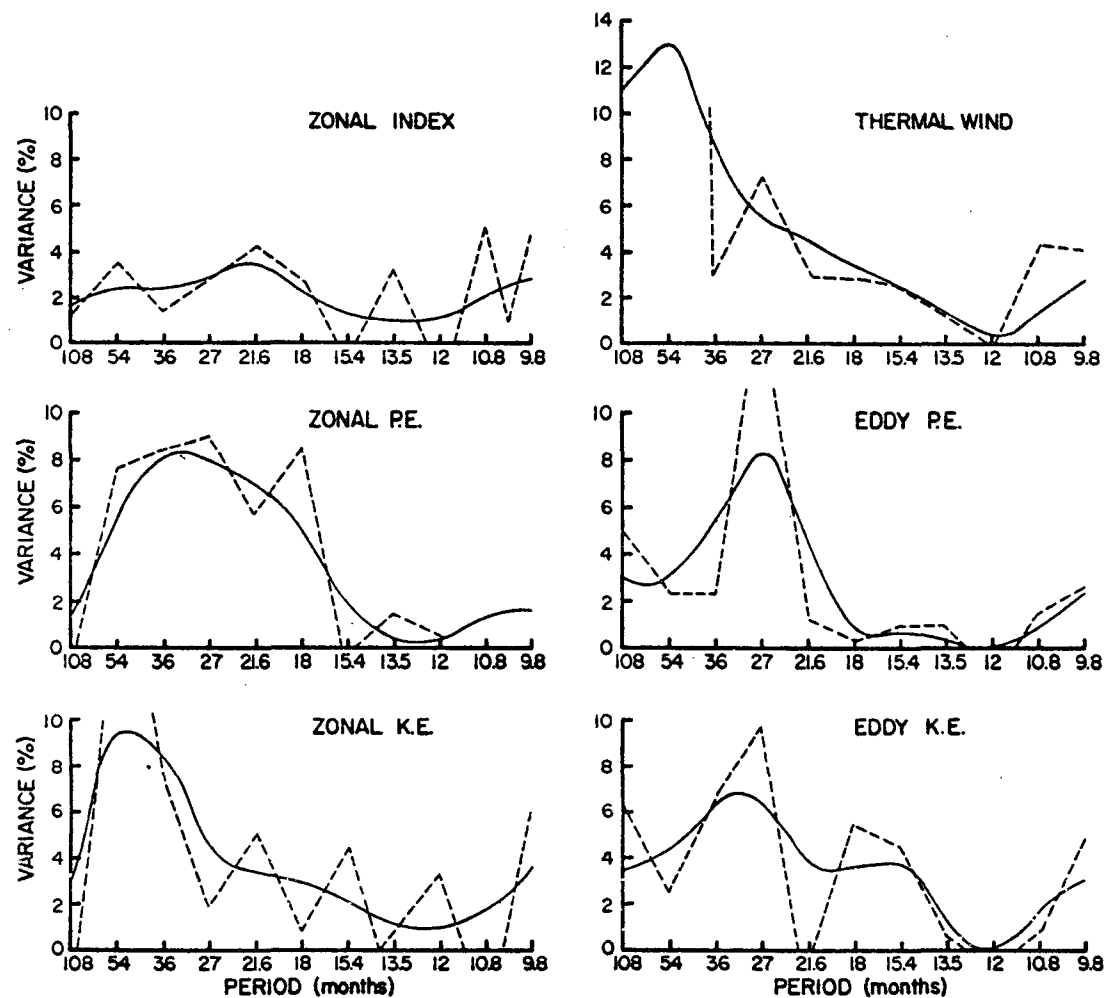


FIGURE 18. Spectrum analysis of general circulation parameters: smoothed spectrum (solid line), unsmoothed spectrum (dashed line).

defined half wavelength from 3 months to 16 months lag. Therefore, it appears that a 26 month oscillation exists in the satellite measurements.

4.1b 3 Month Lag

The next question to be investigated is the 3 month lag in the correlations--a feature common to all general circulation parameters. The phase relationship between ocean storage and the atmospheric circulation might be the best place to look.¹ The seasonal storage curves for the northern hemisphere at latitudes 5N, 30N, and 65N show in the periods March-April and September-October, no net energy transfer between oceans and atmosphere (Fig. 19). If the oceanic storage is the primary agent contributing to a 3 month lag, then, during these periods, no large lag relationship should exist.

Examination of the month to month correlations between interannual variations in zonal available potential energy (P_m) and the net radiation gradient (RN) with both no lag and a 3 month lag might give evidence of the oceanic influence (Fig. 20). The solid bars represent interannual variations in ΔRN while the other bars represent the same variations in P_m . In the period March-April the correlations are nearly as good with and without a lag relationship except that the no lag may be slightly better. The $\Delta RN'$ for March, along with the period May through July (except July, 1966)

¹Professor Verner E. Suomi originally suggested this line of inquiry.

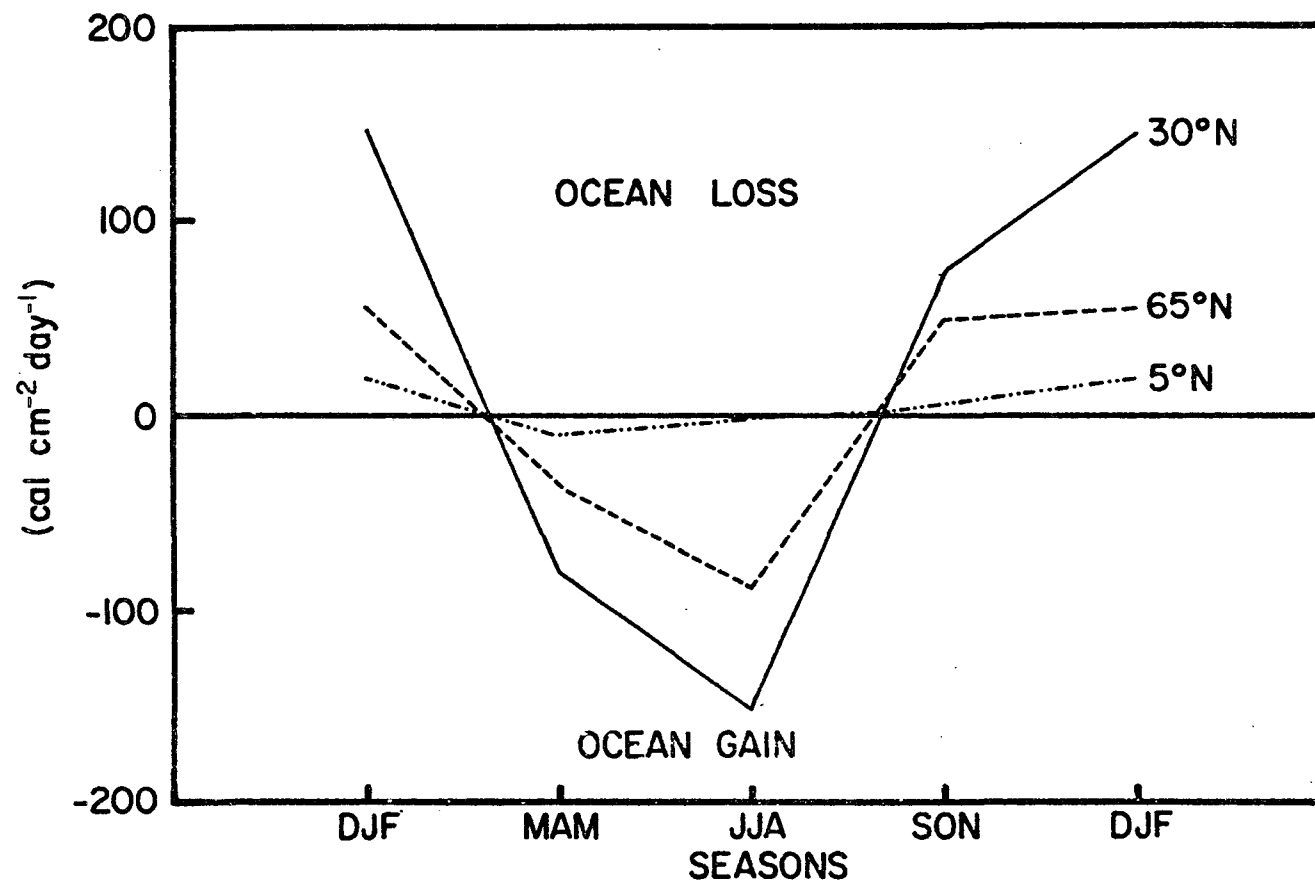


FIGURE 19. Ocean storage curve for selected latitudes of the northern hemisphere (taken from data of Newell et al., 1969).

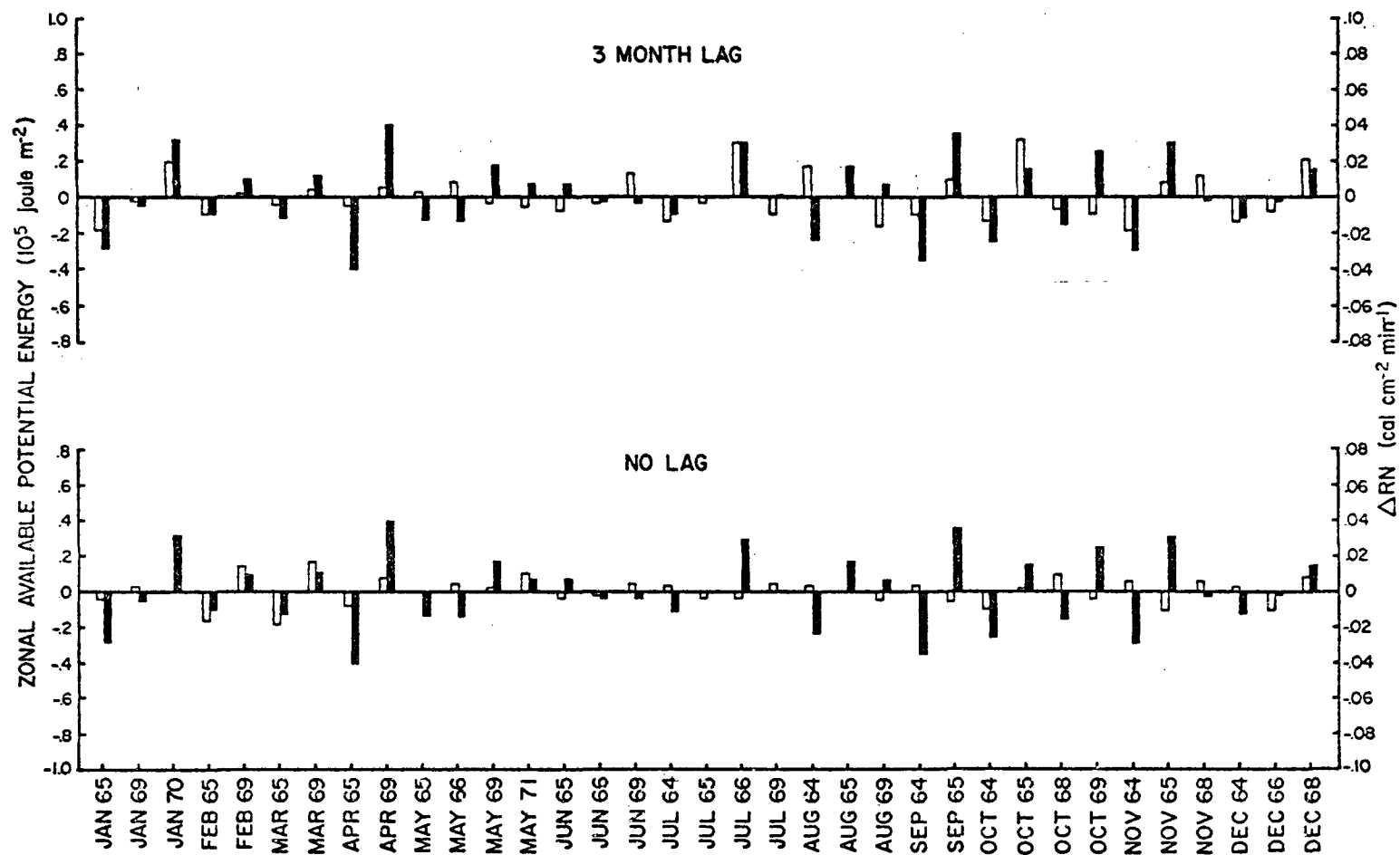


FIGURE 20. Correlation between interannual variations in net radiation gradient (black bars) and zonal available potential energy (light bars) with 3 months lag and no lag.

are within or are very near the bias error of $\pm 0.01 \text{ cal cm}^{-2} \text{ min}^{-1}$ (see section 2.3a) and, therefore, may not be relevant. Looking at the period, September-October, all but one sample shows positive correlation with a 3 month lag and all but one sample shows a negative correlation with no lag--a reverse relationship from what would be expected with the atmosphere-oceans decoupled (no lag) and coupled (3 month lag). Hence, the oceanic storage effect on the lag as hypothesized is not strongly apparent in the correlations.

Correlations are best when interannual variations in ΔRN and the circulation parameters are anomalously large in the same direction. Examination of the interannual variations in ΔRN and zonal kinetic energy with 3 month lag (Fig. 21) reveals a grouping of large anomalous $\Delta RN'$ in the fall pairing up with large anomalous zonal kinetic energy in winter. This same grouping is apparent, but to a lesser extent, with the other circulation parameters (inverse relationship with the eddy parameters). Therefore, it appears that the fall-winter relationship in the correlations is the prime contributor to the 3 month lag.

4.2 Interhemisphere Comparison

The $\Delta RN'$ for the northern hemisphere (solid line) are compared to the $\Delta RN'$ for the southern hemisphere (Fig. 22). All $\Delta RN'$ greater than the maximum bias error of $\pm 0.014 \text{ cal cm}^{-2} \text{ min}^{-1}$ are in phase between hemispheres except for the January months. The January 1970 irregularity is primarily contributed to by the January 1970 gradient anomaly; January 1970 was the month with a very large positive anomaly in the zonal kinetic energy.

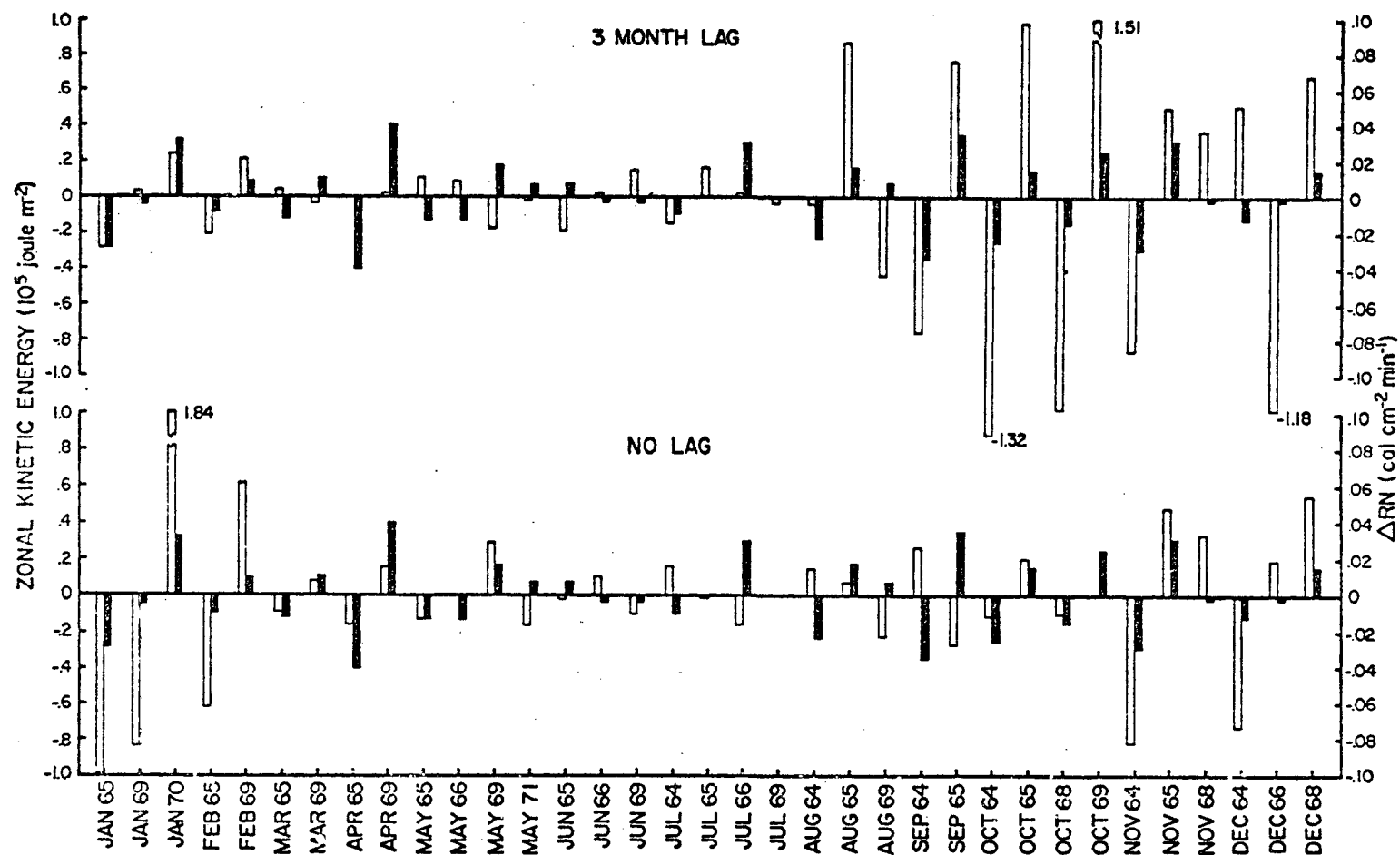


FIGURE 21. Correlations between interannual variations in net radiation gradient (black bars) and zonal kinetic energy (light bars) with 3 months lag and no lag.

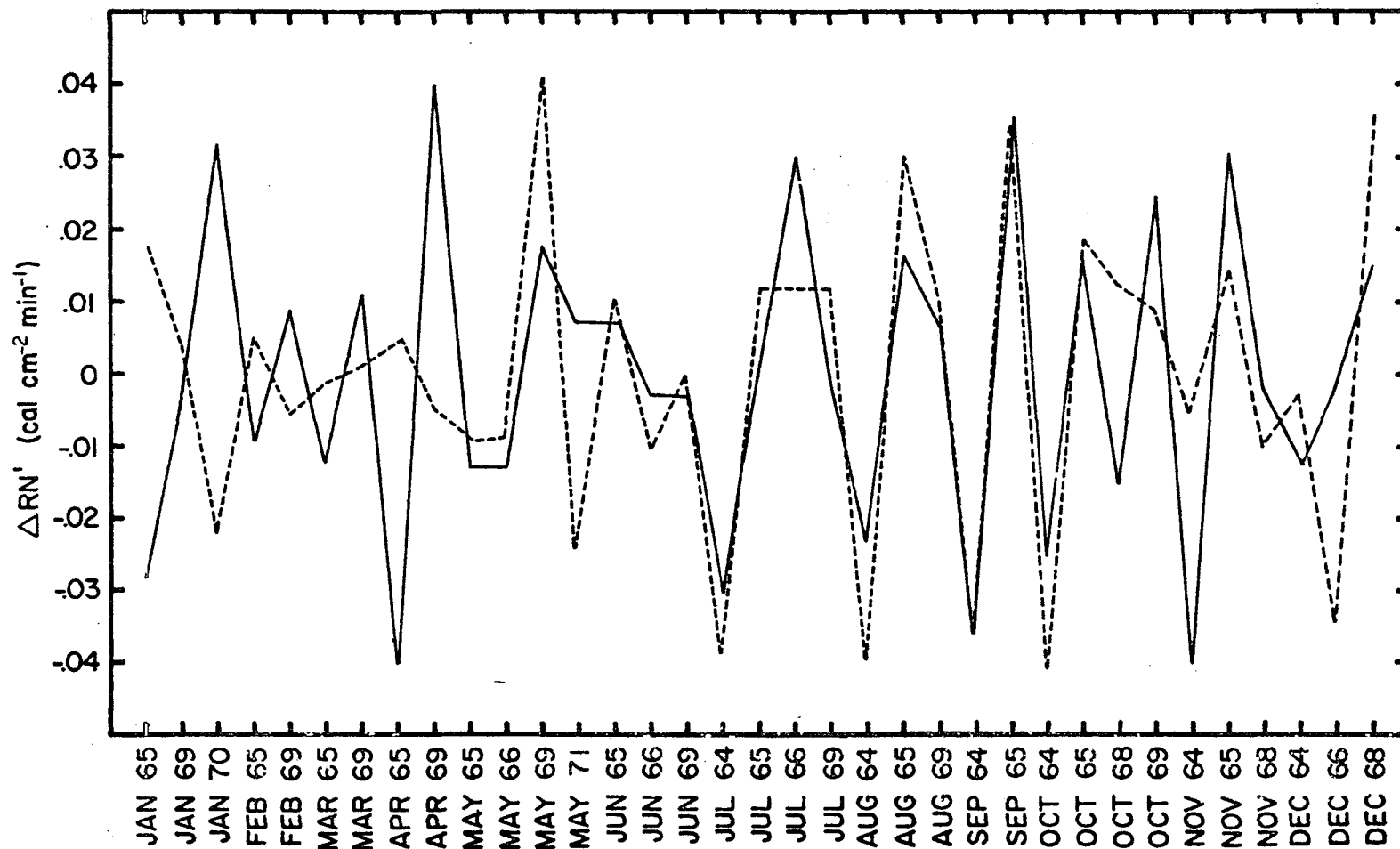


FIGURE 22. Temporal comparison between interannual variations in the net radiation gradient of the northern hemisphere (solid line) and the southern hemisphere (dashed line).

The in phase relationship appearing in the months of June through December implies either one or both of the following:

- (1) the net radiation budget of the tropical region, which is common to both hemispheres, is undergoing large year to year changes, or
- (2) the net radiation budget of both the north and south near polar regions are changing year to year with the same sign. The first of these possibilities is the most logical choice. However the cause cannot be isolated until all radiation data are normalized to eliminate the diurnal variation between data sets.

Regardless of the cause, the $\Delta RN'$ are in general, simultaneously large or small in both hemispheres. If a true relationship exists between $\Delta RN'$ and the general circulation, then one should expect to see a relationship in the year to year variations of the general circulation parameters between each hemisphere. An analysis of the general circulation of the southern hemisphere is needed to confirm such related variations.

4.3 Gradient and Cloudiness

A particular case, April 1965 compared to April 1969, has been selected for study. These two months comprised the strongest inter-annual variation in ΔRN for all the data sets. Allison et al. (1971) found minimum and maximum cloudiness in the eastern tropical Pacific for April 1965 and April 1969, respectively. The zonal averages of albedo were higher in April 1969 (25 percent) than in April 1965 (22 percent). These albedoes were reflected in the net radiation budget at 5N as $0.12 \text{ cal cm}^{-2} \text{ min}^{-1}$ for April 1969 and as $0.15 \text{ cal cm}^{-2} \text{ min}^{-1}$ for April 1965. Therefore, a stronger north-to-south

net radiation gradient would prevail with the less tropical cloudiness period of April 1965.

However, overcompensating changes took place at 65N so that the gradient was much stronger in the more tropical cloudiness period of April 1969. The change from April 1965 to April 1969 at 65N was an increase in both the albedo and longwave loss from 37 to 52 percent and 0.24 to $0.29 \text{ cal cm}^{-2} \text{ min}^{-1}$, respectively; thus, changing the radiation budget from 0.01 to $-0.10 \text{ cal cm}^{-2} \text{ min}^{-1}$. These changes in the later period (1969) could be indicative of above normal low and middle cloudiness at 65N.

For this particular case, changes in the near polar region had a greater effect on the gradient than the apparent extreme change in cloudiness in the tropical regions. All general circulation parameters relate positively to the April 1965 and April 1969 change in ΔRN (except for the eddy components which show inverse relationship) for both no lag and 3 month lags. The zonal index and zonal kinetic energy show a preference for a stronger positive relationship with no lag. Hence, the interannual variations in both ΔRN and general circulation parameters appear to be related in this particular case. So here is a case exemplifying the need for study in the near polar regions for a better understanding of anomalies in the atmosphere.

5.0 SUMMARY AND CONCLUSIONS

The pole to equator gradient of net radiation and the general circulation of the atmosphere were brought together in an interrelated study for the first time. Interannual variations in the gradient of net radiation and the intensity of the general circulation appear to be related.

In most cases when variations in the net radiation gradient were large, corresponding large anomalies were found in one or more of the general circulation parameters. However, the study was not restricted to extreme cases.

Statistical correlations between the gradient of net radiation and each of the general circulation parameters, with the annual cycle removed from each variable, were best when the general circulation parameters lagged the net radiation gradient by 3 months. Eddy available potential energy showed the best correlation at -0.73 followed by the thermal wind, zonal kinetic energy, zonal available potential energy, and eddy kinetic energy at +0.64, +0.56, +0.49, and -0.38, respectively. Statistical significant correlations were found at 16 to 18 months lag in all the circulation parameters but with an inverse sign from those at 3 months lag. A similar inverse trend appeared with a lead of 9 to 11 months. All correlations taken together show a wave with a wavelength of 26 to 27 months which is either 3 months or 9 to 10 months out of phase with the net radiation gradient. Additional satellite data are needed to ascertain the validity of this wave and the phase relationship.

This type of gradient can be obtained on a routine basis as satellite data becomes available. Providing these results continue to bear out, then such statistics will be a step forward towards the prediction of the general circulation on monthly and seasonal basis, a hurdle yet to be surmounted by the primitive equation models.

Future studies should investigate in more depth the role of cloudiness in the gradient of net radiation, and the feedback mechanisms relating the net radiation gradient, cloudiness, and the intensity of the general circulation.

REFERENCES

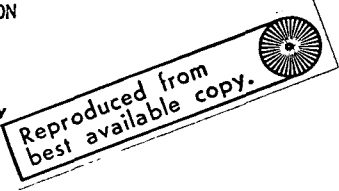
- Allison, L. J., J. Steranka, R. J. Holub, J. Hansen, F. A. Godshall, and C. Prabhakara, 1971: Air sea interaction in the tropical Pacific ocean. U. S. Dept. of Commerce N71-27648.
- Brier, G. W., 1969: Long range weather prediction of the zonal westerlies and some problems in data analysis. Rev. Geoph., 6, 4, pp. 525-551.
- Garstang, M. and T. R. Visvanathan, 1967: Solar and lunar influences on rainfall. Department of Meteorology, Florida State Univ., Tallahassee, Florida.
- Kutzback, J. E., R. A. Bryson, and W. C. Shen, 1968: An evaluation of the thermal Rossby number in the Pleistocene, Met. Mono., 8, 30, pp. 134-138.
- Landsberg, H. E., J. M. Mitchell, Jr., H. L. Crutcher and J. T. Quinlan, 1963: Surface signs of the biennial atmospheric pulse. Mon. Wea. Rev., 91, 10-12, pp. 549-556.
- MacDonald, T. H., 1969: Private communication.
- MacDonald, T. H., 1970: Data reduction processes for spinning flat-plate satellite-borne radiometers. ESSA Tech. Report NESC 52.
- MacDonald, T. H., 1972: Private communications.
- Miller, A. J., S. Teweles, and H. M. Woolf, 1967: Quasi-biennial cycles in angular momentum transports at 500 mb. Jour. Atmos. Sci., 24, 3, pp. 298-304.
- Namias, J., 1950: The index cycle and its role in the general circulation. Jour. of Met., 7, 2, pp. 130-139.
- Newell, R. E., D. G. Vincent, T. G. Dopplick, D. Ferruzza, and J. W. Kidson, 1969: The energy balance of the global atmosphere. AMS-RMS Joint Conference on Global Circulation of the Atmosphere, London, England.
- Oort, A. H., 1964: On estimates of the atmospheric energy cycle. Mon. Wea. Rev., 92, 11, pp. 483-493.
- Raschke, E., 1968: The radiation balance of the earth-atmosphere system from radiation measurements of the Nimbus II meteorological satellite. NASA TN D-4589.
- Raschke, E. and W. R. Bandeen, 1970: The radiation balance of the planet earth from radiation measurements of the satellite Nimbus 2. Jour. Appl. Met., 9, 2, pp. 215-238.

- Raschke, E., T. H. Vonder Haar, W. R. Bandeen, and M. Pasternak, 1971: The radiation balance of the earth-atmosphere system from Nimbus 3 radiation measurements. NASA TN (in press).
- Reiter, E. R., 1969: Atmospheric transport processes, Part I: Energy transfers and transformations. U. S. Atomic Energy Commission, TID-24868.
- Smith, W. L., 1972: Private communication.
- Vonder Haar, T. H., 1968: Variations of the earth's radiation budget, Ph.D. thesis, Department of Meteorology, University of Wisconsin, Madison, Wisconsin.
- Vonder Haar, T. H., and V. E. Suomi, 1969: Satellite observations of the earth's radiation budget. Science, Vol. 163, pp. 667-669.
- Vonder Haar, T. H. and V. E. Suomi, 1971: Measurements of the earth's radiation budget from satellites during a five-year period, Part I: Extended time and space means. Jour. Atmos. Sci., 28, 3, pp. 305-314.

THE ALBEDO OF SNOW IN RELATION TO THE SUN POSITION

Hans Clausen Korff
Meteorologisches Institut der Universität Bonn
present affiliation: Colorado State University

Thomas H. Vonder Haar
Colorado State University
Fort Collins, Colorado 80521



The temperature difference between the equator and the poles is a major factor in controlling the intensity of the frontal zone and thru this, the climate of the middle latitudes (Korff and Flohn, 1968). But due to the fact, that the temperature conditions in the tropics are very stable, one approach to the global problem is to concentrate on the heating processes in the polar zones. Fortunately, since the time of polar orbiting satellites we have a large amount of information about the radiation budget of these remote areas. For climatological purposes, however, the knowledge of the radiation of the system earth-plus-atmosphere is only the first step (Vonder Haar, Suomi, 1971). Next we have to examine the separate heat budget of the surface and of the atmosphere. This requires an estimate of the global radiation at the surface and generalized values for the albedo of snow in relation to sun position and cloudiness (Lettau, Lettau, 1969).

For information on this subject, radiation measurements were made over a snowfield at Pingree Park, Colorado in January and February 1972. The place is 2740 m high and located at 40° 34.1' N and 105° 35.5' W (U. S. Geological Survey, 1962). The horizon has a mean elevation of 11.1°, 7.5° at the point of sunrise and 9.5° at sunset.

For the observation of global and reflected radiation a set of Eppley black and white pyrrometers was used. For a perfect separation of the upper and the lower hemisphere and to avoid uncontrolled temperature gradients inside the instrument, two ventilated aluminum disks were mounted at the level of the sensors. The dependence of the output from the cosine law was checked (Hinzpeter, 1952) and found reasonable, compared with other instruments (Dirnhirn, 1959). The calibration was made by the shading method (WMO, 1971). An Eppley normal incidence pyrheliometer served as a reference instrument. In addition, the direct solar radiation and the turbidity of the atmosphere were derived from that instrument on cloud-free days (Peyinghaus, 1972).

The observation period lasted for ten days. During that time all types of sky condition occurred. As an example for a completely cloud-free day the 31st of January was chosen. At that time the snow at the site was dry, fine-grained and lightly windpacked. The global radiation that day was 327 ly, but only 77 ly were absorbed by the surface. This would not even compensate a mean effective longwave radiation of .06 ly/min. The actual infrared value, however, on a cloud-free day with an atmospheric water-content of .24 cm ppw and a turbidity factor 3 =

.01 is certainly higher (Geiger, 1961). So, if at all, we can expect a positive radiation balance at the surface only at noon time. The trend of global radiation and its components, as well as temperature and albedo for the 31st is shown in Fig. 1. That day the sun reached an elevation of 10° at 8:13 a.m., 20° at 9:23 a.m. and 32° at local noon (12:11 p.m.). In the afternoon it went down to 20° again at 3:00 p.m. and to 10° at 4:09 p.m.

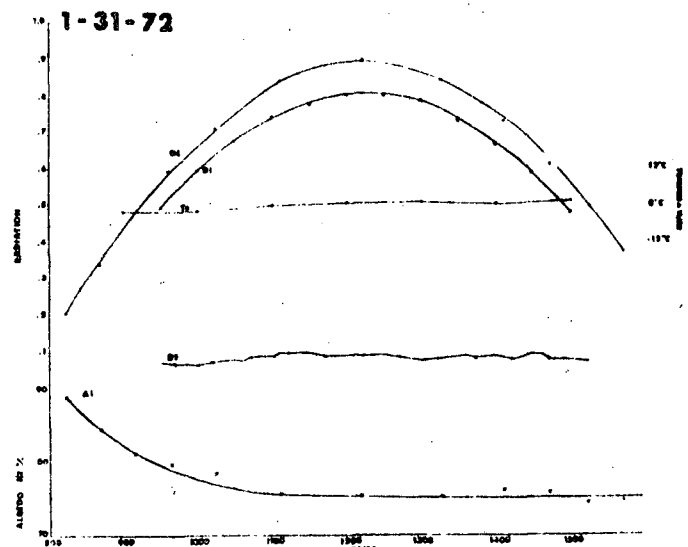


FIGURE 1: Radiation, temperature (T_e) and albedo (Al) on 31st of January, G_t - global radiation, D_i - direct radiation, D_f - diffuse radiation of the sky.

Completely different conditions were found on a cloudy day, for example, the 28th of January. The total global radiation just reached 81 ly and only 9 ly were absorbed by the snow. The maximum intensity did not exceed 13 ly/min and the albedo varied between 85 and 90%. There seemed to be a trend of albedo parallel to the sun elevation, but due to the low radiative intensity, the radiometer output was near the noise limit.

The question may be raised as to whether the properties of a snowfield in middle latitudes are equal to those in polar areas. A comparison with results from Antarctica of several authors lead to a positive answer. Only Hoinkes (1961) gives noticeably higher albedo values. Hanson (1968) however, covers our results completely with reflectivities from 74 to 83% for clear days with elevation angles around 20°. Due to the astronomical conditions

at the south pole, he could not give a daily trend. [This we get from Liljequist (1956), who observed the same asymmetric trend of albedo that we measured in Pingree Park (in December and January at Maudheim [71° S]). He explains it as an effect of metamorphosis of snow. In November he found a symmetric trend for morning and afternoon. Rusin (1964) shows the albedo in relation to sun elevation, but does not say whether these values were only observed in the morning or also in the afternoon.

The daily trend, however, must not be confused with the effect of longterm aging. While the latter causes a permanent decrease of albedo with the age of a snowfield, the daily trend does not lead to permanent change of the reflectivity. A strong case of aging is described by Kalitin (1930) who found a change of albedo from 80% to 50% in 10 days over a nonmelting snowfield near Leningrad. Scheibner and Mahringer (1968) found a drop of 10% during 10 days in the Alps and explained it with a pollution of the snow by rock dust. In Pingree Park, however, we only found a decrease of reflectivity of 1 - 2% after the first day of sunshine, caused by a packing of the snow (Dirmhirn, Trojer, 1955). Due to Hanson (1960), this is also the only process of aging found in Antarctica. So, for a generalization of the albedo, we can neglect it.

For a general daily trend we compare the albedo-values of different authors as given in Fig. 2. That our gradient is steeper than the others, might be caused by the fact, that the snowfield was inclined by about 2° towards SE. So we chose as a generalized value for clear days over a windpacked snowfield a reflectivity of 78% at a zenith distance of the sun of 60°. With an increasing distance of 10° we assume the albedo will decrease by 3.5%. This adopted line is not as steep as ours and lies between that of Rusin (1964) and Liljequist (1956). In the central area of Antarctica and Greenland we will use these values in the morning as well as in the afternoon. In the more marginal zones we take the noon value constant for the rest of the day. On cloudy days we will apply to an albedo-value of 89% all day long.

For processing measurements from the satellite NIMBUS Raschke et. al. (1972) used a curve based on Rusin's work. A comparison of the proposed generalized reflectivity and our results from Pingree Park is shown in Fig. 3. The data have been normalized against the value of 60° zenith distance. This makes it easier to use this graph also for other snow conditions than defined above, e.g. for new unpacked snow, where we observed a 5% higher reflectivity than usual.

ACKNOWLEDGEMENTS

Mr. J. Gailiun assisted with all field measurements, Mrs. P. Brant with preparation of the manuscript. Data were gathered at Pingree Park with the aid of members of the College of Forestry and Natural Resources, especially J. Meiman and V. Noonan. The research was supported by NASA under GRANT NGR-06-002-102.

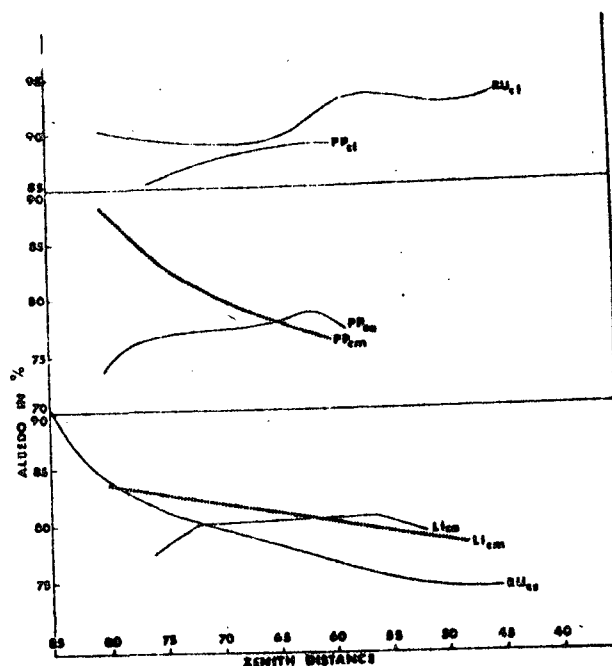


FIGURE 2: Daily mean trend of albedo for Pingree Park (PP), from Rusin (RU) and from Liljequist (LI). cm - clear morning, ca - clear afternoon, cs - clear sky, cl - cloudy sky.

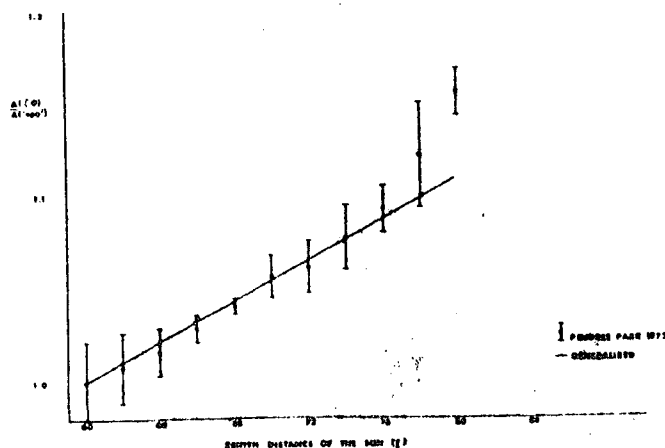
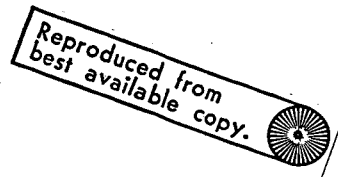


FIGURE 3: Trend of albedo relative to 60° with increasing zenith distance of the sun.

Reproduced from
best available copy.

REFERENCES

- Dirmhirn, I., 1959: Untersuchungen an Sternpyranometern. Arch. Met. Geoph. Biokl. B, 9, 124-148.
- _____ and E. Trojer, 1955: Albedountersuchungen am Hintereisferner. Arch. Met. Geoph. Biokl. B, 6, 400-416.
- Geiger, R., 1961: Das Klima der bodennahen Luftschicht. Braunschweig, Friedr. Vieweg & Sohn, 646 pp.
- Hanson, K. J., 1960: Radiation Measurement on the Antarctic Snowfield, a Preliminary Report. J. Geoph. Res., 65, 935-946.
- Hinzpeter, H., 1952: Bericht über neuere Arbeiten zum Solarimeter nach Gorczynski. Zeitschr. f. Met., 6, 118-121.
- Kalitin, N. N., 1930: The Measurement of the Albedo of a Snow Cover. Mon. Wea. Rev., 58, 59-61.
- Korff, H. C. and H. Flohn, 1968: Zusammenhang zwischen dem Temperaturgefälle Äquator - Pol und den planetarischen Luftdruckgürteln. Ann. Met. N. F., 4, 163-164.
- Lettau, H. and K. Lettau, 1969: Shortwave Radiation Climatology. Tellus, 21, 208-222.
- Liljequist, G. H., 1956: Energy Exchange of an Antarctic Snowfield. Norwegian - British - Swedish Expedition, 1949-52, Scientific Results, Vol. II, Part 1A, 11-109.
- Peyinghaus, W., 1972: Ein rechnerisches Verfahren zur Bestimmung der atmosphärischen Trübung aus Aktinometermessungen. Bonn, Meteorologisches Institut der Universität.
- Raschke, E., T. H. Vonder Haar, W. R. Bandeen and M. Pasternak, 1972: The Radiation Balance of the Earth - Atmosphere System from Nimbus 3 Radiation Measurements (15 April 1969 - 3 February 1970). NASA Tech. Note, in preparation.
- Rusin, N. P., 1964: Meteorological and Radiational Regime of Antarctica. Jerusalem, Israel Program for Scientific Translations, 355 pp.
- Scheibner, F. and W. Mahringer, 1968: Die Albedo der Sonnblickgletscher und ihre zeitlichen Variationen. Arch. Met. Geoph. Biokl. B, 16, 174-194.
- U. S. Geological Survey, 1962: Pingree Park Quadrangle. 7.5 Minute Series (Topographic), N 4030 - W 10530.
- Vonder Haar, T. H., V. Suomi, 1971: Measurements of the Earth's Radiation Budget from Satellites During a Five - Year Period. Part I: Extended Time and Space Means. J. Atmos. Sci., 28, 305-314.
- WMO (World Meteorological Organization), 1971: Guide to Meteorological Instrument and Observing Practices. Chapter 9: Measurement of Radiation and Sunshine. Geneva, 4th edition.



A STUDY OF EXTREME AND PERSISTENT CLOUDINESS
BASED ON SATELLITE OBSERVATIONS
(1969 - 1970)

by

Patrick H. Downey

Steven J. Lassman

Thomas H. Vonder Haar

May 1972

ABSTRACT

One of the biggest advances in meteorology on the global scale will be achieved in the near future with the routine launching of meteorological satellites with the capability of remotely sensing temperature and moisture profiles. At the present time, development has not proceeded to the point where a sounding may be made through thick cloud cover and hence, surface augmentation must be supplied to those areas of the globe with thick, prolonged cloud cover.

Many cloud atlases have been published using data from recent meteorological satellites. This paper is not an atlas; it gives the results of research conducted at Colorado State University into the problem of persistent cloudiness.

A year of brightness data from ESSA 9 and several months of data from ITOS 1 have been assembled and processed in such a manner that sequences of extensive, opaque cloudiness may be depicted. Results indicate that the observing system over the sparsely populated regions of the southern hemisphere should possibly use meteorological buoys to augment remote satellite sensing of the atmosphere. Locations for buoy deployment are noted.

Preceding page blank

ACKNOWLEDGMENTS

The authors wish to thank Roy Jenne and Stan Ruttenberg of the National Center for Atmospheric Research (NCAR) for co-sponsoring this study on the NCAR computer and also for their helpful thoughts and suggestions. We also appreciate the programming assistance received from Dennis Joseph at NCAR and the work of Lyn Koch in preparing this report.

This research was supported by the National Aeronautics and Space Administration under Grant NGR 06-002-12.

TABLE OF CONTENTS

	<u>page</u>
ABSTRACT	iii
ACKNOWLEDGEMENTS	iv
LIST OF FIGURES.	vi
Introduction	1
1.0 Data Availability and Reduction	2
2.0 Methodology	4
3.0 Application to the Global Study	6
4.0 A Look at the General Circulation on a Short Time Scale - March 1970	8
5.0 Northern and Southern Hemisphere Seasonal Summaries	12
6.0 Interannual Variations of Cloudiness.	18
7.0 Annual Summary.	20
8.0 SUMMARY	21
9.0 REFERENCES	22
APPENDIX	23

LIST OF FIGURES

1. Mean 700-mb (decameters) for March 1970
2. Mean 700-mb isotachs (meters per second) for March 1970
3. Percentage of Mean Monthly snowfall, March 1970
- A-1 Northern Hemisphere - Number of cloudy days March 1-31
- A-2 Northern Hemisphere - Maximum number of consecutive cloudy days March 1-31
- A-3 Northern Hemisphere - Number of occurrences of 3 consecutive cloudy days March 1-31
- A-4 Northern Hemisphere - Number of cloudy days December 1969, January 1970 and February 1970
- A-5 Northern Hemisphere - Number of occurrences of 3 consecutive cloudy days December 1969, January 1970 and February 1970
- A-6 Northern Hemisphere - Number of cloudy days March 1970, April 1969 and May 1969
- A-7 Northern Hemisphere - Number of occurrences of 3 consecutive cloudy days March 1970, April 1969 and May 1969
- A-8 Northern Hemisphere - Number of cloudy days June 1969, July 1969 and August 1969
- A-9 Northern Hemisphere - Number of occurrences of 3 consecutive cloudy days June 1969, July 1969 and August 1969
- A-10 Northern Hemisphere - Number of cloudy days September 1969, October 1969 and November 1969
- A-11 Northern Hemisphere - Number of occurrences of 3 consecutive cloudy days September 1969, October 1969 and November 1969

LIST OF FIGURES (Cont.)

- B-1 Southern Hemisphere - Number of cloudy days June 1969, July 1969 and August 1969
- B-2 Southern Hemisphere - Number of occurrences of 3 consecutive cloudy days June 1969, July 1969 and August 1969
- B-3 Southern Hemisphere - Number of cloudy days September 1969, October 1969 and November 1969
- B-4 Southern Hemisphere - Number of occurrences of 3 consecutive cloudy days September 1969, October 1969 and November 1969
- B-5 Southern Hemisphere - Number of cloudy days December 1969, January 1970 and February 1970
- B-6 Southern Hemisphere - Number of occurrences of 3 consecutive cloudy days December 1969, January 1970 and February 1970
- B-7 Southern Hemisphere - Number of cloudy days March 1970, April 1969 and May 1969
- B-8 Southern Hemisphere - Number of occurrences of 3 consecutive cloudy days March 1970, April 1969 and May 1969
- C-1 Southern Hemisphere - Number of cloudy days October 1969
- C-2 Southern Hemisphere - Number of cloudy days October 1970
- C-3 Southern Hemisphere - Number of occurrences of 3 consecutive cloudy days October 1969
- C-4 Southern Hemisphere - Number of occurrences of 3 consecutive cloudy days October 1970
- C-5 Southern Hemisphere - Number of occurrences of 3 consecutive cloudy days January 1970
- C-6 Southern Hemisphere - Number of occurrences of 3 consecutive cloudy days January 1971

LIST OF FIGURES (Cont.)

- D-1 Northern Hemisphere - Number of cloudy days (annual)
- D-2 Northern Hemisphere - Number of occurrences of 3 consecutive cloudy days (annual)
- D-3 Southern Hemisphere - Number of occurrences of 3 consecutive cloudy days (annual)
- D-4 Southern Hemisphere - Number of occurrences of 3 consecutive cloudy days (annual)

Introduction

Recent advances in the capabilities of meteorological satellites have made possible an objective, but as yet uncalibrated, nephanalysis. For many years vidicons on the ESSA series of satellites have provided brightness data which can be digitized and mapped over the entire globe on almost a daily basis. Since January 1967, an archive of brightness data has been maintained and is available on magnetic tape at the National Weather Records Center (NWRC), Asheville, North Carolina 28801.

A global cloud climatology would serve many meteorological purposes. However, the vidicon brightness data are suitable only for the detection of the brightest cloud masses. It is just this type of cloud that significantly interferes with vertical sounding of the atmosphere from satellites. Until microwave radiometers are used to overcome part of this cloud problem, it will be necessary to know which portions of the globe are inaccessible to remote sensing. Those selected portions of the globe with prolonged periods of thick overcast must have surface reports to complement the satellite sensor and round out a global observing system. If the present surface observation network does not sufficiently cover these areas of persistent cloud cover then a new surface observation network may be needed.

In addition to the application of the results of this study to the planning of a global observing system for the Global Atmospheric Research Program (GARP), motivation for the work arose equally:

- a) from the knowledge that cloud cover is the primary variable influencing changes in the earth's radiation budget, presently under study at Colorado State University (CSU), and
- b) because methods to parameterize the energy budget of our atmosphere must be heavily based on the occurrence of opaque cloudiness.

1.0 Data Availability and Reduction

The ESSA 9 satellite was launched February 26, 1969 by the National Aeronautics and Space Administration into a nearly circular, sun-synchronous polar orbit at an average altitude of 910 statute miles above the earth's surface. The orbit is inclined at 102° (retrograde) to the equatorial plane with an equatorial crossing of approximately 1430 local time.

The original vidicon data tapes received at NCAR (3 days of data per tape) had to be reduced in resolution for economic reasons. Digitized data from ESSA 9 is resolved each day into two 4096×4096 matrices, which present polar stereographic views of both Northern and Southern hemispheres. A 64×64 submatrix of this full resolution data corresponds to a Numerical Weather Prediction (NWP) grid. Thus, there are 4096 NWP grid squares per hemisphere. The term "meso-scale" refers to an 8×8 submatrix of the NWP grid square and, hence, has an area $1/64$ of an NWP grid square. Meso-scale data covers a 512×512 square grid per hemisphere which has a resolution that varies from 16 nautical miles at the equator to 32 nautical miles at the poles. Each meso-scale grid originally contained 64 data points with integral values from 0 (darkest) to 14 (brightest), representing a measure of the brightness of clouds, background, or a composite of both. The original brightness data with a range 0-14 was reduced at the National Environmental Satellite Center, into 5 equal classes from 1-5, thus achieving a threefold reduction in dynamic range prior to processing by CSU. Space reduction was achieved by combining the frequency distributions of 16 meso-scale data grid points, thus providing a $\frac{1}{4}$ NWP grid mesh resolution (190 km

at 60°N) for the present study. In a $\frac{1}{4}$ NWP there are 1024 data points (the population of the new frequency distribution). Those interested in a description of the tape format of the satellite data should consult Booth and Taylor (1968).

The original data tapes have now been reduced to a workable form consisting of 30 days data per tape. Checks were then made on the quality of the compressed data and a day classified as missing when:

- 1) A day is missing from the original meso-scale tapes,
- 2) a) The number of data records per day is >1028 or <1020 (there would normally be 512 data records per hemisphere),
b) More than 20% of the $\frac{1}{4}$ NWP grids have populations >1024 ,

and $\frac{1}{4}$ NWP's classified as missing when:

- 3) There are fewer than 5/16 meso-scale grids in a $\frac{1}{4}$ NWP,
- 4) The cumulative population of a frequency distribution for any $\frac{1}{4}$ NWP is ≤ 100 .

Using criteria 1 and 2, the following days have been deleted from the original data bank:

	<u>Julian Day</u>		<u>Julian Day</u>
April 6, 1969	96	November 5, 1969	309
April 27, 1969	117	November 6, 1969	310
May 18, 1969	138	November 11, 1969	315
July 15, 1969	196	December 1, 1969	335
August 6, 1969	218	December 19, 1969	353
August 12, 1969	224	January 8, 1970	8
August 26, 1969	238	February 1, 1970	32
August 27, 1969	239	February 4, 1970	35
August 30, 1969	242	February 21, 1970	52
August 31, 1969	243	March 1, 1970	60
September 11, 1969	254	March 14, 1970	73
September 17, 1969	260	March 15, 1970	74
October 10, 1969	283	March 21, 1970	80

2.0 Methodology

Miller (1971) converted brightness data to octas of cloud cover through the simple weighting scheme shown below:

Orig. Brightness Range	Class	Contribution to total cloud amount	Weights	
			October-May	June-Sept.
0, 1, 2	1	0%	0	0
3, 4, 5	2	25%	2	2.5*
6, 7, 8	3	88%	7	7.5*
9, 10, 11	4	100%	8	8
12, 13, 14	5	100%	8	8

* The summer and winter weights were applied according to the hemispheric season.

Miller's weighting scheme was designed to yield total cloud amount. We have not examined his results; however, the scheme would not be effective for determining opaque cloud cover because it weights clouds with low albedo (class 2). The values used in this study to determine opaque cloud cover are listed below:

Orig. Brightness Range	Class	Contribution to total opaque cloud amount	Weights ¹
0, 1, 2	1	0%	0
3, 4, 5	2	0%	0
6, 7, 8	3	100%	1
9, 10, 11	4	100%	1
12, 13, 14	5	100%	1

¹ Cloud cover in this study is not determined on an octal, but rather a binary (yes, no) basis.

Even after the new weighting scheme was applied, the brightness response on ESSA 9 still didn't yield a satisfactory simple correlation with opaque cloud cover. The problem arose from noise characteristics of the vidicon sensor used to determine the presence of clouds. For instance, if 1 of 1024 data points fell in class 1 or 2, then the entire $\frac{1}{4}$ NWP was considered clear. Thus, the final output allows 4% (41 of 1024) of the population to fall in class 1 or 2. This step is necessary primarily to correct for instrument dropout since allowing less than 4% tolerance yields output delineating only the ice caps.

Comparisons of the resultant cloud cover have been made with minimum albedo maps from Nimbus 3 to determine whether background noise (surface albedo) will bias the nephanalysis. As it turns out, with the weighting scheme above, the output yields results only for an equivalent albedo $\geq 35\%$. Thus, the only background problem exists in areas covered with ice and snow and the North African deserts.

More checks were made to determine the quality of the output by comparison with Nimbus 3 albedo maps, Miller's weighted output, actual surface observations over the United States, and actual cloud photographs. The results were encouraging and verified the fact that a 4% tolerance must be made for instrument dropout. Allowing more than tolerance would reveal larger areas of cloud cover but in reality, if allowance was made above the 4% threshold, the baby would be thrown out with the bath.

3.0 Application to the Global Study

Owing to the great potential offered by the possibility of remote sounding of the atmosphere, research has been directed toward determining areas of the globe which are subjected to persistent opaque cloudiness. Initial research into this problem centered around finding adjacent clusters of $\frac{1}{4}$ NWP grids with persistent cloudiness. It was found that most global cloud cover is transitory in nature with 5 day occurrences of cloudiness almost nonexistent. A maximum of 3 consecutive days of cloud cover was found to be an appropriate upper threshold when dealing with persistent cloudiness, but the fact that longer time intervals are possible have been taken into account in the final output.

Specifically, 3 parameters were used in this nephanalysis study:

- a) Maximum number of consecutive cloudy days (parameter 1)
- b) Number of occurrences of 3 consecutive cloudy days (reckoned as 1, 2, 3; 2, 3, 4; 3, 4, 5; etc.) (parameter 2)
- c) Total number of cloudy days (parameter 3)

All of the above have been examined for time intervals of 15, 30 (monthly), 90 (seasonal) and 365 (annual) days.

Clarification should be made at this point as to the dependence of strings of cloudy days on missing data. The first missing day in a $\frac{1}{4}$ NWP square is said to be cloudy (clear) if the preceeding day is cloudy (clear). Note that the following day does not enter into the decision. Given a second missing day in the same $\frac{1}{4}$ NWP, this day will always be considered clear and any string of cloudy days will be terminated. Several examples of this procedure are given on the next page:

☐ = cloudy

0 = clear

m = missing day

Day										Parameter	Parameter	Parameter	Total Days
1	2	3	4	5	6	7	8	9	10	1	2	3	Reported
☐	☐	☐	☐	0	0	0	☐	☐	☐	4	3	7	10
☐	☐	m	0	0	0	0	0	0	0	3	1	3	9
0	m	☐	☐	☐	☐	m	☐	☐	☐	8	6	8	8
0	☐	m	☐	0	☐	☐	m	0	0	3	2	6	8
☐	☐	m	☐	☐	☐	☐	☐	m	☐	8	6	9	8

4.0 A Look at the General Circulation on a Short Time Scale - March 1970

Many features of the general circulation can be seen by looking at the March 1970 cloud cover, Fig. A-1. The number of cloudy days over the Eastern U. S. was well above normal which correlates well with the mean trough position shown in Fig. 1. In the Pacific, wind speeds were as much as 14 m sec^{-1} faster than normal along a jet maximum that was located very near the March normal (Fig. 2) and thus accounts for the cloudiness seen in the mid-Pacific. The east coast of mainland China was frequented by copious cloudiness of prolonged duration (Figure A-2 and A-3), which can be explained by a major stationary trough in the western Pacific (Fig. 1). The Himalaya Mountains which have a high albedo due to snowpack in the spring are depicted well in Figures A-1, A-2, and A-3. Even though thin cirrus clouds do not have a high enough albedo to appear in this study, areas with large intertropical convergence and thick cloud cover appear in the western Pacific from $1-6^{\circ} \text{ N}$ (Fig. A-1).

Temperatures in the U. S. were below normal in March 1970 because the mean storm track was much further south than normal (Fig. 2). Highest percentages of normal precipitation were generally consistent with the southward track of synoptic scale cyclones. Heavy precipitation combined with below normal temperature anomalies, produced exceptionally heavy snowfall throughout most of the eastern three-fourths of the U. S. (Fig. 3). Undoubtedly the albedo of this abnormal snowfall accounts for most of the "cloudy" days over the U. S. (Fig. A-1) during this time period, as strong and persistent background brightness of ice, sand and snow are similar to the brightness of extremely cloudy areas.

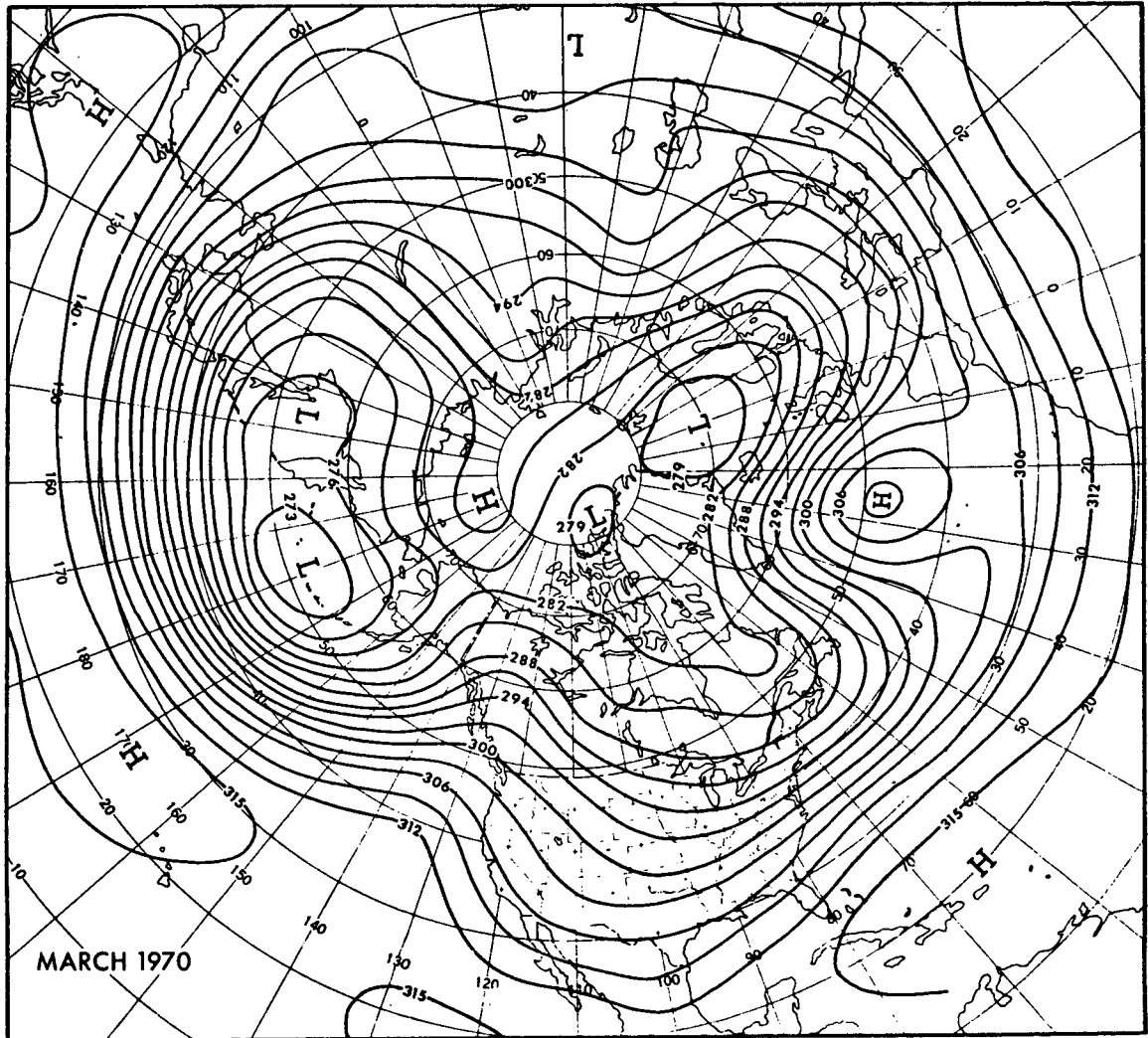


FIGURE 1 -- Mean 700-mb contours (decameters) for March 1970.
(after Green 1970).

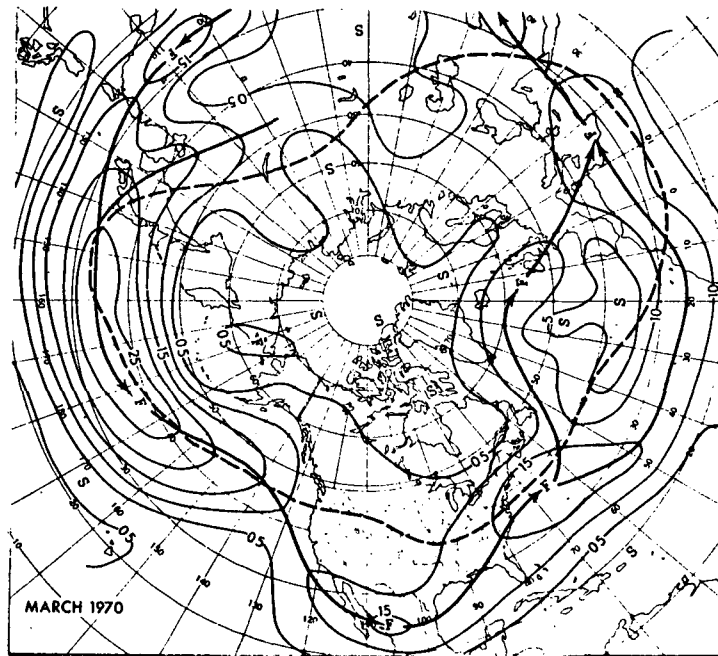


FIGURE 2 -- Mean 700-mb isotachs (meters per second) for March 1970. Heavy arrows indicate axes of maximum wind speed, dashed line the normal. (after Green 1970).

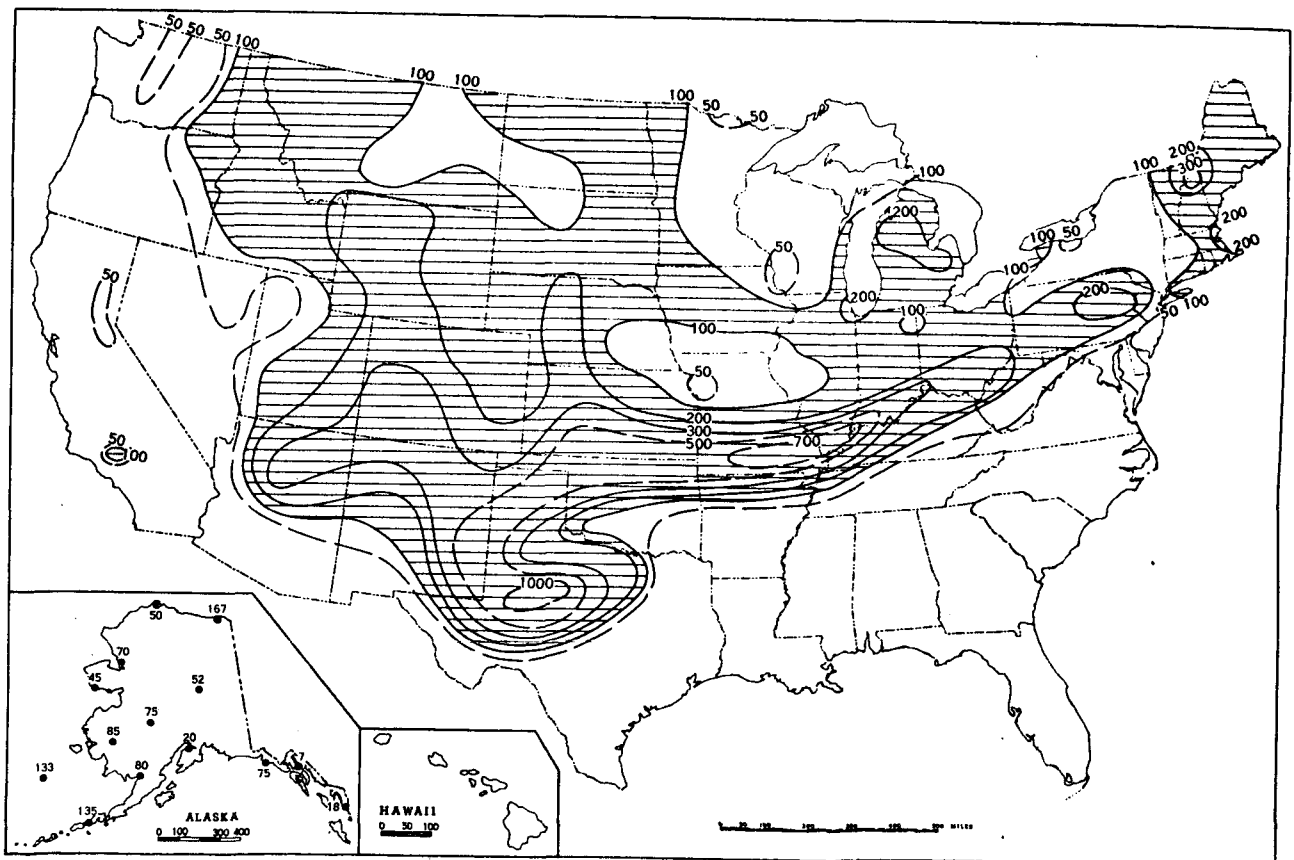


FIGURE 3 -- Percentage of Mean Monthly Snowfall, March 1970 (after U. S. Dept. of Commerce, 1970).

Background also accounts for most of the "cloudy" days poleward of 50°N during this month. Geographical features such as the deserts of Saudi Arabia and North Africa, and the Greenland ice cap (Fig. A-1, A-2 and A-3) are clearly delineated. Noticeably clear areas exist over regions dominated by the subtropical highs in the Atlantic and Pacific oceans.

Note should be made that May, June and July 1969 not only portray desert areas very poorly, but cloud cover too. This discrepancy is due to instrument degradation of the Advanced Vidicon Camera System (AVCS) aboard ESSA 9. Taylor and Winston (1968) have shown how brightness values can vary substantially with time due to changes in camera calibration and degradation in camera response.

5.0 Northern and Southern Hemisphere Seasonal Summaries

Northern Hemisphere - Winter (December, January and February)

Caution must be exercised when analyzing the winter season because of the magnitude of the background problem, as grid locations poleward of 40°N may actually have more background reported than actual cloud cover. Equatorward of 40°N one can immediately detect the mean location of the subtropical highs and also the Intertropical Convergence Zone (ITC) (Fig. A-4). The total number of cloudy days and also the persistence of cloud cover in the ITC is not as great as one would anticipate due to the poor reflectivity and variability of the cirrus cloudiness in this region (Fig. A-4 and A-5). Thick persistent cloud cover may be detected in the regions of climatological troughing (Gulf of Alaska, East China and the east coast of the U. S.). Up to 23 occurrences of 3 consecutive days of cloudiness were detected in the Gulf of Alaska and 12 off the China coast. The maximum of cloud cover over the Pacific may be attributed to the jet stream which was centered around 40°N .

Spring (March, April and May)

Climatology predicts the strengthening of the subtropical highs in the Spring. This theory can readily be verified from Fig. A-6 which shows that vast areas of the Atlantic and Pacific are cloud free. Less persistent cloud cover in the ITC (see Fig. A-7) is evidenced in spring than was present in winter. Trough positions remain in approximately the same location as they were in winter, but the jet stream over the Pacific has exhibited a 5° meridional migration toward the pole. The persistent

cloud pattern has greatly diminished in intensity with a maximum of 14 occurrences of 3 consecutive days of cloudiness off the China coast and only 3 occurrences in the Gulf of Alaska.

Summer (June, July and August)

One of the major summertime features of interest is the Indian/Southeast Asia monsoon caused by an inflow of moisture from sea toward land. Fig. A-8 and A-9 show a greater persistence and total cloud cover over this region than could be seen in winter or spring. With the subtropical high a maximum, the troughs are at a minimum and this is reflected by a drastic reduction of cloudiness over China, the Gulf of Alaska and the western Atlantic. Another explanation of the weak seasonal response is the degradation of the AVCS units which were brought back to original specifications in late July. Mention should also be made of the slight northward movement of the ITC and the jet stream. Some stratus type cloudiness is in evidence from the west coast of Central America to southern California consisting of 20 days of opaque cloudiness which has a maximum of 6 occurrences of 3 consecutive cloudy days. Background noise at higher latitudes is much reduced over wintertime conditions.

Fall (September, October and November)

Autumnal cloud cover shows a marked change from the summertime pattern just discussed. Fig. A-10 and A-11 depict an abrupt transition in

progress. Some persistent cloud cover still lingers over India and Southeast Asia, while the troughs reassert themselves over the east coast of China, the Gulf of Alaska and the western Atlantic. The ITC has strengthened in total cloud amount but not in persistence as winter approaches. Fall is the hurricane season and the increased oceanic cloud cover may be attributed to these devastating storms. Stratus remains off the Central America and California coast, but will rapidly fade with the onset of winter. The most persistent cloudiness appears just south of Greenland where there were 20 occurrences of 3 consecutive cloudy days. Finally, one can detect a southward movement in the jet stream, especially over the Pacific.

Southern Hemisphere - Winter (June, July and August)

Climatology would predict an intensification and extension of the subtropical high during winter. Coupled with poor AVCS response for this same time period in the northern hemisphere, one would expect little cloudiness. This is readily apparent from the information displayed in Figures B-1 and B-2.

Perhaps most obvious from these figures is the stratus cloudiness off the west coasts of Africa and South America. Figure B-1 shows a maximum of 27 cloudy days off the African coast and 31 days off the South American coast. This cloud cover displays a tendency toward being persistent with up to 14 occurrences of 3 consecutive cloudy days. One may also note that this type of cloudiness, associated with oceanic upwelling, is present to a much smaller extent in the other seasons.

Previous estimates by Lamb (1958) point out that the Antarctic ice field would not extend equatorward of 60°S during the winter. At first glance one would tend to attribute the circumpolar brightness to background, but since Lamb has shown this region to be free of ice, one must attribute the brightness response to the intense circumpolar trough. More persistent cloud cover is seen in the area bounded by 10°E - 50°W and 50° - 60°S than at any other southern hemisphere location during this season (Figure B-2). Other regions of the southern hemisphere are nearly void of persistent cloudiness and should not pose a problem for remote sensing of the atmosphere.

A comet shaped cloud pattern in the Pacific is distinguishable in all four seasons. This type of formation represents the stagnation of frontal systems and a large area of surface convergence. These stagnant systems dissipate after several days, providing little persistent cloud cover with a maximum of 6 occurrences of 3 consecutive days of opaque cloudiness.

Some convective cloudiness is visible in the region 1 - 10°S and 70° to 100°E , accounting for 20 cloudy days, but only 7 occurrences of 3 consecutive cloudy days.

Spring (September, October and November)

Continental heating is beginning to increase convective activity over Africa and South America while other features closely resemble the winter season (see Figures B-3 and B-4). An apparent deepening in the circumpolar trough which may actually be due to improved AVCS response has achieved more cloudiness in the latitude belt 50 - 60°S ,

but as in the winter season, the most persistent cloudiness appears in the region bounded by 10°W - 30°E and 50 - 60°S .

In the Pacific, the comet type pattern of cloud cover still exists but is predominantly transient in nature showing a maximum of 8 occurrences of 3 consecutive cloudy days. Cloudiness has increased considerably off the southeast coast of South America with a maximum of 30 cloudy days, but this cloudiness too is transient in nature with a maximum of 8 occurrences of 3 consecutive cloudy days.

Summer (December, January and February)

Most noticeable on the summer representation is the lack of stratus clouds off the coasts of South America and Africa (Figures B-5 and B-6). As expected, convection over the continental areas is a maximum while the bulk of the cloudiness over the Pacific has moved westward leaving a vast area of the eastern Pacific void of any cloudiness whatsoever. Much more equatorial development is present during the summer season, but it generally lacks any persistent nature.

Cloudiness in the circumpolar trough which has weakened somewhat from its winter maximum has remained constant with regard to the total number of cloudy days, but has become less persistent than previous months with only selected locations showing more than 10 occurrences of 3 consecutive cloudy days.

Fall (March, April and May)

Perhaps the best time to conduct remote sensing experiments would be in the southern hemisphere fall. The number of cloudy days on a hemispheric scale has been drastically reduced (Fig. B-7) and the areas of persistent cloudiness (Figure B-8) are almost non-existent.

In general, the same features of the general circulation are present in the fall as in the other seasons. Stratus clouds are beginning to appear off the South American and African coasts, the minor Pacific trough has induced some cloudiness and there is still some convective cloudiness over the continental regions.

6.0 Interannual Variations of Cloudiness

Also processed were 3 additional months of data (Oct. 1970, January and July 1971) from the Improved Tiros Operational Satellite (ITOS 1) to provide a check on the interannual variations of opaque cloudiness. Like the ESSA 9 satellite, ITOS 1 employs the AVCS system and has a local time equator crossing of about 1500 L. In general, the ITOS 1 vidicon was more responsive than the ESSA 9 vidicon, requiring some calibration to bring the two vidicons into synchronization. This was accomplished by allowing no tolerance for instrument dropout in brightness intervals 1 and 2 on the ITOS 1 data.

October 1969 vs October 1970

Comparison of the interannual variation of cloud cover may be made from Figures C-1 and C-2, between October 1969 and October 1970 in the southern hemisphere. The general features are very similar with convection over the continents and in the equatorial region from 80° - 100° E, stratus cloudiness off the coasts of South America and Africa, Pacific cloudiness and cloudiness associated with the circumpolar trough. The interannual variations of persistent cloudiness (Figures C-3 and C-4) show a greater variation than one would expect. While the stratus cloudiness has increased in persistence off the coasts of Africa and South America, there is a marked decrease in persistence near the circumpolar trough in October of 1970.

January 1970 vs January 1971

A striking similarity exists in the persistence of cloudiness during the southern hemisphere summer between January of 1970 and January of 1971. (see Figures C-5 and C-6). Primarily the difference can be found in the equatorial region from 170°W - 160°E . No explanation is offered as to why there was more convection in this region during the summer of 1970.

July 1970 vs July 1971

July would make for a poor comparison of interannual variations of cloudiness owing to the weak response of both AVCS cameras on ESSA 9, so no attempt will be made to make such a comparison even though such data is available.

7.0 Annual Summary

Northern Hemisphere

On an annual basis, background noise is particularly hard to distinguish from cloudiness. The northern latitudes in Figures D-1 and D-2 reveal not only the maximum opaque cloudiness but also the most persistent. Caution should be used in interpreting this data because the annual summary is actually an annual average, i.e., the four seasonal summaries have been summed and divided by four to give the resultant data. Hence, this data is actually a seasonal average and not an annual summary.

The ITC which is clearly visible in Figure D-1 is absent from Fig. D-2. This area then would pose little problem to remote sounding of the atmosphere. Near New Foundland one can see 12 occurrences of 3 consecutive cloudy days, probably due to stratus cloudiness which in general has low tops, and would not pose a serious problem to remote sensing.

Southern Hemisphere

Background is not nearly the problem in the southern hemisphere as it was in the northern hemisphere and thus the southern hemisphere is a better indicator of true cloudiness. Figures D-3 and D-4 indicate vast amounts of cloudiness but little persistent cloud cover outside of the circumpolar trough. It is evident that the region 50° - 60° S will present a serious problem for remote sounding of the atmosphere.

8.0 Summary

Caution must be exercised with regard to the ESSA vidicon data as AVCS degradation and apparent lack of calibration would preclude the use of this data for many meteorological purposes. This study was completed only after a careful comparison between the ESSA 9 and Nimbus 3 data revealed a general correlation between regions of extreme ESSA brightness (binary indicators) and Nimbus albedo. This relationship denies however, the capability to distinguish background from true cloud cover. Yet another shortcoming of the AVCS data is the failure to distinguish cloud tops - a serious consideration in many meteorological applications. A more appropriate approach would take into consideration simultaneous use of infrared radiation measurements with the reflected solar radiation data (Vonder Haar, 1970).

In short, this study has been designed to give an overall view of the seasonal course of persistent opaque cloudiness. Results must be carefully reviewed to take into account background response which simulates actual cloudiness. It was found that in the northern hemisphere an annual summary is not really a sufficient summary because of the high seasonal variation of albedo. On the other hand, the southern hemisphere annual summary is much more indicative of true opaque cloudiness which seems to be most persistent in the circumpolar trough 50 - 60°S.

Throughout the text, comments regarding occurrence of persistent opaque cloudiness as a function of time and location have a variety of meteorological applications.

9.0 References

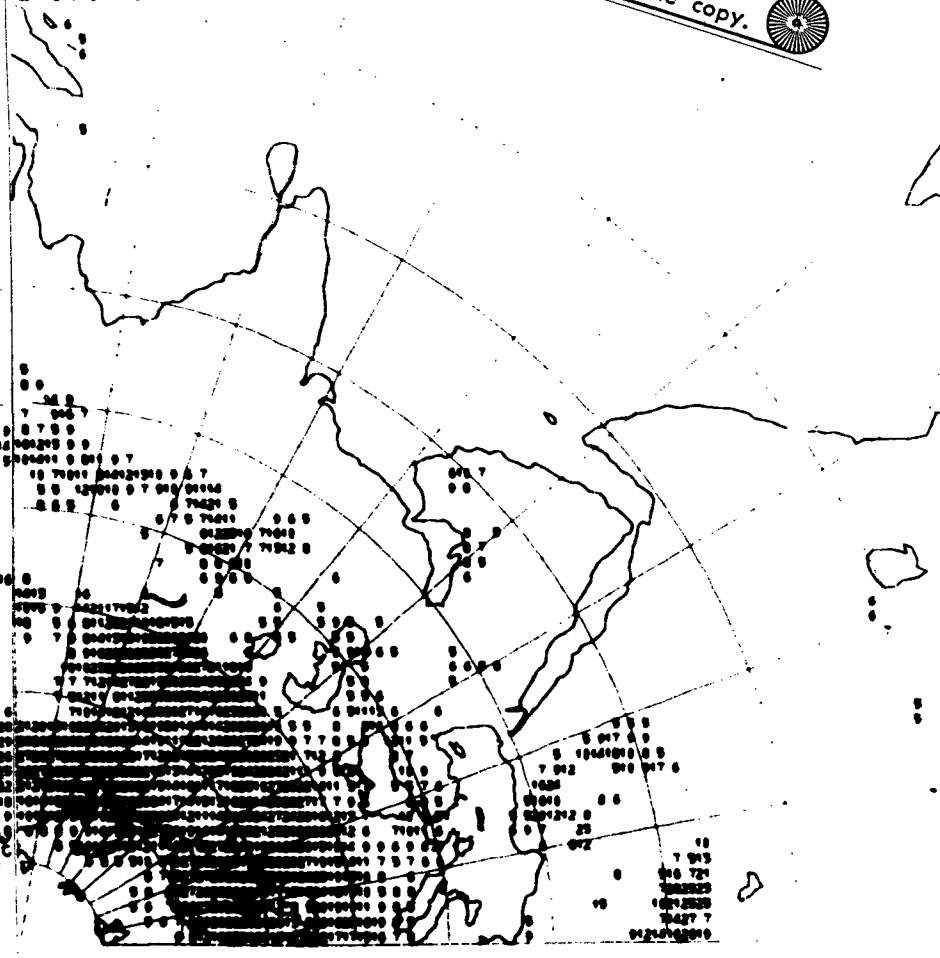
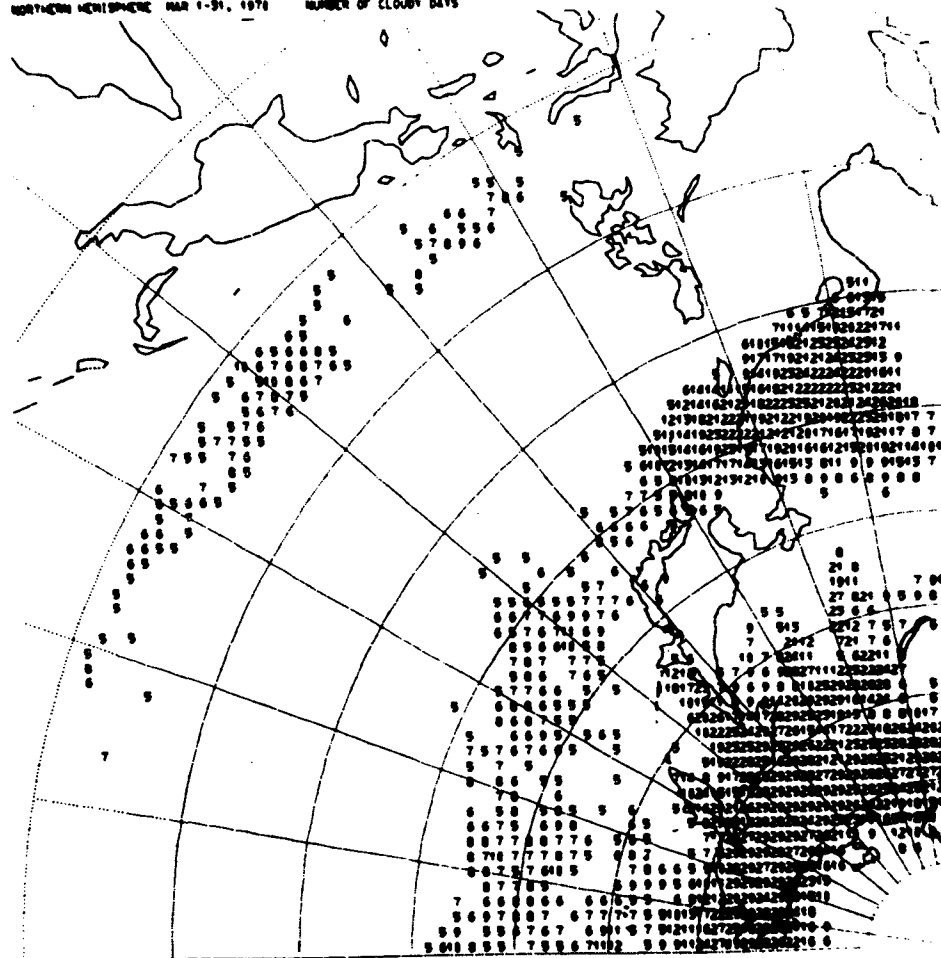
- Booth, A. L. and V. R. Taylor: "Meso-scale archive and products of digitized video data from ESSA satellites", ESSA Technical Memorandum NESCTM-9, National Environmental Satellite Center, Suitland, Maryland, October 1968.
- Green, R. A.: "The weather and circulation of March 1970", Monthly Weather Review, 98, 6, June 1970, pp. 480-485.
- Lamb, H. H.: "Differences in the meteorology of the Northern and Southern polar regions", Meteorological Magazine, 87, 1038, December, 1958, pp. 364-379.
- Miller, D. B.: Global Atlas of Relative Cloud Cover 1967-70, U. S. Department of Commerce, Washington, D. C., September 1971.
- Taylor, V. R. and Winston, J. S.: "Monthly and seasonal mean global charts of brightness from ESSA 3 and ESSA 5 digitized pictures, February 1967 - February 1968", ESSA Technical Report NESC 46, National Environmental Satellite Center, Suitland, Maryland, 1968, 18 pp.
- United States Department of Commerce: Monthly Climatic Data for the World, 23, 3, Marcy 1970.
- Vonder Haar, T. H.: "Application of simultaneous infrared radiation measurements and cloud photographs from satellites", Journal of Applied Meteorology, Vol. 9, No. 6, December 1970, pp. 955-958.

APPENDIX

NORTHERN HEMISPHERE MAR 1-31, 1978 NUMBER OF CLOUDY DAYS

NORTHERN HEMISPHERE MAR 1-31, 1978 NUMBER OF CLOUDY DAYS

Reproduced from
best available copy.



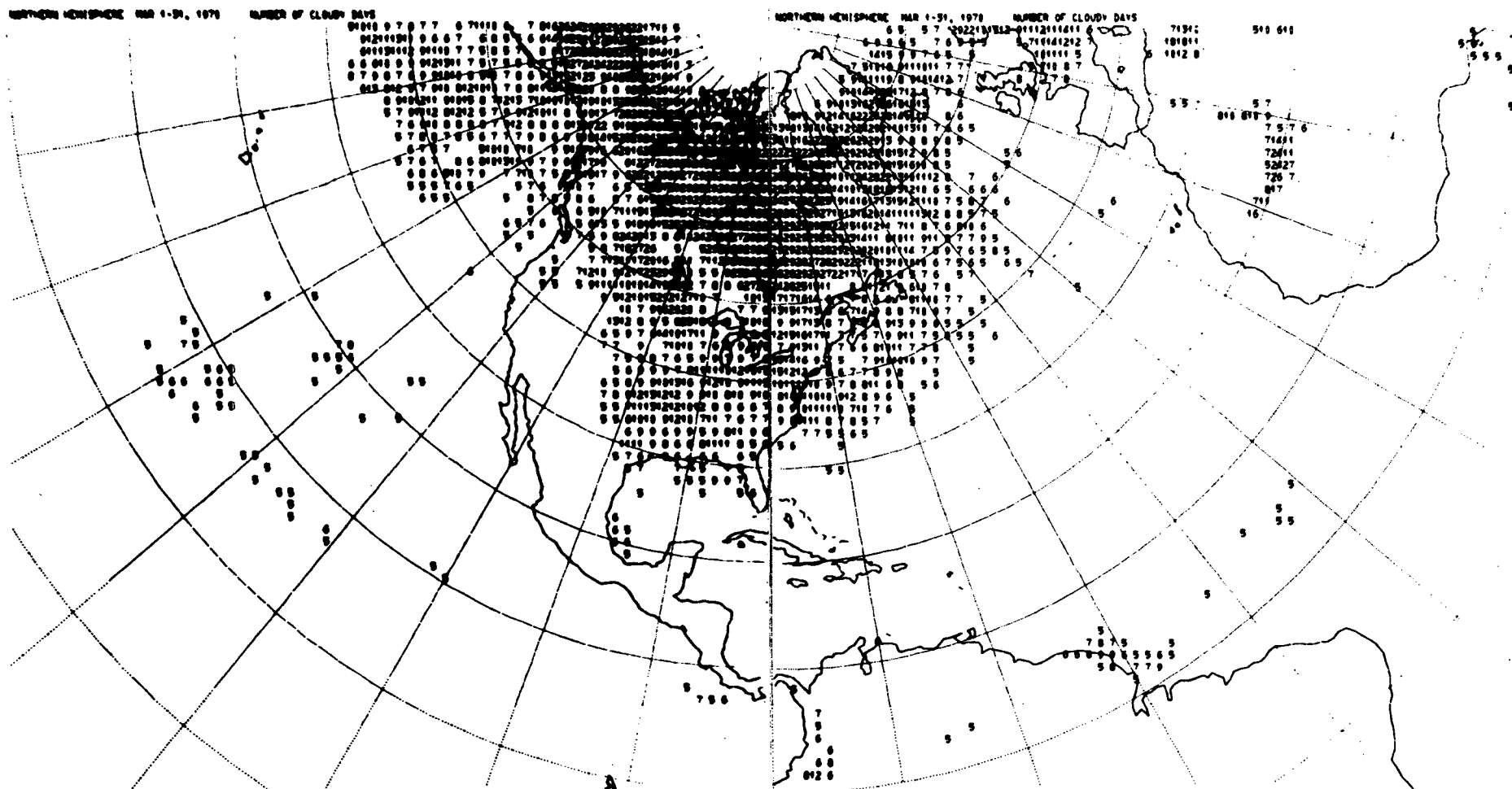
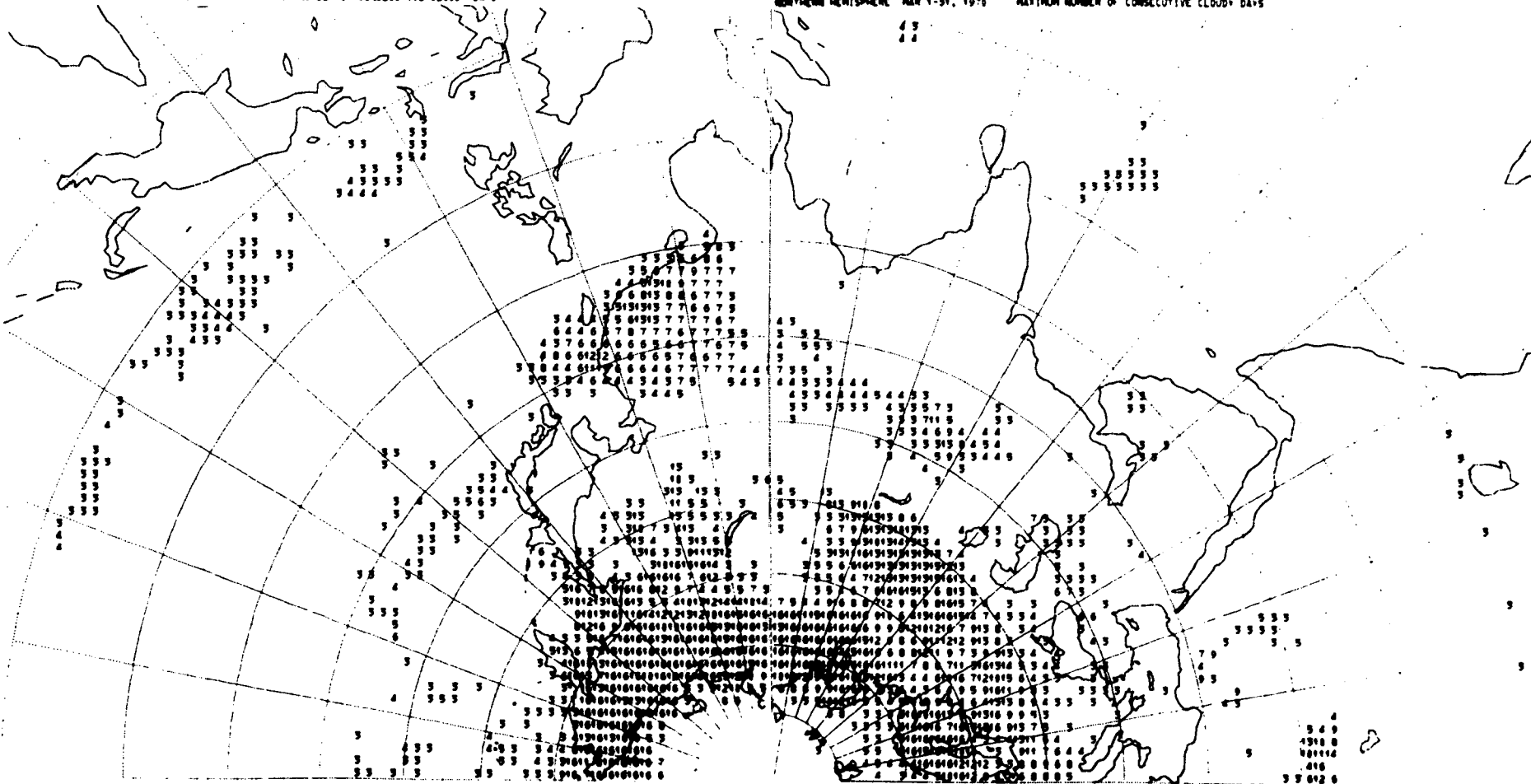


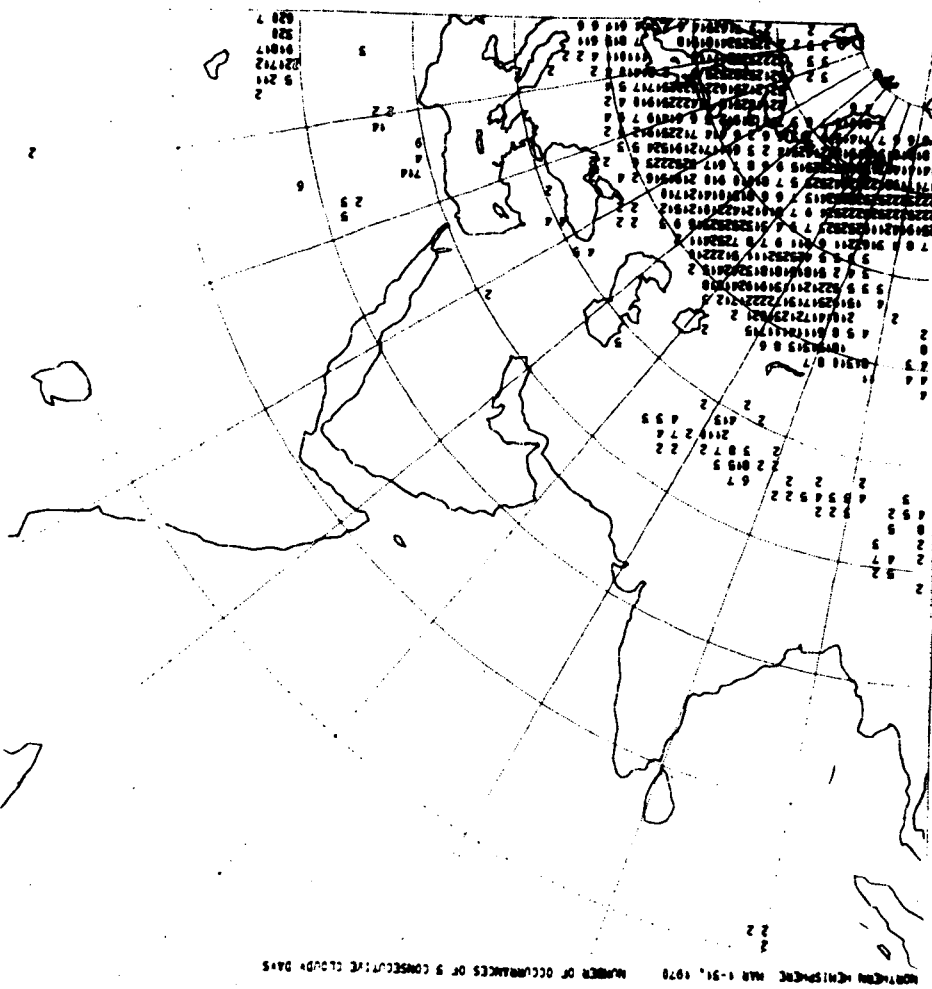
FIGURE A-1: Number of cloudy days March 1-31

NORTHERN HEMISPHERE MAR 1-31, 1970 MAXIMUM NUMBER OF CONSECUTIVE CLOUDY DAYS

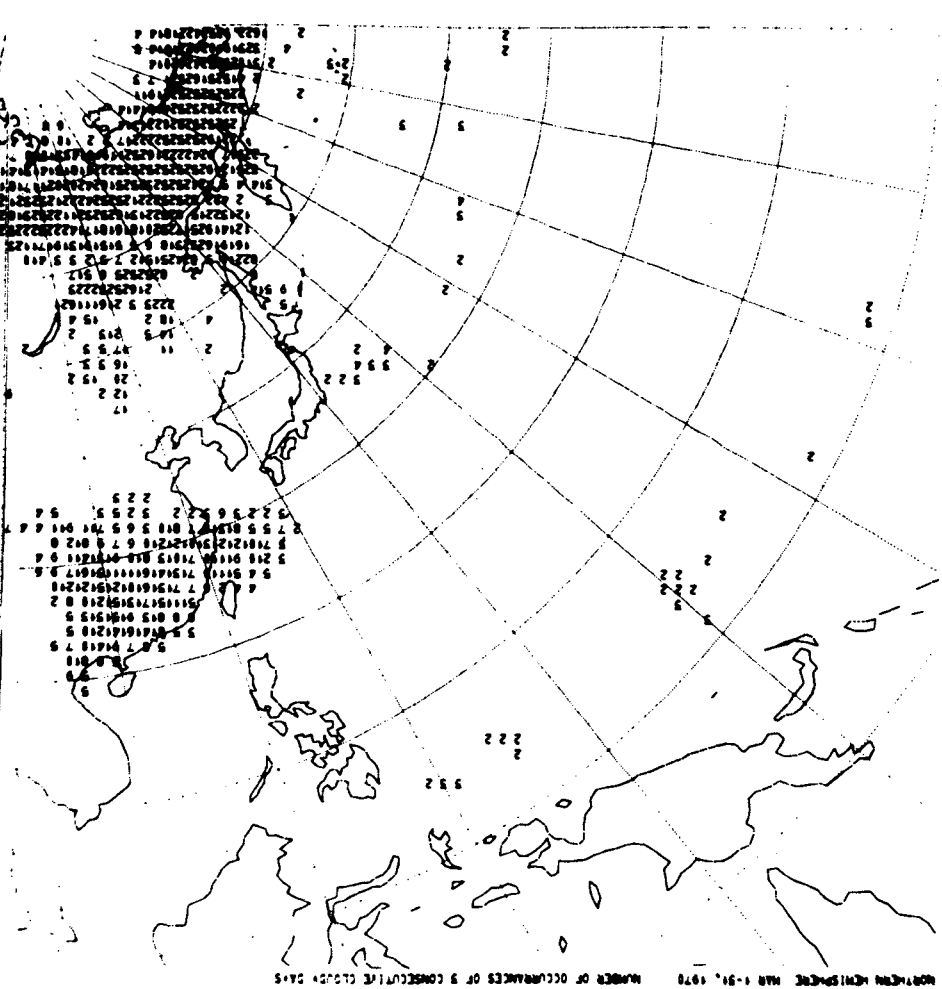
NORTHERN HEMISPHERE MAR 1-31, 1970 MAXIMUM NUMBER OF CONSECUTIVE CLOUDY DAYS



NORTH HEMISPHERE JAN 1-31, 1970
NUMBER OF OCCURRENCES OF 9 CONSECUTIVE CLOUDY DAYS

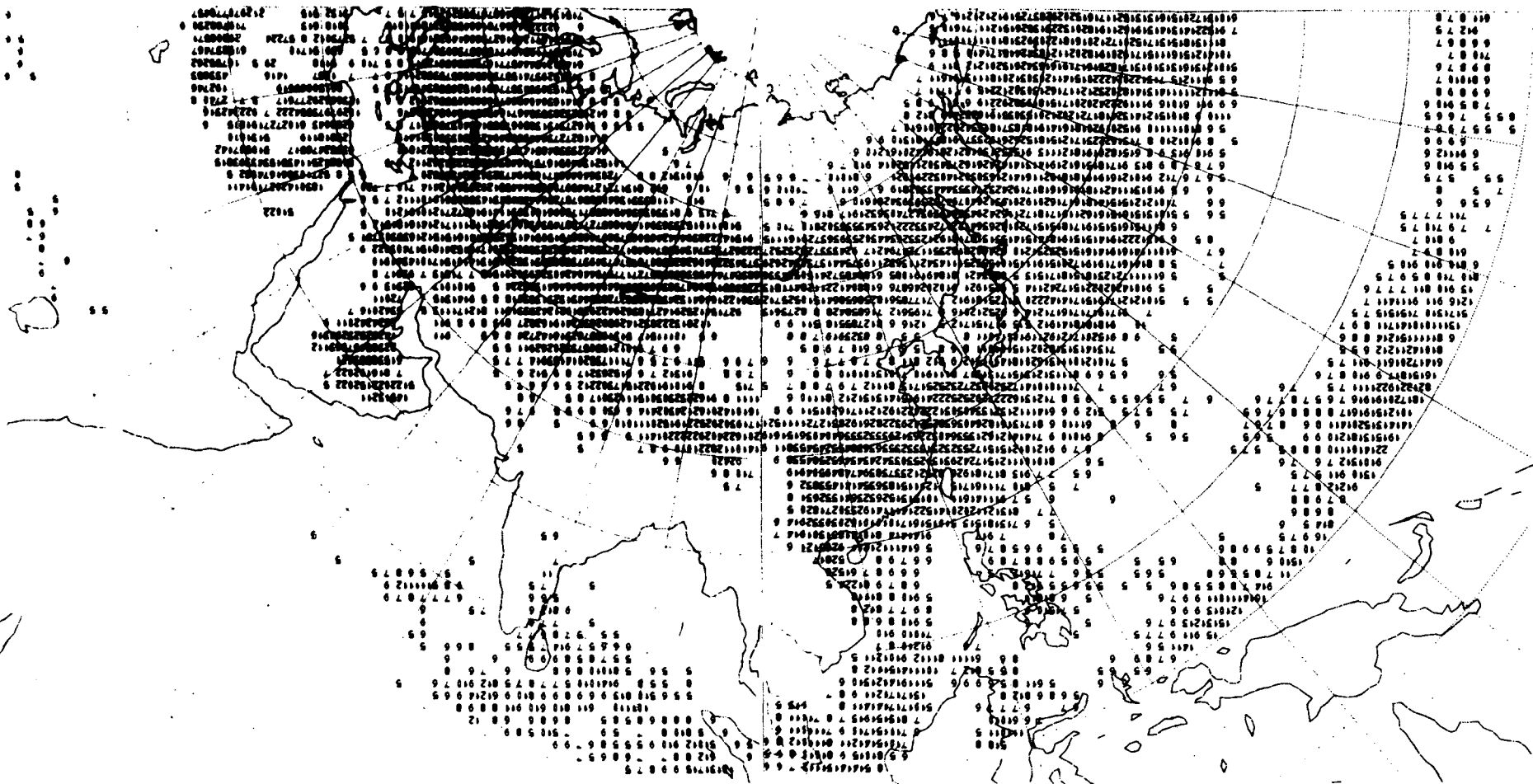


NORTH HEMISPHERE JAN 1-31, 1970
NUMBER OF OCCURRENCES OF 9 CONSECUTIVE CLOUDY DAYS



NORTHERN HEMISPHERE DECEMBER JANUARY FEBRUARY

NORTHERN HEMISPHERE DECEMBER JANUARY FEBRUARY



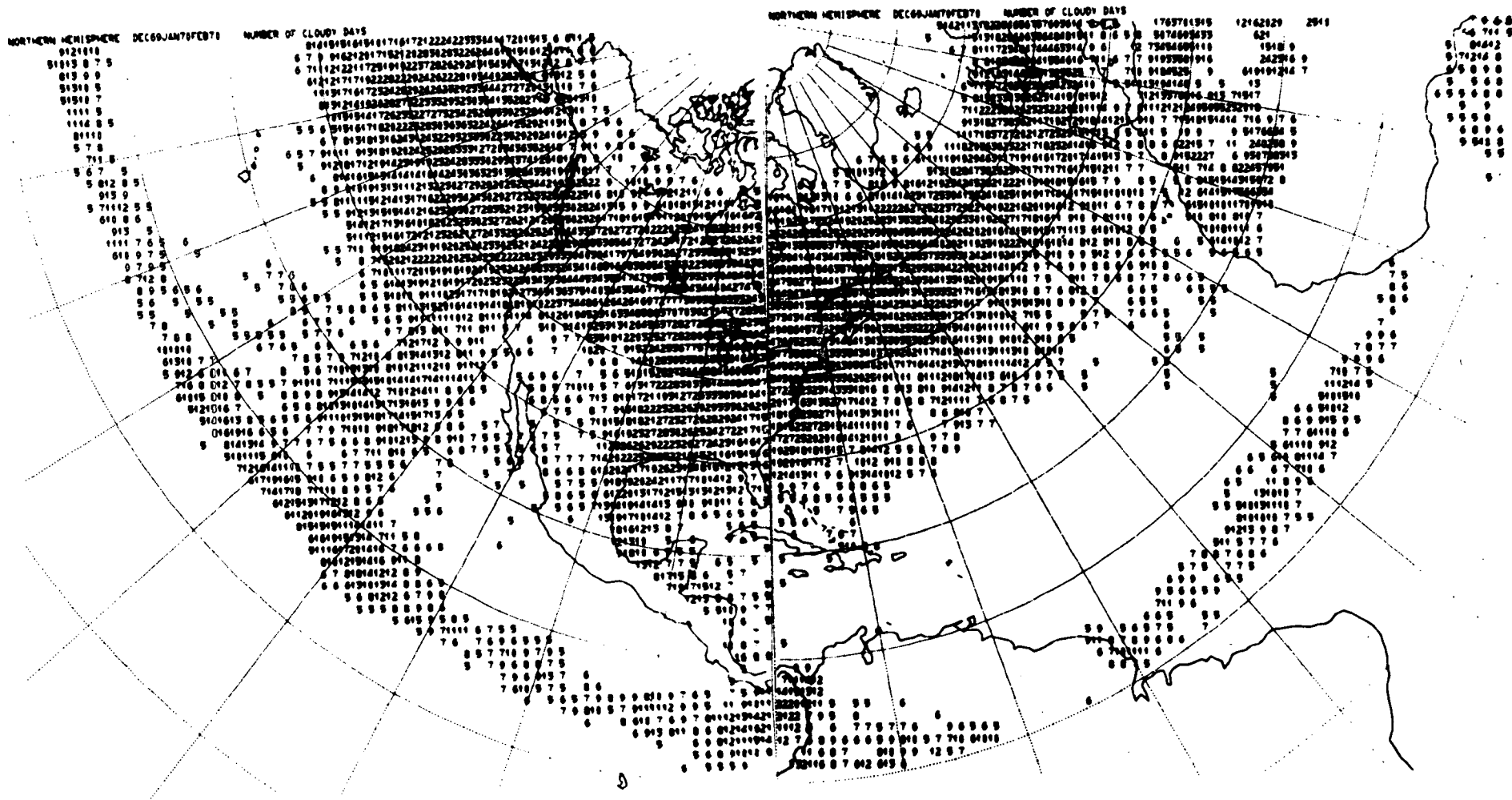
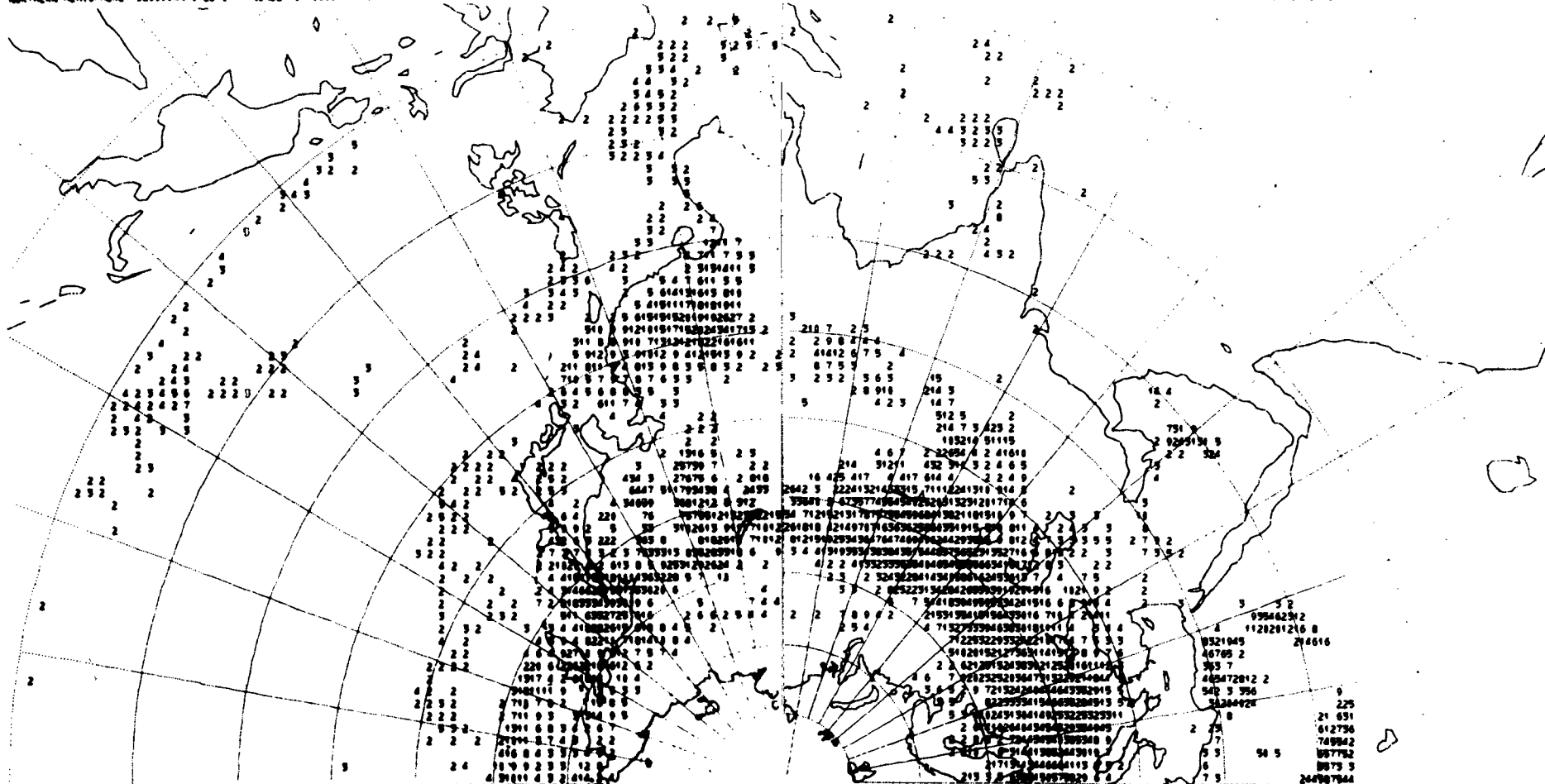


FIGURE A-4: Number of cloudy days December 1969, January 1970 and February 1970

NORTHERN HEMISPHERE DEC69JAN78FEB78 NUMBER OF OCCURRENCES OF 5 CONSECUTIVE CLOUDY DAYS

NORTHERN HEMISPHERE DEC69JAN78FEB78 NUMBER OF OCCURRENCES OF 5 CONSECUTIVE CLOUDY DAYS



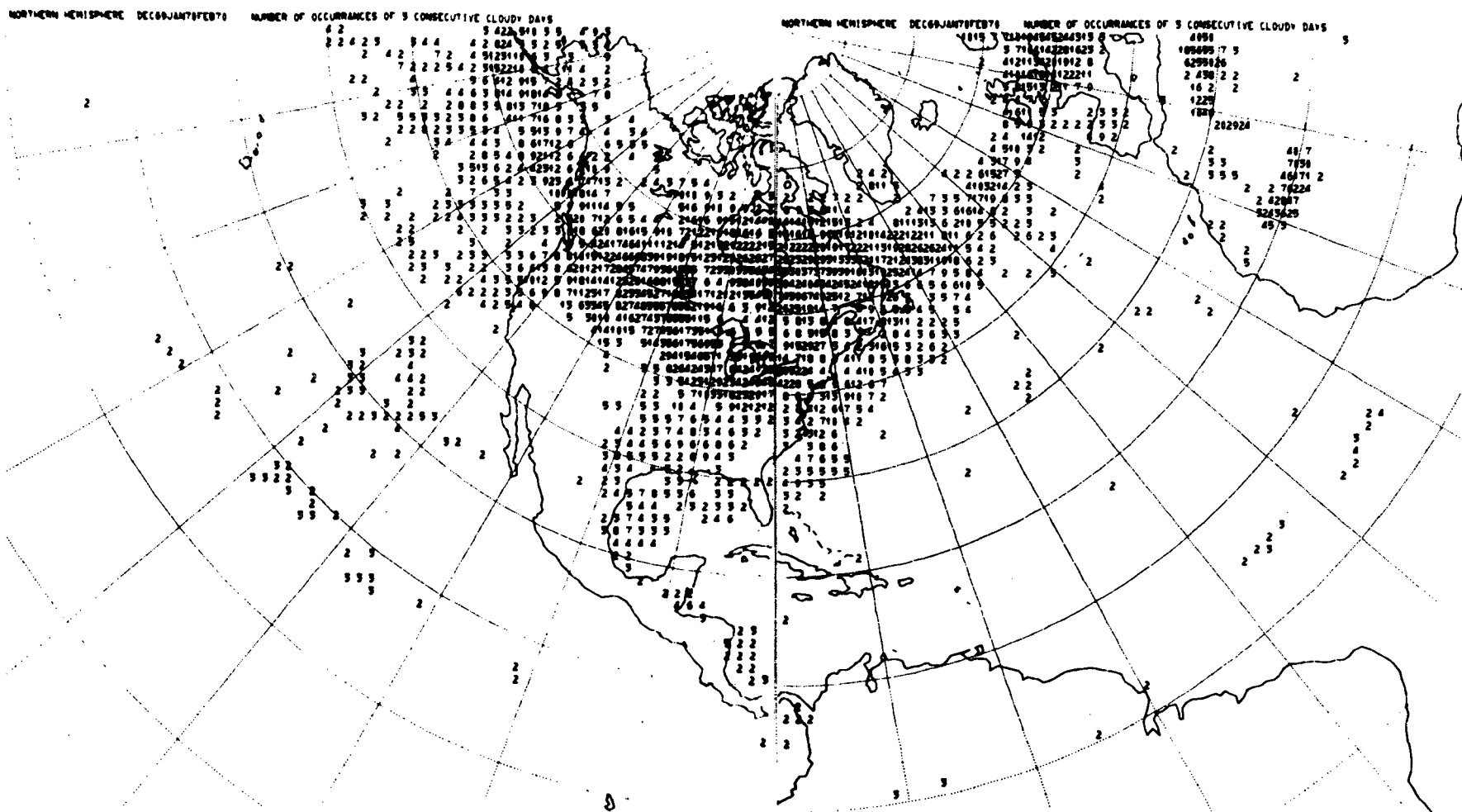


FIGURE A-5: Number of occurrences of 3 consecutive cloudy days December 1969, January 1970 and February 1970

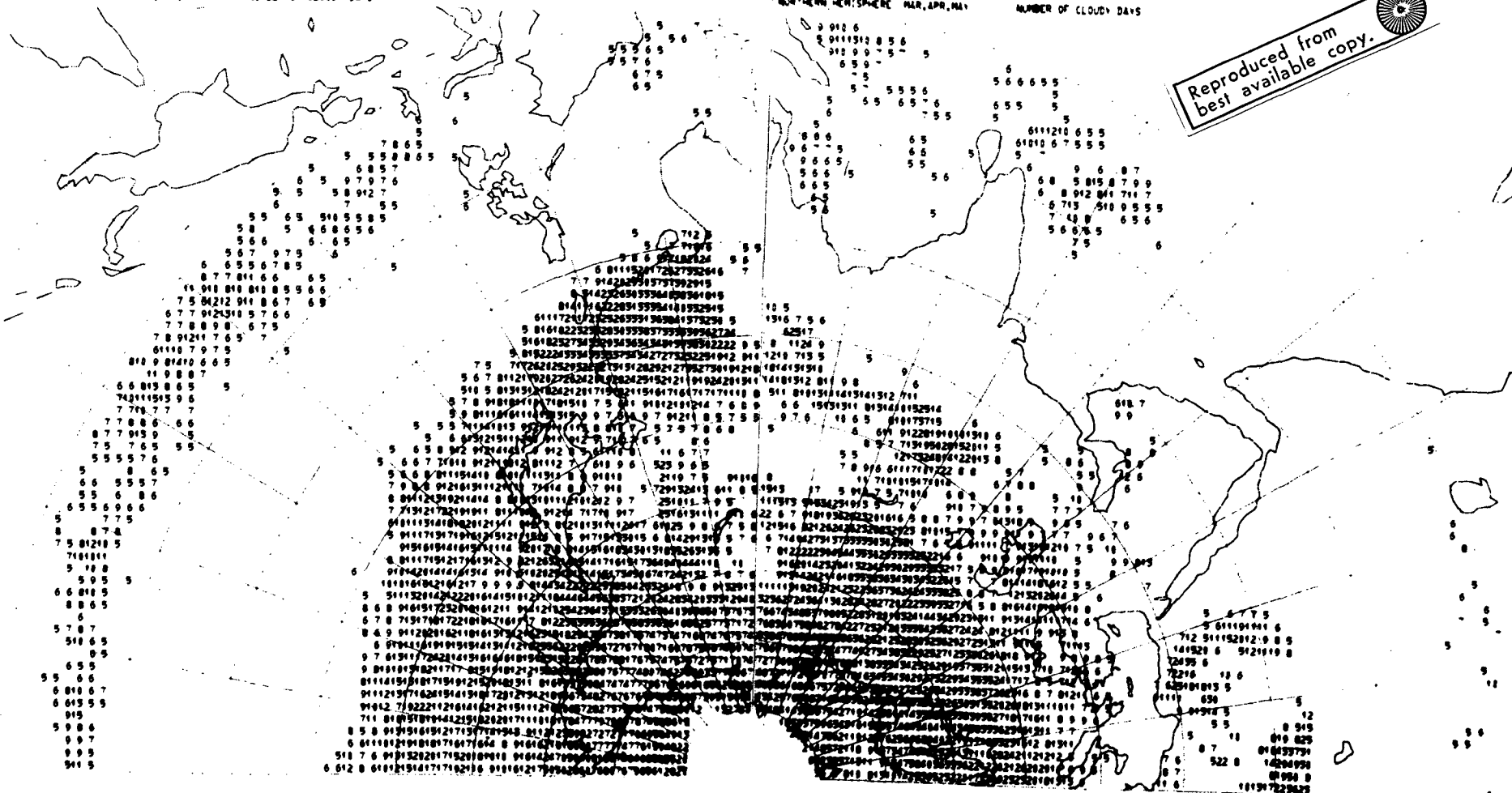
NORTHERN HEMISPHERE MAR, APR, MAY

NUMBER OF CLOUDY DAYS

NORTHERN HEMISPHERE MAR, APR, MAY

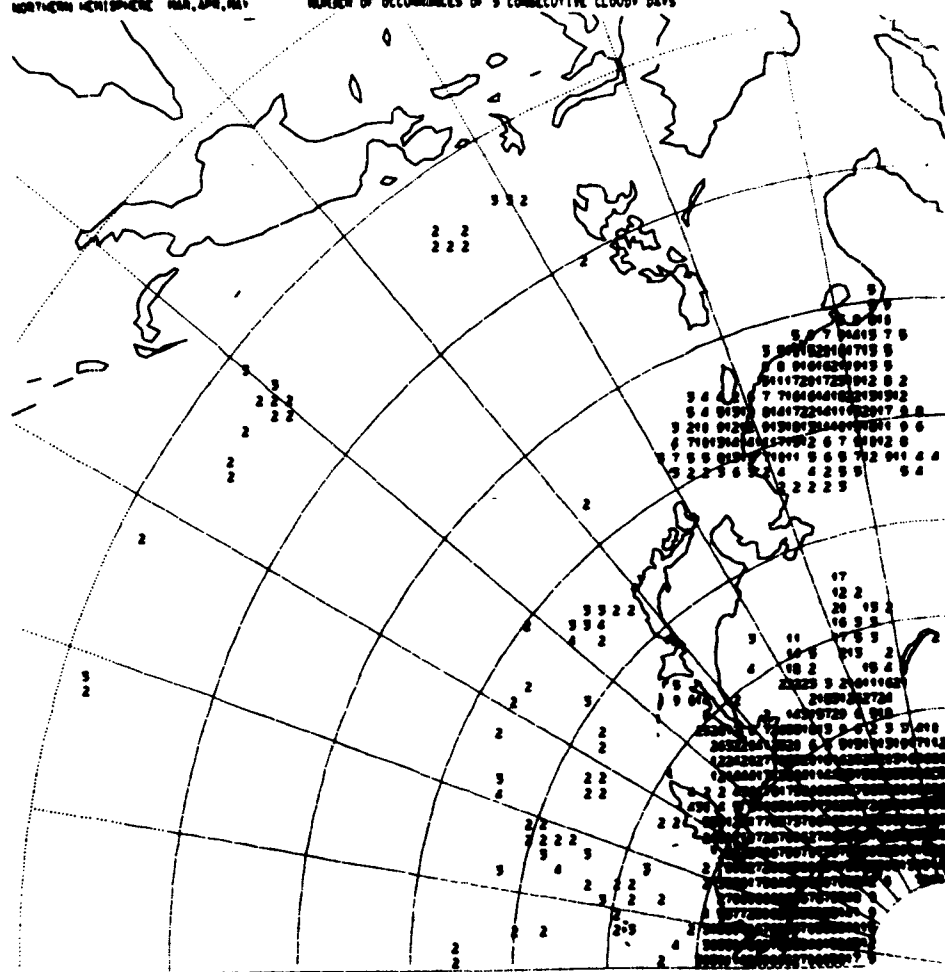
NUMBER OF CLOUDY DAYS

Reproduced from
best available copy.



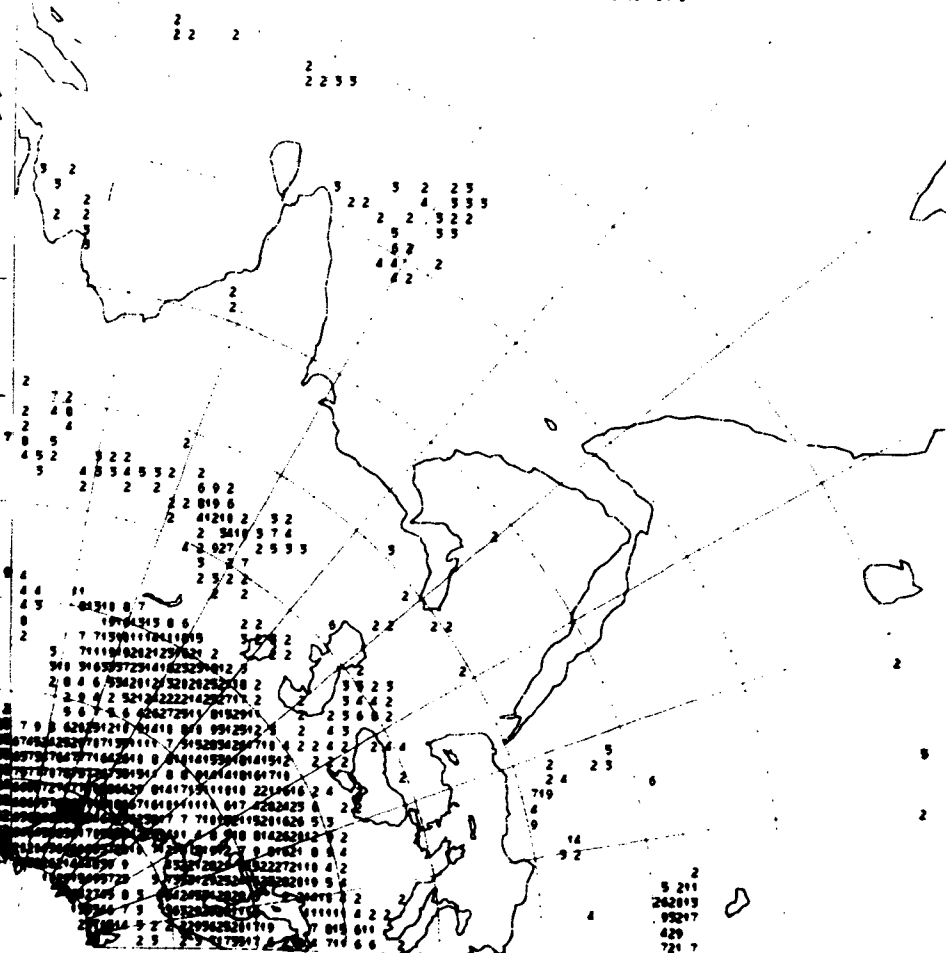
NORTHERN HEMISPHERE MAR, APR, MAY

NUMBER OF OCCURRENCES OF 5 CONSECUTIVE CLOUDY DAYS



NORTHERN HEMISPHERE MAR, APR, MAY

NUMBER OF OCCURRENCES OF 5 CONSECUTIVE CLOUDY DAYS



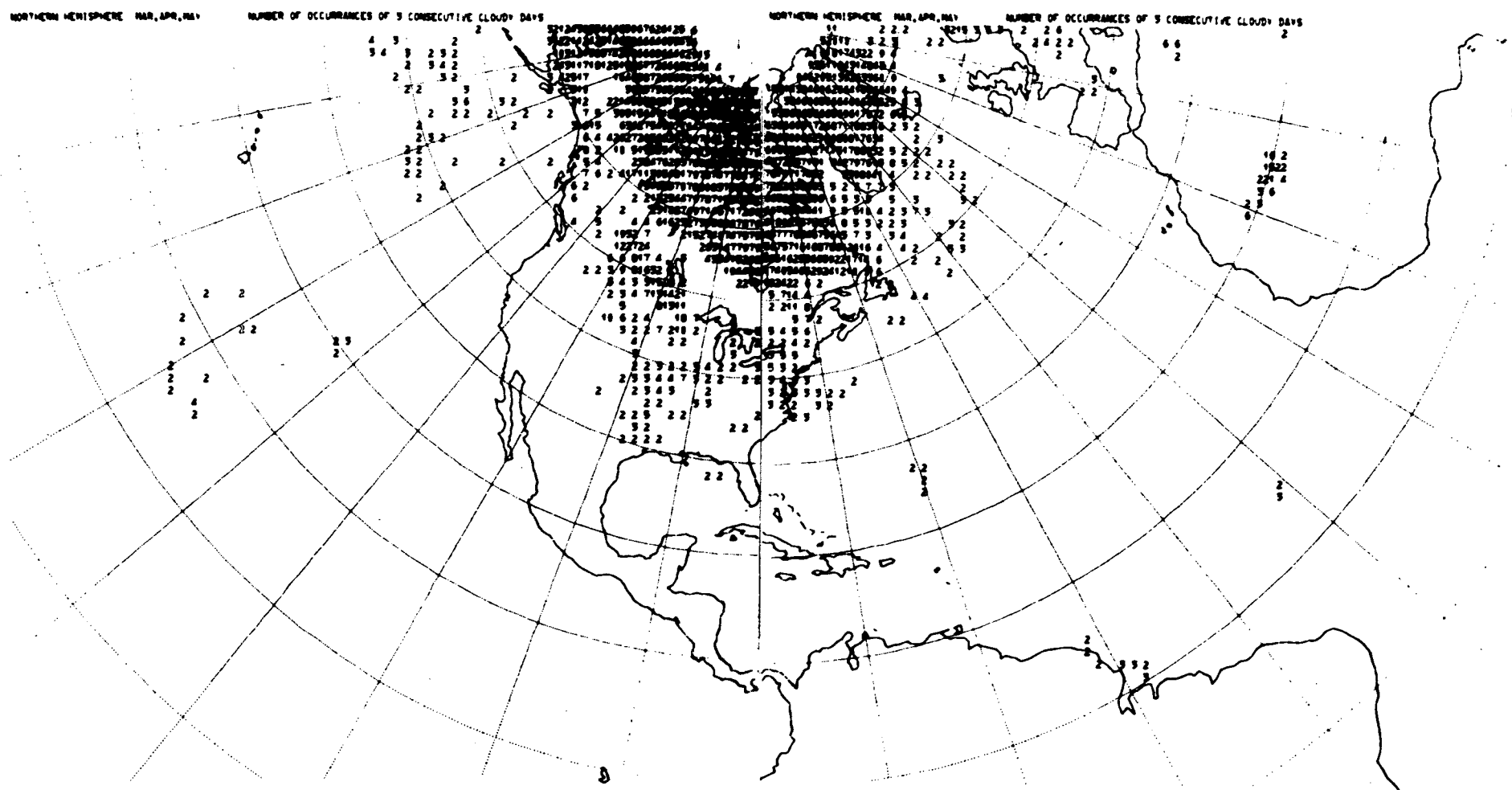


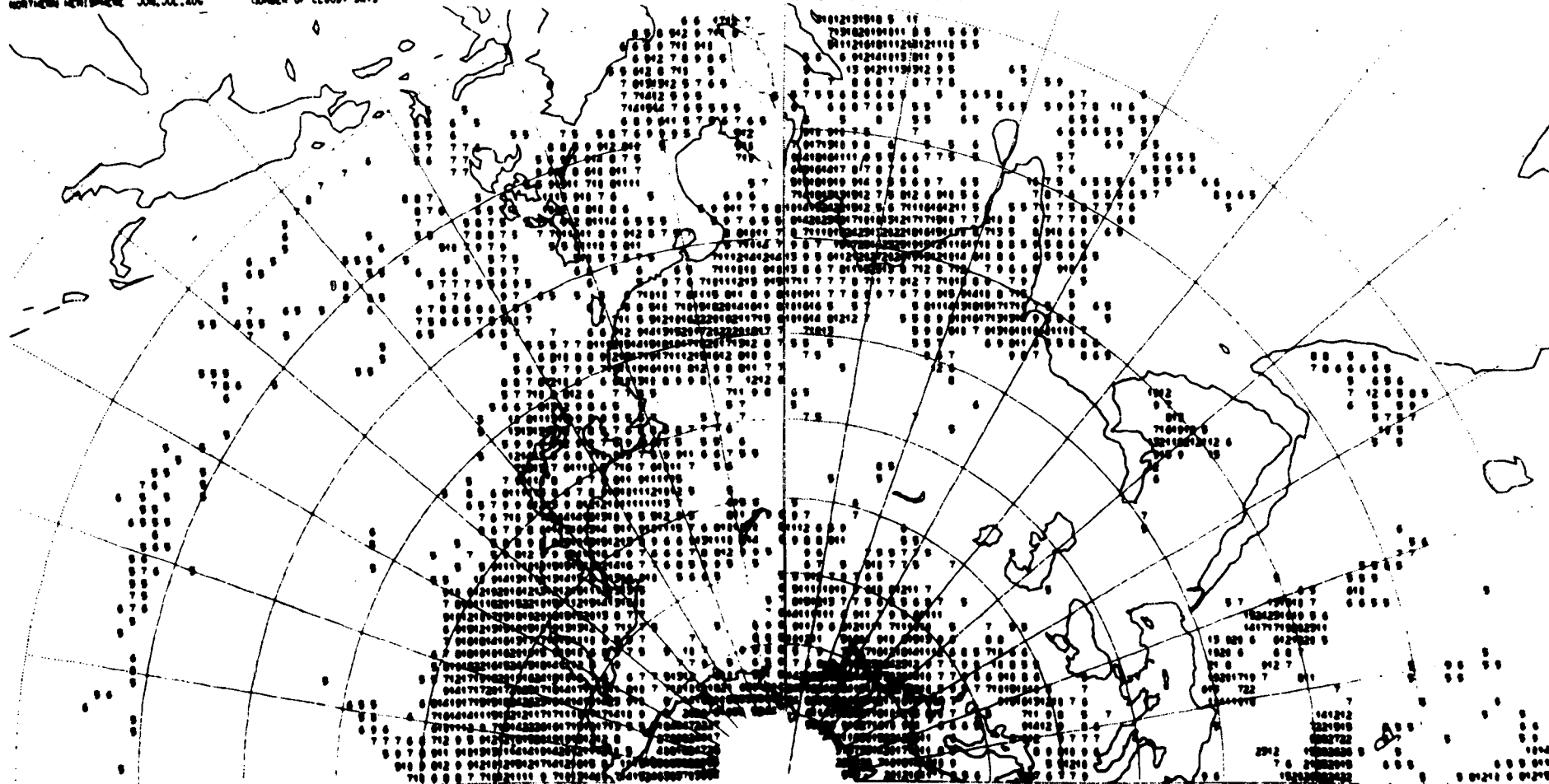
FIGURE A-7: Number of occurrences of 3 consecutive cloudy days March 1970, April 1969 and May 1969

NORTHERN HEMISPHERE JAN, JUL, AUG

NUMBER OF CLOUDY DAYS

NORTHERN HEMISPHERE JAN, JUL, AUG

NUMBER OF CLOUDY DAYS

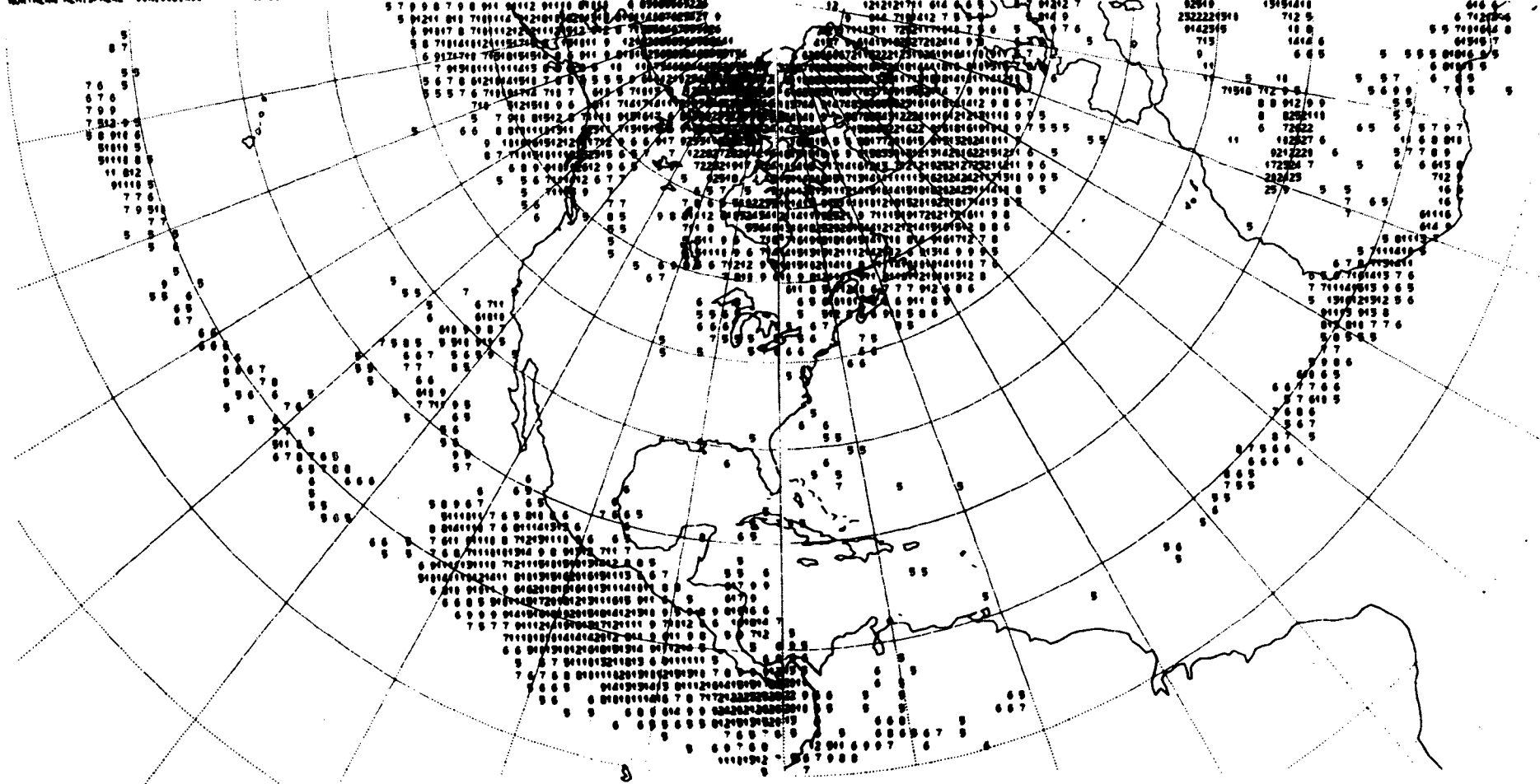


NORTHERN HEMISPHERE JUN, JUL, AUG

NUMBER OF CLOUDY DAYS

NORTHERN HEMISPHERE JUN, JUL, AUG

NUMBER OF CLOUDY DAYS



Reproduced from
best available copy.

FIGURE A-8: Number of cloudy days June 1969, July 1969 and August 1969

NORTHERN HEMISPHERE JUN, JUL, AUG

NUMBER OF OCCURRENCES OF 3 CONSECUTIVE CLOUDY DAYS

NORTHERN HEMISPHERE JUN, JUL, AUG

NUMBER OF OCCURRENCES OF 3 CONSECUTIVE CLOUDY DAYS

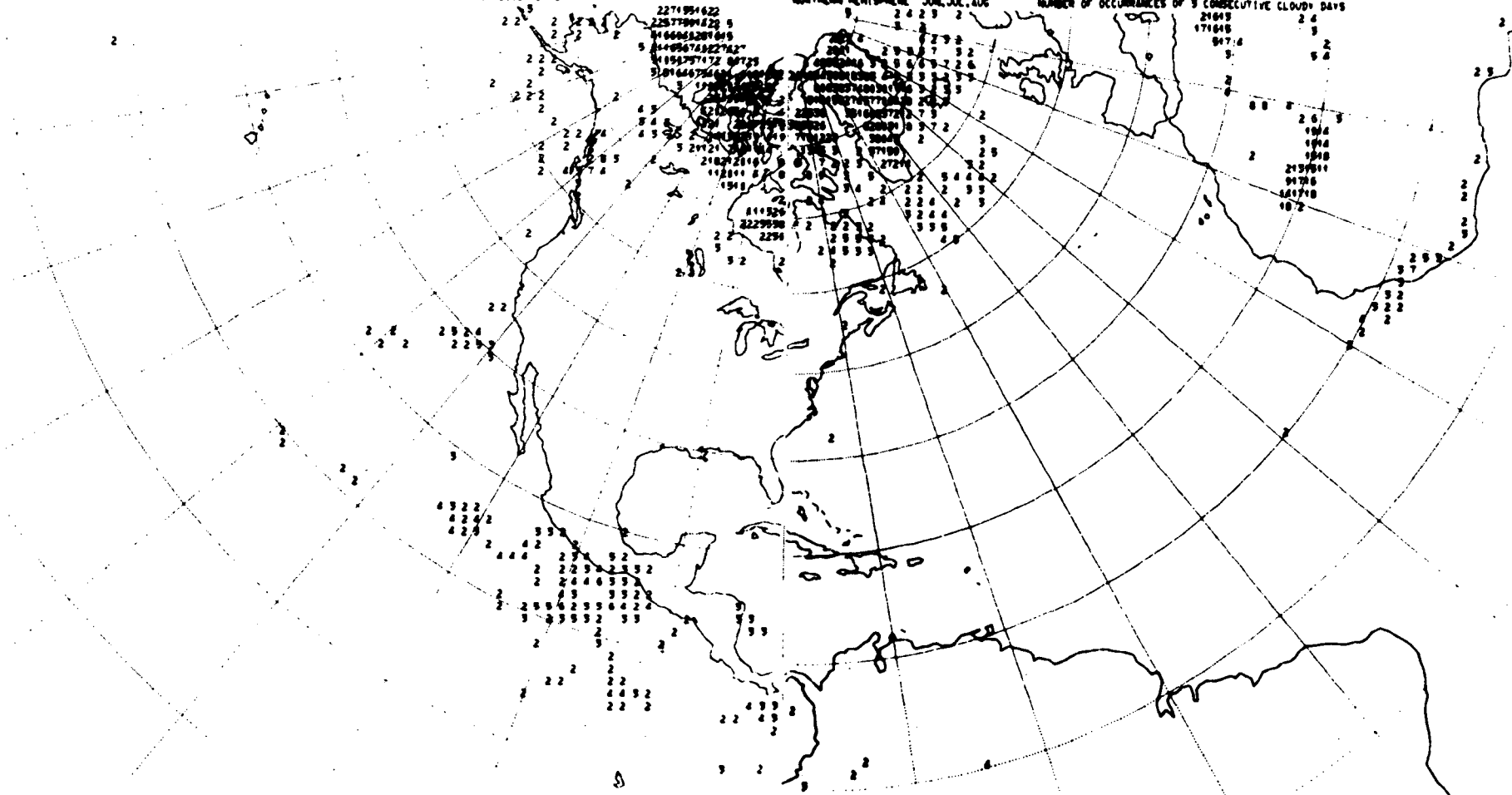
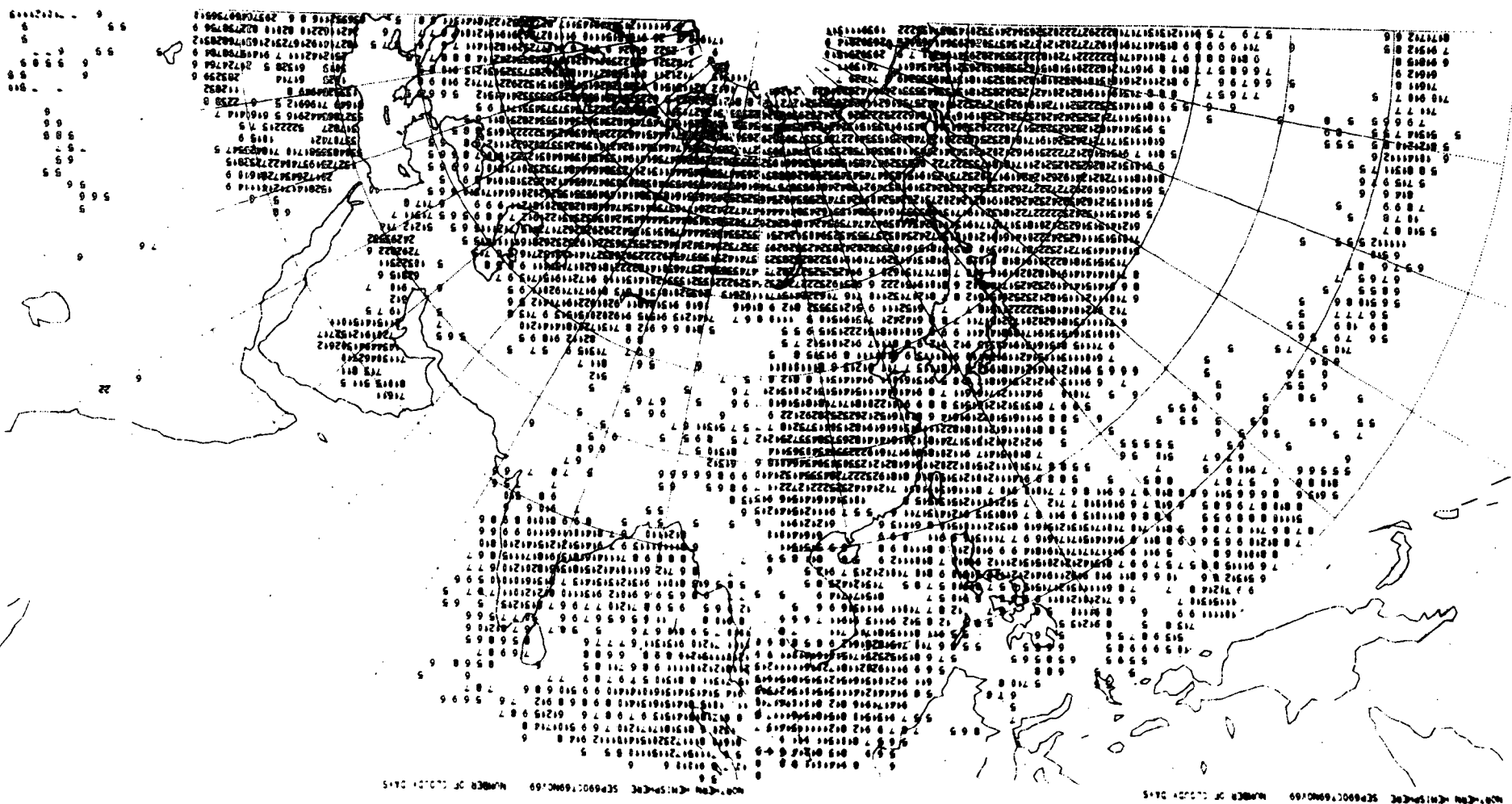


FIGURE A-9: Number of occurrences of 3 consecutive cloudy days June 1969, July 1969 and August 1969



MAP OF THE UNITED STATES
NUMBER OF CITIES IN EACH STATE

MAP OF THE UNITED STATES
NUMBER OF CITIES IN EACH STATE

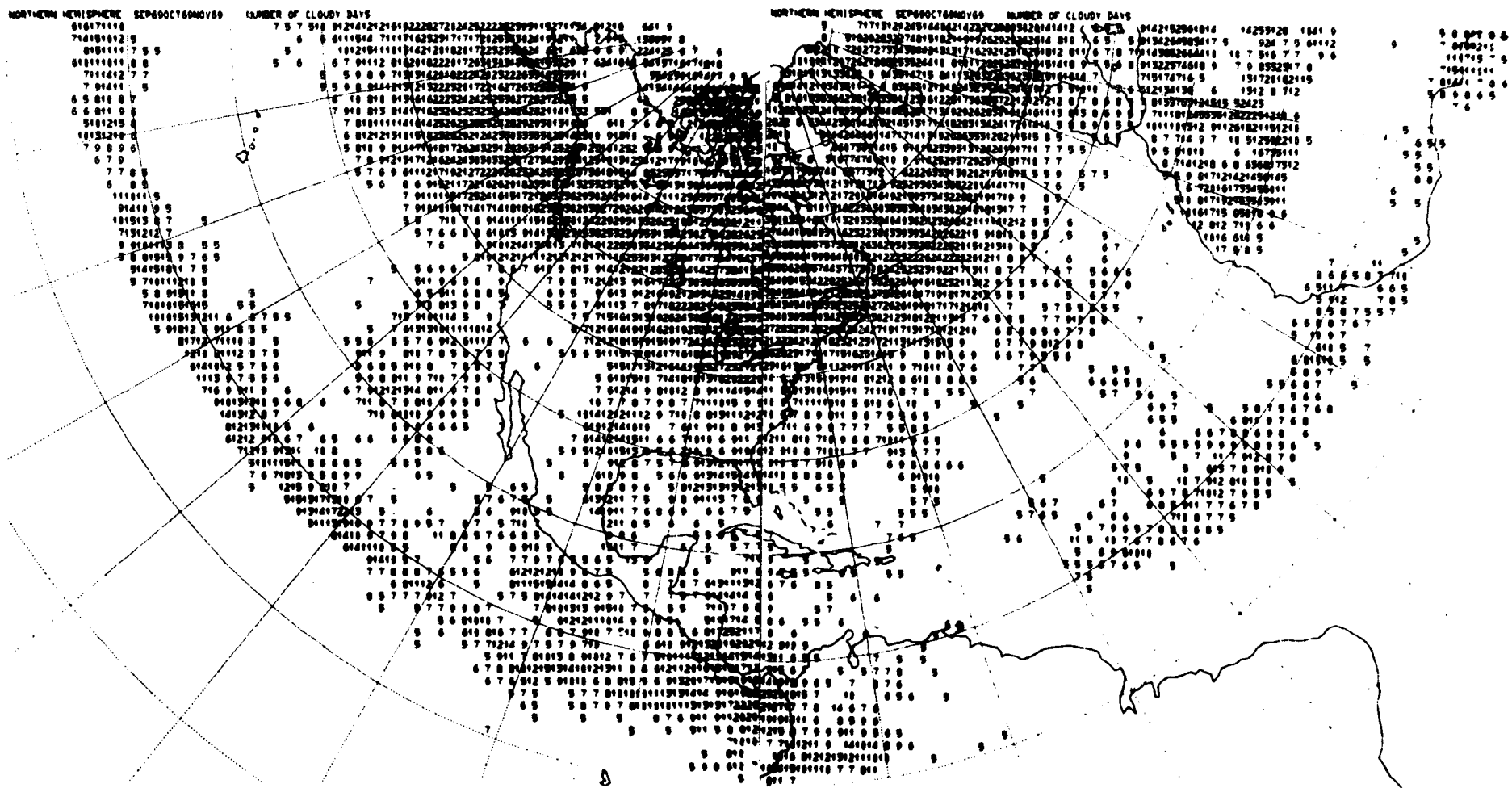
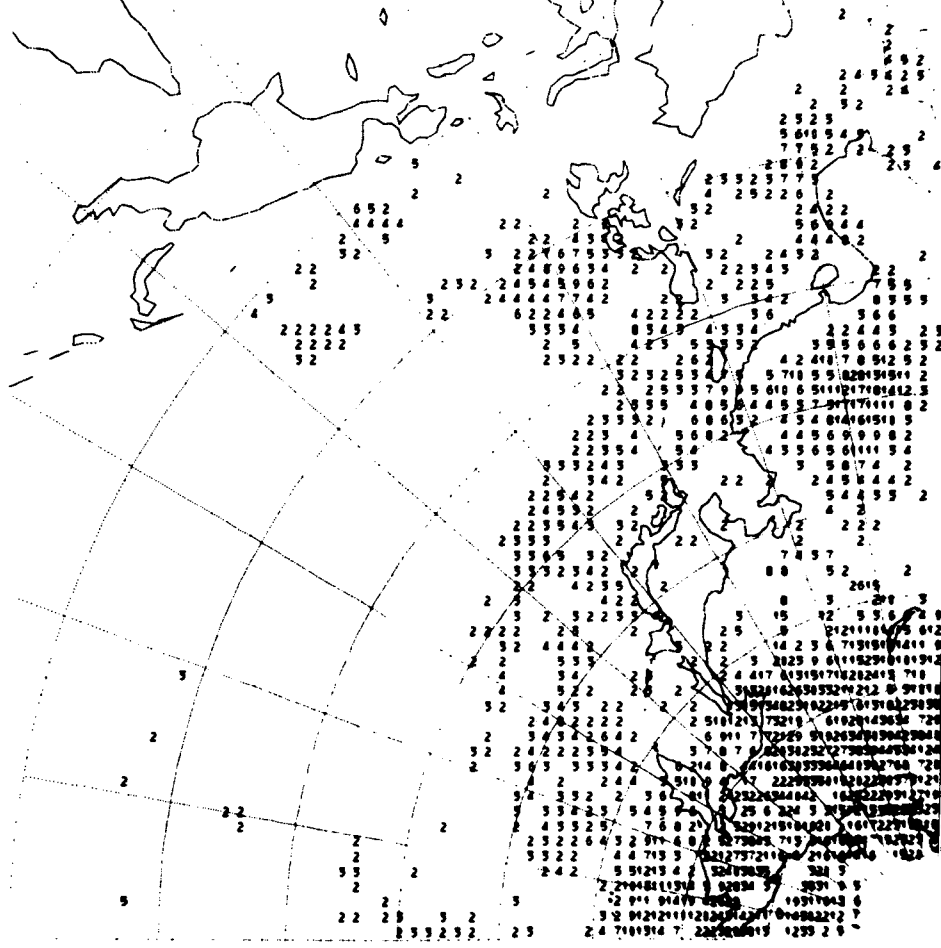


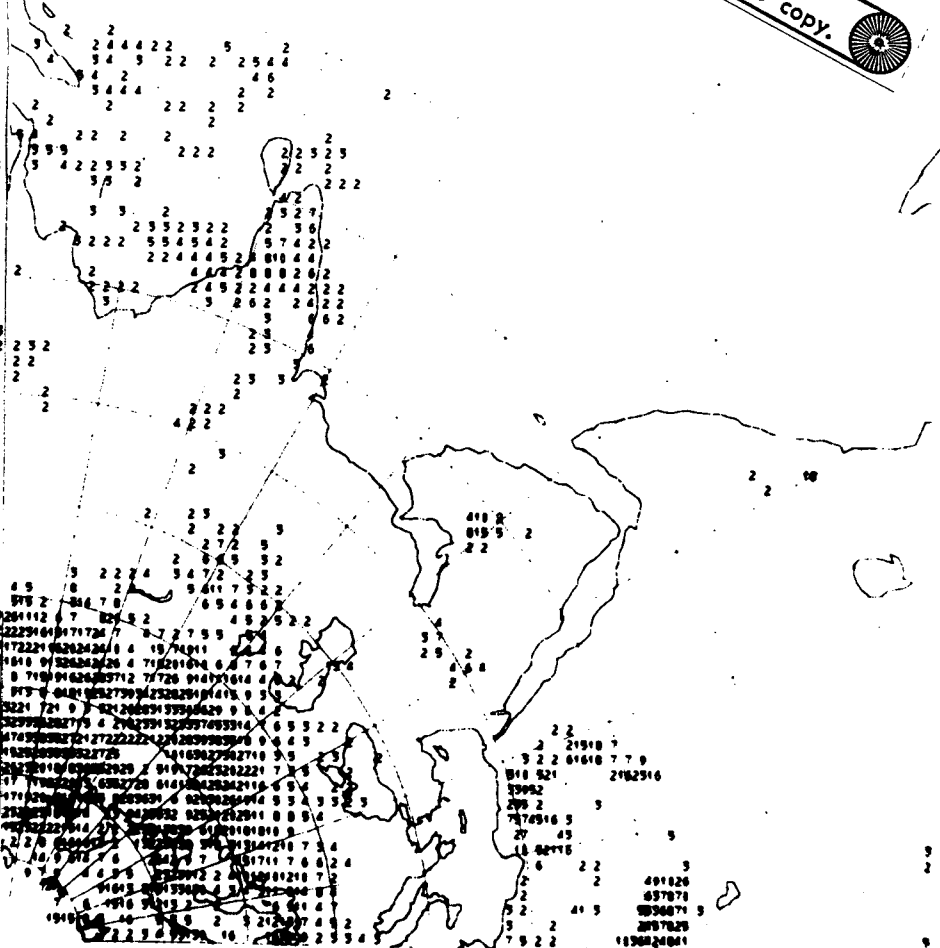
FIGURE A-10: Number of cloudy days September 1969, October 1969 and November 1969

Reproduced from
best available copy.

NORTHERN HEMISPHERE SEP690CT69NOV69 NUMBER OF OCCURRENCES OF 5 CONSECUTIVE CLOUDY DAYS



NORTHERN HEMISPHERE SEP690CT69NOV69 NUMBER OF OCCURRENCES OF 5 CONSECUTIVE CLOUDY DAYS



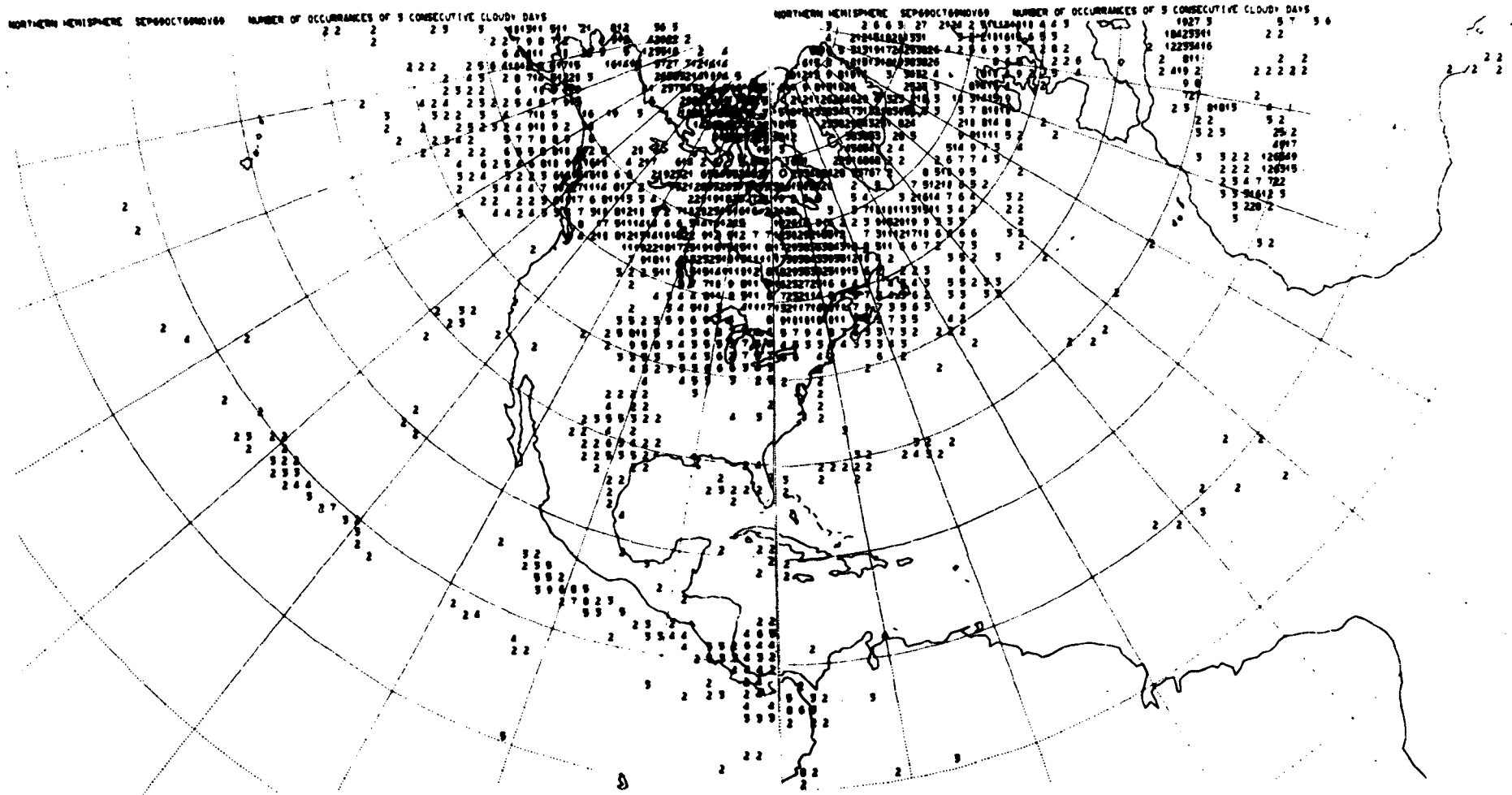


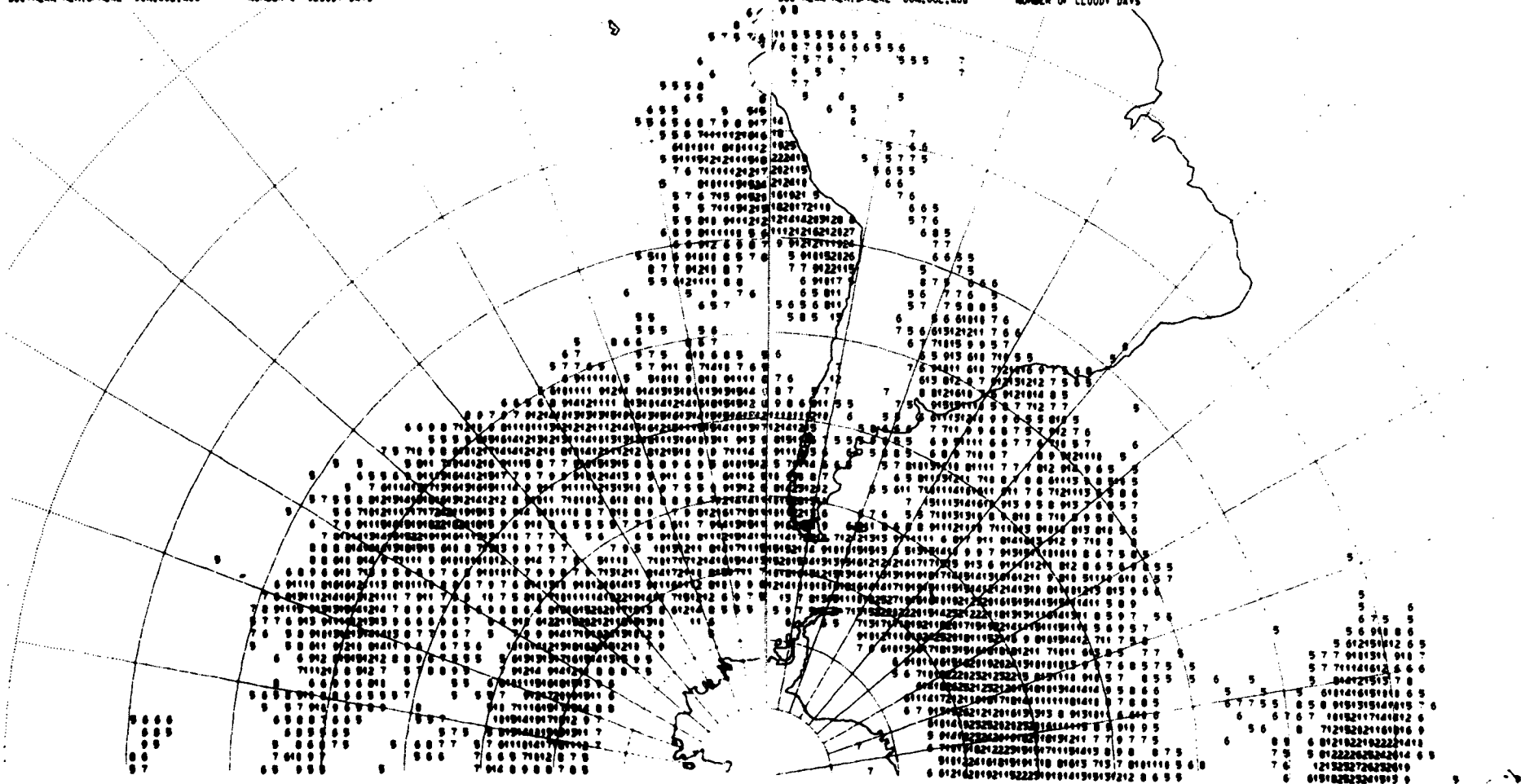
FIGURE A-11: Number of occurrences of 3 consecutive cloudy days September 1969, October 1969 and November 1969

SOUTHERN HEMISPHERE JAN, JUL, AUG

NUMBER OF CLOUDY DAYS

SOUTHERN HEMISPHERE JAN, JUL, AUG

NUMBER OF CLOUDY DAYS



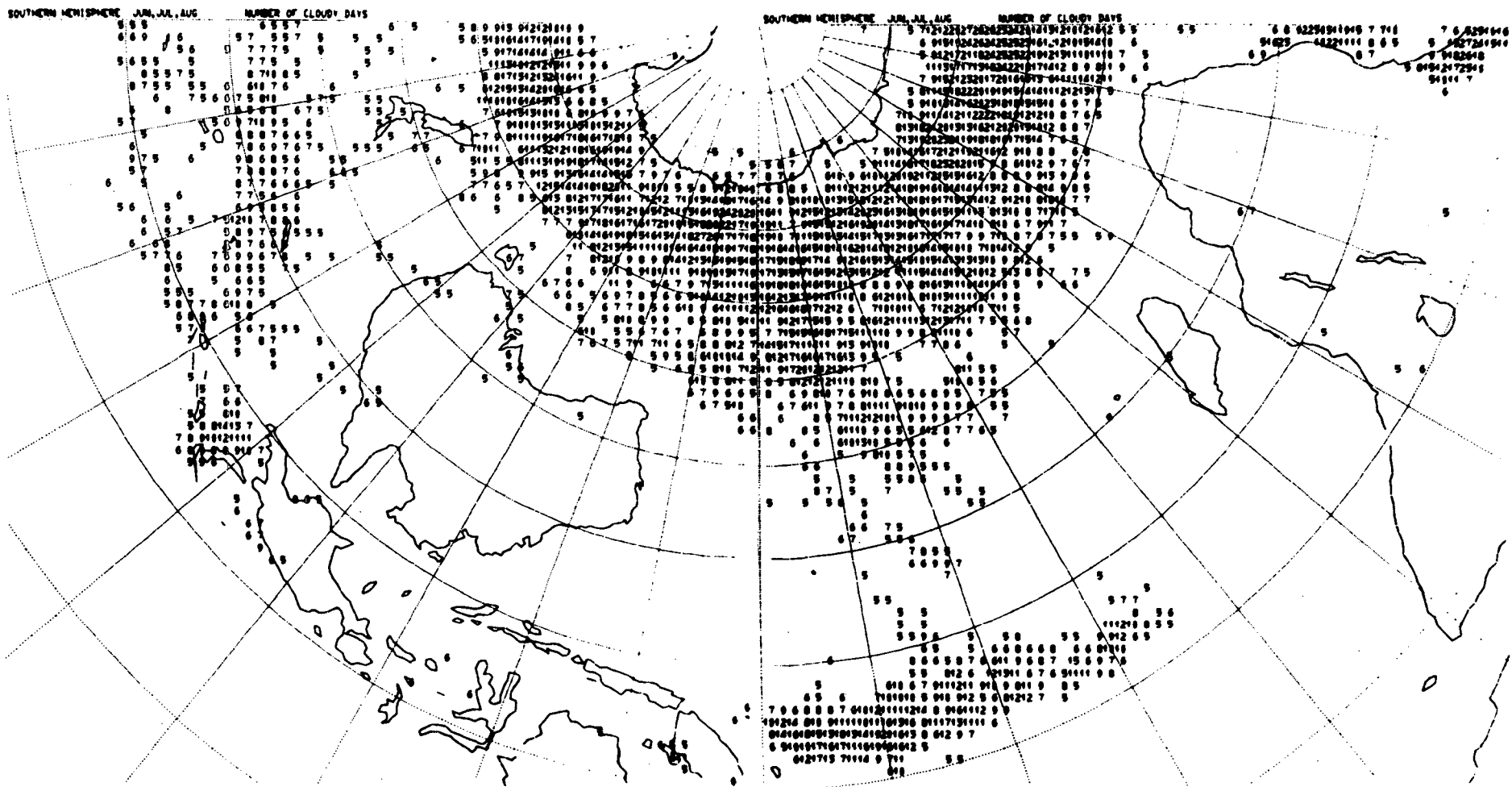


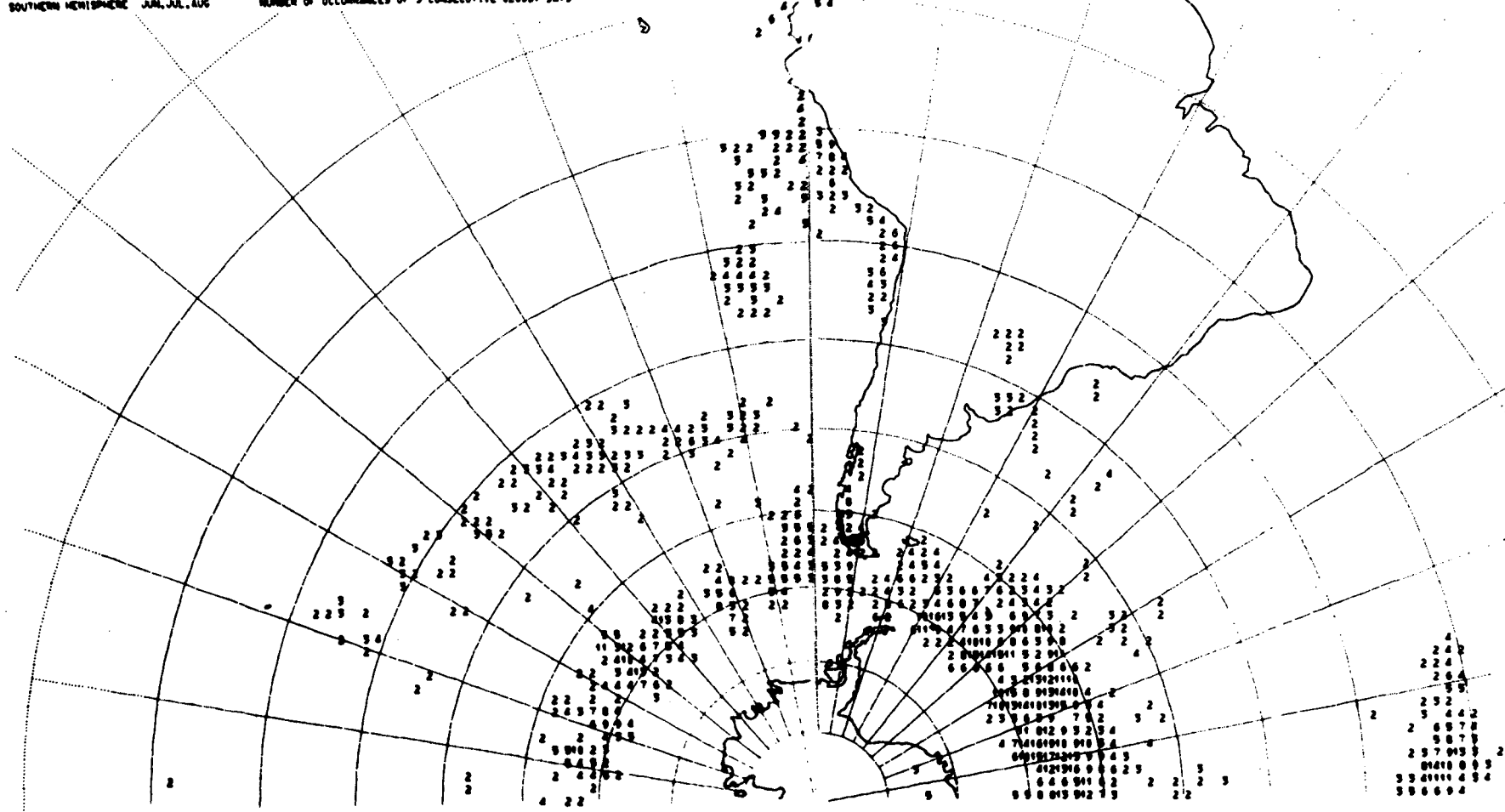
FIGURE B-1: Number of cloudy days June 1969, July 1969 and August 1969

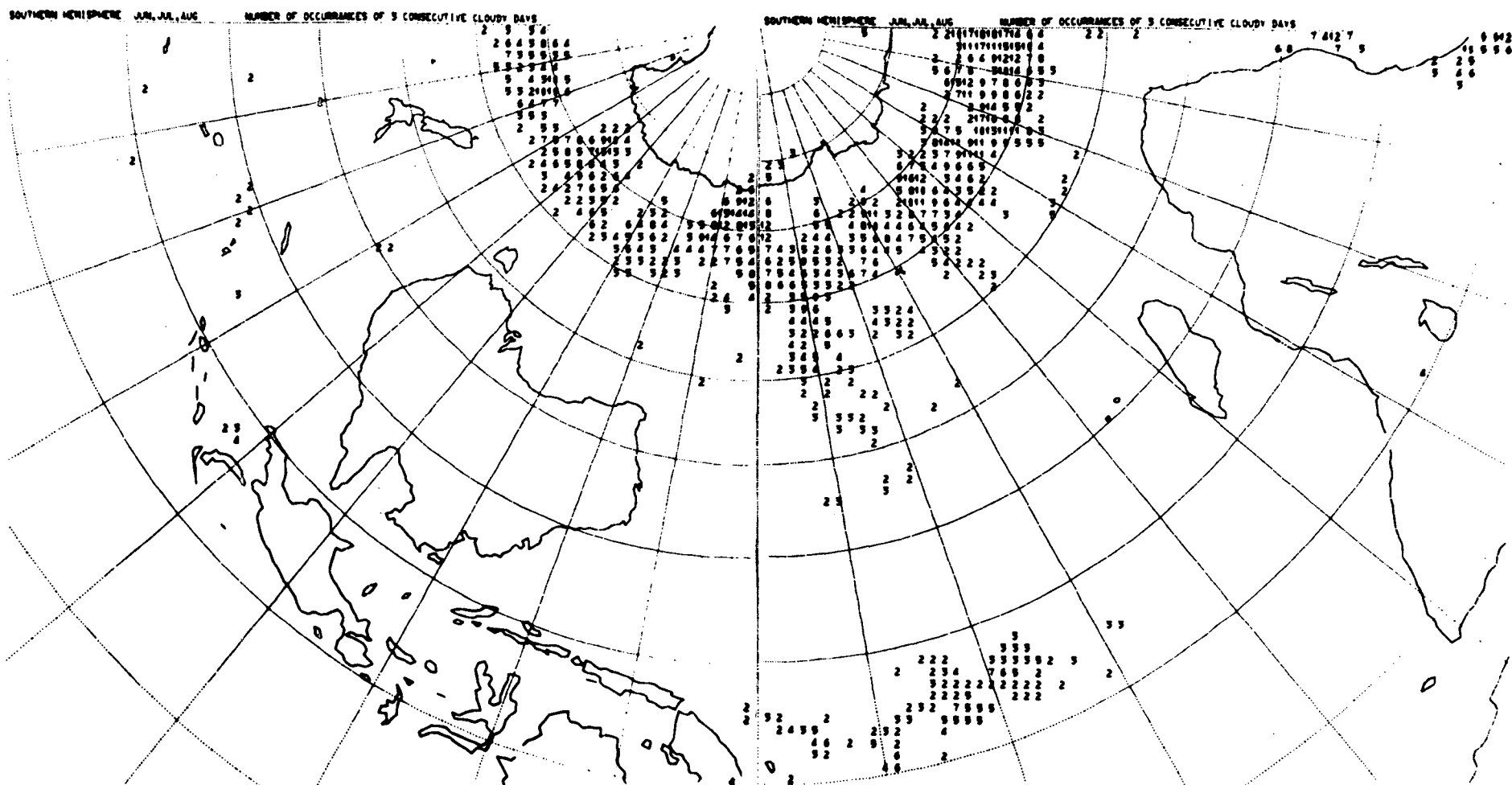
SOUTHERN HEMISPHERE JUN, JUL, AUG

NUMBER OF OCCURRENCES OF 3 CONSECUTIVE CLOUDY DAYS

SOUTHERN HEMISPHERE JUN, JUL, AUG

NUMBER OF OCCURRENCES OF 3 CONSECUTIVE CLOUDY DAYS



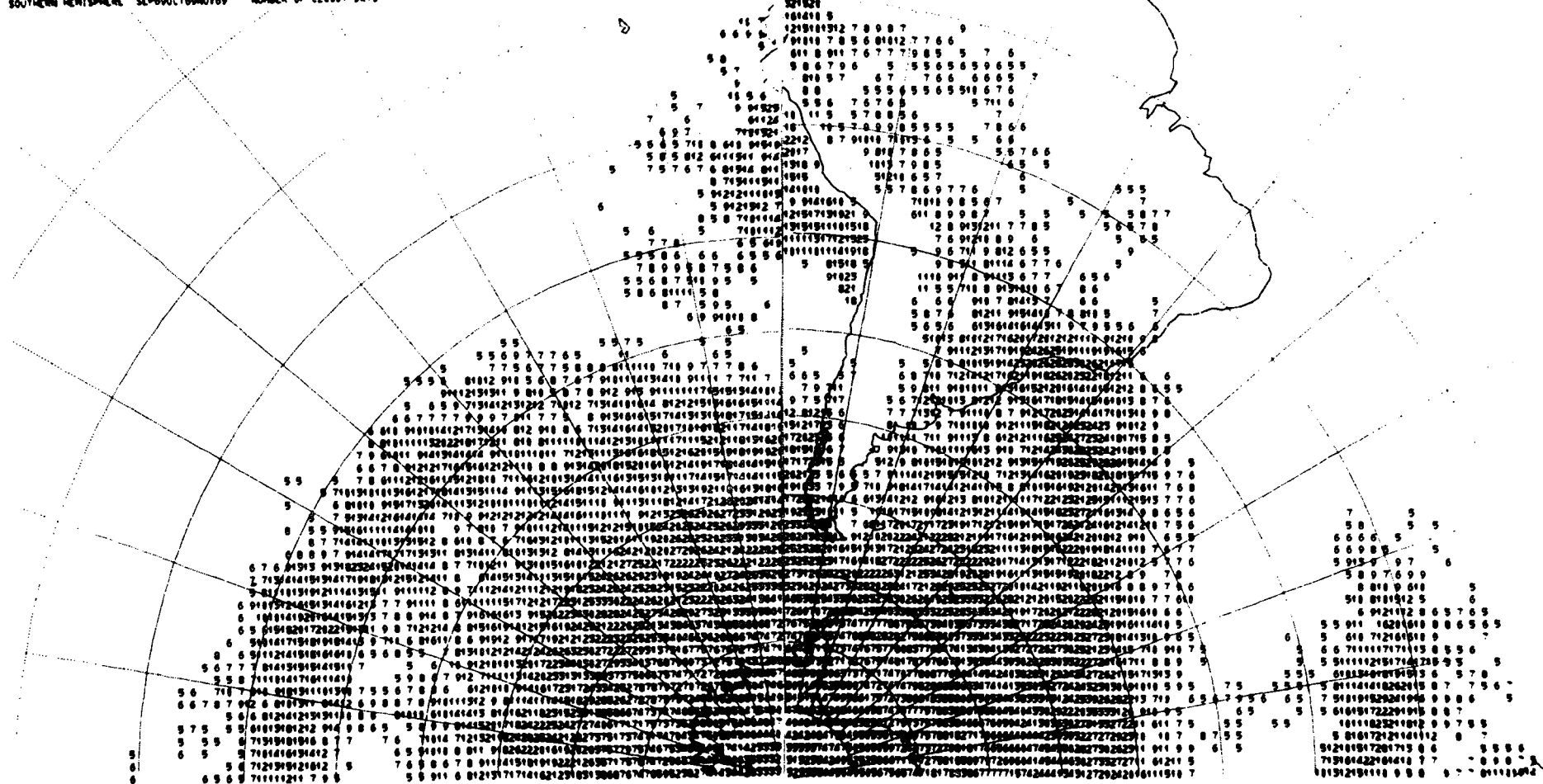


Reproduced from
best available copy.

FIGURE B-2: Number of occurrences of 3 consecutive cloudy days June 1969, July 1969 and August 1969

SOUTHERN HEMISPHERE SEP60OCT60NOV60 NUMBER OF CLOUDY DAYS

SOUTHERN HEMISPHERE SEP60OCT60NOV60 NUMBER OF CLOUDY DAYS



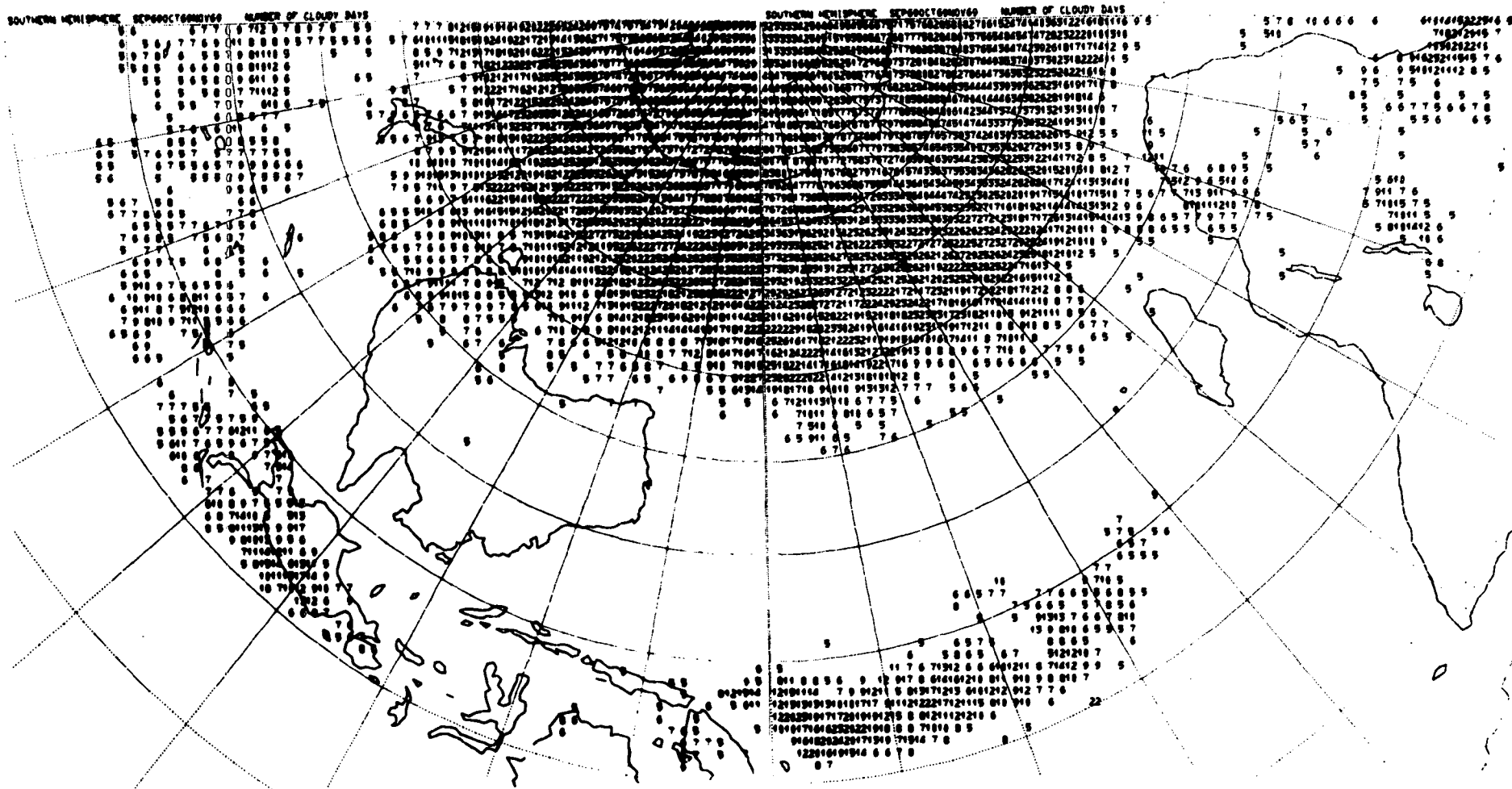
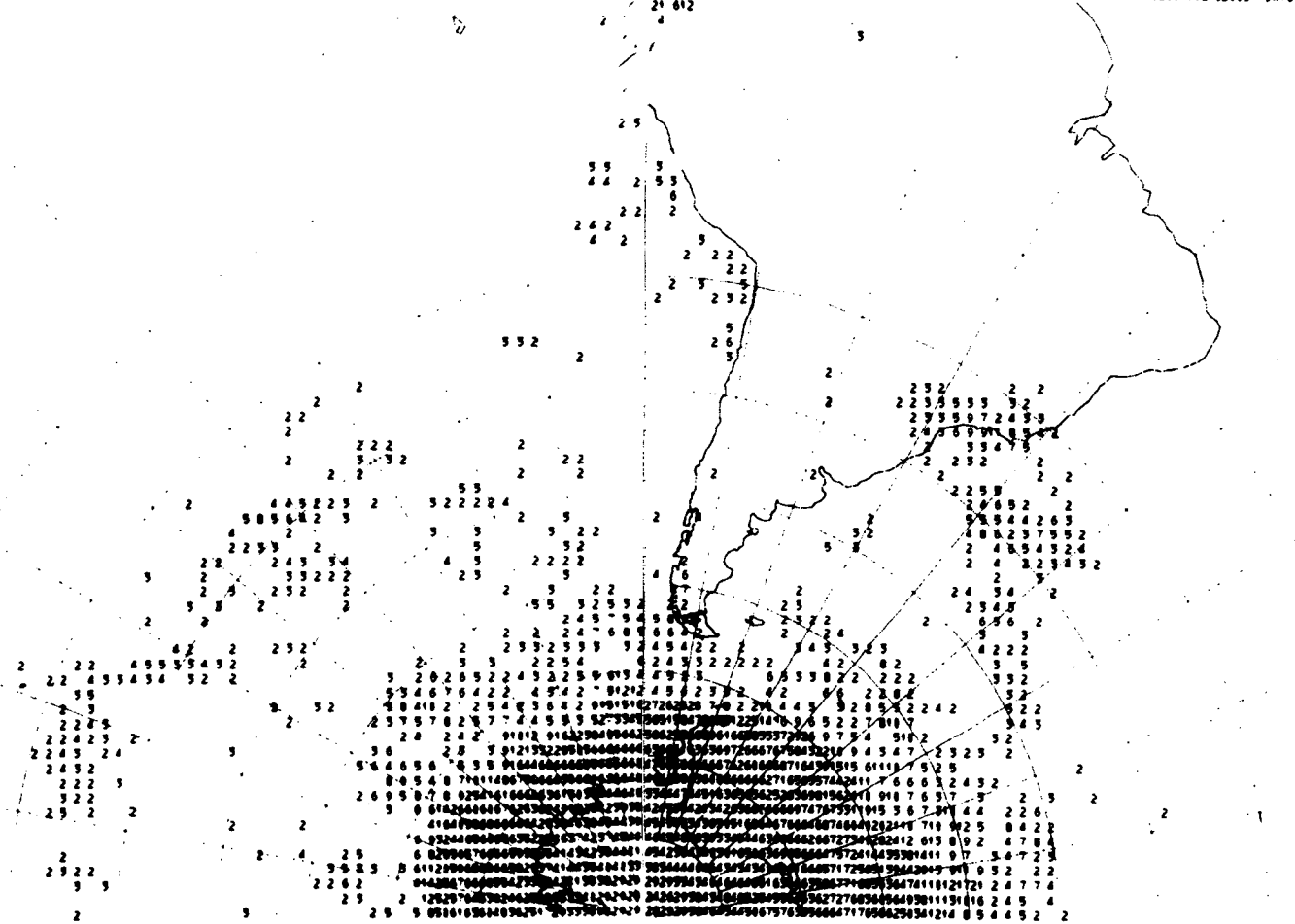


FIGURE B-3: Number of cloudy days September 1969, October 1969 and November 1969

SOUTHERN HEMISPHERE SEP69OCT69NOV69 NUMBER OF OCCURRENCES OF 5 CONSECUTIVE CLOUDY DAYS

SOUTHERN HEMISPHERE SEP69OCT69NOV69 NUMBER OF OCCURRENCES OF 5 CONSECUTIVE CLOUDY DAYS



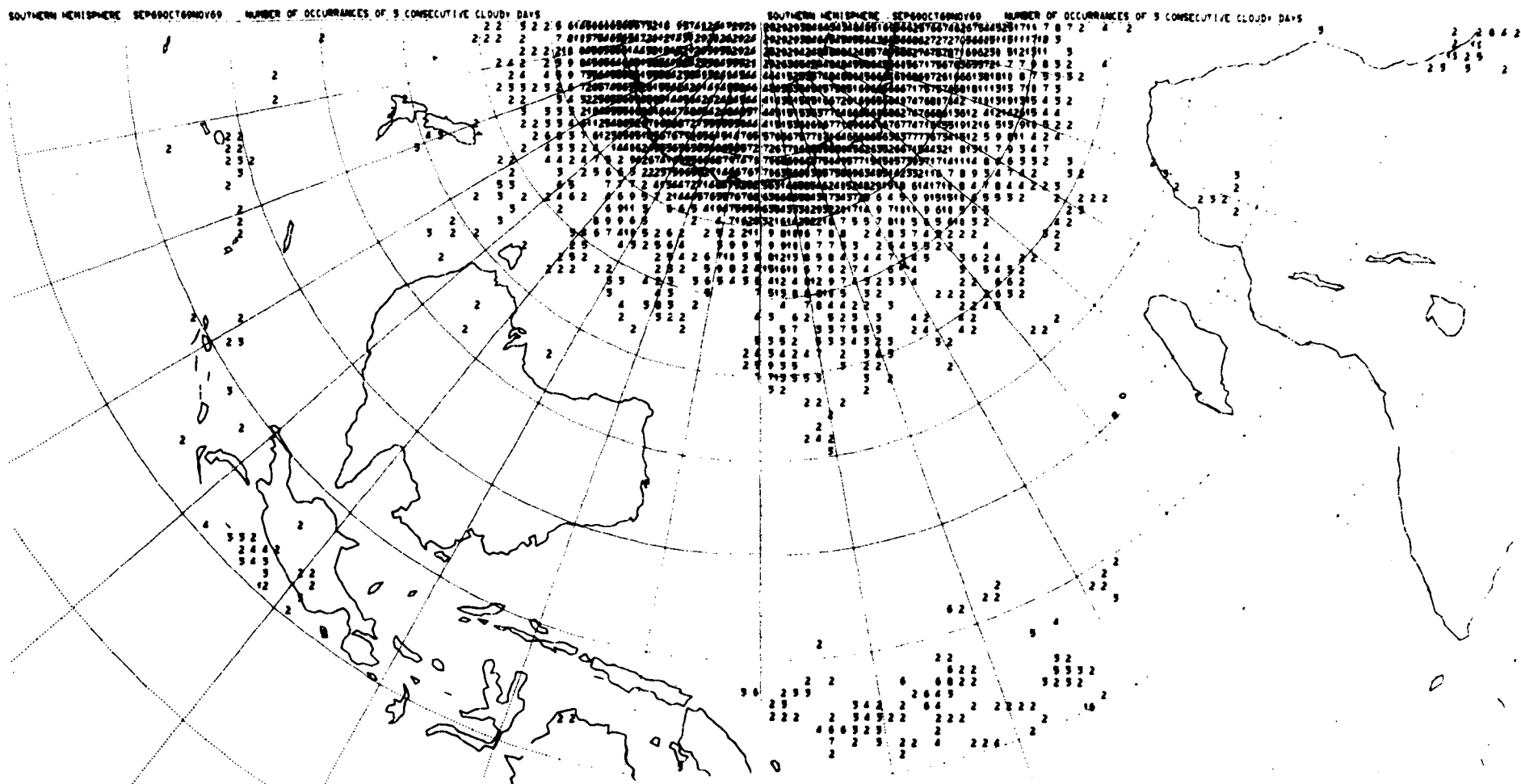


FIGURE B-4: Number of occurrences of 3 consecutive cloudy days September 1969, October 1969 and November 1969

SOUTHERN HEMISPHERE DEC60JAN781E870 NUMBER OF CLOUDY DAYS

SOUTHERN HEMISPHERE DEC60JAN781E870 NUMBER OF CLOUDY DAYS

Reproduced from
best available copy.



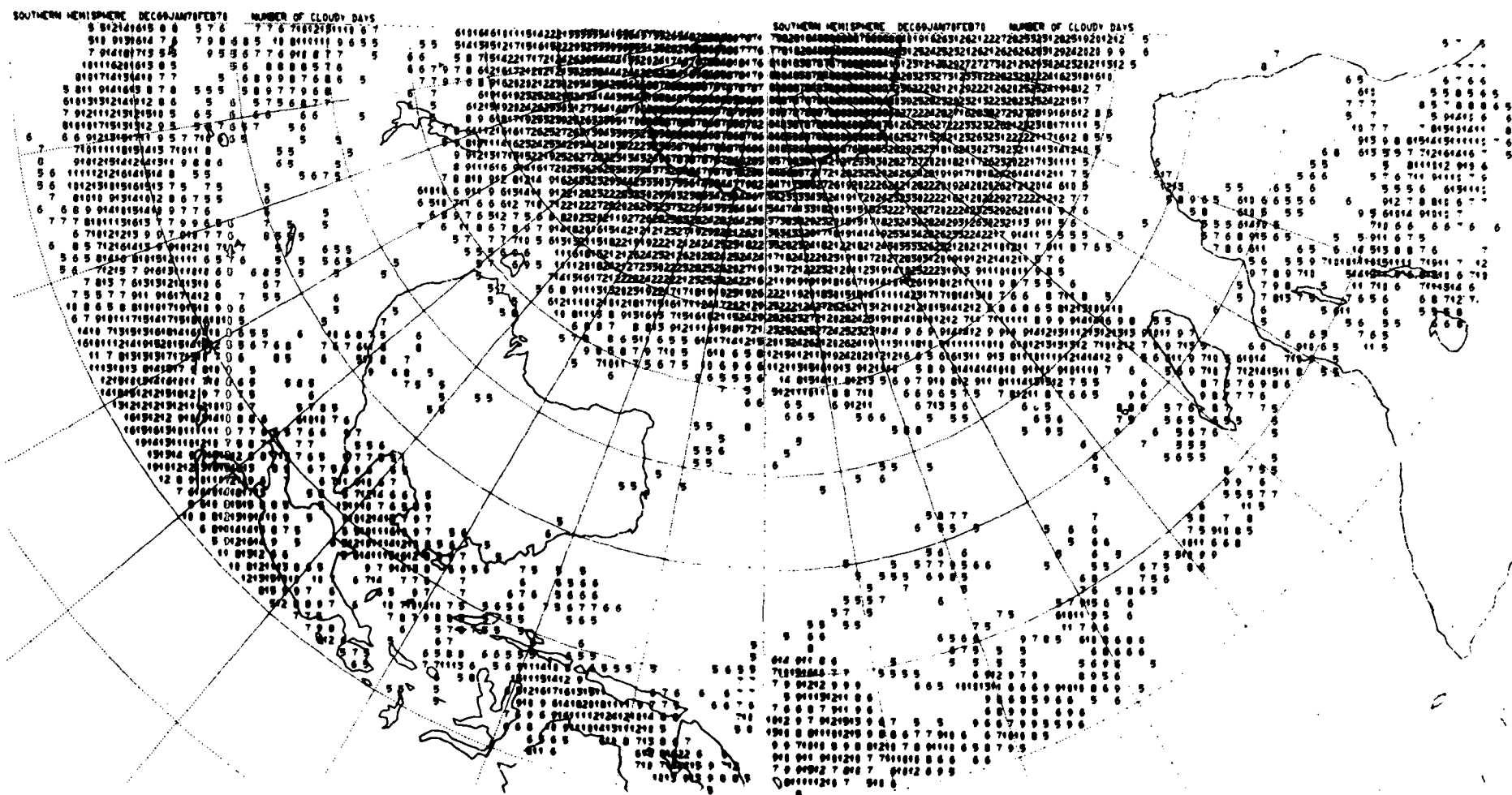
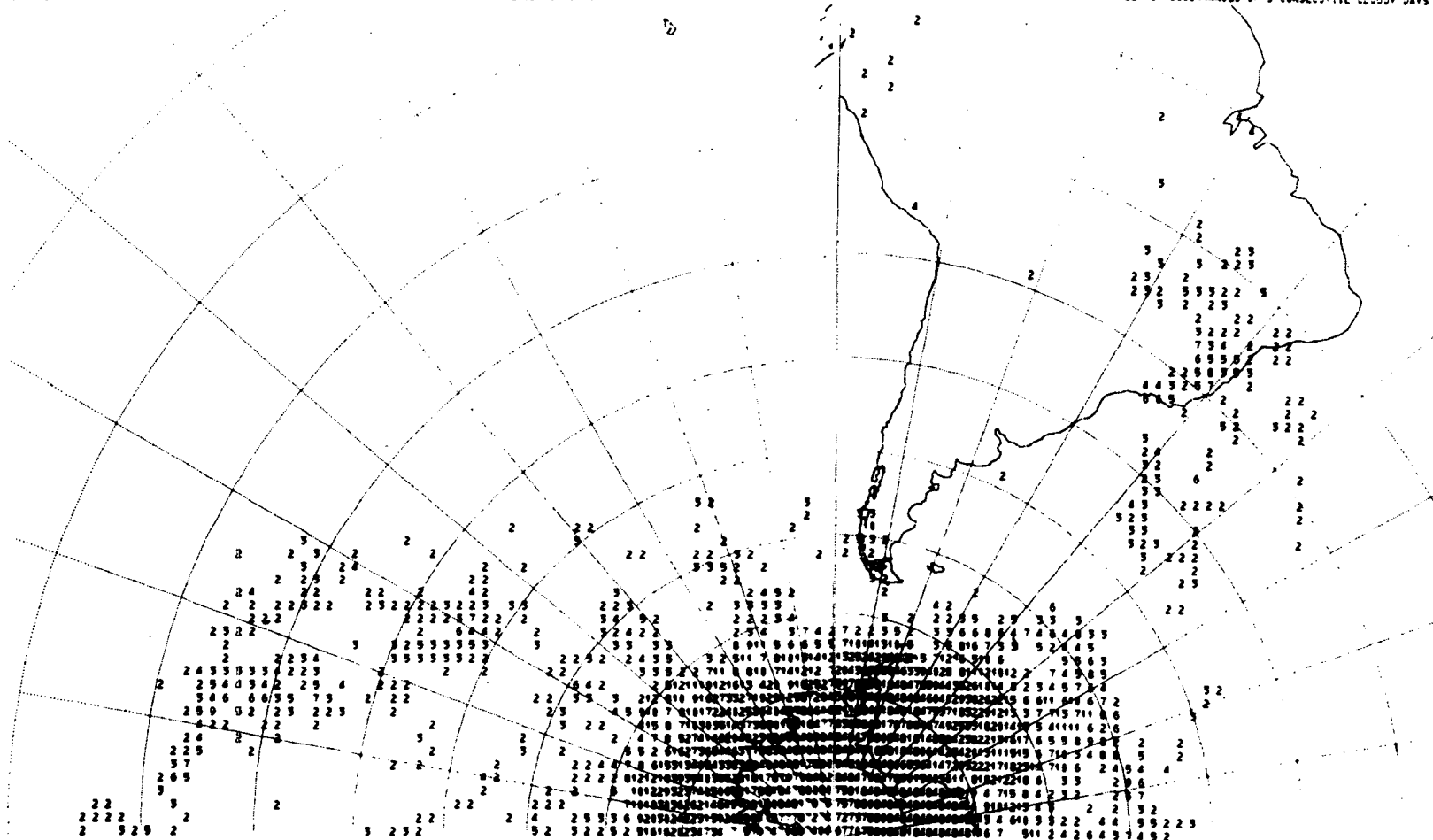


FIGURE B-5: Number of cloudy days December 1969, January 1970 and February 1970

SOUTHERN HEMISPHERE DEC69:JAN78FEB70 NUMBER OF OCCURRENCES OF 5 CONSECUTIVE CLOUDY DAYS

SOUTHERN HEMISPHERE DEC69:JAN78FEB70 NUMBER OF OCCURRENCES OF 5 CONSECUTIVE CLOUDY DAYS



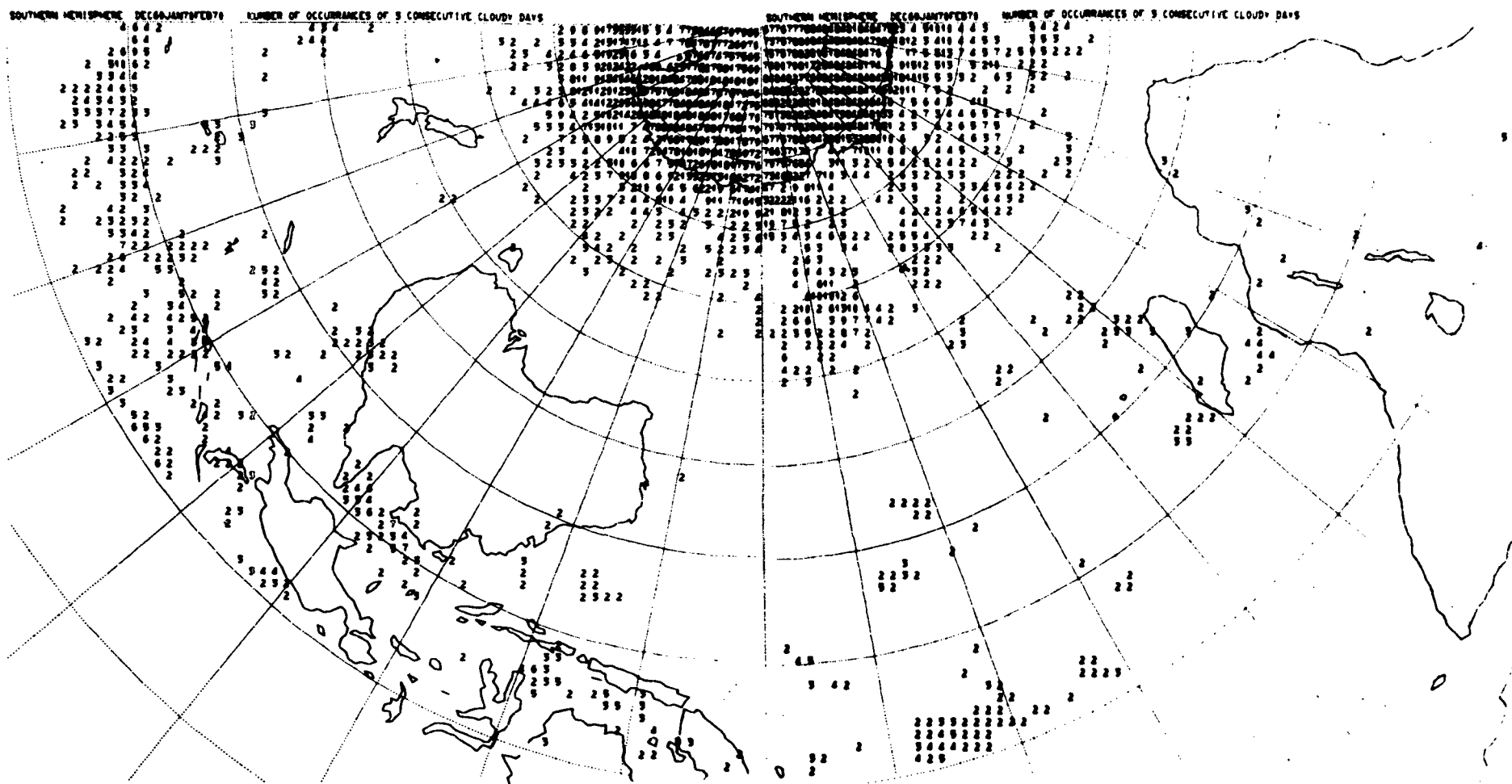
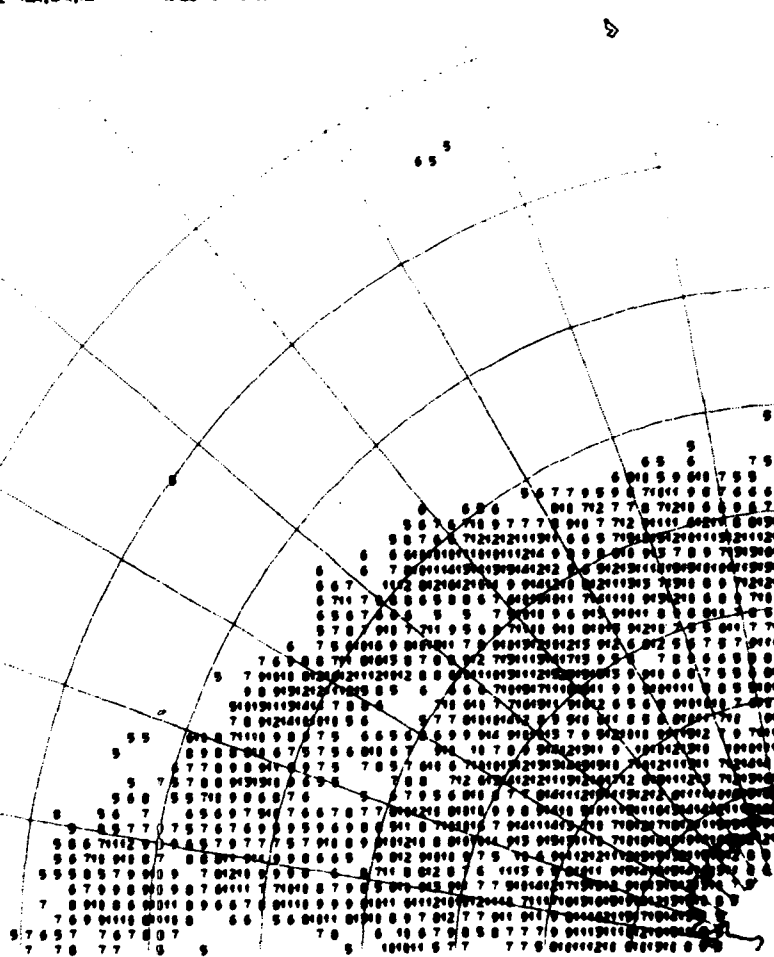


FIGURE B-6: Number of occurrences of 3 consecutive cloudy days December 1969, January 1970 and February 1970

SOUTHERN HEMISPHERE MAR, APR, MAY

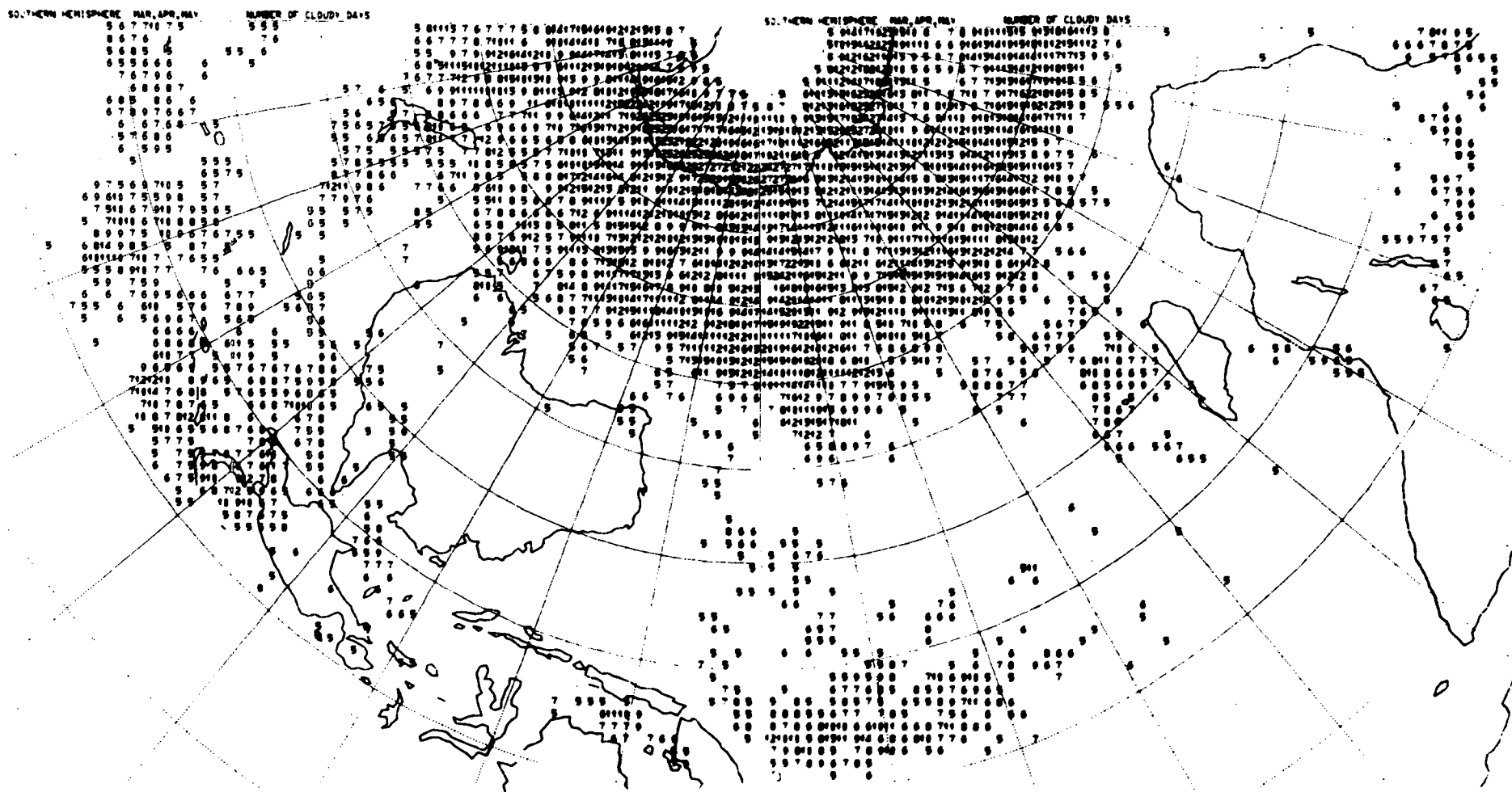
NUMBER OF CLOUDY DAYS



SOUTHERN HEMISPHERE MAR, APR, MAY

NUMBER OF CLOUDY DAYS





Reproduced from
best available copy.

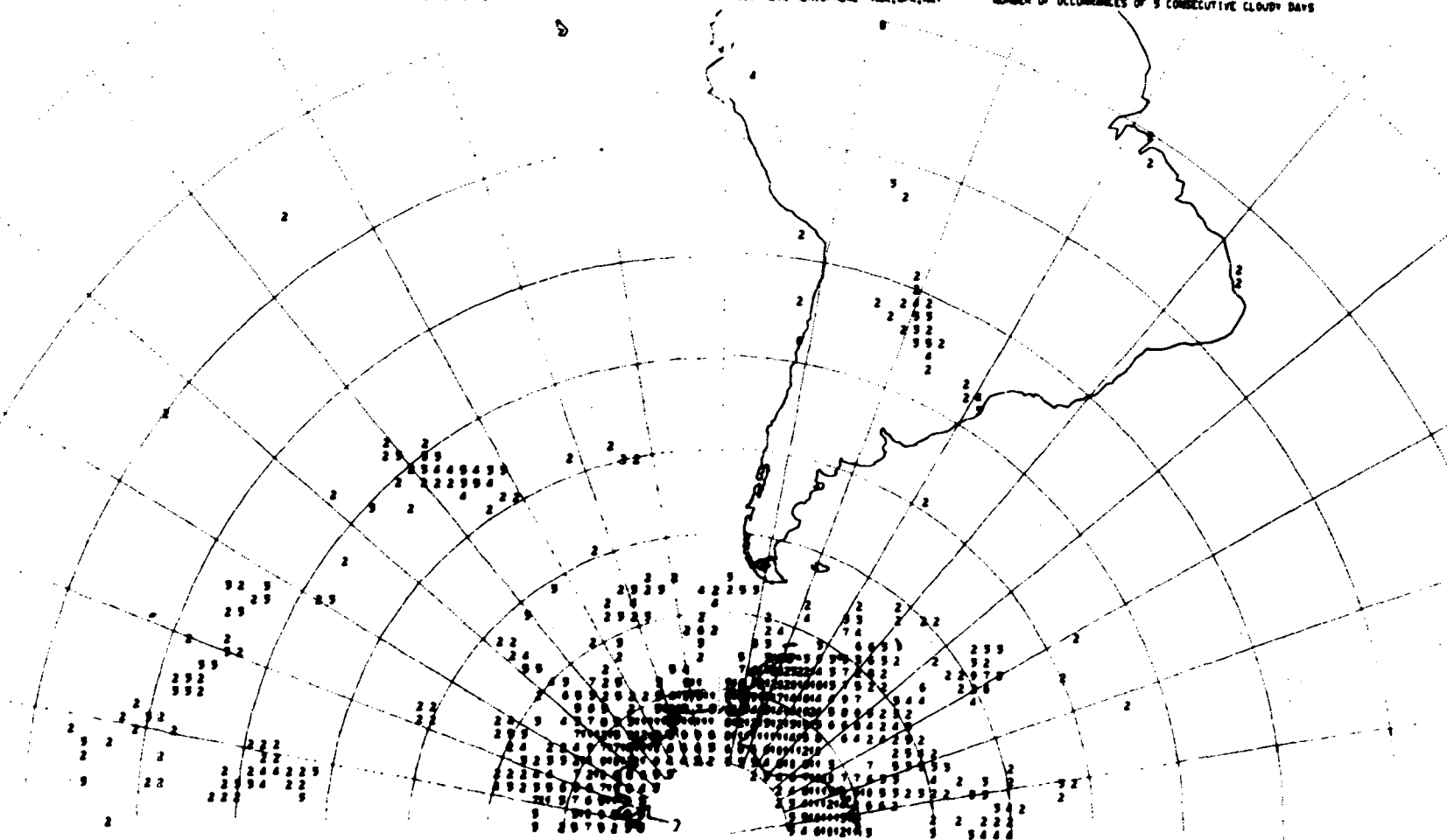
FIGURE B-7: Number of cloudy days March 1970, April 1969 and May 1969

SOUTHERN HEMISPHERE MAR, APR, MAY

NUMBER OF OCCURRENCES OF 5 CONSECUTIVE CLOUDY DAYS

SOUTHERN HEMISPHERE MAR, APR, MAY

NUMBER OF OCCURRENCES OF 5 CONSECUTIVE CLOUDY DAYS



SOUTHERN HEMISPHERE MAR, APR, MAY

NUMBER OF OCCURRENCES OF 3 CONSECUTIVE CLOUDY DAYS

SOUTHERN HEMISPHERE MAR, APR, MAY

NUMBER OF OCCURRENCES OF 3 CONSECUTIVE CLOUDY DAYS

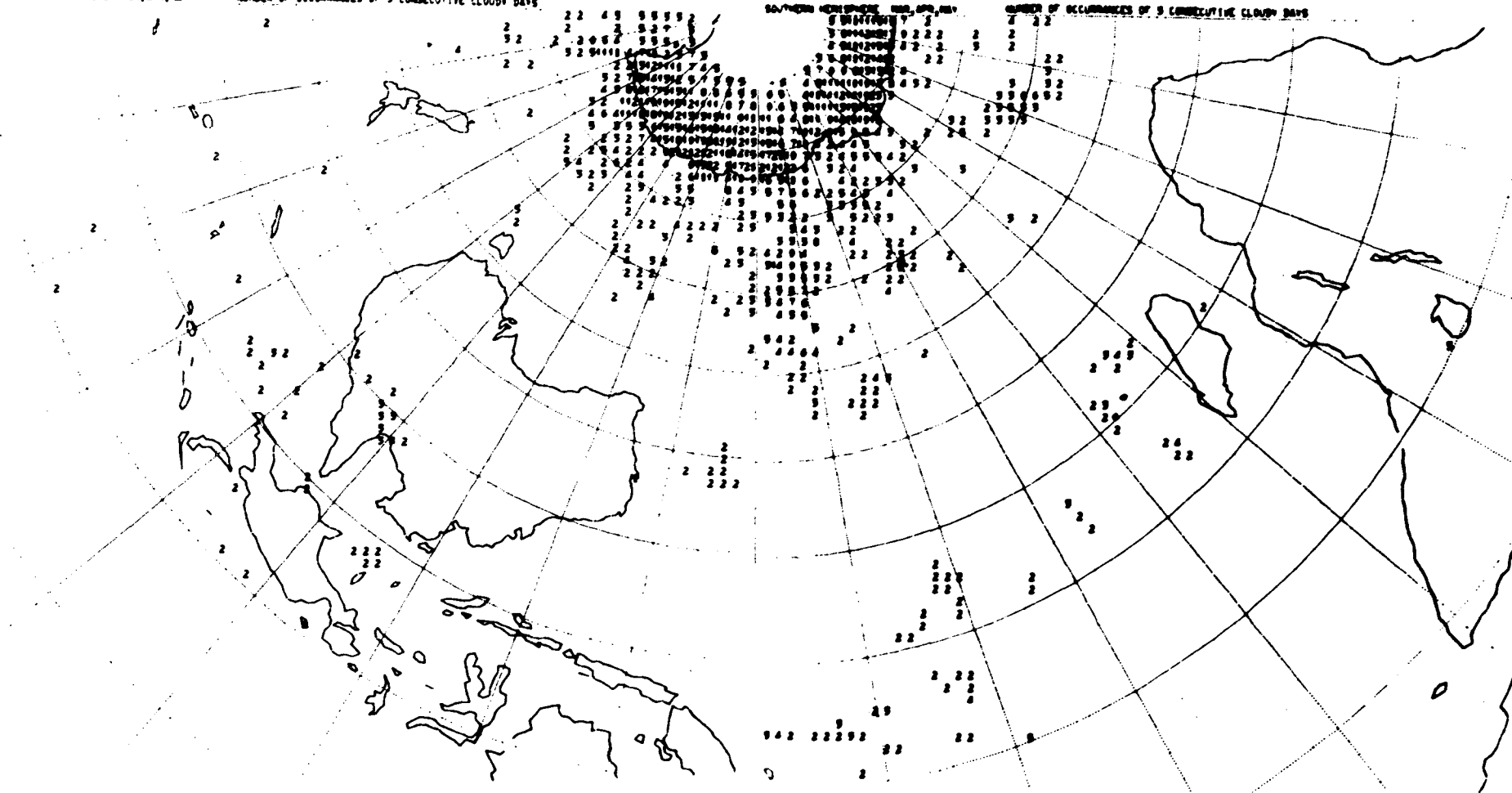
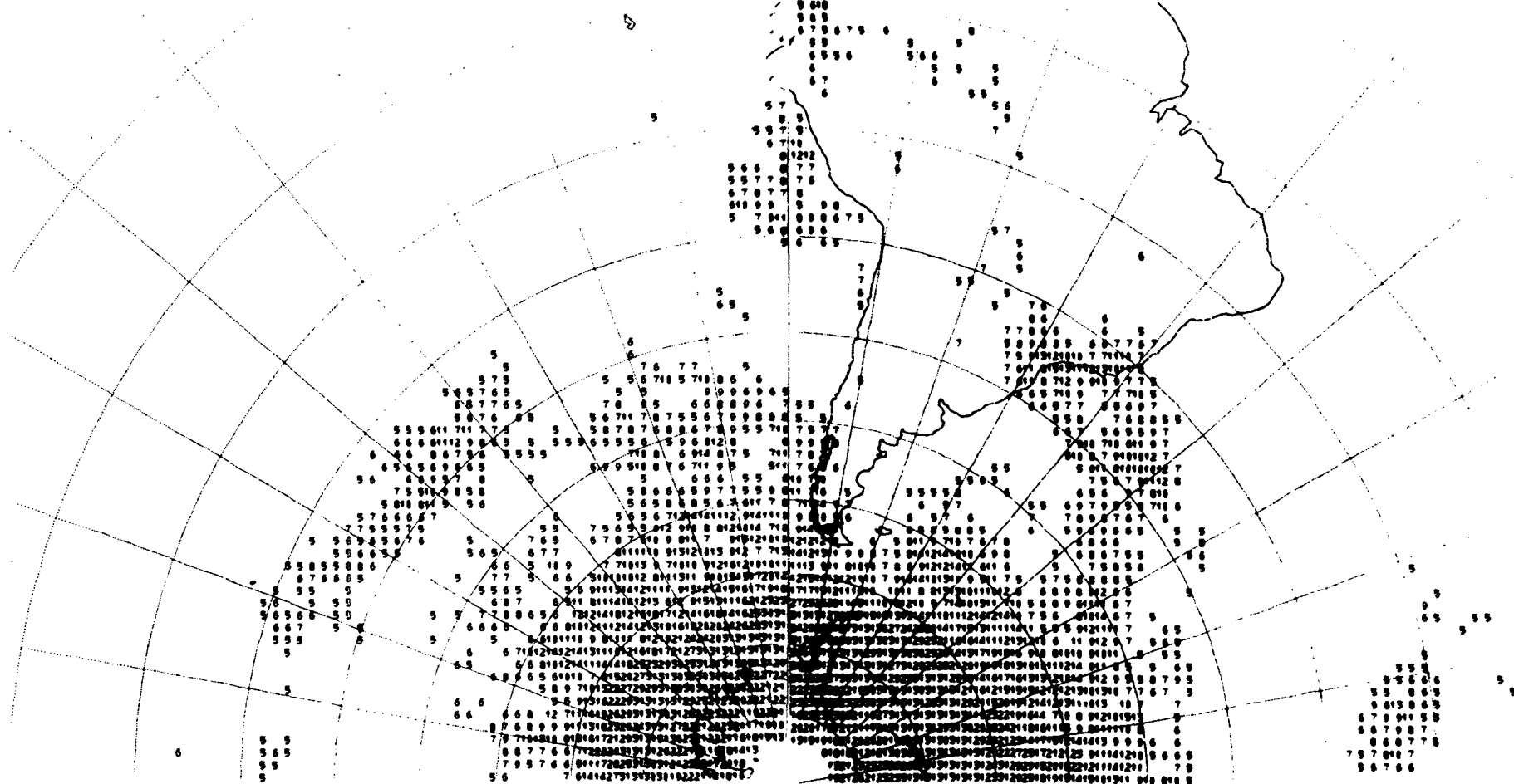


FIGURE B-8: Number of occurrences of 3 consecutive cloudy days March 1970, April 1969 and May 1969

SOUTHERN HEMISPHERE OCT 1-31, 1969 NUMBER OF CLOUDY DAYS

SOUTHERN HEMISPHERE OCT 1-31, 1969 NUMBER OF CLOUDY DAYS



SOUTHERN HEMISPHERE OCT 1-31, 1969 NUMBER OF CLOUDY DAYS

SOUTHERN HEMISPHERE OCT 1-31, 1969 NUMBER OF CLOUDY DAYS

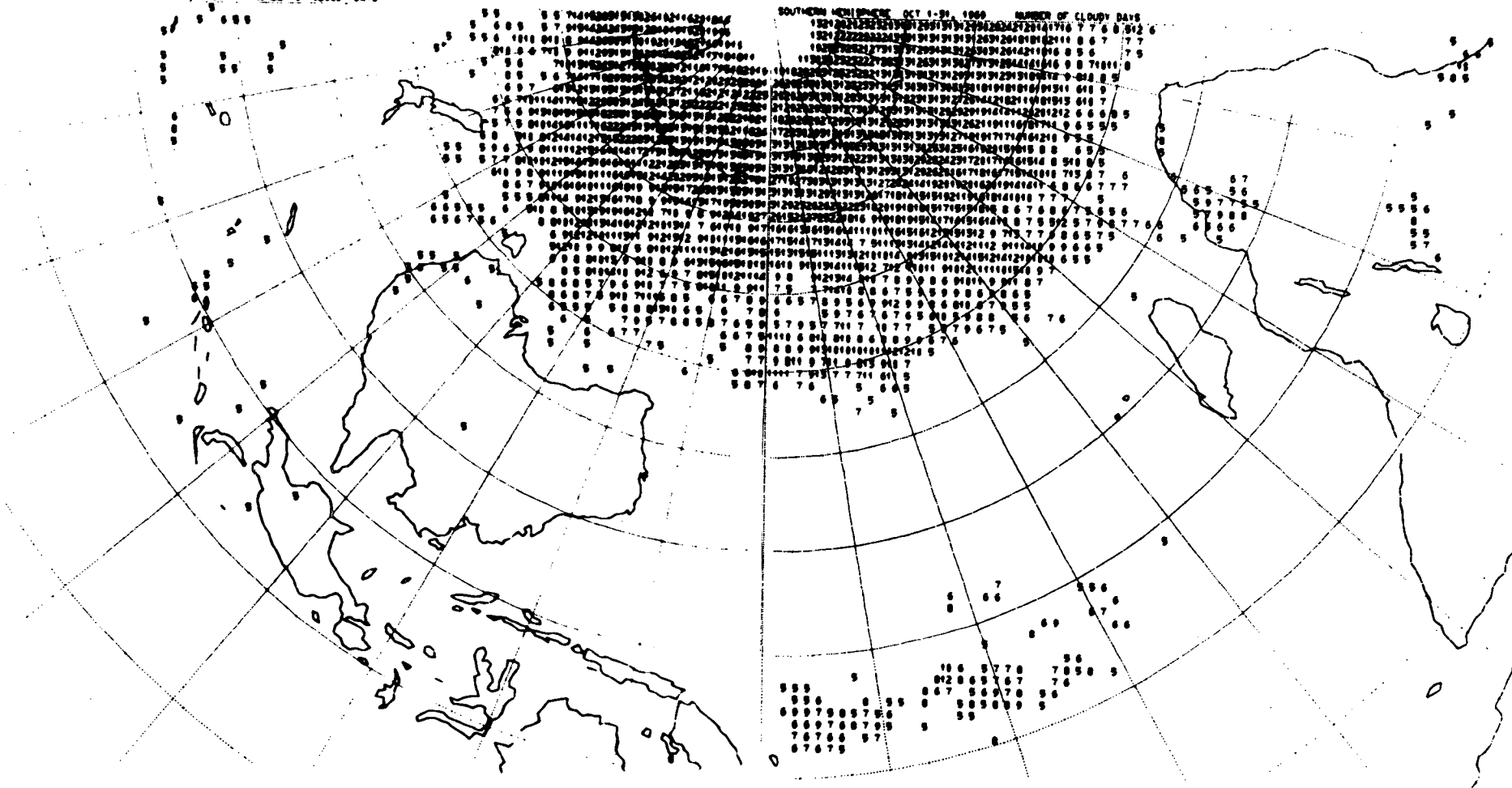


FIGURE C-1: Number of cloudy days October 1969

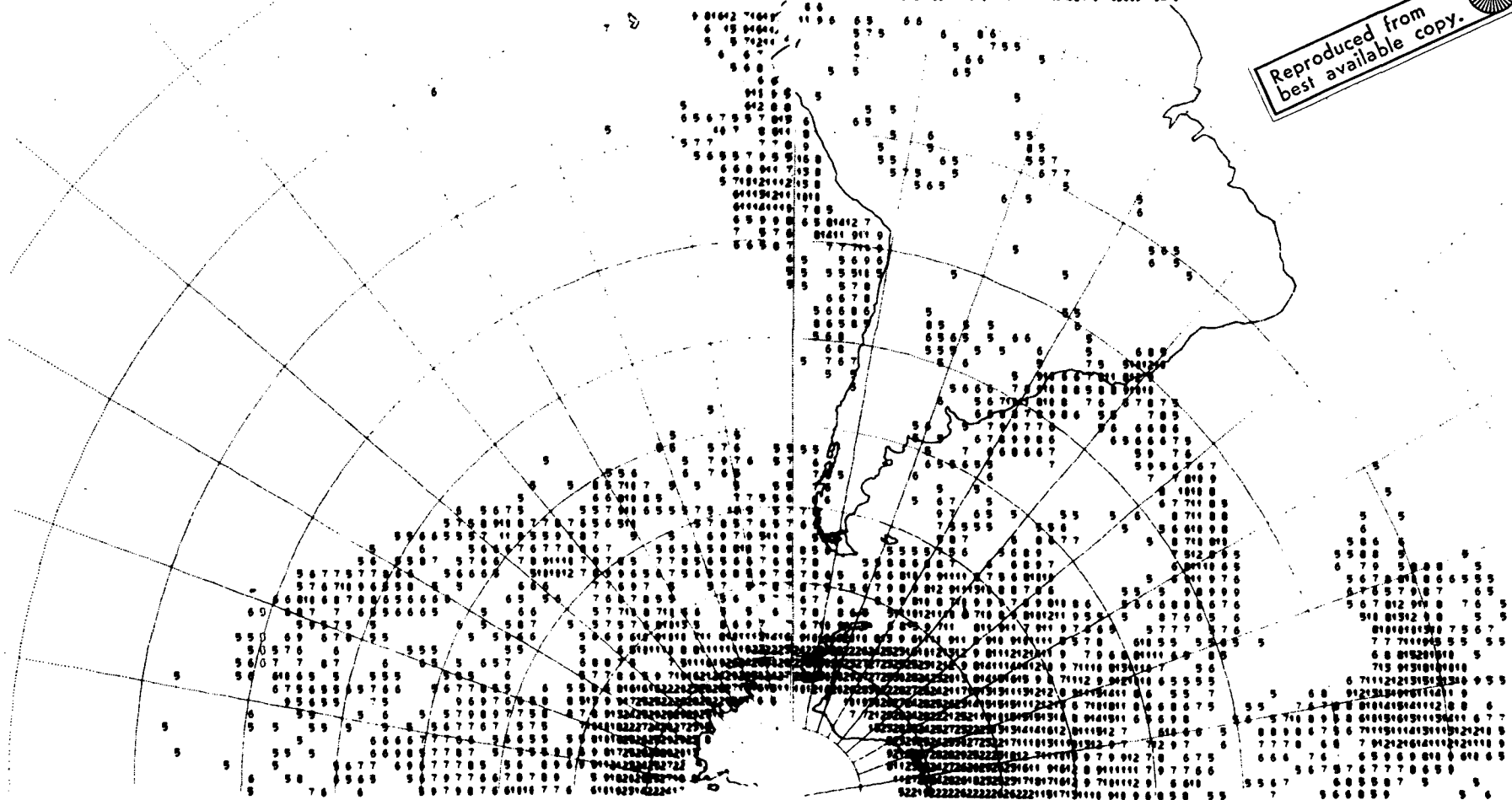
SOUTHERN HEMISPHERE OCT 1-31, 1970

NUMBER OF CLOUDY DAYS

SOUTHERN HEMISPHERE OCT 1-31, 1970

NUMBER OF CLOUDY DAYS

Reproduced from
best available copy.



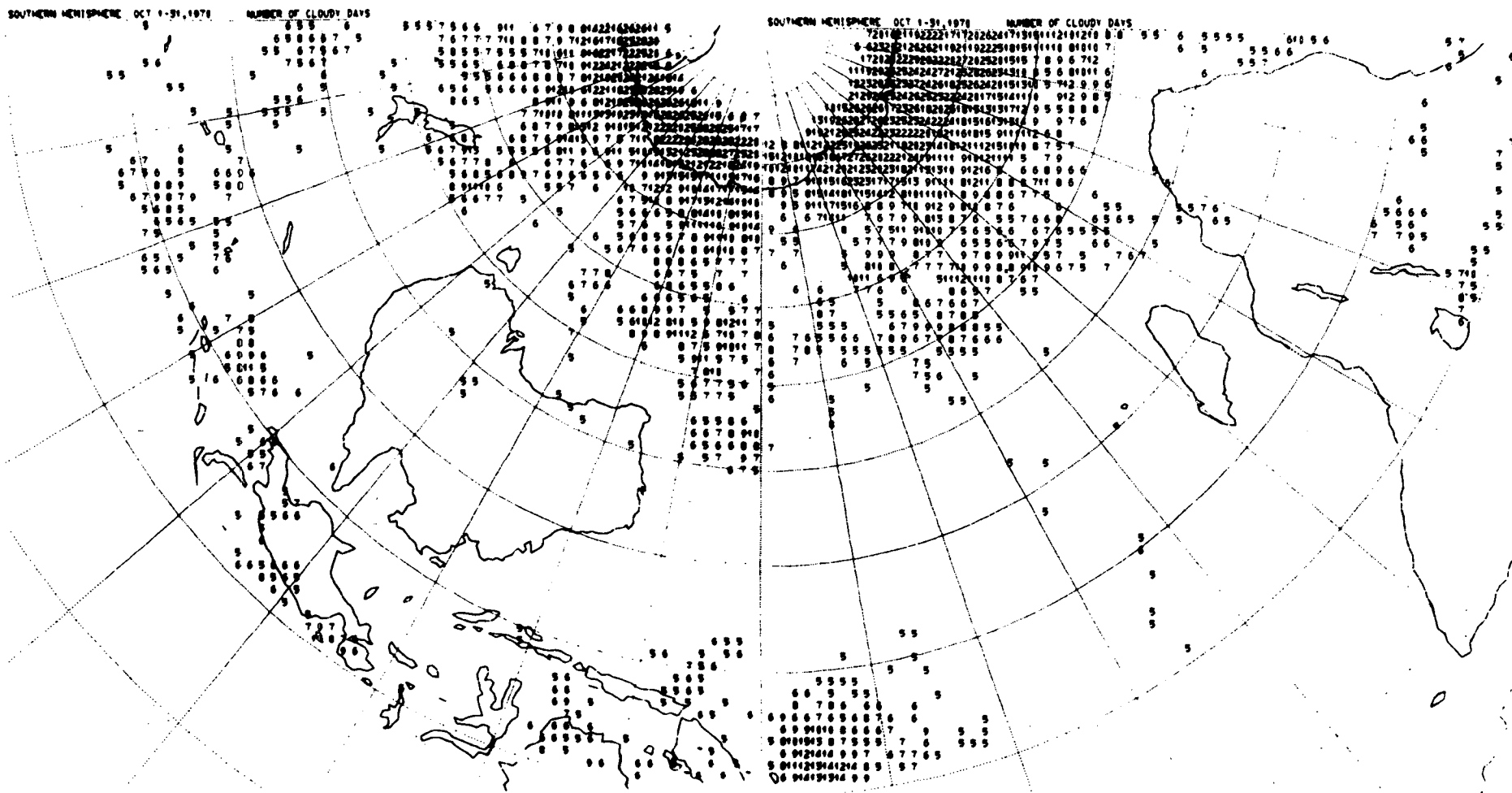
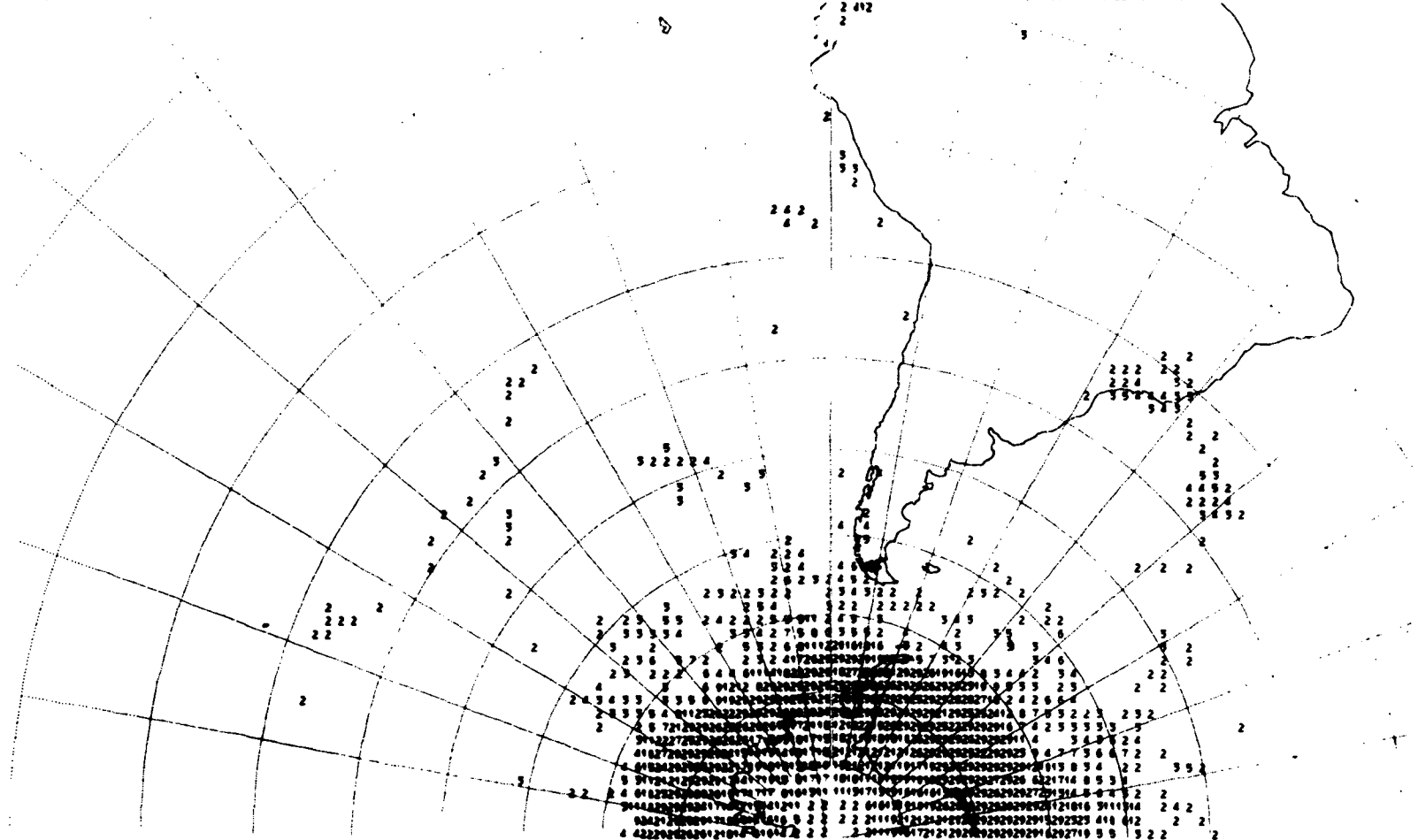


FIGURE C-2: Number of cloudy days October 1970

SOUTHERN HEMISPHERE OCT 1-31, 1969 NUMBER OF OCCURRENCES OF 9 CONSECUTIVE CLOUDY DAYS

SOUTHERN HEMISPHERE OCT 1-31, 1969 NUMBER OF OCCURRENCES OF 9 CONSECUTIVE CLOUDY DAYS



SOUTHERN HEMISPHERE OCT 1-31, 1969 NUMBER OF OCCURRENCES OF 3 CONSECUTIVE CLOUDY DAYS

SOUTHERN HEMISPHERE OCT 1-31, 1969 NUMBER OF OCCURRENCES OF 3 CONSECUTIVE CLOUDY DAYS

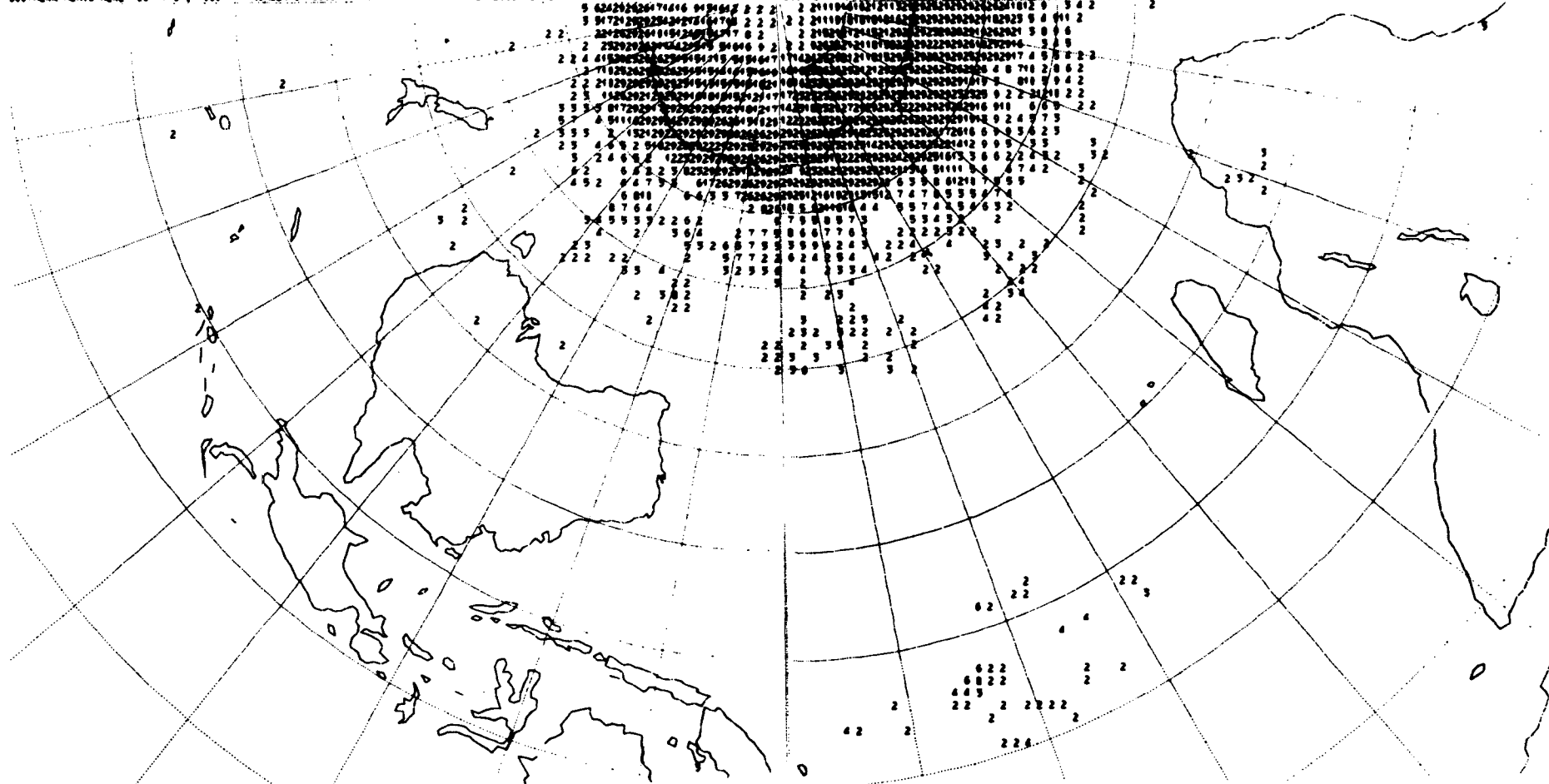
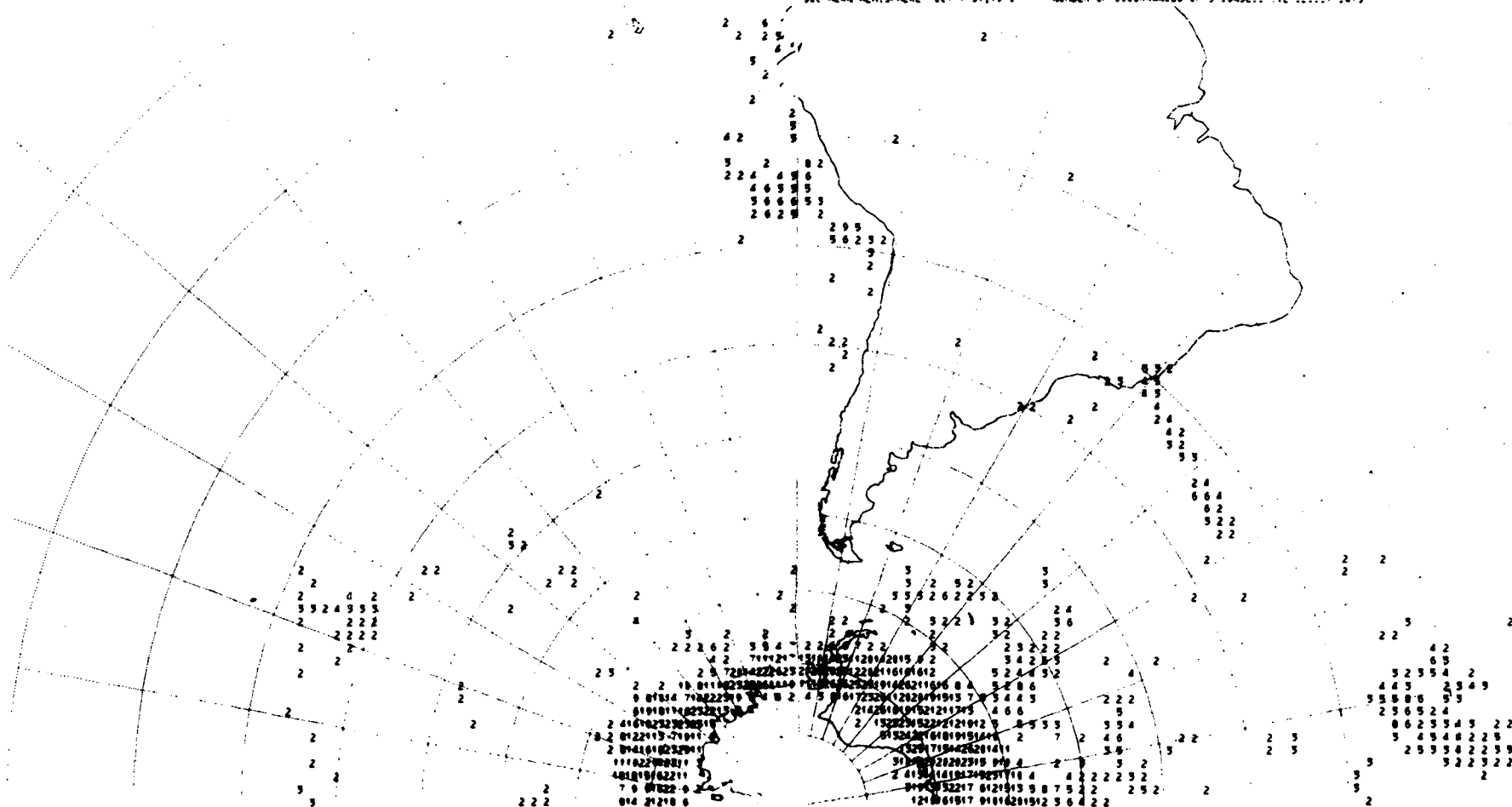


FIGURE C-3: Number of occurrences of 3 consecutive cloudy days October 1969

SOUTHERN HEMISPHERE OCT 1-31, 1970

NUMBER OF OCCURRENCES OF 3 CONSECUTIVE CLOUDY DAYS

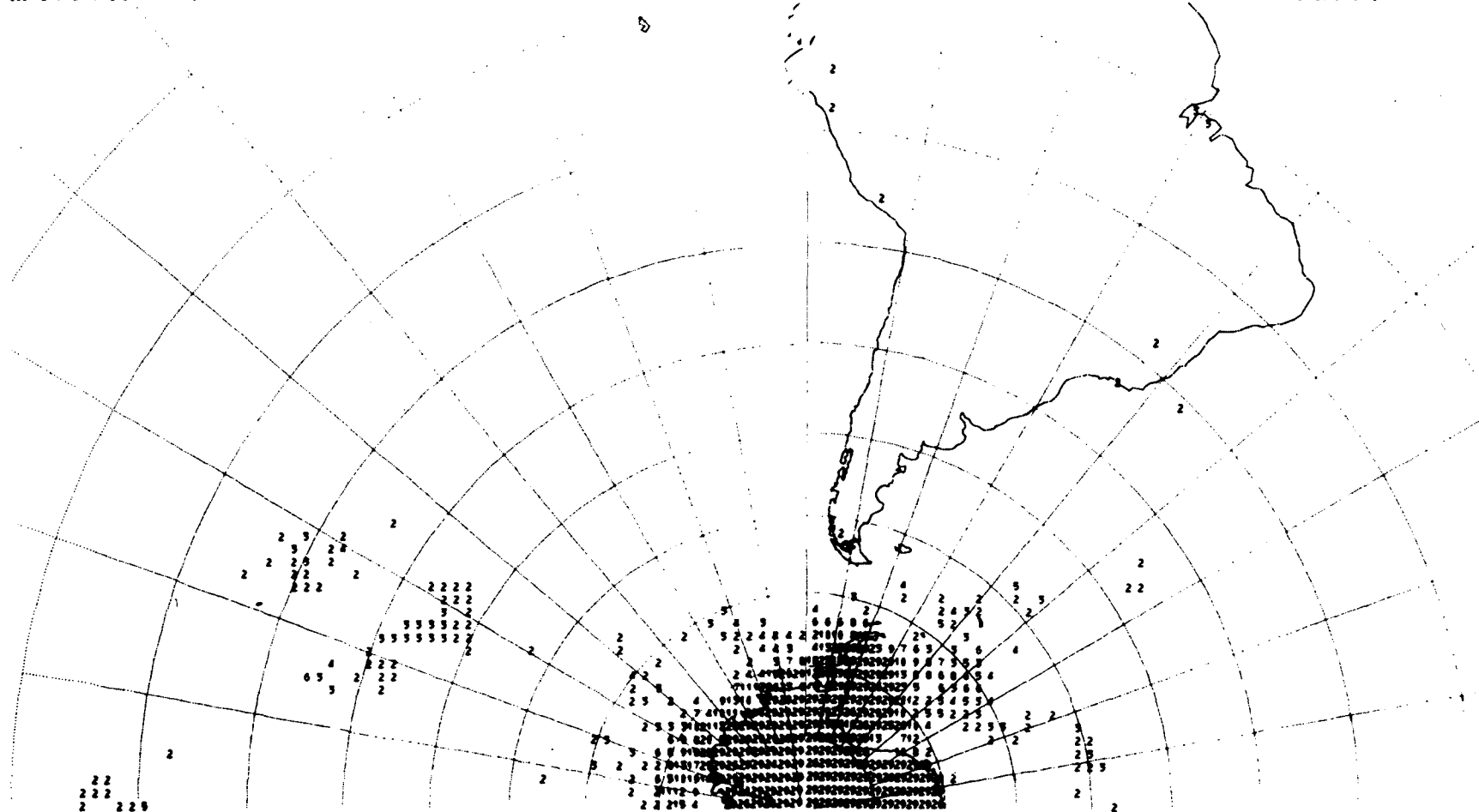


SOUTHERN HEMISPHERE OCT 1-31, 1970

NUMBER OF OCCURRENCES OF 3 CONSECUTIVE 1000, 24.5

SOUTHERN HEMISPHERE JAN 1-31, 1970 NUMBER OF OCCURRENCES OF 3 CONSECUTIVE CLOUDY DAYS

SOUTHERN HEMISPHERE JAN 1-31, 1970 NUMBER OF OCCURRENCES OF 3 CONSECUTIVE CLOUDY DAYS



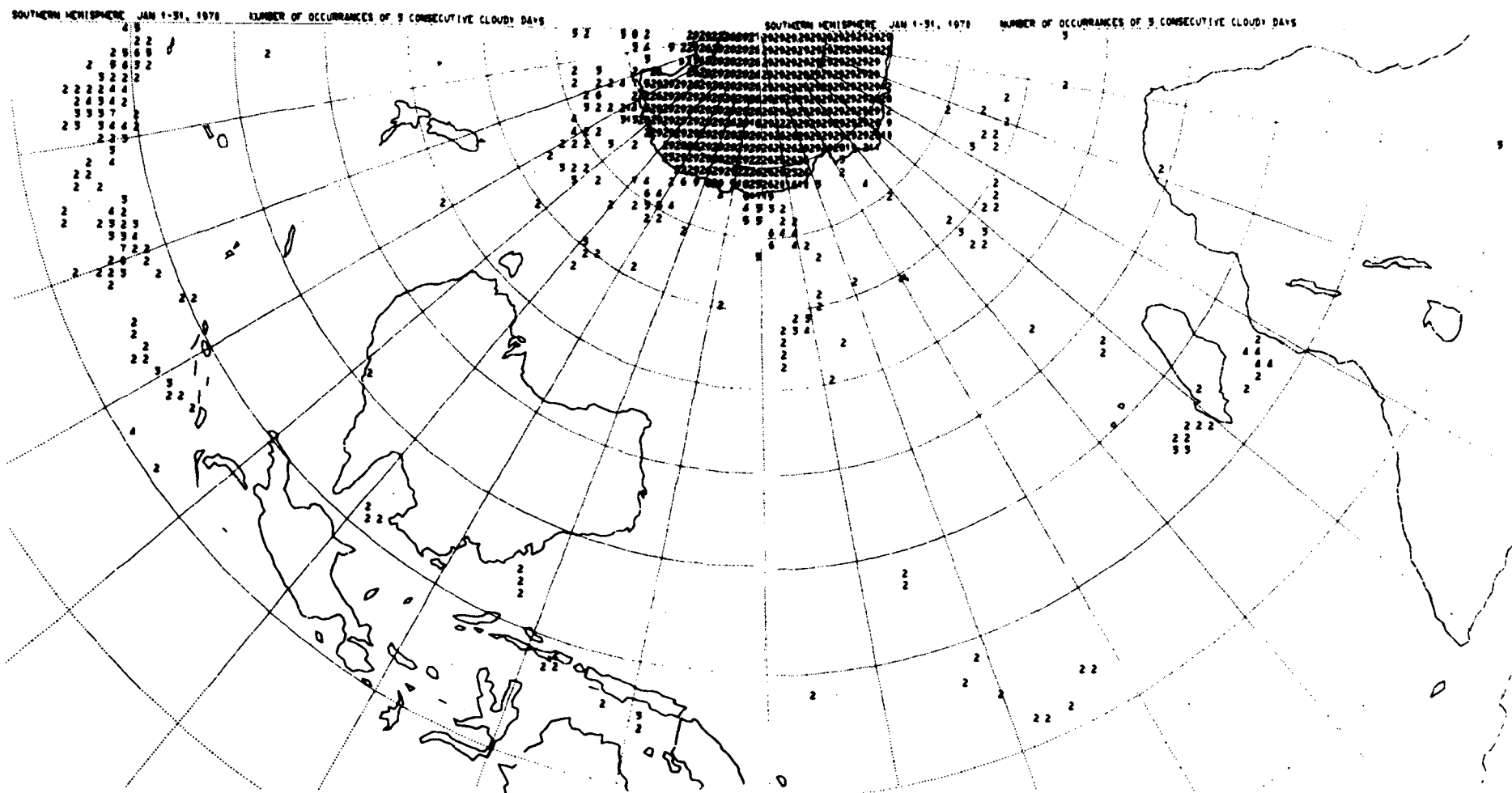


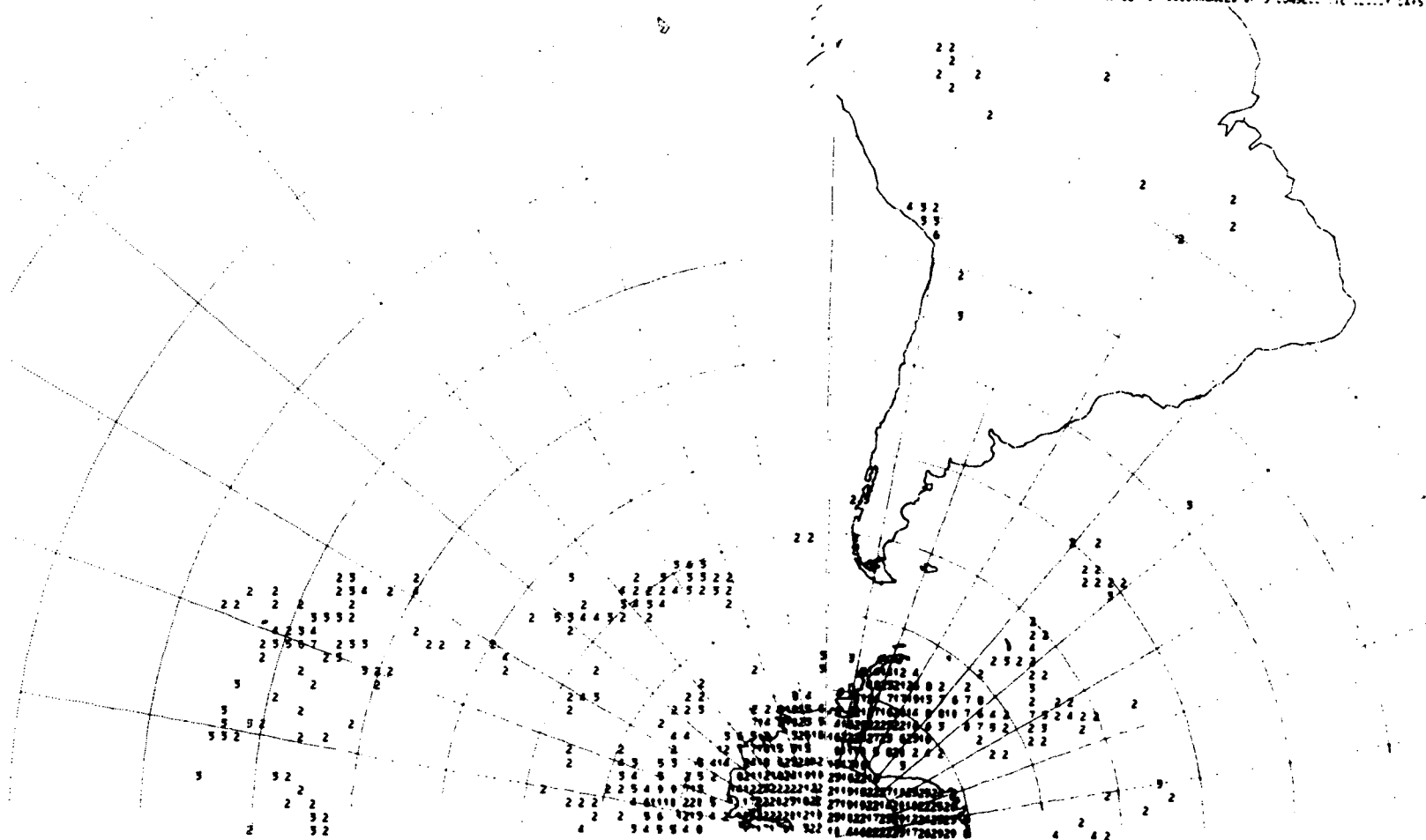
FIGURE C-5: Number of occurrences of 3 consecutive cloudy days January 1970

SOUTHERN HEMISPHERE JAN 1-31, 1971

NUMBER OF OCCURRENCES OF 3 CONSECUTIVE CLOUDY DAYS

SOUTHERN HEMISPHERE JAN 1-31, 1971

NUMBER OF OCCURRENCES OF 3 CONSECUTIVE CLOUDY DAYS



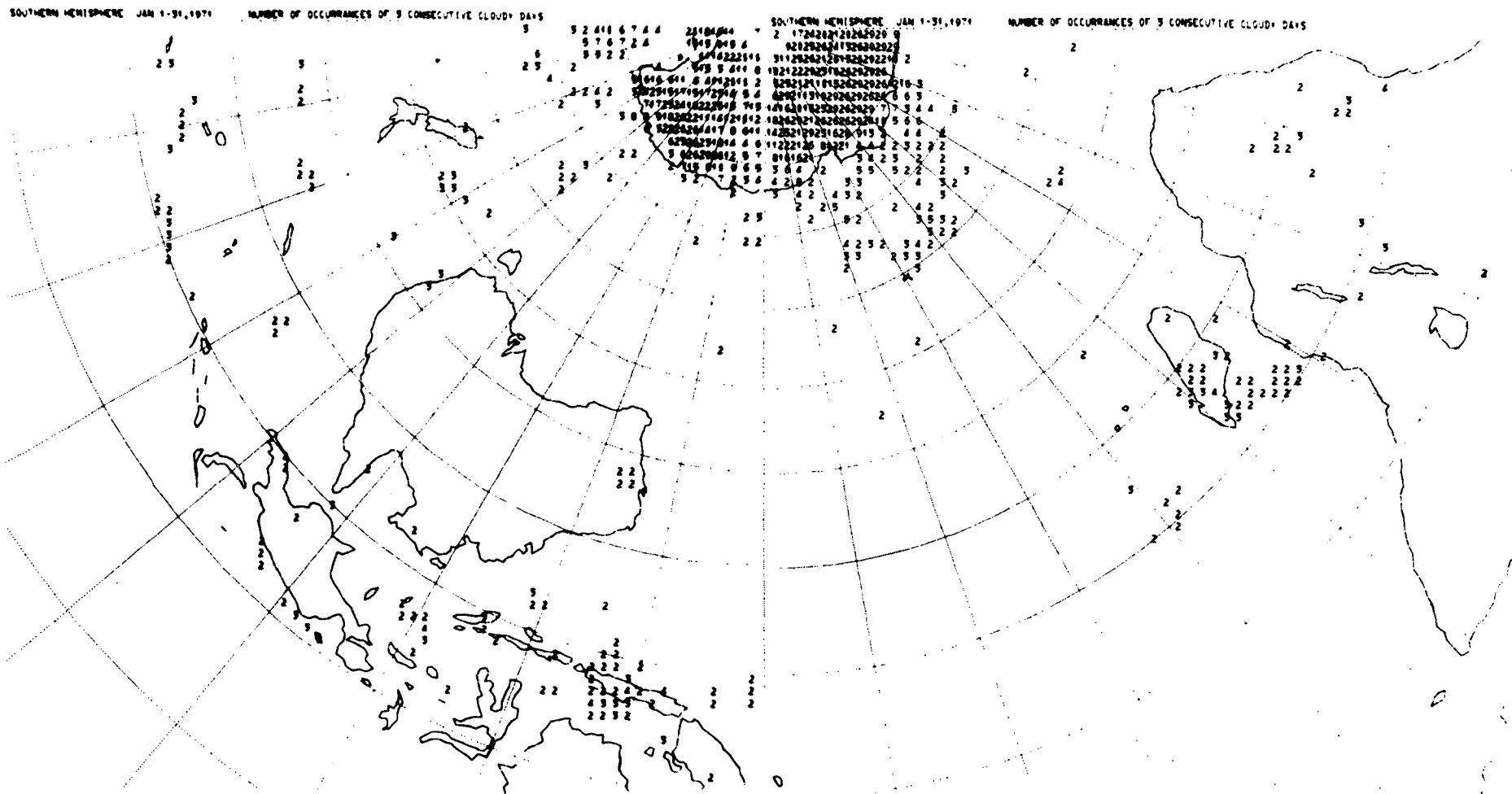


FIGURE C-6: Number of occurrences of 3 consecutive cloudy days January 1971

NORTHERN HEMISPHERE ANNUAL

NUMBER OF CLOUDY DAYS

NORTHERN HEMISPHERE ANNUAL

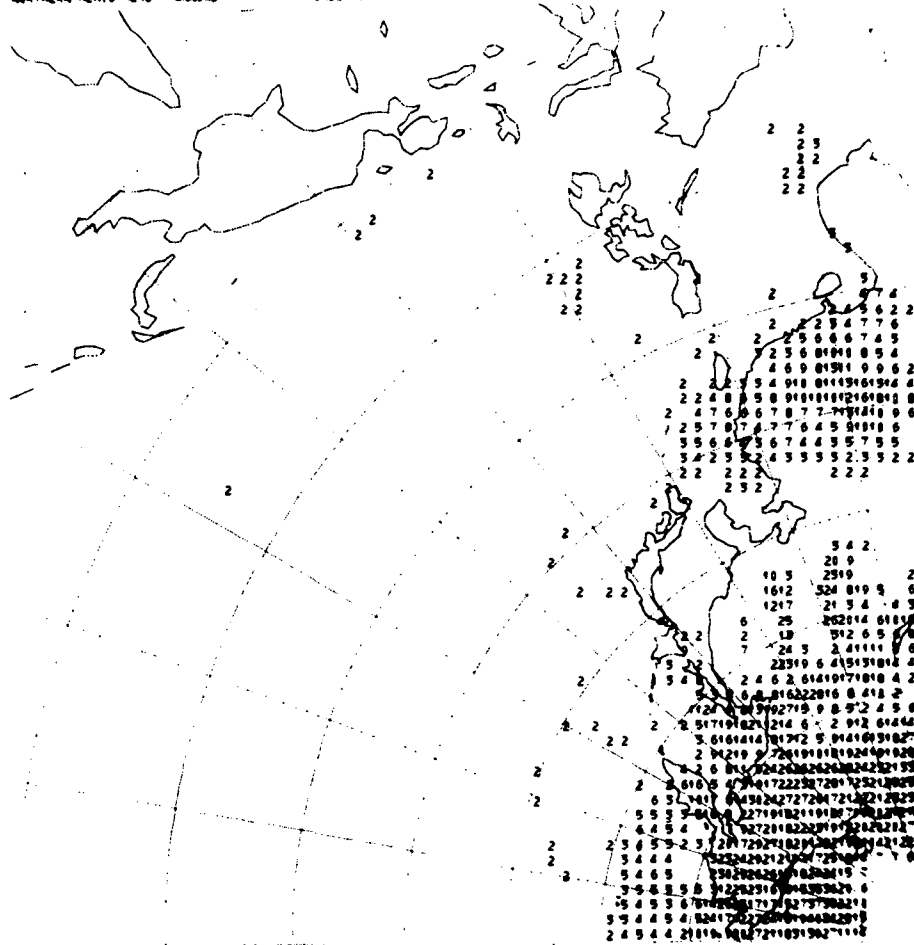
NUMBER OF CLOUDY DAYS

Reproduced from
best available copy.



NORTHERN HEMISPHERE ANNUAL

NUMBER OF OCCURRENCES OF 5 CONSECUTIVE CLOUDY DAYS



NORTHERN HEMISPHERE ANNUAL

NUMBER OF OCCURRENCES OF 5 CONSECUTIVE CLOUDY DAYS



NORTHERN HEMISPHERE ANNUAL

NUMBER OF OCCURRENCES OF 3 CONSECUTIVE CLOUDY DAYS

NORTHERN HEMISPHERE ANNUAL

NUMBER OF OCCURRENCES OF 3 CONSECUTIVE CLOUDY DAYS

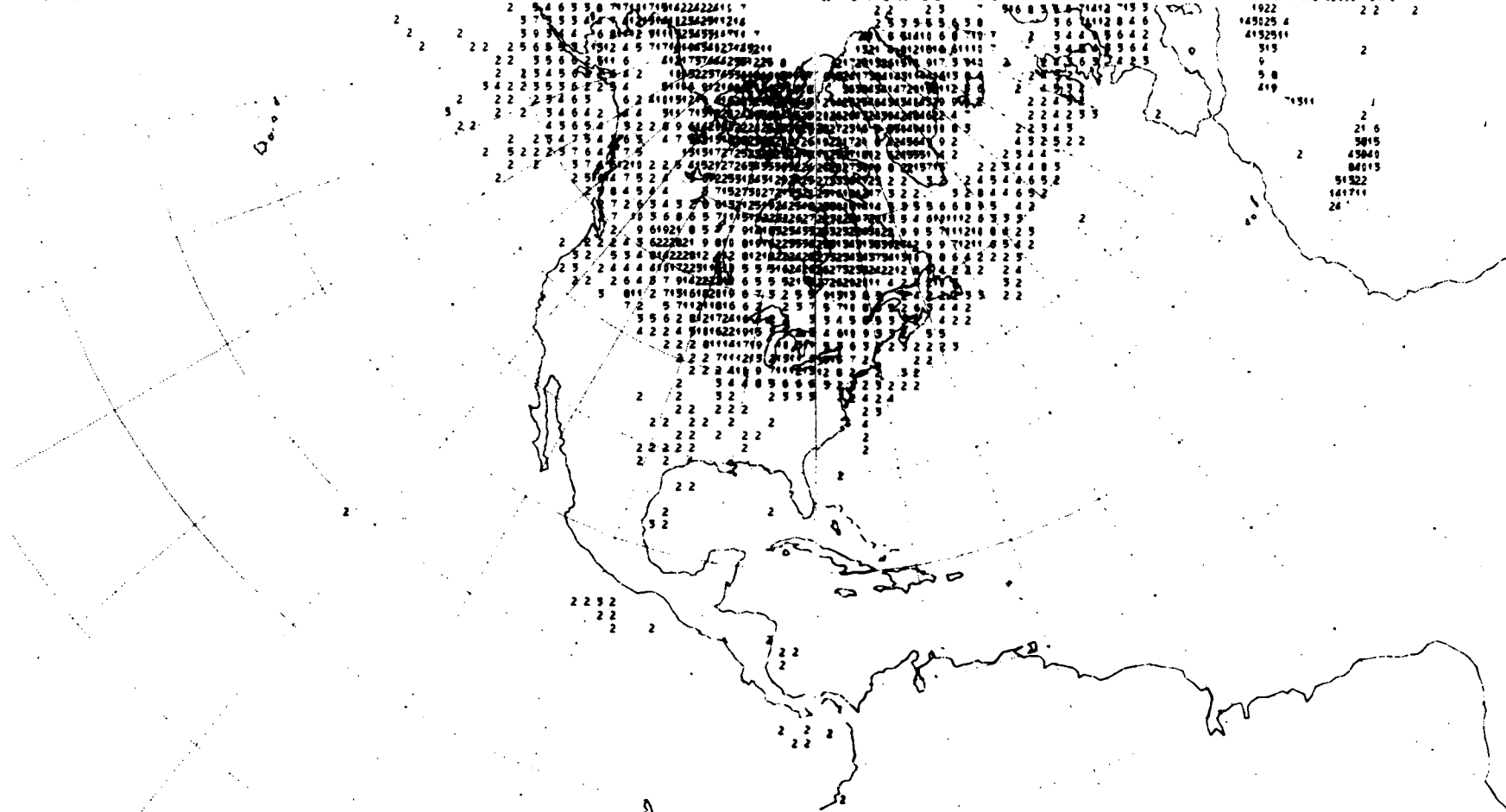


FIGURE D-2: Number of occurrences of 3 consecutive cloudy days (annual)

SOUTHERN HEMISPHERE ANNUAL

NUMBER OF CLOUDY DAYS

SOUTHERN HEMISPHERE ANNUAL

NUMBER OF CLOUDY DAYS



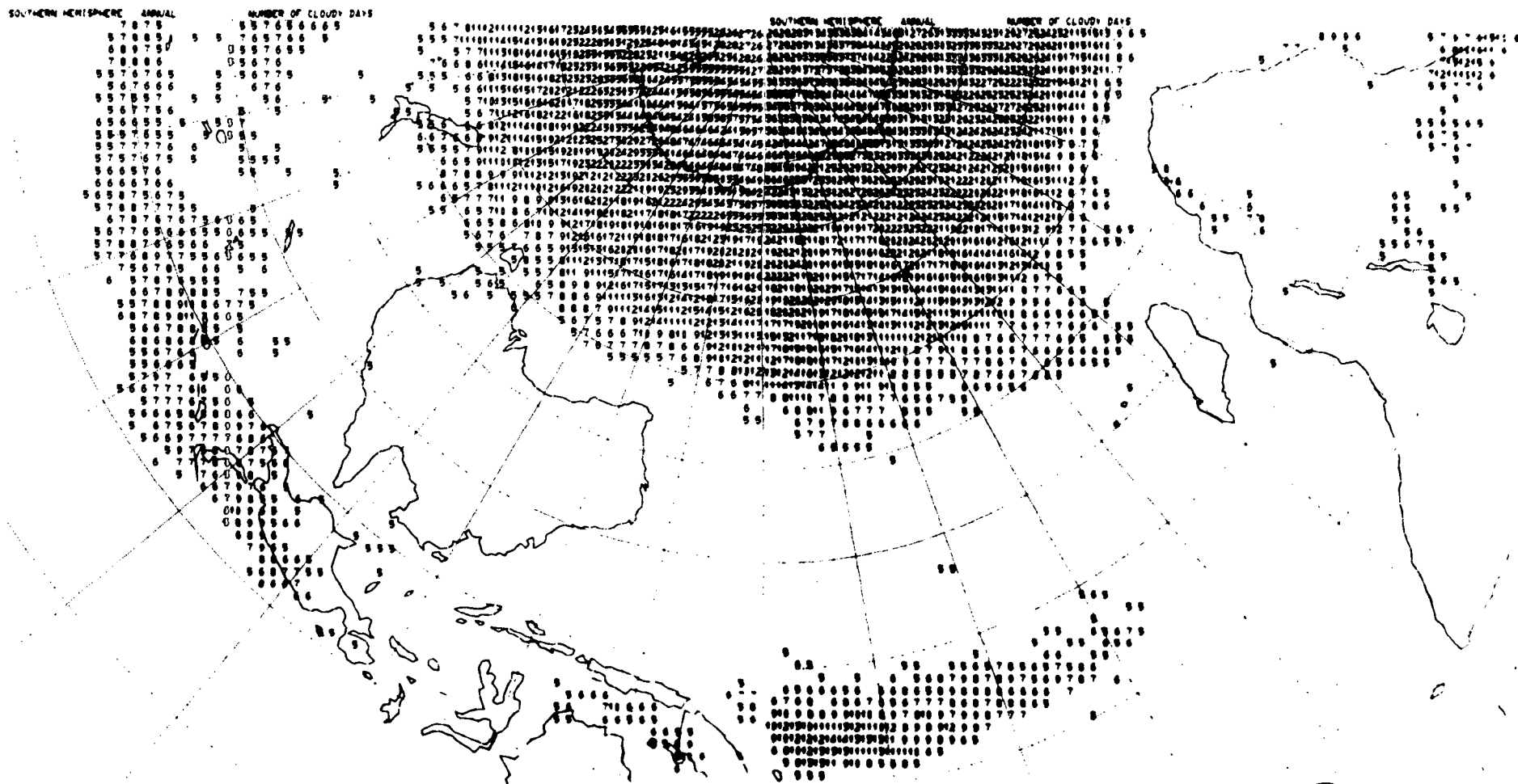


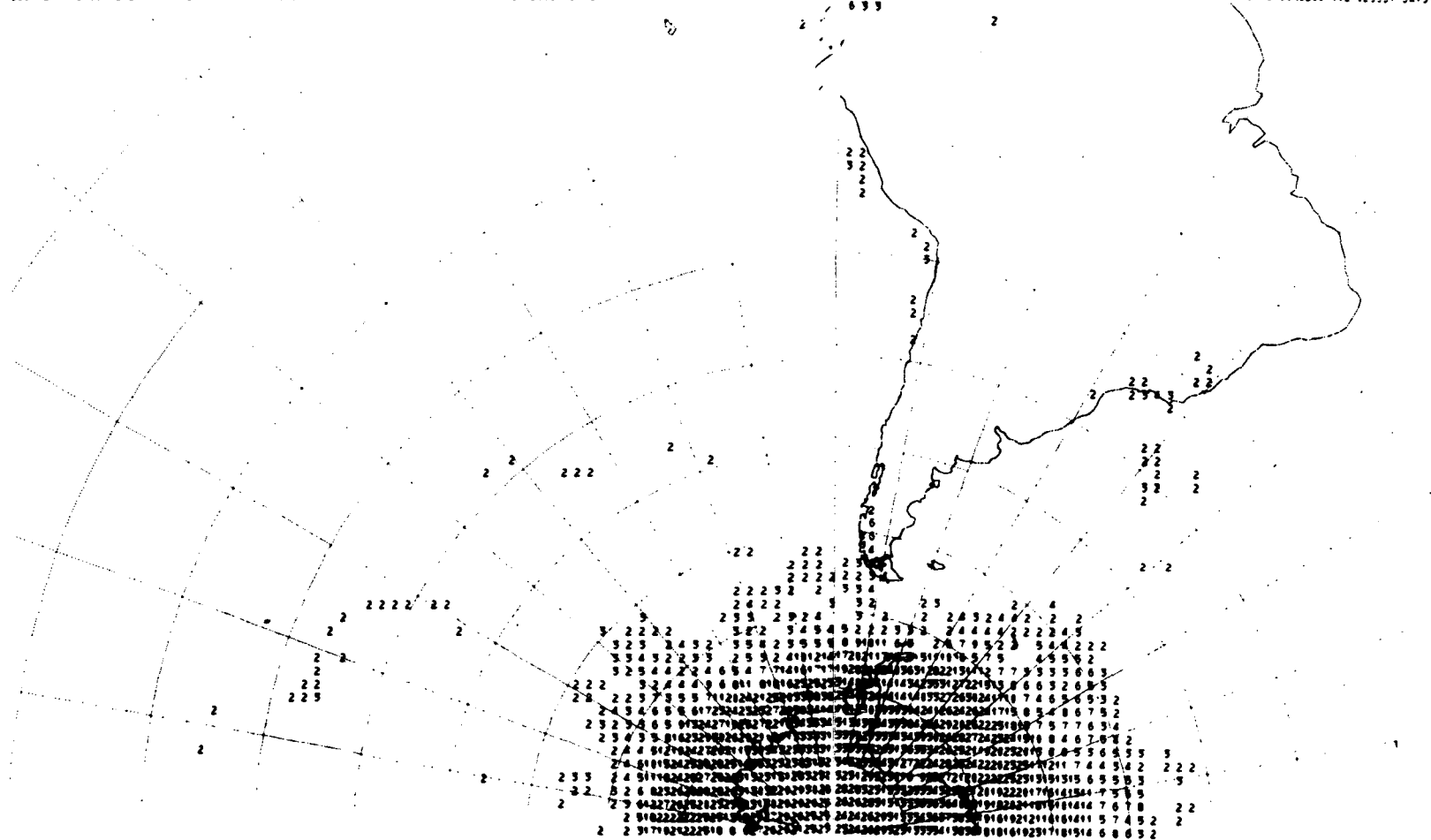
FIGURE D-3: Number of cloudy days (annual)

SOUTHERN HEMISPHERE ANNUAL

NUMBER OF OCCURRENCES OF 5 CONSECUTIVE CLOUDY DAYS

SOUTHERN HEMISPHERE ANNUAL

NUMBER OF OCCURRENCES OF 5 CONSECUTIVE CLOUDY DAYS



SOUTHERN HEMISPHERE ANNUAL

NUMBER OF OCCURRENCES OF 3 CONSECUTIVE CLOUDY DAYS

SOUTHERN HEMISPHERE ANNUAL

NUMBER OF OCCURRENCES OF 3 CONSECUTIVE CLOUDY DAYS

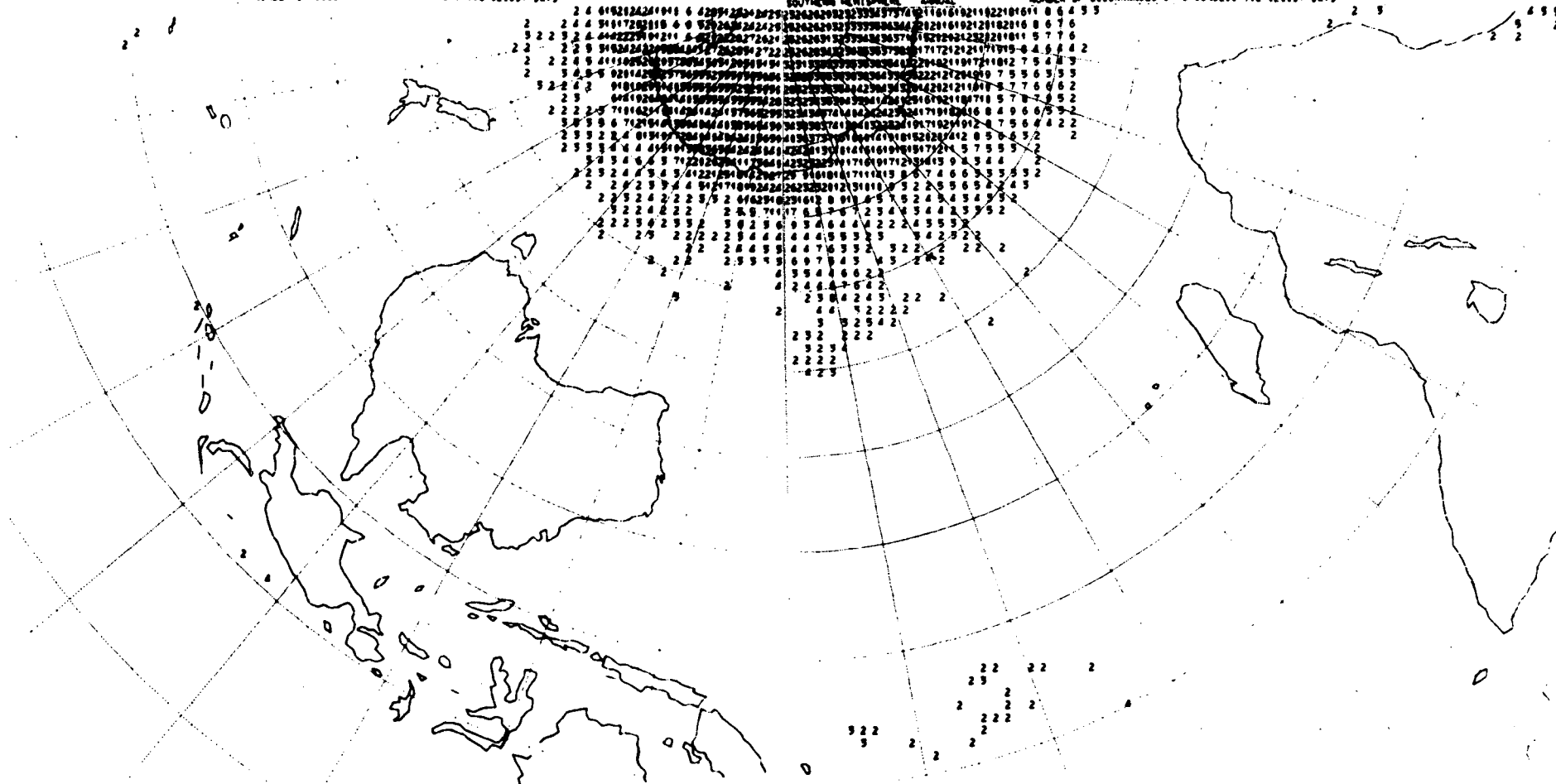


FIGURE D-4: Number of occurrences of 3 consecutive cloudy days (annual)